Electronic Thesis and Dissertation Repository

8-11-2014 12:00 AM

Functional Imaging of Malignant Gliomas with CT Perfusion

Timothy Pok Chi Yeung
The University of Western Ontario

Supervisor
Drs. Glenn Bauman
The University of Western Ontario Joint Supervisor
Slav Yartsev
The University of Western Ontario

Recommended Citation

Functional Imaging of Malignant Gliomas with CT Perfusion

(Thesis format: Integrated Article)

by

Timothy Pok Chi <u>Yeung</u>

Graduate Program in Medical Biophysics

A thesis submitted in partial fulfillment
of the requirements for the degree of
Doctor of Philosophy

The School of Graduate and Postdoctoral Studies
The University of Western Ontario
London, Ontario, Canada

Abstract

The overall survival of patients with malignant gliomas remains dismal despite multimodality treatments. Computed tomography (CT) perfusion is a functional imaging tool for assessing tumour hemodynamics. The goals of this thesis are to 1) improve measurements of various CT perfusion parameters and 2) assess treatment outcomes in a rat glioma model and in patients with malignant gliomas.

Chapter 2 addressed the effect of scan duration on the measurements of blood flow (BF), blood volume (BV), and permeability-surface area product (PS). Measurement errors of these parameters increased with shorter scan duration. A minimum scan duration of 90 s is recommended.

Chapter 3 evaluated the improvement in the measurements of these parameters by filtering the CT perfusion images with principal component analysis (PCA). From computer simulation, measurement errors of BF, BV, and PS were found to be reduced. Experiments showed that CT perfusion image contrast-to-noise ratio was improved.

Chapter 4 investigated the efficacy of CT perfusion as a potential early imaging biomarker of response to stereotactic radiosurgery (SRS). Using the C6 glioma model, we showed that responders to SRS (surviving > 15 days) had lower relative BV and PS on day 7 post-SRS when compared to controls and non-responders ($P < 0.05$). Relative BV and PS on day 7 post-SRS were predictive of survival with 92% accuracy.

Chapter 5 examined the use of multiparametric imaging with CT perfusion and 18F-Fluorodeoxyglucose positron emission tomography (FDG-PET) to identify tumour sites that are likely to correlate with the eventual location of tumour progression. We developed a method to generate probability maps of tumour progression based on these imaging data.

Chapter 6 investigated serial changes in tumour volumetric and CT perfusion parameters and their predictive ability in stratifying patients by overall survival. Pre-surgery BF in the non-enhancing lesion and BV in the contrast-enhancing lesion three months after radiotherapy had the highest combination of sensitivities and specificities of $\geq$ 80% in predicting 24 months overall survival.

Optimization and standardization of CT perfusion scans were proposed. This thesis also provided corroborating evidence to support the use of CT perfusion as a biomarker of outcomes in patients with malignant gliomas.

Keywords

Co-Authorship Statement

This thesis contains material from manuscripts that were previously published. The copyright(s) agreement for these publications are provided in the Appendix D: Permission to Reproduce Previously Published Materials.

The literature review from Chapter 1 will be submitted to the *Journal of Neuro-Oncology* as a review article entitled "MR and CT perfusion imaging for malignant gliomas: A review of clinical evidence". The authors are Yeung TPC, Yartsev S, Macdonald D, Fainardi E, Lee TY, and Bauman G. I was responsible for conducting a systematic review, analyzing and interpreting the published data, and writing the manuscript. The other authors helped with the interpretation of the literature and editing the manuscript.

Chapter 2, "The effect of scan duration on the measurement of perfusion parameters in CT perfusion studies of brain tumours" was published in *Academic Radiology*, 2013; 20(1):59-65 by Yeung TPC, Yartsev S, Bauman G, He W, Fainardi E, Lee TY. I was responsible for the design of the study, analysis and interpretation of the data, and wrote the manuscript. All authors contributed to the interpretation of the data and helped with editing the manuscript. Drs. Bauman and Fainardi were also responsible for recruiting patients. Dr. He helped with statistical analysis of the data.

Chapter 3, "Improving quantitative CT perfusion parameter measurements using principal component analysis" was published in *Academic Radiology*, 2014; 21(5):624-632 by Yeung TPC, Dekaban M, De Haan N, Morrison L, Hoffman L, Bureau Y, Chen X, Yartsev S, Bauman G, and Lee TY. I was responsible for designing the study, collecting and analyzing the data, and writing the manuscript. Mr. Mark Dekaban and Dr. Xiaogang Chen helped with the computer programming while Mr. Nathan De Haan helped with some of the data collection. Dr. Yves Bureau provided statistical consultations. Miss Laura Morrison and Dr. Lisa Hoffman helped with the *in vivo* experiments. Drs Bauman, Yartsev, and Lee edited the manuscript and provided supervision and mentorship. Dr. Lee was also instrumental in the design of the simulation study.

Chapter 4 is based on the paper entitled "CT perfusion imaging as an early biomarker of differential response to stereotactic radiosurgery". This manuscript will be submitted to

the journal *PLOS ONE* in July 2014 to be considered for publication. The authors of this manuscript are Yeung TPC, Kurdi M, Wang Y, Al-Khazraji B, Morrison L, Hoffman L, Jackson D, Crukley C, Lee TY, Bauman G, Yartsev S. I was responsible for designing the study, collecting the data, analyzing and interpreting the results, and writing the manuscript. Drs. Maher Kurdi and Yong Wang helped with the analysis of the histology data. Baraa Al-Khazraji, Cathie Crukley, and Dr. Dwayne Jackson helped with the histology and immhunohistochemistry. Dr. Lisa Hoffman and Laura Morrison helped with the *in vivo* experiments. Drs Bauman, Yartsev, and Lee helped design the study, provided supervision, and edited the manuscript. Dr. Yartsev also helped with animal irradiation.

Chapter 5, "Relationship of computed tomography perfusion and positron emission tomography to tumour progression in malignant glioma" was published in the *Journal of Medical Radiation Sciences*, 2014; 61(1):4-13 by Yeung TPC, Yartsev S, Lee TY, Wong E, He W, Fisher B, VanderSpek LL, Macdonald D, and Bauman G. I was responsible for the analysis and interpretation of the data, and I also wrote the manuscript. Dr. Bauman was the principal investigator, and Drs VanderSpek, Fisher, Macdonald, Lee, and Wong were the co-investigators of this study. Dr. He and Wong provided statistical consultations regarding the analysis of the data and edited the manuscript. Drs Bauman, Yartsev, and Lee provided supervision, mentorship, and also edited the manuscript.

Chapter 6 is based on the paper entitled "Treatment monitoring in high-grade gliomas: A longitudinal CT perfusion and MR study", which will be submitted to the *Journal of Neuro-Oncology* in July 2014 by Yeung TPC, Wang Y, Urbini B, Yartsev S, Bauman G, Lee TY, Fainardi E, and The Project of Emilia-Romagna region on Neuro-Oncology (PERNO) study group. I was responsible for analyzing and interpreting the results of this clinical study. Drs Fainardi and Urbini collected all the radiological, clinical, and therapeutic data. The PERNO group provided financial support for this longitudinal study. Dr. Yong Wang read and interpreted all the radiologic images and delineated all the lesions so the data can be collected. Drs Bauman, Yartsev, and Lee provided supervision, mentorship, and also edited the manuscript.

Acknowledgments

This Ph.D. dissertation is truly a collaborative effort from a village of people. I would like to express my sincere gratitude to many people whom I have worked with during the past 5 years. I have been fortunate enough to receive mentorship from a number of individuals who navigated through the uncharted waters of science with me. I was also very blessed to have worked with a number of individuals whom without their assistance this Ph.D. dissertation would have been impossible.

First and foremost, I would like to thank my three supervisors **Drs. Glenn Bauman**, **Slav Yartsev**, and **Ting-Yim Lee**. Your mentorship have been invaluable during my PhD training and everything you taught me will benefit me for years to come. Dr. Bauman: thank you for your guidance, support, and encouragement over the course of my Ph.D. training. The speed at which you return emails and review drafts of my papers and abstracts still fascinates me. Your attitude towards collaboration and research, which comes across daily in your dedication to your work, staff, and trainees are important lessons you taught me. Dr. Yartsev: your efficiency, attention to detail, and ability to foster independent thinking are important skills that you taught me and they will stay with me for a lifetime. Thank you very much for doing the afterhours experiments with me and thank you for never hesitating to help me in any possible way. Dr. Lee: you are truly a model scientist and philosopher. Although I cannot be your "student" on administrative paperwork, you have treated me as one of your own students. For that I am forever grateful! Your dedication to research, our thought-provoking conversations, and your emphasis on scientific inquiry have pushed me to excel.

I also want to thank my advisors: **Drs. Eugene Wong** and **Dwayne Jackson**. Dr. Wong: you are undoubtedly the best and most enthusiastic physics professor I know. I truly enjoyed all the classes you taught, particularly statistical mechanics. Thank you for the insightful conversations and your enthusiasm towards my research. Dr. Jackson: thank you for your guidance in immunohistochemistry. You provided me with great learning opportunities in your lab and helped me bridge medical imaging with biology.

I would also like to express my gratitude to a number of collaborators, staff, and

Table of Contents

List of Tables

List of Figures

List of Abbreviations

ACRIN	American College of Radiology Imaging Network
Ang	Angiopoietin
α-SMA	Alpha-smooth muscle actin
ANOVA	Analysis of variance
ASIR	Adaptive statistical iterative reconstruction
ASL	Arterial Spin labeling
AUC	Area under the curve
BBB	Blood-brain barrier
BF	Blood flow
BTV	Biologic target volume
BV	Blood volume
CEL	Contrast-enhancing lesion
CI	Confidence interval
CNR	Contrast-to-noise ratio
CT	Computed tomography
DCE-CT	Dynamic contrast-enhanced computed tomography
DCE-MR	Dynamic contrast-enhanced magnetic resonance
DNA	Deoxyribonucleic acid
DSC-MR	Dynamic susceptibility-contrast magnetic resonance
E	Extraction fraction
EES	Extravascular extracellular space
FDG	Fluorodeoxyglucose
FOV	Field of view
FLAIR	Fluid attenuated inversion recovery
FRI	Fractional residual information
GBM	Glioblastoma multiforme
H&E	Hematoxylin and eosin
HIF-1	Hypoxia-inducible factor 1

HIF-1α	Hypoxia-inducible factor 1-alpha
HR	Hazard ratio
IDH1	Isocitrate dehydrogenase 1
iAUC	Initial area under the curve
k_{ep}	Efflux rate constant
KDR	Kinase insert domain receptor
K^{trans}	Transfer constant
mAUCR$_H$	The ratio between the iAUC and the final AUC from a DCE-MR scan gives the AUCR. The histogram of AUCR of a region is bimodal or skewed, the mean for the higher peak of this distribution is calculated to give the mAUCR$_H$.
MGMT	O(6)-methylguanine-DNA methyltransferase
MMP-9	Matrix metalloproteinase-9
MR	Magnetic resonance
MTT	Mean transit time
MVA	Microvessel area
MVCP	Microvascular cellular proliferation
MVD	Microvessel density
nBF	Normalized blood flow
nBV	Normalized blood volume
nMTT	Normalized mean transit time
NEL	Non-enhancing lesion
OS	Overall survival
PCA	Principal Component Analysis
PET	Positron emission tomography
PFS	Progression-free survival
PO$_2$	Partial pressure of oxygen
PRISMA	Preferred Reporting Items for Systematic Reviews and Meta-analysis
PS	Permeability-surface area product
QA	Quality assurance
RANO	Response Assessment in Neuro-Oncology
rBF	Relative blood flow
rBV	Relative blood volume

ROC	Receiver operating characteristic
ROI	Region of interest
RTOG	Radiation Therapy Oncology Group
SD	Standard deviation
SE	Standard error of the mean
SPECT	Single-photon emission computed tomography
SRS	Stereotactic radiosurgery
SUV	Standard uptake value corrected for body surface area
TAC	Time attenuation curve
TIN	Treatment-induced necrosis
v_e	Volume of extravascular extracellular space per unit volume of tissue
VEGF	Vascular endothelial growth factor
VEGFR-2	Vascular endothelial growth factor receptor-2
V_p	Volume of 'flowing' blood within the vasculature per unit mass
WHO	World Health Organization

List of Appendices

Epigraph

"The brick walls are there for a reason. The brick walls are not there to keep us out. The brick walls are there to give us a chance to show how badly we want something. Because the brick walls are there to stop the people who don't want it badly enough. They're there to stop the other people.

Dr. Randy Pausch, *The Last Lecture*

Dedication

To my Mom,

You continue to exemplify courage, endurance, and resilience.

I could not have done it without you.

Chapter 1

1 Introduction

1.1 Overview

Until recently, clinical imaging of brain tumours has been limited largely to magnetic resonance (MR) and computed tomography (CT). MR is used routinely for diagnosis, surgical and radiotherapy guidance, and assessment of treatment response. CT is the workhorse for radiotherapy planning. Both imaging modalities are used for depicting the anatomy, size, and location of brain tumours. However, they have limited capabilities in providing functional information that relate to tumour pathophysiology. There is mounting evidence that functional imaging techniques, such as tumour perfusion imaging, are promising tools in this regard. Perfusion imaging, using CT or MR, can evaluate brain tumour hemodynamics. At present, perfusion imaging is not incorporated into the routine clinical care of patients because the uncertainties in the acquisition and analysis of these images make optimization and standardization difficult. Moreover, perfusion changes in response to different treatments are complex and not yet well understood. These problems make clinical interpretation of perfusion imaging information difficult. Optimization and standardization of image acquisition and analysis can help facilitate the implementation of perfusion imaging in clinical practice. Serial imaging of perfusion changes can improve the interpretation of the perfusion imaging data for evaluating response and prognosis in patients. This thesis focuses on optimizing the use and interpretation of CT perfusion imaging data based on computer simulation, pre-clinical experiments, and clinical studies. This introductory chapter provides an overview of the basic biology and treatment of malignant glioma, angiogenesis, a review of clinical perfusion imaging studies, and an outline of this thesis.

1.2   Malignant Glioma

More than 22,200 North Americans are diagnosed with cancers of the brain and central nervous system each year (1,2). Glial cells are non-neuronal cells that maintain homeostasis, and support and protect neurons in the central nervous system. Gliomas are brain tumours derived from glial cells with astrocytomas being the most common type of glioma. The World Health Organization (WHO) classifies astrocytomas into four grades based on histological features (3). Both pilocytic (WHO grade I) and diffuse (WHO grade II) gliomas are considered low-grade gliomas and typically behave in an indolent fashion. WHO grade III and IV gliomas are high-grade or malignant gliomas, and they account for approximately 70% of all malignant brain tumours (1,4). Anaplastic astrocytomas (WHO grade III) are diffusely infiltrating, demonstrate a high degree of anaplasia, and tend to progress to glioblastoma multiformes (GBMs). Nuclear atypia and mitotic activity are the criteria for diagnosing anaplastic astrocytomas. GBM (WHO grade IV) is the most malignant form of astrocytoma. It is composed of differentiated neoplastic astrocytes. It shows increased mitotic activity, proliferation of microvasculature, and necrosis. Neovascularization and necrosis are histologic hallmarks of GBM reflecting the dysregulated blood supply of these tumours. Despite aggressive treatment with combinations of surgery, radiation and chemotherapy, the median survival of patients with GBM is approximately 12 to 15 months, while it is two to five years for those with anaplastic gliomas (4).

1.3   Current Treatment Strategy for Malignant Glioma

The standard of care for patients with malignant gliomas involves maximal surgical resection when feasible, followed by radiotherapy and concurrent and adjuvant Temozolomide chemotherapy (4,5). Patients usually undergo at least a biopsy to determine tumour grade and often undergo surgical resection to debulk the tumour mass to palliate symptoms and improve function. Within six weeks after surgery, patients will receive 40 to 60 Gy of external beam radiotherapy. The target for radiotherapy is defined

using MR and CT. The gross tumour volume includes the contrast-enhancing lesion (CEL) depicted on pre-surgical MR/CT. The clinical target volume includes a margin (2 − 3 cm) to encompass microscopic spread of cancer (6). The planning target volume is created by an additional 0.3 cm margin to encompass treatment uncertainties (6). External beam radiotherapy is delivered in 2 Gy per fraction, given once daily for five days a week over a period of four to six weeks. Patients also receive concurrent Temozolomide at a dose of 75 mg/m^2 per day, given 7 days per week until the last day of radiotherapy. Six cycles of adjuvant Temozolomide start at four weeks after the end of radiotherapy based on a five day schedule every 28 days (5).

1.4   Prognostic Factors and Recurrence Patterns

Advanced age ($\geq$ 50 years old), WHO grade IV, poor Karnofsky performance status, and unresectable tumours are the most important pretreatment prognostic factors that predict poor survival (7). The extent of resection, radiation dose, and O6-methylguanine-DNA methyltransferase (MGMT) promoter status are predictors of survival and recurrence patterns after treatment of GBM.

Malignant gliomas often cannot be completely resected due to its infiltrative nature and its proximity to adjacent brain tissues that serve important neurologic functions. In a retrospective study that involved 1215 patients with malignant gliomas, the median survival times after gross-total resection, near-total resection, and subtotal resection were 13, 11, and 8 months, respectively. Survival benefits were significant for gross-total resection versus near-total resection ($P < 0.05$), and near-total resection versus subtotal resection ($P < 0.05$) (8). Therefore, maximal surgical resection is favorable because survival is influenced by the extent of resection (8–10).

Radiotherapy plays an important role in prolonging the survival of these patients. It has long been established that a dose-survival relationship exist below 60 Gy (11). However, radiotherapy does not eliminate the risk of recurrence, and most patients will recur despite adjuvant radiotherapy. Over 80% of recurrence occurs within 2 cm of the

irradiated volume (12–17). For this reason, treatment volume is limited to the nearby surrounding region of the brain in order to reduce the toxicity associated with large field radiotherapy. The adoption of partial brain radiotherapy and new radiation technologies including three-dimensional conformal radiotherapy (18–20), intensity-modulated radiotherapy (21–23), stereotactic radiosurgery (SRS) (24–29), and interstitial brachytherapy have attempted to escalate the dose to beyond 60 Gy (30–34). Despite the use of high dose radiotherapy (90-120 Gy), dose escalation alone has not resulted in survival benefit. The target for dose escalation in these studies was typically defined as the CEL on CT or MR after contrast injection, but a few reports showed such procedure may not represent the entire tumour. Using ^{123}I-α-methyl-tyrosine single-photon emission computed tomography (SPECT) and ^{11}C-methionine positron emission tomography (PET) studies have detected areas of increased metabolic activity that were not visible on contrast-enhanced CT or MR (35–38). In a group of patients with recurrent malignant gliomas, reirradiation of gross tumour volumes based on PET/SPECT + CT/MRI resulted in improved survival compared to reirradiation of gross tumour volumes based on CT/MR alone (9 vs. 5 months, log-rank $P = 0.03$) (35). This result suggests that functional imaging can provide complimentary information to that of CT/MR, and may define a _biologic_ target for dose escalation that is distinct from that delineated by typical contrast-enhanced imaging.

Gliomas are known to be infiltrative neoplasms with the ability to migrate large distances in the brain. It is postulated that as treatment of the local tumour improves, distant failures beyond the typical 2 cm boundary around the irradiated brain volume may become more common. As of yet, however, even in the most favorable instances (completely resected tumours + receiving adjuvant radiotherapy and chemotherapy), the majority of failures are still in close proximity to the original tumour. The O(6)-methylguanine-DNA methyltransferase (MGMT) promoter methylation is a prognostic factor of survival and recurrence patterns after radiotherapy and Temozolomide chemotherapy. One mechanism of DNA injury induced by Temozolomide is the methylation of DNA (39). The DNA-repair protein O^6-alkylguanine-DNA-alkyltransferase is encoded by the gene MGMT, which repairs Temozolomide-induced DNA damage by removing the alkylating lesions at the O^6 position of guanine. The

MGMT gene promoter is often methylated in malignant gliomas leading to the silencing of the MGMT gene and rendering tumour cells unable to repair Temozolomide-induced DNA damage (40). Patients with methylated MGMT promoter (i.e. silenced) had significantly longer survival than patients with unmethylated MGMT promoter (21.7 vs. 12.7 months, respectively; log-rank $P < 0001$) (41). MGMT promoter gene status is also associated with different patterns of recurrence. Recurrences within or at the margin of the irradiated volume were more frequent amongst patients with unmethylated MGMT status than those with methylated MGMT status ($P = 0.01$) although local recurrences still predominated (42).

1.5   The Blood Brain Barrier and Tumour Angiogenesis

A solid tumour cannot grow beyond 1 to 2 mm^3 unless new vasculatures are formed to supply oxygen and nutrients to the growing tumour (43–45). Blood flow and the exchange of materials between the brain and systemic circulation are tightly regulated by the blood brain barrier (BBB). The BBB has important implications in tumour development and the growth of new blood vessels.

Brain vasculature is highly specialized and is unlike those found in other organs. The passage of molecules between the systemic circulation and the cerebral parenchyma is regulated physically (via tight junctions) and metabolically (via enzymes and transport systems) by the BBB. It maintains a constant supply of oxygen, glucose and other nutrients for neurons, and excludes exogenous molecules from entering the brain. This regulation is primarily established by three types of cells: endothelial cells, pericytes, and astrocytes (Figure 1-1). Endothelial cells form the lumen of blood vessels, which is the interface for material exchange between the blood and the brain. Pericytes are undifferentiated perivascular cells that envelope the outer surface of arterioles, venules, and capillaries (46). They play important roles in regulating blood flow (47) and maintaining the integrity of the BBB (48). Astrocytes are glial cells that cover more than 99% of the BBB endothelium (46).
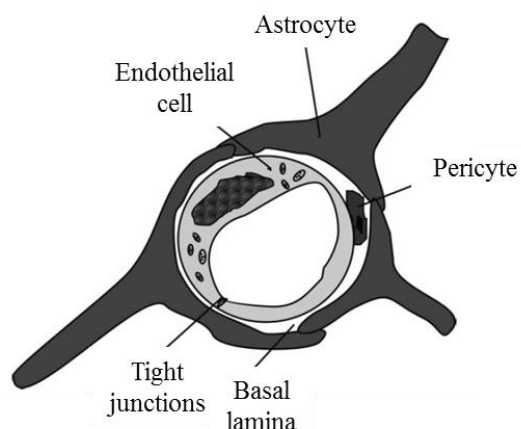
Figure 1-1: Schematic diagram of a brain capillary. The capillary lumen is surrounded by an endothelial cell, which is connected at both ends by tight junctions. Pericytes are attached to the outer surface of the endothelial cell. The endothelial cell and pericyte are ensheathed by a layer of basal lamina. This capillary is then enveloped by astrocytes. Figure adapted from Hawkins and Davis. Pharmacol Rev. 2005;57(2):173-185. Reprinted with permission.

Tight junctions between adjacent endothelial cells are responsible for the unique impermeability of the BBB. They are regions where adjacent endothelial cell membranes are tightly associated with each other through the interactions of various tight junction proteins (46). This arrangement is continuous and lacks fenestration. The outer leaflets of adjacent endothelial cell membranes appear to be fused. The BBB physically prevents plasma proteins and hydrophilic molecules (> 500 kDa) from passively diffusing into the brain parenchyma (49). For exogenous molecules that can cross the BBB, there are several active, receptor-mediated transport proteins that function to export these molecules from the brain back into the systemic circulation (50,51). The brain is considered a "sanctuary" site for cancer cells because the BBB contributes to drug-

resistance by excluding many exogenous molecules (e.g. drugs) from entering the brain (49).

1.5.1   The Blood Brain Barrier in Brain Tumours

The integrity of the blood brain barrier is compromised in malignant brain tumours. The expressions of tight junction proteins are decreased or completely lost in primary and metastatic brain tumours (52–54). This leads to increased vascular permeability and may clinically manifest as vasogenic edema. The reduced number of pericytes (55) and astrocytes (56,57) in an aggressive brain tumour further contributes to a dysfunctional BBB. Tumour cells further increase BBB permeability by secreting a variety of factors that down regulate the expression of tight junction proteins (58,59). One such factor is the vascular endothelial growth factor (VEGF), which was originally discovered as the vascular permeability factor (49,58). VEGF is also a driver of tumour vessel formation. The resulting vessels are structurally and functionally compromised and lack the BBB of normal vasculature.

1.5.2   Tumour Hypoxia

Mammalian cells are usually located within 100 to 200 μm of nearby blood vessels, which is the oxygen diffusion limit (60,61). The partial pressure of oxygen (PO_2) in normal tissue ranges between 10 to 80 mm Hg, but PO_2 within certain tumour regions are often less than 5 mm Hg (62). Hypoxia occurs when the tumour grows beyond the oxygen diffusion limit because the vascular supply cannot meet its metabolic demand. This type of hypoxia is called chronic hypoxia, which can lead to tumour necrosis. Cycling hypoxia, sometimes known as acute or intermittent hypoxia, occurs in tumour regions that are poorly perfused due to chaotic and sluggish tumour vasculature (63). Hypoxia is associated with treatment resistance (64,65) and promotes the formation of new tumour blood vessels (66,67). The growth of a solid tumour is dependent on the growth of new blood vessels (44). There are four mechanisms for brain tumours to form new blood vessels, they are co-option, angiogenesis, vasculogenesis, and intussusception.

1.5.3   Formation of Tumour Blood Vessels

1.5.3.1   Co-option

Initial brain tumour vessel formation (< 1 mm in diameter) is believed to occur by the co-option of pre-existing blood vessels (68,69). Early reports demonstrated that pre-existing vessels that were co-opted by tumour cells were not influenced by the tumour as these vessels were not leaky (68,70). This also suggests that this type of vessel formation might not be detected by contrast-enhanced CT or MR since these imaging techniques detect tumour based on the extravasation of contrast agents (68).

1.5.3.2   Angiogenesis

Angiogenesis is a common mechanism for gliomas to grow and progress. Tumour angiogenesis in the brain involves three major steps: 1) regression of pre-existing blood vessels, 2) breakdown of the basement membrane and extracellular matrix, and 3) the migration of endothelial cells to form new blood vessels. The initiation of angiogenesis is known as the angiogenic switch. This switch is turned on when the pro-angiogenic factors in a tumour outweigh the anti-angiogenic factors. The secretion of pro-angiogenic factors are triggered by microenvironmental conditions including hypoxia and acidosis (71), and by genetic factors such as alterations in oncogene (e.g. ras) or tumour suppressor gene (e.g. p53) functions (72,73). The hypoxia-inducible factor 1 (HIF-1) pathway is a well-characterized signaling pathway by which hypoxic tumours initiate and orchestrate cellular responses to hypoxia. HIF-1 activates the transcription of more than 100 genes that help tumour cells "cope" with low oxygen conditions (74). The expression of VEGF, one of the most potent pro-angiogenic factors, is activated by this pathway (71,73).

The initial response to VEGF overexpression includes increased vascular permeability (75–77) and diameter (49). In a normal brain, angiopoietin (Ang-1) binds to its receptor Tie-2 to facilitate a close association between endothelial cells and pericytes

(48,78). Under hypoxic conditions, Ang-2, an antagonist of Tie-2, is upregulated and is suggested to be involved in the detachment of pericytes from endothelial cells and leads to the regression of blood vessels (79–81). Increased Ang-2 and hypoxia then lead to the expression of matrix-metalloproteinase molecules that mediate the breakdown of the basement membrane and the extracellular matrix (82). At the same time, molecules including VEGF, Ang-1, and Ang-2 stimulate endothelial cell proliferation and migration towards the cancer cells (49,79). The end product of angiogenesis is an abnormal, highly tortuous, sluggish, and leaky vascular network (49,63).

1.5.3.3 Vasculogenesis

Angiogenesis forms new blood vessels from pre-existing ones, whereas vasculogenesis forms blood vessels without pre-existing endothelial cells. It is a process by which bone marrow-derived cells (83–85), such as circulating progenitor cells (86,87), are recruited to the tumour to form new blood vessels. This process is also initiated by hypoxia through the HIF-1 pathway (88,89). It has been shown that blocking vasculogenesis can prevent or delay local recurrence of GBM after irradiation (88). This suggests circulating cells outside the radiation field colonize and stabilize tumour vasculature and support the remaining viable tumour cells after irradiation.

1.5.3.4 Intussusception

Intussusception refers to the remodeling and expansion of pre-existing blood vessels by inserting transluminal pillars into vessel lumens that result in partitioning of vessel lumens (79,90). Intussusception occurs faster than angiogenesis; it does not primarily depend on the proliferation of endothelial cells, degradation of basement membrane, and invasion of connective tissue (90,91). It appears to increase the complexity and density of tumour vascular networks established by angiogenesis (90).

1.6 Conventional Imaging of Malignant Gliomas

Visualization of brain tumours on contrast-enhanced MR and CT is made possible because the compromised BBB in brain tumours allow imaging contrast to extravasate into the brain parenchyma after contrast injection. The standard MR protocol for imaging brain tumours usually involves a T2-weighted or a fluid attenuated inversion recovery (FLAIR) MR and a gadolinium-enhanced T1-weighted MR (Figure 1-2) (92). Gadolinium-enhanced T1-weighted MR provides excellent soft tissue contrast, and depicts the contrast-enhancing component of the tumour. However, malignant gliomas are infiltrative tumours with microscopic processes that extend beyond regions of contrast-enhancement. Vasogenic edema, which may be induced by infiltrating tumour cells, is a major clinical feature of the non-enhancing portions of these tumours and can be visualized on T2-weighted or FLAIR MR.
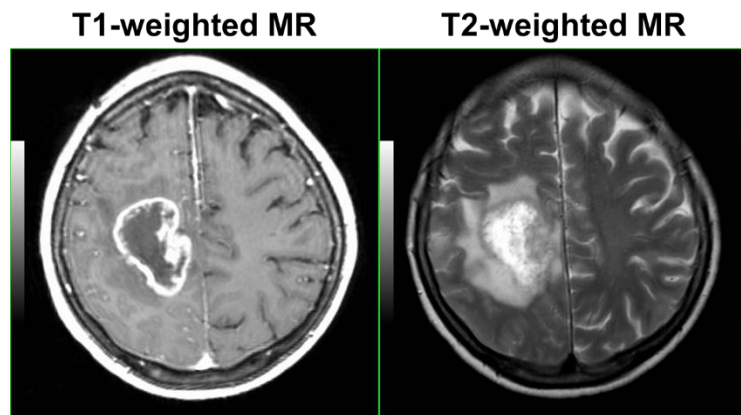
Figure 1-2: Contrast-enhanced T1-weighted magnetic resonance (MR) and T2-weighted MR of a patient with glioblastoma multiforme (GBM).

1.7 Criteria for Assessing Treatment Response

Radiographic response assessment of brain tumours is primarily based on changes in the size of the contrast-enhancing part of the tumour. The Macdonald criteria were introduced in 1990 for assessing response in gliomas (93). Tumour size is measured using

the product of the maximal perpendicular diameters of the enhancing tumour depicted on gadolinium-enhanced T1-weighted MR or iodinated contrast-enhanced CT. The use of corticosteroid and clinical status are also taken into account. Response can be categorized into four categories; they are complete response, partial response, stable disease, and progression (Table 1-1).

Table 1-1: The Macdonald criteria for assessing treatment response of malignant gliomas.*

Response	Criteria
Complete Response	Requires all of the following: complete disappearance of all enhancing measurable and non-measurable diseases sustained for at least 4 weeks; no new lesions; no corticosteroid; and stable or improved clinically
Partial Response	Requires all of the following: ≥ 50% decrease compared with baseline in the sum of products of perpendicular diameters of all measurable enhancing lesions sustained for at least 4 weeks; no new lesions; stable or reduced corticosteroid dose; and stable or improved clinically
Stable Disease	Requires all of the following: does not qualify for complete response, partial response, or progression; and stable clinically
Progression	Defined by any of the following: ≥ 25% increase in the sum of products of perpendicular diameters of enhancing lesions; any new lesion; or clinical deterioration

*Reprinted with permission. © (2010) American Society of Clinical Oncology. All rights reserved. Table adapted from Wen PY, Macdonald DR, Reardon DA, et al. J Clin Oncol. 2010;28(11):1963-1972.

The Macdonald criteria have a few limitations. A two dimensional measurement of tumour size can be influenced by a number of factors (94–96). Measurement is difficult with an irregularly shaped tumour, multifocal tumour, and enhancing wall of a surgical cavity. It is also prone to interobserver variability (97). Contrast-enhanced MR or CT is a snapshot of tissue contrast-enhancement after contrast injection, so it reflects the

extravasation of materials across a disrupted BBB regardless of the cause of disruption. Changes in corticosteroid dose, inflammation, post-surgical changes, pseudoprogression due to treatment effects, radiation-induced necrosis, and pseudoresponse due to anti-angiogenic therapies are all factors that can influence contrast-enhancement (98–102). In addition, the Macdonald criteria do not take into account the non-enhancing component of the tumour.

Recently, the Macdonald criteria were updated. In 2010, The Response Assessment in Neuro-Oncology (RANO) Working Group developed new standardized criteria for assessing response in patients with malignant gliomas (92). Size measurement of the non-enhancing component of the tumour using T2-weighted or FLAIR MR is incorporated into the assessment criteria. It also recognized early changes in contrast-enhancement could be treatment related (e.g. pseudoprogression and pseudoresponse), which could confound the diagnosis of tumour progression or response. To address this issue, a time period has been defined for which pseudoprogression can be excluded from true progression. For instance, true progression can only be determined within the first 12 weeks of completion of radiotherapy if the majority of new contrast-enhancement is outside the radiation field (80% isodose line) or if there is pathologic confirmation of tumour progression (92).

The RANO working group recognized that there are still unsolved problems associated with these criteria. Better imaging techniques are needed to predict tumour response, differentiate treatment-induced changes from tumour progression, and differentiate non-enhancing tumours from other etiologies of increased T2-weighted or FLAIR signals. The group also recognized that functional imaging, particularly the imaging of tumour perfusion and permeability, are promising tools to address these challenges.

1.8   Perfusion Imaging of Malignant Gliomas

A growing number of studies demonstrated that perfusion imaging can provide physiologic information about tumour aggressiveness and disease prognosis. Dynamic susceptibility-contrast MR (DSC-MR), dynamic contrast-enhanced MR (DCE-MR), and DCE-CT are commonly used perfusion imaging techniques for evaluating tumour hemodynamics and vessel permeability surface area (PS) product in the research setting. In this thesis, DCE-CT and CT perfusion are used interchangeably.

Perfusion imaging refers to imaging techniques that characterize tissue hemodynamics by tracking the passage of a bolus of contrast agent as it traverses through human tissue. Following injection, contrast passes through the microvasculature of brain tissue and produces a change in image signal intensity. DCE-MR and DSC-MR measure gadolinium contrast concentration via its effect on surrounding water molecules, while DCE-CT measures iodinated contrast concentration via its attenuation of x-rays. Quantitative evaluation of hemodynamics and PS from tracer kinetic analysis (103) consists of three main steps:

1. Image signal intensity is converted to contrast concentration to obtain the time-concentration curve $C_t(t)$ of brain (tumour) tissue.

2. Image signal intensity in pixels corresponding to an input artery to the brain is similarly converted to the arterial input function $C_a(t)$. It is the time-concentration curve of contrast that enters the tissue of interest via the selected input artery.

3. Based on the tracer kinetic model adopted, hemodynamic parameters such as blood flow (BF) and PS can be estimated. Definitions of the different tracer kinetic parameters that can be derived are listed in Table 1-2. The tissue time-concentration curve $C_t(t)$ is equal to blood flow (BF) multiplying the convolution of the arterial input function $C_a(t)$ and an impulse residue function $R(t)$. This relationship can be mathematically expressed as:

$$C_t(t) = BF \cdot C_a(t) \otimes R(t) = C_a(t) \otimes BF \cdot R(t)$$

$$C_t(t) = \int_0^t C_a(\tau) \cdot [BF \cdot R(t - \tau)]d\tau \ \ldots \text{Equation 1-1}$$

The impulse residue function *R(t)* describes the tissue time-concentration curve when the arterial input function is $\frac{1}{BF}\delta(t)$ or when an unit amount of contrast is introduced into the arterial input of the tissue instantaneously. Empirically, it is the fraction of contrast that remains in the tissue as a function of time after instantaneous contrast injection at the arterial input. In practice, contrast is injected intravenously over a period of time (15-25 s) such that the arterial input function *Ca(t)* is dispersed in time instead of a delta function $\delta(t)$. Provided the image signal varies linearly with concentration and BF is stationary (constant within the period of measurement), the tissue time-concentration curve *Ct(t)* is by the convolution between the arterial input function *Ca(t)* and the impulse residue function *R(t)* using the principle of linear superposition.

Below we discuss the technical aspects of DSC-MR, DCE-MR, and DCE-CT.

Table 1-2: Glossary of perfusion imaging parameters.

Terms	Definitions (units)
Blood flow (BF)	Flow rate of blood per unit mass or volume of tissue (ml·min·100g^{-1} or ml·min·100ml^{-1}).
Blood volume (BV)	Volume of 'flowing' blood within the vasculature per unit mass or volume of tissue (ml·100g^{-1} or ml·100ml^{-1}).
Extraction fraction (E)	Fraction of contrast that extravasates from the intravascular space into the EES in the first pass through the vasculature
Initial Area Under the Curve (iAUC)	A semi-quantitative measure of contrast enhancement used in DCE-MR. It is related to the dose of contrast injected, the blood volume, and permeability surface product of the BBB.
mAUCR$_H$	The ratio between the iAUC and the final AUC from a DCE-MR scan gives the AUCR. The histogram of AUCR of a region is bimodal or skewed, the mean for the higher peak of

	this distribution is calculated to give the mAUCR$_H$.
Mean transit time (MTT)	Average time (s) for blood to traverse from the arterial to the venous end of the vasculature.
Normalized BV (nBV)	BV of a region-of-interest normalized to the contralateral normal brain. The normal appearing white matter is used for normalization.
Normalized Maximum Slope	A semi-quantitative estimation of BF. It is the maximum slope of a tissue time-contrast enhancement curve normalized by the maximum of the arterial time-contrast enhancement curve.
Peak Height (PH)	A measure of maximum contrast enhancement from the baseline signal during the first pass of contrast.
Normalized Peak Height	PH of the tumour can be normalized to the contralateral normal brain to give the normalized peak height.
Percent Recovery	It is the measure of how much signal has recovered from the baseline signal after the first pass of contrast. It is a semi-quantitative measure of microvascular leakage in DSC-MR.
Permeability	Unidirectional flux rate of contrast agent from the blood plasma into the brain parenchyma (i.e. interstitial space) normalized by the total surface area of capillaries per unit mass of tissue. It is often estimated using the parameters permeability-surface area product (PS) and transfer rate constant (K^{trans}).
Permeability-surface area product (PS)	Product of permeability and total surface area of capillaries per unit mass of tissue (ml·min·100g^{-1}).
Efflux Rate constant (k_{ep})	Rate constant of contrast efflux rate from the brain parenchyma back into the blood plasma (min^{-1}).
Transfer Constant (K^{trans})	Flow rate constant of contrast from the blood plasma to the brain parenchyma (min^{-1}).
V_p	Volume of 'flowing' blood within the vasculature per unit mass or volume of tissue (ml·100g^{-1} or unitless)
Extravascular volume (v_e)	Volume of extravascular extracellular space per unit volume of tissue for contrast to distribute into (ml·100g^{-1} or unitless).

Abbreviations: EES, extravascular extracellular space; DCE-MR, dynamic contrast-enhanced magnetic resonance; BBB, blood brain barrier; DSC-MR, dynamic susceptibility-contrast magnetic resonance

1.8.1 Dynamic Susceptibility-Contrast Magnetic Resonance (DSC-MR)

DSC-MR imaging measures signal change during the first passage of contrast through the tissue vasculature when the contrast remains intravascular using a T2- or T2*-weighted sequence. At high concentration (0.1 − 0.2 mmol/kg), the contrast agent creates a susceptibility gradient in tissue that decreases T2* signal intensity. A temporal resolution of 1 − 2 s is required because the minimum transit time of contrast agent in brain tissue is a few seconds. A typical scan duration of 1 − 2 minutes is used. The indicator dilution method is appropriate for calculating BF and BV in DSC-MR imaging (104). DSC-MR assumes that the degree at which contrast is diluted in the blood is a function of blood flow (BF) and blood volume (BV) and that contrast remains intravascular during imaging. BV is estimated from the ratio of the areas under the tissue time-concentration curve $C_t(t)$ and the arterial time-concentration curve $C_a(t)$. BF can be solved by the deconvolution of Equation 1-1. DSC-MR assumes that the contrast agent compartmentalizes in the intravascular space and does not leak into the brain parenchyma. However, violation of this assumption can underestimate BV when high leakage of contrast material occurs (105). This effect can be minimized by pre-saturating the brain parenchyma with a pre-loading dose of contrast agent, dual echo sequence, or post-processing mathematical correction (105,106).

1.8.2   Dynamic Contrast-Enhanced Magnetic Resonance (DCE-MR)

DCE-MR refers to the acquisition of serial MR images using a T1-weighted sequence. The increase in T1 relaxation rate from corresponding increase in contrast concentration is measured as an increase in signal intensity. DCE-MR scan duration is 5 – 10 min in order to measure the rate of extravasation of contrast from the intravascular space into the extravascular extracellular space (EES) (i.e. PS or K^{trans}). By assuming the intravascular space and the EES as two well-mixed tissue compartments, the compartmental model is used to estimate the rate of contrast transfer from the intravascular space into the EES (107). This quantity is commonly called K^{trans} and can be solved using the following equation:

$$C_t(t) = BV \cdot C_a(t) + K^{trans} \int_0^t C_a(u)e^{-\frac{K^{trans}}{v_e}(t-u)} du \ldots \text{ Equation 1-2}$$

where v_e is the volume of extravascular extracellular space per unit volume of tissue. K^{trans} is generally interpreted as a measure of tissue permeability (107). However, K^{trans} is the product between BF and extraction fraction (E). Thus, K^{trans} should be used for permeability interpretation with caution because either BF or E may be the dominating factor. A temporal resolution of 5 – 10 s per image is commonly used to balance spatial resolution, scan coverage, and signal-to-noise ratio, but it is too slow for the measurements of BF and BV where a finer temporal resolution (1 – 2 s) is required (108). However, techniques such as multi-channel parallel imaging and compressed sensing can achieve a finer temporal resolution (109).

1.8.3   Dynamic Contrast-Enhanced Computed Tomography (DCE-CT)

DCE-CT refers to the acquisition of serial CT images to track the passage of a bolus of iodinated contrast agent. The typical DCE-CT protocol takes 2 – 3 minutes, and

it involves rapid acquisition of images (1 – 2 s per image) during the initial phase of imaging (45 s) to capture the first pass of contrast for the calculation of BF and BV. A second phase that involves less frequent acquisition (10 – 15 s per image) is required to calculate PS or K^{trans} (110). Both compartmental and distributed parameter models have been used to calculate tracer kinetic parameters from DCE-CT images. The Johnson and Wilson model (111) is an example of a distributed parameter model. An adiabatic approximation to the Johnson and Wilson model allows the simultaneous determination of BF, BV, and permeability-surface area product (PS) by giving a closed-form solution to the impulse residue function $R(t)$ (112). The $R(t)$ is defined as:

$$R(t) = \begin{cases} 1 & 0 < t \le \frac{BV}{BF} \\ E e^{-\frac{BF \cdot E}{v_e}\left(t - \frac{BV}{BF}\right)} & t > \frac{BV}{BF} \end{cases} \quad \text{… Equation 1-3}$$

The extraction fraction E is calculated as:

$$E = 1 - e^{-\frac{PS}{BF}} \quad \text{… Equation 1-4}$$

The distributed parameter model enables the separation of BF and E; thus, enabling the calculation of the permeability-surface area product (PS). It assumes a contrast concentration gradient inside the intravascular space along the length of capillaries (110). An advantage of the distributed parameter model is the determination of BF, BV, and PS from a single perfusion scan.

The clinical use of DCE-CT was slow to progress initially due to its relatively limited scan volume (2 – 4 cm coverage) and associated radiation dose (2 – 5 mSv) (113). The advent of large multi-row detector technology enables the coverage of 16 cm of anatomy (114). Shuttle mode imaging can also increase the scan coverage (115). Reconstruction methods such as adaptive statistical iterative reconstruction technique (116) and reducing the temporal resolution of image acquisition ($\le$ 3 s) in the first phase (117) are effective ways to reduce radiation dose. Figure 1-3 shows maps of BF, BV, and PS from a DCE-CT study of a patient with GBM. Table 1-3 summarizes and compares the key aspects of DSC-MR, DCE-MR, and DCE-CT.
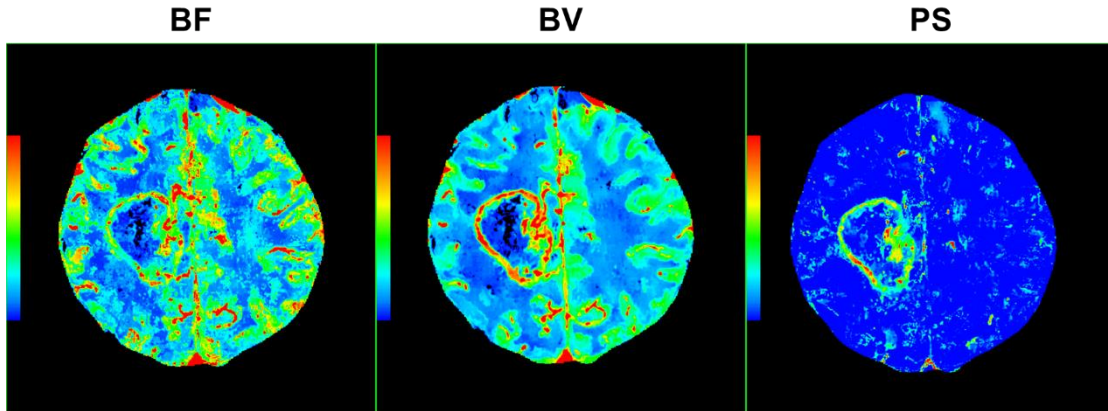
Figure 1-3: Blood flow (BF), blood volume (BV), and permeability-surface area (PS) product maps calculated from dynamic contrast-enhanced computed tomography (DCE-CT) images of the same patient as Figure 1-2.

Table 1-3: Comparison of typical brain perfusion imaging techniques.

Parameter	DSC-MR	DCE-MR	DCE-CT
Typical contrast agent	Gadopentetate dimeglumine	Gadopentetate dimeglumine	Iopamidol
Tracer kinetic analysis method	Indicator dilution theory	Compartmental model	Compartmental and distributed parameter models
Scan coverage	8 − 10 or 16 − 20 slices covering the entire brain (~ 10 cm)	16 − 32 slices covering 3 to 16 cm of anatomy	4, 8, and 16 cm coverage with multi-detector CT. Shuttle mode imaging can achieve whole brain coverage
Molecular weight of contrast agent	938 g/mol (0.938 kDa)	938 g/mol (0.938 kDa)	777 g/mol (0.777 kDa)
Typical temporal resolution	1 − 2 s	5 − 10 s	First phase: 1 − 2 s Second phase: ≤ 5 s for Patlak analysis and 10

			– 15 s for Johnson and Wilson model
Typical scan duration	1 – 2 min	5 – 10 min	2 – 3 min
Source of signal	Decrease in T_2^* (or T_2) of surrounding water molecules	Decrease in T_1 of surrounding water molecules	Attenuation of x-ray by iodinated contrast
Change in signal intensity	Signal loss	Signal gain	Signal gain
Signal-to-contrast concentration relationship	$\Delta R_2^*(t) = -\dfrac{1}{TE}\ln\left(\dfrac{S(t)}{S(0)}\right)$ $C = k \cdot \Delta R_2^*$	$C = \dfrac{\left(\dfrac{1}{T1} - \dfrac{1}{T1_0}\right)}{R1}$	Linear
Quantitative Techniques	Mostly relative	Relative and absolute	Relative and Absolute

Abbreviations: DSC-MR, dynamic-susceptibility contrast magnetic resonance; DCE-MR, dynamic contrast-enhanced magnetic resonance; DCE-CT, dynamic contrast-enhanced computed tomography; ΔR_2^*, Change in relaxation rate; S(0), baseline signal intensity; S(t), signal intensity at time *t*; R1, longitudinal relaxivity of the contrast agent; C, concentration; Hct, hematocrit; *k*, proportionality constant that depends on the tissue, contrast agent, field strength, and pulse sequence parameters.

1.8.4 Other Important Perfusion Imaging Techniques

Arterial spin labeling (ASL) is a promising technique that can measure BF in brain tumours. ASL uses arterial blood water as an endogenous tracer by magnetically labeling blood water that is proximal to the tissue of interest. ASL is a technology that is gaining interest in neuro-oncology in recent years (118,119) since it does not require the injection of exogenous contrast agent and it has no radiation dose. The ASL method makes serial perfusion scans even more feasible for monitoring treatment response.

Tumour perfusion can also be investigated using nuclear medicine techniques. Positron emission tomography (PET) using ^{15}O-labeled water has been used in previous

reports (120,121), and is considered to be the "gold standard" in quantitative perfusion imaging. However, the need for an onsite cyclotron and the short half-life of ^{15}O (2 minutes) limits its feasibility in the clinic. Limited spatial resolution is also a disadvantage of PET when compared to CT and MR.

1.9   Literature Review of Perfusion Imaging

Here, we provide a review of the literature in perfusion imaging of malignant gliomas. To comprehensively survey the literature, a PubMed search was performed from January 2002 to May 2012 using the terms ('glioma' OR 'glioblastoma') AND ('perfusion imaging', 'dynamic contrast-enhanced', 'DCE', 'computed tomography', 'CT', 'dynamic susceptibility', 'DSC', 'magnetic resonance', OR 'MR') to identify relevant clinical studies. The search was limited to include studies that involved human subjects and published in the English language. Preclinical studies, studies that evaluated only low-grade gliomas, and studies with a sample size ≤ 5 patients were excluded.

We categorized each article according to the investigated application. Five key areas were identified; they are 1) correlations with molecular and histopathologic markers, 2) diagnostic efficacy of differentiating high grade from low grade gliomas, 3) differentiation of malignant gliomas from other malignant lesions, 4) differentiation of true progression from post-treatment effects, and 5) prediction of survival. Literature search for applications 4 and 5 were extended to include studies published before January 2014. When considering articles that evaluated tumour grade, only articles that reported the sensitivity and specificity to differentiate high and low grade gliomas were included. The article selection process is summarized in Figure 1-4.
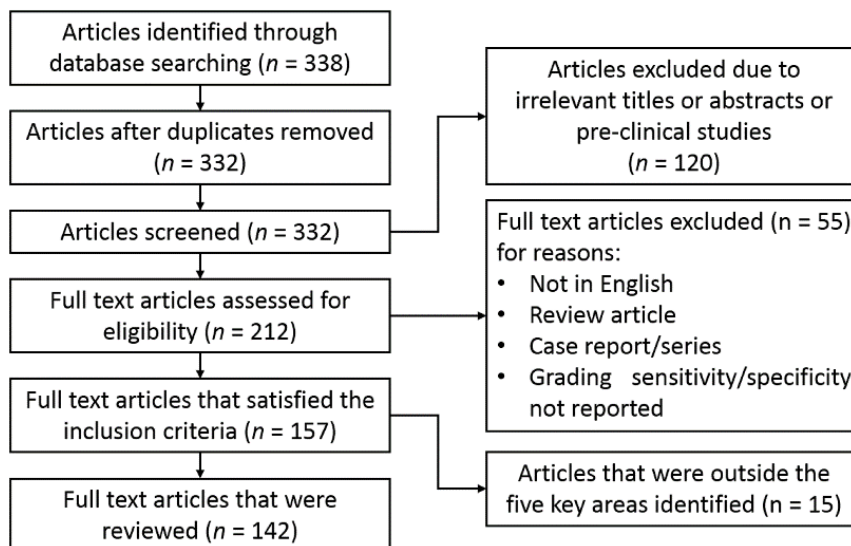
Figure 1-4: Article selection flowchart according to the Preferred Reporting Items for Systematic Reviews and Meta-analysis (PRISMA) guidelines.

1.9.1 Correlation with Molecular and Histopathologic Markers

An understanding of the relationships between histopathologic markers and perfusion imaging could justify the use of perfusion imaging as non-invasive surrogates for these tissue assays (Table 1-4).

Table 1-4: Correlation of perfusion imaging parameters with histopathologic markers.

Histopathologic Markers	Techniques	Parameters	Correlation coefficients (range)	References
Tumour cellularity or cell density	DSC-MR	nBV	0.57	(122)
	DCE-CT	BF	0.498	(123)
		BV	0.482	

		PS	0.409	
Microvessel density (MVD)	DSC-MR	nBV	0.32 – 0.46	(122,124)
	DCE-MR	nBV	0.821 – 0.896	(125,126)
	DCE-CT	BF	0.527	(123)
		BV	0.649	
Microvessel area (MVA)	DSC-MR	nBV	0.83	(124)
Microvascular cellular proliferation (MVCP)	DSC-MR	nBV	nBV were higher in the presence of MVCP	(127)
	DCE-CT	PS	0.647	(123)
Vascular endothelial growth factor (VEGF)	DSC-MR	nBV	nBV values correlated with VEGF expression	(128)
	DCE-MR	nBV	0.765 – 0.884	(125,126,129)
		nBF	0.849	(129)
Matrix metalloproteinase-9 (MMP-9)	DCE-MR	K_{trans}	0.585	(130)
		k_{ep}	0.765 – 0.871	(129,130)
		v_e	0.509	(130)
Hypoxia inducible factor 1-alpha (HIF1-α)	DCE-MR	nBV	0.557	(129)
Ki-67	DSC-MR	nBV	0.628 (marginal significance)	(131)
		nMTT	0.644 (marginal significance)	
MIB-1	DSC-MR	nBV	0.66	(132)

Abbreviations: DSC-MR, dynamic susceptibility-contrast magnetic resonance; DCE-MR, dynamic contrast-enhanced magnetic resonance; DCE-CT, dynamic contrast-enhanced computed tomography; nBV, normalized blood volume; BF, blood flow; PS, permeability-surface area product; nBF, normalized blood flow; K_{trans}, transfer constant;

k_{ep}, efflux rate constant; v_e, volume of extravascular extracellular space per unit volume of tissue; nMTT, normalized mean transit time.

Microvessel density (MVD) is a histopathologic measure of angiogenesis and a prognosticator of survival (133). Correlations between MVD and BV were weak for DSC-MR (< 0.4), moderate for DCE-CT (< 0.7), and strong for DCE-MR (> 0.8). Microvessel area (MVA) is a more useful predictor of survival than MVD because MVD cannot characterize the morphological complexity of tumour blood vessels, which are often tortuous and different in sizes (134). Tumour normalized BV (nBV) showed a stronger correlation with MVA than MVD (r = 0.83 and 0.32, respectively; $p \leq 0.05$) (124). Moreover, nBV and MVA correlated with overall survival (OS) while MVD did not. Microvascular cellular proliferation and VEGF expression also showed correlations with perfusion imaging parameters (Table 1-4). Together, these studies suggest that perfusion imaging-based measure of BV may be a surrogate marker of the degree of angiogenesis, which in turn is a predictor of patient survival.

One DCE-CT study explored the associations between the expression of genes that regulate angiogenesis in GBM and different DCE-CT parameters (135). Nineteen and nine genes showed significant associations with PS and BV, respectively. BV and/or PS correlated positively with some pro-angiogenic genes (e.g. KDR (VEGFR-2) and HIF1A) and negatively with some anti-angiogenic genes (e.g. VASH2 and C3). This study suggests a molecular genetic basis for PS and BV as candidate imaging biomarkers.

Angiogenesis is crucial for the proliferation and invasion of malignant gliomas, and it was demonstrated that MVD correlated with tumour proliferation (136). For this reason, studies have investigated the associations between perfusion imaging parameters and proliferative potential of malignant gliomas. Tumour cellularity or cell density is a histologic method to quantify the number of tumour cells. Moderate correlations between DSC-MR or DCE-CT parameters and tumour cellularity ($0.4 < r < 0.6$) were reported (122,123) (Table 1-4). However, cell density cannot distinguish between proliferative,

apoptotic, and senescence cells. Ki-67 or MIB-1 are cellular markers of proliferation, and moderate correlations with DSC-MR parameters have been reported ($r > 0.6$) (131,132).

1.9.2   Differentiation of Tumour Grade

Stereotactic biopsy of tumour specimens for grading can be prone to sampling error. In a study that compared biopsied specimens with surgically resected specimens, as much as 60% of anaplastic astrocytoma (WHO grade III) were upgraded to GBM (137). Imaging techniques that can determine tumour aggressiveness can provide complementary information to establish grade and guide biopsy to sample the most anaplastic part of the tumour. Functional image-guidance can potentially improve the accuracy of diagnosis.

We found 20 studies that reported the sensitivities and specificities of using perfusion imaging to differentiate high versus low grade gliomas (Table 1-5). The sensitivities ranged from 68 to 100% and specificities ranged from 40 to 100% (138–157). Different thresholds were used for differentiating high from low grade gliomas. Thus, while perfusion imaging showed promise for grading, standardization of imaging protocols and consensus thresholds for differentiating tumour grade need to be established.

Not all malignant gliomas are enhancing on post-gadolinium T1-weighted MR images. About 9% of malignant gliomas lack contrast-enhancement and can be mistaken as low-grade gliomas that do not enhance (158). Perfusion imaging can be an important tool in this regard. Using DSC-MR, patients with non-enhancing anaplastic gliomas (WHO grade III) had significantly higher nBV than those with low-grade astrocytomas (WHO grade II) (159). In a study using DCE-CT, nBV demonstrated a sensitivity and specificity of 90.9% and 83.3% for differentiating non-enhancing grade III vs. II gliomas (157).

Table 1-5: Summary of sensitivities and specificities of perfusion imaging in differentiating high grade versus low grade gliomas.

Modality	Parameter	Median sensitivity and specificity (ranges) (%)	References[‡]	Key points from the literature
DSC-MR	[*]nBV	Sensitivity: 94 (67 – 100) Specificity: 86 (50 – 100)	(138–151)	• Regions-of-interest are usually placed in visually contrast-enhancing regions only • BV and BF values are generally higher in high-grade gliomas than low-grade gliomas. • Permeability values (i.e. PS and K_{trans}) are higher in high-grade gliomas than low grade gliomas. • Oligodendrogliomas may demonstrate foci with high blood volume regardless of tumour grade. • Optimal thresholds for differentiating high grade versus low grade gliomas have not been tested in a prospective study • Standardization of imaging protocol is need to reduce the variability in sensitivity and specificity observed in studies
DSC-MR	nBF	Sensitivity: 86 (73 – 100) Specificity: 95 (91 – 100)	(138,142)	
DCE-MR	K_{trans}	Sensitivity: 89 (89 – 89) Specificity: 79 (75 – 82)	(152,153)	
DCE-MR	V_p	Sensitivity: 68 (N/A) Specificity: 89 (N/A)	(153)	
DCE-MR	v_e	Sensitivity: 82 (N/A) Specificity: 94 (N/A)	(152)	
DCE-CT	[†]BV	Sensitivity: 89 (83 – 100) Specificity: 92 (75 – 100)	(154–157)	
DCE-CT	[†]BF	Sensitivity: 83 (71 – 90) Specificity: 94 (82 – 100)	(155–157)	
DCE-CT	K_{trans}	Sensitivity: 97 (N/A) Specificity: 100 (N/A)	(156)	

Modality	Parameter	Median sensitivity and specificity (ranges) (%)	References[‡]	Key points from the literature
	PS	Sensitivity: 100 (N/A) Specificity: 83 (N/A)	(154)	
	MTT	Sensitivity: 93 (N/A) Specificity: 40 (N/A)	(155)	

Abbreviations: nBV, normalized blood volume; nBF, normalized blood flow; K_{trans}, transfer constant between blood plasma and extravascular extracellular space; V_p, volume of 'flowing' blood within the vasculature per unit mass; v_e, volume of extravascular extracellular space per unit volume of tissue; PS, permeability-surface area product; MTT, mean transit time; DSC-MR, dynamic-susceptibility contrast magnetic resonance; DCE-MR, dynamic contrast-enhanced magnetic resonance; DCE-CT, dynamic contrast-enhanced computed tomography; N/A, not applicable.

[*]nBV refers to mean or maximum nBV

[†]BV and BF refers to absolute or normalized BV and BF, respectively

Almost all low-grade gliomas eventually progress to high-grade gliomas at an unpredictable time. In a cohort of low-grade glioma patients that received repeated DSC-MR, a continuous increase in nBV was found in those with malignant transformation up to the point when contrast-enhancement became apparent on post-gadolinium T1-weighted images. The nBV for transformers significantly increased to 5.36 at the time of transformation ($p < 0.05$), while nBV remained stable and increased to only 1.52 in non-transformers ($p > 0.05$) (160). Together, these studies suggest perfusion imaging is a useful method for grading gliomas even in cases where the tumours lack contrast-enhancement, and can be an important tool for active surveillance of low grade gliomas.

Perfusion imaging differentiation of tumour grade in oligodendroglial tumours should be interpreted with caution. Oligodendroglial tumours can have higher BV than astrocytic tumours irrespective of tumour grade (161) while high grade oligodendroglial tumours may or may not have higher BV than low grade oligodendroglial tumours (161,162). Thus, perfusion imaging of oligodendroglial tumours should be considered separately from astrocytic tumours, and perfusion imaging alone is not reliable for differentiating oligodendroglial tumour grade.

1.9.3   Differentiation of Malignant Brain Lesions

Solitary brain metastases with no history of primary cancer are found in approximately 15% of patients and may appear similar to primary malignant gliomas on MR images (163). We found 18 studies that used perfusion imaging to differentiate brain metastases from malignant gliomas. Two factors should be considered when using perfusion imaging to differentiate these two entities. Firstly, current evidence suggests that BV in the contrast-enhancing lesion of metastasis depends on the site of origin. Metastases from melanoma and renal carcinoma are reported to have higher BV than malignant gliomas (164). Studies that considered different sites of origin as one entity (or those that did not mention the sites of origin) showed that BV of the enhancing metastatic lesions were either similar (165–168) or lower (141,169,170) than malignant gliomas. For

example, nBV in studies with mostly lung and breast cancer metastases may be similar to (164,171) or lower than malignant gliomas (141,169). Together, these studies suggest that the differentiation of brain metastasis from malignant glioma based on BV of the contrast-enhancing lesion alone is challenging.

Secondly, BV in the non-enhancing lesion shows more promise for distinguishing metastases from primary malignant gliomas. The non-enhancing lesion is the hyperintense region on T2 or FLAIR images outside the contrast-enhancing lesion. BV in the non-enhancing lesion of brain metastases were lower than that of malignant gliomas (141,166,170–177). T2/FLAIR changes primarily represent edema without tumour infiltration in brain metastases (178). In contrast, the high BV in the non-enhancing lesion of malignant gliomas can be attributed to their aggressive and infiltrative growth, which often extends into the T2-hyperintense region. The median sensitivity and specificity for distinguishing the two entities using non-enhancing lesion nBV were 90% (range, 77 − 100%) and 95% (64 − 100%), respectively (141,169,170). In contrast, the median sensitivity and specificity for contrast-enhancing lesion nBV were 87% (80 − 91%) and 72% (64 − 88%), respectively (141,171,174–176) .

Perfusion imaging has also been used to differentiate malignant gliomas from other primary brain tumours. These included differentiating primary lymphomas from malignant gliomas (165,168,176,177,179–183), meningiomas from malignant gliomas (165,167,184), hemangioblastomas from malignant gliomas (165), and schwannomas from malignant gliomas (165). A few studies have used perfusion imaging to differentiate subtypes of primary brain tumours (161,185–189). Grade II and III oligodendroglial tumours showed higher nBV than both grade II and III oligoastrocytic and astrocytic tumours, and oligoastrocytic tumours showed higher maximum nBV than astrocytic tumours (161). A sensitivity and specificity of 100 and 88% were found when nBV was used to differentiate grade II and III oligodendroglial tumours from astrocytic tumours. Although there were differences in BV between different types of primary brain tumours, the number of brain tumour types make this method of differentiation impractical.

1.9.4   Differentiation of Progression from Post-treatment Effects

A change in the size of the contrast-enhancing tumour is used as a radiologic measure of progression, but it can be confounded by other causes of contrast enhancement. Pseudoprogression and treatment-induced necrosis (TIN) are post-treatment scenarios with a better prognosis than true progression, but their changes in contrast enhancement can be indistinguishable from progression. Erroneous diagnosis of pseudoprogression or TIN as tumour progression can lead to unnecessary treatment or premature abandonment of treatment while the opposite scenario will delay treatment.

Pseudoprogression occurs in $20-30\%$ of malignant glioma patients treated with chemoirradiation and manifests as a transient increase in tumour contrast-enhancement at one to three months post-treatment that eventually subsides (92,190,191). Although its pathophysiology remains unclear, chemoirradiation is believed to induce a transient local inflammatory reaction, edema and increased vessel permeability, which manifests as increased contrast-enhancement (192). Using DSC-MR, true progression showed a higher maximum nBV than pseudoprogression when confirmed by radiologic and clinical follow-ups (sensitivity and specificity of 81.5% and 77.8%, respectively) (191,193). Another study showed that both nBV and normalized peak height (definition in Table 1-2) could distinguish pseudoprogression from progression with sensitivities and specificities $\geq 75\%$ (194). Histogram analysis of nBV to characterize percent changes in nBV skewness and kurtosis is also a potential biomarker to differentiate pseudoprogression from true progression (195).

In a prospective study, a decrease in nBV at week three of chemoirradiation was associated with a higher risk of early progression (190). It is unclear why a decrease in nBV during chemoirradiation is associated with progression (190) while a higher nBV is found at the time of progression in other studies (191,193). These results suggest that the vascular response to chemoirradiation is complex, and the time of imaging must be considered when using perfusion imaging to distinguish between tumour progression and pseudoprogression.

TIN occurs three to 12 months after radiotherapy in 3 – 24% of patients (192). Histopathologic confirmation of necrosis and recurrence were available in some or all of the patients in each study. Table 1-6 summarizes the performance of 12 perfusion imaging studies for differentiating TIN from progression (118,196–206). Radiation-induced necrosis and pseudoprogression were collectively defined as radiation-induced injury in eight DSC-MR studies (196,207–213). Mean and maximum nBV were reported to differentiate radiation-induced injury from true progression with sensitivities and specificities ranging from 86 – 100% and 80 – 100%, respectively (207–213). Radiation-induced injury and true progression often co-exist in patients. Hu et al. showed that DSC-MR was able to estimate the fractional tumour burden (i.e. progression) and post-treatment effect (i.e. radiation-induced injury) within the same MR contrast-enhancing lesion (213). This fractional tumour burden strongly correlated with the histologic tumour fraction obtained from stereotactic biopsy ($r = 0.82$, $P < 0.0001$) and correlated with the OS ($P < 0.02$). These results demonstrate that DSC-MR may be a useful clinical tool to differentiate progression from post-treatment effects.

Table 1-6: Differentiation between treatment-induced necrosis and true progression.

Modality	Parameter	Sensitivity and specificity ranges (%)	References[†]
DSC-MR	[*]nBV	Sensitivity: 67 – 100% Specificity: 70 – 100%	(118,196–200)
	% Recovery	Sensitivity: 78% Specificity: 76%	(198)
	Peak Height	Sensitivity: 89% Specificity: 81%	(198)
DCE-MR	K^{trans}	Sensitivity: 100% Specificity: 83%	(202)
	iAUC	Sensitivity: 71 – 85% Specificity: 71 – 78%	(201,202)

	mAUCR$_H$	Sensitivity: 94% Specificity: 88%	(203)
	Normalized maximum slope	Sensitivity: 95% Specificity: 78%	(201)
	BV	Sensitivity: 100% Specificity: 100%	(204)
DCE-CT	BF	Sensitivity: 94% Specificity: 88%	(206)
	BV	Sensitivity: 82 – 83% Specificity: 90 – 100%	(205,206)
	PS	Sensitivity: 82% Specificity: 82%	(205)
	MTT	Sensitivity: 94% Specificity: 75%	(206)

Abbreviations: DSC-MR, dynamic susceptibility-contrast magnetic resonance; DCE-MR, dynamic contrast-enhanced magnetic resonance; DCE-CT, dynamic contrast-enhanced computed tomography; nBV, normalized blood volume; K^{trans}, transfer constant between blood plasma and extravascular extracellular space; iAUC, initial area under curve; mAUCR$_H$, see Table 1-2 for definition; BF, blood flow; PS, permeability-surface area product; MTT, mean transit time.

*nBV refers to mean or maximum nBV

1.9.5   Survival after Radiotherapy and Chemotherapy

The value of perfusion imaging in predicting progression-free survival (PFS) and OS has been investigated in numerous studies (124,130,140,148,214–237). The interpretation of perfusion imaging data for predictive survival depends on treatment regimen and imaging schedule. Three perfusion imaging schedules for predicting outcomes have been reported; they are 1) pre-treatment, 2) pre-treatment + mid-treatment, and 3) pre-treatment + post-treatment.

When pre-chemoirradiation DSC-MR images were considered, a higher mean and maximum nBV were associated with poor PFS and OS for gliomas of all grades (140,148,216,221–224,228,235,236). This is also true for gliomas of the same grade. The 2-year OS rate for grade III astrocytomas was significantly lower for patients with maximum nBV > 2.3 (33% vs. 100%, $P < 0.01$), and it was also lower for GBM (5% vs. 25%, $P = 0.013$) (221). Using DCE-CT, a combination of high BV and PS was associated with poor OS for grade III and IV gliomas and grade IV gliomas alone (232,233). In patients with GBM, k_{ep} values ≤ 1.2, between $1.21 - 2.0$, and > 2.0 min^{-1} had 1-year OS rate of 59%, 33%, and 15%, respectively (P value was not reported) (130). These studies suggest that pre-treatment BV, PS, and k_{ep} were associated with more aggressive phenotypes that conferred poor survival.

The prognostic value of comparing pre- and mid-radiotherapy perfusion imaging parameters have been investigated (215,219,220). Based on parametric response map analysis, a decrease in tumour BV and blood flow (BF) at one and three weeks into chemoirradiation were predictive of poor OS (219,220). Specifically, patients with > 6.8% of tumour volume showing a decrease in nBV had shorter OS than those with $\leq$ 6.8% of tumour volume showing a decrease in nBV (median OS = 7.1 and 20.4 months, respectively; $P = 0.001$) (219). A drop in BV during treatment suggest increased tumour hypoxia leading to resistance to chemoirradiation. These studies suggest DSC-MR can potentially identify patients with poor survival even before the completion of chemoirradiation.

Tumour perfusion after the completion of chemoirradiation and its association with survival have also been investigated (225–227,231,237). An increase in maximum nBF between baseline and follow-up (Hazard ratio [HR] = 2.67, $P = 0.010$) was a better prognosticator of shorter PFS than an increase in tumour diameter (HR = 1.14, $p = 0.049$) (231). At one month post-radiotherapy, Mangla et al. showed that an increase in nBV was predictive of poor 1-year OS (sensitivity = 90% and specificity = 69%) while tumour size was not (227). One study showed that perfusion imaging was not predictive of survival while T1 and T2-weighted tumour diameters were (225). Using *Ferumoxytol* as the contrast agent, post-radiotherapy tumour nBV predicted patients with longer OS ($P <$

0.001) (237). In the non-enhancing lesion, Li et al. showed that a higher median nBV immediately after radiation was associated with shorter PFS ($p = 0.026$) (226).

In summary, a high BV before and after chemoirradiation and a decrease in BV during chemoirradiation were associated with poor survival. A high BV before and after treatment is characteristic of tumour growth and progression, while a decrease in BV during treatment could be indicative of tumour hypoxia.

1.9.6   Survival After Anti-angiogenic Therapies

Radiologic assessment of response to anti-angiogenic agents, especially those that target VEGF, should be interpreted with caution because a drop in contrast-enhancement is not necessarily indicative of true response (i.e. pseudoresponse) (92). Batchelor et al. showed that patients treated with Cediranib demonstrated decreased gadolinium enhancement as early as one day after the initiation of treatment despite considerable variability in tumour response (238). Given the vascular effects of anti-angiogenic agents, perfusion imaging could play an important role in assessing response to these agents.

For recurrent GBM, high nBV and K_{trans} prior to anti-VEGF monotherapy or in combination with Temozolomide were associated with poor survival (239,240). Tumour BF (238), nBV (238,241), K^{trans} (238,240,242–246), and v_e (238,242,243,247) decreased shortly after the initiation of Bevacizumab or Cediranib. In the non-enhancing lesion, nBV could also decrease after Bevacizumab treatment suggesting an anti-edema effect (statistical significance was not reported) (248).

There is no consensus on whether a decrease in these parameters is a positive prognosticator. A decrease in K^{trans} and nBV after Bevacizumab treatment did not show a significant association with PFS or OS in some studies (239,240,246). In another study, a decrease in tumour subvolume with nBV > 1.00 after Bevacizumab treatment was associated with longer time-to-progression (229). A reduction in K^{trans} after Cediranib treatment was associated with improved PFS and OS (244). A moderate correlation

(Spearman's ρ = 0.58, P = 0.036) between OS and K^{trans} at 1 week after stereotactic radiosurgery and Bevacizumab was reported in patients with recurrent malignant gliomas (234).

The inconsistent relationships between perfusion imaging parameters and survival suggest that not all patients responded equally to anti-angiogenic agents. Sorensen et al. showed that 25% of patients with recurrent GBM treated with Cediranib exhibited elevated perfusion, and these patients had higher PFS and OS than those with stable or decreased perfusion (230,238,244). This was demonstrated again in patients with newly diagnosed GBM that were treated with radiotherapy, Temozolomide, and Cediranib. Patients with increased perfusion had a significantly longer median OS than patients with decreased perfusion (OS = 504 vs. 321 days; log-rank P < 0.05) (249). Increased perfusion was also associated with improved tumour oxygenation, which could potentially improve the sensitization of tumour cells to chemoirradiation and enhance the delivery of Temozolomide to the tumour. In a study involving patients with recurrent malignant gliomas, independent component analysis of DSC-MR images was used to characterize the extent of abnormal vasculature before and after Bevacizumab treatment. A decrease in the arterio-venous overlap (i.e. a decrease of abnormal vasculature) was associated with longer OS in these patients (P < 0.04), whereas a change in the tumour volume and nBV was not predictive of OS (250). These results suggest that perfusion imaging may be a tool for selecting the appropriate patients for anti-angiogenic therapies.

1.9.7   Future of Perfusion Imaging

Our review reflected the results from more than 6500 brain tumour patients scanned using CT or MR perfusion. These studies were primarily conducted in small cohorts of patients (*median N* = 31 patients) in a research setting. Different perfusion imaging protocols were used, and these variations could have led to uncertainties in the measurements of different perfusion imaging parameters (117,251). Standardization of imaging protocol is very important for incorporating perfusion imaging into prospective multi-institutional trials (252). In addition, different perfusion imaging software packages

were used in these studies. It has been shown that BF and BV values calculated from different commercial software packages can deviate from the true values (253). The uncertainties in the acquisition and analysis of these perfusion imaging studies make optimization and standardization difficult.

In a clinical trial, the imaging protocol should be consistent across the study population. The software and version used to calculate tumour perfusion parameters should also be consistent and reported. Quality control should be performed to ensure consistency in image quality. For example, the Radiation Therapy Oncology Group (RTOG) 0825 trial comparing "radiation + Temozolomide" versus "radiation + Temozolomide + Bevacizumab" is incorporating DSC-MRI and DCE-MRI to study these patients. Participating sites must be qualified through the American College of Radiology Imaging Network (ACRIN). The participating site must perform all advanced MR (e.g. perfusion MR) scans following the protocol-specific parameters, and one set of test MR images acquired from the designated MR scanner must be approved by ACRIN. This study will yield valuable information on the value of serial perfusion imaging.

Our literature review on perfusion imaging showed that perfusion changes in response to chemoirradiation and in combination with anti-angiogenic therapies are complex. Optimization and standardization of image acquisition and analysis can help facilitate the implementation of perfusion imaging in clinical settings. Serial imaging of perfusion changes in response to treatment will improve the understanding of the effect of treatment on tumour hemodynamics, and determine the optimal time for evaluating response and prognosis in patients.

1.10 Animal Models of Malignant Glioma

Animal models of brain tumours play very important roles in understanding the pathophysiology cancer, and in evaluating the safety and efficacy of treatments. There are three general categories of brain tumour models: 1) xenograft models, 2) chemically induced syngeneic models, and 3) genetically engineered mouse models (254). Rat

models have several advantages over mouse models. The rat brain is about three times larger than the mouse brain (1200 vs. 400 mg, respectively) (255). This allows more precise implantation of tumour cells in rat brains and stereotactic radiosurgery of tumours. A larger brain also permits a longer time period for tumour growth before death, and better visualization and localization of the tumour using a variety of imaging modalities. In addition, there are more *in vitro* and *in vivo* studies of rat brain tumours than mouse brain tumours (255).

Xenograft tumour models refer to the growth of human brain tumours within the brains of immunodeficient rats. For example, the U87MG cell line is a commonly used xenograft GBM model. These models exhibit some features of human GBMs, including the expression of mutated genes and display some levels of angiogenesis. However, they do not display many characteristics that are typical in human GBM. For instance, growth patterns are often circumscribed with limited single cell infiltration that are not as extensive as spontaneous human GBM (256,257). Necrosis and microvascular abnormalities, which are typical in human GBM, are also limited or absent in many human cell-derived xenografts (254,256,257).

Chemically induced syngeneic rat models have been used extensively since the 1970s (255). Popular examples include C6, 9L, BT4C, F98, RT-2, and CNS-1 gliomas (255). The C6 glioma model was created by administering methylnitrosourea to rats (258,259). It was morphologically similar to GBM, and showed overexpression of many genes that are also overexpressed in human gliomas. This model has been widely used to evaluate the safety and efficacy of a variety of treatments including radiotherapy (260–262), chemotherapy (263,264), and anti-angiogenic therapy (265,266). Chemically induced syngeneic models can grow in immunocompetent rats; thus, spontaneous tumour rejection is a drawback. A previous report showed that 11% of rats survived after implantation of C6 glioma cells (267). Another drawback of chemically induced syngeneic models is their growth patterns. For example, both C6 and 9L tumour models demonstrate circumscribed masses as opposed to the highly infiltrative growth of human gliomas (255). Despite these drawbacks, the C6 model remains attractive because it is useful for the study of glioblastoma growth, angiogenesis, and development of new

therapies (266). The C6 glioma model is used in the preclinical work presented in this thesis.

1.11 Research Goals and Objectives

The work presented in this thesis is focused on two major goals: 1) improving measurements of DCE-CT parameters, and 2) using DCE-CT to assess treatment response in malignant gliomas. This was accomplished by achieving the following objectives which span the spectrum from technical optimization to preclinical imaging to pilot clinical studies:

1. To improve the measurements of BF, BV, and PS by evaluating the effect of DCE-CT scan duration on these measurements.

2. To reduce measurement errors of BF, BV, and PS by filtering DCE-CT images using principal component analysis.

3. To show that DCE-CT can be used as a potential early imaging biomarker of response to stereotactic radiosurgery in the C6 malignant rat glioma model.

4. To assess the relationship between DCE-CT imaging measurements and eventual sites of tumour progression in patients with malignant gliomas.

5. To correlate patient survival with DCE-CT and MR volumetric imaging measurements.

1.12 Thesis Outline

1.12.1 The Effect of Scan Duration on the Measurement of DCE-CT Parameters (*Chapter 2*)

Scan duration is a key factor that influences the measurement of different perfusion parameters. We investigated the effect of scan duration on BF, BV, and PS measurements in human gliomas and evaluated the systematic and random errors associated with reduced scan durations. This chapter is adapted from the published paper entitled "The effect of scan duration on the measurement of perfusion parameters in CT perfusion studies of brain tumours", published in *Academic Radiology* 20(1): 69-65 (2013) by Yeung TPC, Yartsev S, Bauman G, He W, Fainardi E, and Lee TY.

1.12.2 Improving Quantitative DCE-CT Measurements Using Principal Component Analysis (*Chapter 3*)

The measurements BF, BV, and PS are affected by DCE-CT image contrast-to-noise ratio (CNR). We validated whether principal component analysis (PCA) filtering can improve the accuracy and precision of these measurements by using a digitally designed CT phantom. We then evaluated the improvement in image CNR and changes in tumour BF, BV, and PS after filtering DCE-CT images of tumour bearing rats. This chapter is adapted from the published paper entitled "Improving quantitative CT perfusion parameter measurements using principal component analysis", published in *Academic Radiology* 21(5): 624-632 (2014) by Yeung TPC, Dekaban M, De Haan N, Morrison L, Hoffman L, Bureau Y, Chen X, Yartsev S, Bauman G, and Lee TY.

1.12.3   DCE-CT Imaging as an Early Biomarker of Differential Response to Stereotactic Radiosurgery (*Chapter 4*)

Stereotactic radiosurgery delivers radiation in one or few large dose fractions of 8 to 30 Gy that can result in vascular damage. Timely and accurate assessment of tumour response is crucial for treatment modification if no response to radiation is detected. This chapter evaluated serial vascular changes following stereotactic radiosurgery using DCE-CT, and determined whether DCE-CT can be an early predictor of survival. This chapter is based on the paper entitled "CT perfusion imaging as an early biomarker of differential response to stereotactic radiosurgery", which will be submitted to the journal *PLOS ONE* in July 2014 by Yeung TPC, Kurdi M, Wang Y, Al-Khazraji B, Morrison L, Hoffman L, Jackson D, Crukley C, Lee TY, Bauman G, and Yartsev S.

1.12.4   Relationship of DCE-CT and PET to Tumour Progression in Malignant Glioma (*Chapter 5*)

Over 80% of malignant gliomas progress within 2 cm of the irradiated volume after chemoirradiation. Although an increase in the size of the contrast-enhancing lesion is one of the criteria for diagnosing progression, early changes in contrast-enhancement during and after radiotherapy lack utility in identifying active tumour sites that are likely to persist and progress. This chapter investigates whether multiparametric imaging with DCE-CT and 18F-Flurodeoxyglucose PET can identify tumour sites that are likely to correlate to the eventual sites of tumour progression. The chapter is based on the published paper entitled "Relationship of computed tomography perfusion and positron emission tomography to tumour progression in malignant glioma", published in the *Journal of Medical Radiation Sciences* 61(1): 4-13 (2014) by Yeung TPC, Yartsev S, Lee TY, Wong E, He W, Fisher B, VanderSpek L, Macdonald D, and Bauman G.

1.12.5 Treatment Monitoring of Malignant gliomas in using DCE-CT and MR (*Chapter 6*)

Using DCE-CT, this is the first study to evaluate serial changes in tumour BF, BV, and PS in the contrast-enhancing lesion and the non-enhancing lesion of patients with malignant gliomas for up to a year after radiotherapy. This study also tested the predictive values of these data in relation to OS. The chapter is based on the paper entitled "Treatment monitoring in high-grade gliomas: A serial CT perfusion and MR study", which will be submitted to the *Journal of Neuro-Oncology* in July 2014 by Yeung TPC, Wang Y, Urbini B, Yartsev S, Bauman G, Lee TY, Fainardi E, and The Project of Emilia-Romagna region on Neuro-Oncology (PERNO) study group.

1.12.6 Conclusion and Future Work (*Chapter 7*)

In the final chapter, major findings of this thesis are summarized, and their clinical and experimental relevance are discussed. Future investigations pertaining to perfusion imaging of brain tumours are proposed.

1.13 References

1. Ostrom QT, Gittleman H, Farah P, et al. CBTRUS statistical report: Primary brain and central nervous system tumors diagnosed in the United States in 2006-2010. Neuro Oncol. 2013; 15:ii1–56.
2. Canadian Cancer Society's Advisory Committee on Cancer Statistics. Canadian Cancer Statistics 2013. Toronto, ON: Canadian Cancer Society; 2013.
3. Louis D, Ohgaki H, Wiestler O, Cavenee W, Editors. WHO Classification of tumours of the central nervous system. 4th ed. Lyon: International Agency for Research on Cancer; 2007.
4. Wen PY, Kesari S. Malignant gliomas in adults. N Engl J Med. 2008; 359:492–507.

5. Stupp R, Mason WP, van den Bent MJ, et al. Radiotherapy plus concomitant and adjuvant temozolomide for glioblastoma. N Engl J Med. 2005; 352:987–96.

6. Jansen EP, Dewit LG, van Herk M, Bartelink H. Target volumes in radiotherapy for high-grade malignant glioma of the brain. Radiother Oncol. 2000; 56:151–6.

7. Curran WJ, Scott CB, Horton J, et al. Recursive partitioning analysis of prognostic factors in three radiation therapy. J Natl Cancer Inst. 1993; 85:704–10.

8. McGirt MJ, Kaisorn LC, Chaichana M, et al. Independent association of extent of resection with survival in patients with malignant brain astrocytoma. J Neurosurg. 2009; 110:156–62.

9. Lacroix M, Abi-Said D, Fourney DR, et al. A multivariate analysis of 416 patients with glioblastoma multiforme: prognosis, extent of resection, and survival. J Neurosurg. 2001; 95:190–8.

10. Ammirati M, Vick N, Liao Y, Ciric I, Mikhael M. Effect of the extent of surgical resection on survival and quality of life in patients with supratentorial glioblastomas and anaplastic astrocytomas. Neurosurgery. 1987; 21:201–6.

11. Walker M, Strike T, Sheline G. An analysis of dose-effect relationship in the radiotherapy of malignant gliomas. Int J Radiat Oncol Biol Phys. 1979; 5:1725–31.

12. Oppitz U, Maessen D, Zunterer H, Richter S, Flentje M. 3D-recurrence-patterns of glioblastomas after CT-planned postoperative irradiation. Radiother Oncol. 1999; 53:53–7.

13. Liang BC, Thornton a F, Sandler HM, Greenberg HS. Malignant astrocytomas: focal tumor recurrence after focal external beam radiation therapy. J Neurosurg. 1991; 75:559–63.

14. Weber DC, Casanova N, Zilli T, et al. Recurrence pattern after [(18)F]fluoroethyltyrosine-positron emission tomography-guided radiotherapy for high-grade glioma: a prospective study. Radiother Oncol. 2009; 93:586–92.

15. McDonald MW, Shu H-KG, Curran WJ, Crocker IR. Pattern of failure after limited margin radiotherapy and temozolomide for glioblastoma. Int J Radiat Oncol Biol Phys. 2011; 79:130–6.

16. Milano MT, Okunieff P, Donatello RS, et al. Patterns and timing of recurrence after temozolomide-based chemoradiation for glioblastoma. Int J Radiat Oncol Biol Phys. 2010; 78(4):1147–55.

17. Park I, Tamai G, Lee MC, et al. Patterns of recurrence analysis in newly diagnosed glioblastoma multiforme after three-dimensional conformal radiation therapy with respect to pre-radiation therapy magnetic resonance spectroscopic findings. Int J Radiat Oncol Biol Phys. 2007; 69:381–9.

18. Chan JL, Lee SW, Fraass BA, et al. Survival and failure patterns of high-grade gliomas after three-dimensional conformal radiotherapy. J Clin Oncol. 2002; 20:1635–42.

19. Lee SW, Fraass BA, Marsh LH, et al. Patterns of failure following high-dose 3-D conformal radiotherapy for high-grade astrocytomas: a quantitative dosimetric study. Int J Radiat Oncol Biol Phys. 1999; 43:79–88.

20. Nakagawa K, Aoki Y, Fujimaki T, et al. High-dose conformal radiotherapy influenced the pattern of failure but did not improve survival in glioblastoma multiforme. Int J Radiat Oncol Biol Phys. 1998; 40:1141–9.

21. Massaccesi M, Ferro M, Cilla S, et al. Accelerated intensity-modulated radiotherapy plus temozolomide in patients with glioblastoma: A phase I dose-escalation study (ISIDE-BT-1). Int J Clin Oncol. 2013; 18:784–91.

22. Morganti AG, Balducci M, Salvati M, et al. A phase I dose-escalation study (ISIDE-BT-1) of accelerated IMRT with temozolomide in patients with glioblastoma. Int J Radiat Oncol Biol Phys. 2010; 77:92–7.

23. Iuchi T, Hatano K, Narita Y, Kodama T, Yamaki T, Osato K. Hypofractionated high-dose irradiation for the treatment of malignant astrocytomas using simultaneous integrated boost technique by IMRT. Int J Radiat Oncol Biol Phys. 2006; 64(5):1317–24.

24. Sarkaria JN, Mehta MP, Loeffler JS, et al. Radiosurgery in the initial management of malignant gliomas: survival comparison with the RTOG recursive partitioning analysis. Radiation Therapy Oncology Group. Int J Radiat Oncol Biol Phys. 1995; 32:931–41.

25. Tsao MN, Mehta MP, Whelan TJ, et al. The American Society for Therapeutic Radiology and Oncology (ASTRO) evidence-based review of the role of radiosurgery for malignant glioma. Int J Radiat Oncol Biol Phys. 2005; 63:47–55.

26. Shrieve DC, Alexander E, Black PM, et al. Treatment of patients with primary glioblastoma multiforme with standard postoperative radiotherapy and radiosurgical boost: prognostic factors and long-term outcome. J Neurosurg. 1999; 90:72–7.

27. Larson D, Gutin P, McDermott M. Gamma knife for glioma: Selection factors and survival. Int J Radiat Oncol Biol Phys. 1996; 36:1045–53.

28. Nwokedi E, DiBiase S, Jabbour S, Herman J, Amin P, Chin LS. Gamma knife stereotactic radiosurgery for patients with glioblastoma multiforme. Neurosurgery. 2002; 50:41–7

29. Prisco FE, Weltman E, de Hanriot RM, Brandt RA. Radiosurgical boost for primary high-grade gliomas. J Neurooncol. 2002; 57:151–60.

30. Aiken AH, Chang SM, Larson D, Butowski N, Cha S. Longitudinal magnetic resonance imaging features of glioblastoma multiforme treated with radiotherapy with or without brachytherapy. Int J Radiat Oncol Biol Phys. 2008; 72:1340–6.

31. Loeffler JS, Alexander E 3rd, Hochberg FH, et al. Clinical patterns of failure following stereotactic interstitial irradiation for malignant gliomas. Int J Radiat Oncol Biol Phys. 1990; 19:1455–62.

32. Laperriere NJ, Leung PM, McKenzie S, et al. Randomized study of brachytherapy in the initial management of patients with malignant astrocytoma. Int J Radiat Oncol Biol Phys. 1998; 41:1005–11.

33. Sneed PK, Gutin PH, Larson DA, et al. Patterns of recurrence of glioblastoma multiforme after external irradiation followed by implant boost. Int J Radiat Oncol Biol Phys. 1994; 29:719–27.

34. Agbi CB, Bernstein M, Laperriere N, Leung P, Lumley M. Patterns of recurrence of malignant astrocytoma following stereotactic interstitial brachytherapy with iodine-125 implants. Int J Radiat Oncol Biol Phys. 1992; 23:321–6.

35. Grosu AL, Weber WA, Franz M, et al. Reirradiation of recurrent high-grade gliomas using amino acid PET (SPECT)/CT/MRI image fusion to determine gross

tumor volume for stereotactic fractionated radiotherapy. Int J Radiat Oncol Biol Phys. 2005; 63:511–9.

36. Grosu AL, Weber WA, Riedel E, et al. L-(methyl-11C) methionine positron emission tomography for target delineation in resected high-grade gliomas before radiotherapy. Int J Radiat Oncol Biol Phys. 2005; 63:64–74.

37. Grosu AL, Feldmann H, Dick S, et al. Implications of IMT-SPECT for postoperative radiotherapy planning in patients with gliomas. Int J Radiat Oncol Biol Phys. 2002; 54:842–54.

38. Grosu AL, Weber W, Feldmann HJ, et al. First experience with I-123-alpha-methyl-tyrosine SPECT in the 3-D radiation treatment planning of brain gliomas. Int J Radiat Oncol Biol Phys. 2000; 47:517–26.

39. Gerson SL. MGMT: Its role in cancer aetiology and cancer therapeutics. Nat Rev Cancer. 2004; 4:296–307.

40. Esteller M, Hamilton SR, Burger PC, Baylin SB, Herman JG. Inactivation of the DNA repair gene O6-methylguanine-DNA methyltransferase by promoter hypermethylation is a common event in primary human neoplasia. Cancer Res. 1999; 59:793–7.

41. Hegi ME, Diserens AC, Gorlia T, et al. MGMT gene silencing and benefit from temozolomide in glioblastoma. N Engl J Med. 2005; 352:997–1003.

42. Brandes AA, Tosoni A, Franceschi E, et al. Recurrence pattern after temozolomide concomitant with and adjuvant to radiotherapy in newly diagnosed patients with glioblastoma: Correlation with MGMT promoter methylation status. J Clin Oncol. 2009; 27:1275–9.

43. Folkman J. Tumor angiogenesis: Therapeutic implications. N Engl J Med. 1971; 285:1182–6.

44. Folkman J. What is the evidence that tumors are angiogenesis dependent? J Natl Cancer Inst. 1990; 82:4–6.

45. Folkman J, Cole P, Zimmerman S. Tumor behavior in isolated perfused organs: In vitro growth and metastases of biopsy material in rabbit thyroid and canine intestinal segment. Ann Surg. 1966;164:491–502.

46. Persidsky Y, Ramirez SH, Haorah J, Kanmogne GD. Blood-brain barrier: structural components and function under physiologic and pathologic conditions. J Neuroimmune Pharmacol. 2006; 1:223–36.

47. Rucker HK, Wynder HJ, Thomas WE. Cellular mechanisms of CNS pericytes. Brain Res Bull. 2000; 51:363–9.

48. Bergers G, Song S. The role of pericytes in blood-vessel formation and maintenance. Neuro Oncol. 2005; 7:452–64.

49. Jain RK, di Tomaso E, Duda DG, Loeffler JS, Sorensen AG, Batchelor TT. Angiogenesis in brain tumours. Nat Rev Neurosci. 2007; 8:610–22.

50. Neuwelt EA. Mechanisms of Disease: The Blood-Brain Barrier. Neurosurgery. 2004; 54:131–42.

51. Schinkel AH, Wagenaar E, Mol CA, van Deemter L. P-glycoprotein in the blood-brain barrier of mice influences the brain penetration and pharmacological activity of many drugs. J Clin Invest. 1996; 97:2517-24.

52. Liebner S, Fischmann A, Rascher G, et al. Claudin-1 and claudin-5 expression and tight junction morphology are altered in blood vessels of human glioblastoma multiforme. Acta Neuropathol. 2000; 100:323–31.

53. Papadopoulos MC, Saadoun S, Woodrow CJ, et al. Occludin expression in microvessels of neoplastic and non-neoplastic human brain. Neuropathol Appl Neurobiol. 2001; 27:384–95.

54. Papadopoulos MC, Saadoun S, Davies DC, Bell BA. Emerging molecular mechanisms of brain tumour oedema. Br J Neurosurg. 2001; 15:101–8.

55. Barlow KD, Sanders AM, Soker S, Ergun S, Metheny-Barlow LJ. Pericytes on the tumor vasculature: Jekyll or Hyde? Cancer Microenviron. 2013; 6:1–17.

56. Papadopoulos MC, Saadoun S, Binder DK, Manley GT, Krishna S, Verkman AS. Molecular mechanisms of brain tumor edema. Neuroscience. 2004; 129:1011–20.

57. Janzer RC, Raff MC. Astrocytes induce blood–brain barrier properties in endothelial cells. Nature. 1987; 325:253–7.

58. Bates DO, Harper SJ. Regulation of vascular permeability by vascular endothelial growth factors. Vascul Pharmacol. 2002; 39:225–37.

59. Lamszus K, Laterra J, Westphal M, Rosen EM. Scatter factor/hepatocyte growth factor (SF/HGF) content and function in human gliomas. Int J Dev Neurosci. 1999; 17:517–30.

60. Krogh A. The anatomy and physiology of capillaries. New Haven: Yale University Press; 1922.

61. Torres Filho IP, Leunig M, Yuan F, Intaglietta M, Jain RK. Noninvasive measurement of microvascular and interstitial oxygen profiles in a human tumor in SCID mice. Proc Natl Acad Sci U S A . 1994; 91:2081–5.

62. Hill R, Bristow R. The scientific basis of radiotherapy. In: Tannok I, Hill R, Bristow R, Harrington L, editors. The Basic Science of Oncology. 4th ed. United States: Publishing, McGraw-Hill Professional; 2005. p. 289–321.

63. Dewhirst MW. Relationships between cycling hypoxia, HIF-1, angiogenesis and oxidative stress. Radiat Res. 2009; 172:653–65.

64. Dewhirst MW. Intermittent hypoxia furthers the rationale for hypoxia-inducible factor-1 targeting. Cancer Res. 2007; 67:854–5.

65. Martinive P, Defresne F, Bouzin C, et al. Preconditioning of the tumor vasculature and tumor cells by intermittent hypoxia: Implications for anticancer therapies. Cancer Res. 2006; 66:11736–44.

66. Dvorak HF. Vascular permeability factor/vascular endothelial growth factor: A critical cytokine in tumor angiogenesis and a potential target for diagnosis and therapy. J Clin Oncol. 2002; 20:4368–80.

67. Pettersson A, Nagy JA, Brown LF, et al. Heterogeneity of the angiogenic response induced in different normal adult tissues by vascular permeability factor/vascular endothelial growth factor. Lab Invest. 2000; 80:99–115.

68. Leenders WP, Küsters B, de Waal RM. Vessel co-option : How tumors obtain blood supply in the absence of sprouting angiogenesis. Endothelium. 2002; 9:83–7.

69. Holash J, Maisonpierre PC, Compton D, et al. Vessel cooption, regression, and growth in tumors mediated by angiopoietins and VEGF. Science. 1999; 284:1994–8.

70. Küsters B, Leenders WP, Wesseling P, et al. Vascular endothelial growth factor-A(165) induces progression of melanoma brain metastases without induction of sprouting angiogenesis. Cancer Res. 2002; 62:341–5.

71. Fukumura D, Xu L, Chen Y, Gohongi T, Seed B, Jain RK. Hypoxia and acidosis independently up-regulate vascular endothelial growth factor transcription in brain tumors in vivo. Cancer Res. 2001; 61:6020–4.

72. Rak J, Mitsuhashi Y, Bayko L, et al. Mutant ras oncogenes upregulate VEGF/VPF expression: Implications for induction and inhibition of tumor angiogenesis. Cancer Res. 1995; 55:4575–80.

73. Semenza GL. Targeting HIF-1 for cancer therapy. Nat Rev Cancer. 2003; 3:721–32.

74. Jensen RL. Brain tumor hypoxia: Tumorigenesis, angiogenesis, imaging, pseudoprogression, and as a therapeutic target. J Neurooncol. 2009; 92:317–35.

75. Senger DR, Galli SJ, Dvorak AM, Perruzzi CA, Harvey VS, Dvorak HF. Tumor cells secrete a vascular permeability factor that promotes accumulation of ascites fluid. Cancer Res. 1983; 219:983–5.

76. Luo JC, Yamaguchi S, Shinkai A, Shitara K, Shibuya M. Significant expression of vascular endothelial growth factor/vascular permeability factor in mouse ascites tumors. Cancer Res. 1998; 58:2652–60.

77. Dvorak HF, Brown LF, Detmar M, Dvorak AM. Vascular permeability factor/vascular endothelial growth factor, microvascular hyperpermeability, and angiogenesis. Am J Pathol. 1995; 146:1029–39.

78. Reiss Y, Machein MR, Plate KH. The role of angiopoietins during angiogenesis in gliomas. Brain Pathol. 2005; 15:311–7.

79. Carmeliet P, Jain RK. Angiogenesis in cancer and other diseases. Nature; 407:249–57.

80. Zagzag D, Amirnovin R, Greco MA, et al. Vascular apoptosis and involution in gliomas precede neovascularization: a novel concept for glioma growth and angiogenesis. Lab Invest. 2000; 80:837–49.

81. Stratmann A, Risau W, Plate KH. Cell type-specific expression of angiopoietin-1 and angiopoietin-2 suggests a role in glioblastoma angiogenesis. Am J Pathol. 1998; 153:1459–66.

82. Tate MC, Aghi MK. Biology of angiogenesis and invasion in glioma. Neurotherapeutics. 2009; 6:447–57.

83. Ceradini DJ, Kulkarni AR, Callaghan MJ, et al. Progenitor cell trafficking is regulated by hypoxic gradients through HIF-1 induction of SDF-1. Nat Med. 2004; 10:858–64.

84. Orlic D, Kajstura J, Chimenti S, Bodine DM, Leri A, Anversa P. Bone marrow stem cells regenerate infarcted myocardium. Pediatr Transplant. 2003; 7:86–8.

85. Takahashi T, Kalka C, Masuda H, et al. Ischemia- and cytokine-induced mobilization of bone marrow-derived endothelial progenitor cells for neovascularization. Nat Med. 1999; 5:434–8.

86. Lyden D, Hattori K, Dias S, et al. Impaired recruitment of bone-marrow-derived endothelial and hematopoietic precursor cells blocks tumor angiogenesis and growth. Nat Med. 2001; 7:1194–201.

87. Lyden D, Young AZ, Zagzag D, et al. Id1 and Id3 are required for neurogenesis, angiogenesis and vascularization of tumour xenografts. Nature. 1999; 401:670–7.

88. Kioi M, Vogel H, Schultz G, Hoffman RM, Harsh GR, Brown JM. Inhibition of vasculogenesis , but not angiogenesis , prevents the recurrence of glioblastoma after irradiation in mice. J Clin Invest. 2010; 120:694–705.

89. Du R, Lu KV, Petritsch C, et al. HIF1alpha induces the recruitment of bone marrow-derived vascular modulatory cells to regulate tumor angiogenesis and invasion. Cancer Cell. 2008; 13:206–20.

90. Döme B, Hendrix MJ, Paku S, Tóvári J, Tímár J. Alternative vascularization mechanisms in cancer: Pathology and therapeutic implications. Am J Pathol. 2007; 170:1–15.

91. Kurz H, Burri PH, Djonov VG. Angiogenesis and vascular remodeling by intussusception: From form to function. News Physiol Sci. 2003;18:65–70.

92. Wen PY, Macdonald DR, Reardon DA, et al. Updated response assessment criteria for high-grade gliomas: Response assessment in neuro-oncology working group. J Clin Oncol. 2010; 28:1963–72.

93. Macdonald DR, Cascino TL, Schold SC Jr, Cairncross JG. Response criteria for phase II studies of supratentorial malignant glioma. J Clin Oncol. 1990; 8:1277–80.

94. van den Bent MJ, Vogelbaum MA, Wen PY, Macdonald DR, Chang SM. End point assessment in gliomas: Novel treatments limit usefulness of classical Macdonald's Criteria. J Clin Oncol. 2009; 27:2905–8.

95. Sorensen AG, Batchelor TT, Wen PY, Zhang WT, Jain RK. Response criteria for glioma. Nat Clin Pract Oncol. 2008; 5:634–44.

96. Henson JW, Ulmer S, Harris GJ. Brain tumor imaging in clinical trials. AJNR Am J Neuroradiol. 2008; 29:419–24.

97. Vos MJ, Uitdehaag BM, Barkhof F, et al. Interobserver variability in the radiological assessment of response to chemotherapy in glioma. Neurology. 2003; 60:826–30.

98. Cairncross JG, Macdonald DR, Pexman J, Ives FJ. Steroid-induced CT changes in patients with recurrent malignant glioma. Neurology. 1988; 38:724–6.

99. Watling CJ, Lee DH, Macdonald DR, Cairncross JG. Corticosteroid-induced magnetic resonance imaging changes in patients with recurrent malignant glioma. J Clin Oncol. 1994; 12:1886–9.

100. Finn MA, Blumenthal DT, Salzman KL, Jensen RL. Transient postictal MRI changes in patients with brain tumors may mimic disease progression. Surg Neurol. 2007; 67:246–50.

101. Kumar AJ, Leeds NE, Fuller GN, et al. Malignant gliomas: MR imaging spectrum of radiation therapy- and chemotherapy-induced necrosis of the brain after treatment. Radiology. 2000;217:377-84.

102. Henegar MM, Moran CJ, Silbergeld DL. Early postoperative magnetic resonance imaging following nonneoplastic cortical resection. J Neurosurg. 1996; 84:174–9.

103. Sourbron SP, Buckley DL. Tracer kinetic modelling in MRI: Estimating perfusion and capillary permeability. Phys Med Biol. 2012; 57:R1–33.

104. Østergaard L. Cerebral perfusion imaging by bolus tracking. Top Magn Reson Imaging. 2004; 15:3–9.

105. Boxerman J, Schmainda KM, Weisskoff R. Relative cerebral blood volume maps corrected for contrast agent extravasation significantly correlate with glioma tumor grade, whereas uncorrected maps do not. AJNR Am J Neuroradiol. 2006; 27:859–67.

106. Paulson ES, Schmainda KM. Comparison of dynamic susceptibility-weighted contrast-enhanced MR methods: Recommendations for measuring relative cerebral blood volume in brain tumors. Radiology. 2008; 249:601–13.

107. Tofts PS, Brix G, Buckley DL, et al. Estimating kinetic parameters from dynamic contrast-enhanced T 1-weighted MRI of a diffusable tracer: Standardized quantities and symbols. J Magn Reson Imaging. 1999; 10:223–32.

108. Ingrisch M, Dietrich O, Attenberger U, et al. Quantitative pulmonary perfusion magnetic resonance imaging: influence of temporal resolution and signal-to-noise ratio. Invest Radiol. 2010; 45(1):7–14.

109. Essig M, Shiroishi MS, Nguyen TB, et al. Perfusion MRI: The five most frequently asked technical questions. AJR Am J Roentgenol. 2013; 200:24–34.

110. Lee T, Purdie T, Stewart E. CT imaging of angiogenesis. Q J Nucl Med. 2003; 47:171–87.

111. Johnson JA, Wilson TA. A model for capillary exchange. Am J Physiol. 1966; 210: 1299–303.

112. St Lawrence KS, Lee TY. An adiabatic approximation to the tissue homogeneity model for water exchange in the brain: I. Theoretical derivation. J Cereb blood flow Metab. 1998; 18:1365–77.

113. Yeung TPC, Yartsev S, Bauman G, He W, Fainardi E, Lee TY. The effect of scan duration on the measurement of perfusion parameters in CT perfusion studies of brain tumors. Acad Radiol. 2013; 20:59–65.

114. Coolens C, Breen S, Purdie TG, et al. Implementation and characterization of a 320-slice volumetric CT scanner for simulation in radiation oncology. Med Phys. 2009; 36:5120-7.

115. Youn SW, Kim JH, Weon YC, Kim SH, Han MK, Bae HJ. Perfusion CT of the brain using 40-mm-wide detector and toggling table technique for initial imaging of acute stroke. AJR Am J Roentgenol. 2008; 191:W120–6.

116. Prakash P, Kalra MK, Kambadakone AK, et al. Reducing abdominal CT radiation dose with adaptive statistical iterative reconstruction technique. Invest Radiol. 2010; 45:202–10.

117. Wiesmann M, Berg S, Bohner G, et al. Dose reduction in dynamic perfusion CT of the brain: effects of the scan frequency on measurements of cerebral blood flow, cerebral blood volume, and mean transit time. Eur Radiol. 2008; 18:2967–74.

118. Ozsunar Y, Mullins ME, Kwong K, et al. Glioma recurrence versus radiation necrosis? A pilot comparison of arterial spin-labeled, dynamic susceptibility contrast enhanced MRI, and FDG-PET imaging. Acad Radiol. 2010; 17:282–90.

119. Weber MA, Henze M, Tüttenberg J. Biopsy targeting gliomas: Do functional imaging techniques identify similar target areas? Invest Radiol. 2010; 45:755–68.

120. Leenders KL. PET: blood flow and oxygen consumption in brain tumors. J Neurooncol. 1994; 22:269–73.

121. Bruehlmeier M, Roelcke U, Schubiger P, Ametamey S. Assessment of hypoxia and perfusion in human brain tumors using PET with 18F-fluoromisonidazole and 15O-H2O. J Nucl Med. 2004; 45:1851–9.

122. Sadeghi N, D'Haene N, Decaestecker C, et al. Apparent diffusion coefficient and cerebral blood volume in brain gliomas: relation to tumor cell density and tumor microvessel density based on stereotactic biopsies. AJNR Am J Neuroradiol. 2008; 29:476–82.

123. Jain R, Gutierrez J, Narang J, et al. In vivo correlation of tumor blood volume and permeability with histologic and molecular angiogenic markers in gliomas. AJNR Am J Neuroradiol. 2011; 32:388–94.

124. Hu LS, Eschbacher JM, Dueck AC, et al. Correlations between perfusion MR imaging cerebral blood volume, microvessel quantification, and clinical outcome using stereotactic analysis in recurrent high-grade glioma. AJNR Am J Neuroradiol. 2012; 33:69–76.

125. Haris M, Gupta RK, Singh A, et al. Differentiation of infective from neoplastic brain lesions by dynamic contrast-enhanced MRI. Neuroradiology. 2008; 50 :531–40.

126. Haris M, Husain N, Singh A, et al. Dynamic contrast-enhanced derived cerebral blood volume correlates better with leak correction than with no correction for vascular endothelial growth factor, microvascular density, and grading of astrocytoma. J Comput Assist Tomogr. 2008; 32:955–65.

127. Sadeghi N, Salmon I, Decaestecker C, et al. Stereotactic comparison among cerebral blood volume, methionine uptake, and histopathology in brain glioma. AJNR Am J Neuroradiol. 2007; 28:455–61.

128. Maia AC Jr, Malheiros SM, da Rocha AJ, et al. MR cerebral blood volume maps correlated with vascular endothelial growth factor expression and tumor grade in nonenhancing gliomas. AJNR Am J Neuroradiol. 2005; 26:777–83.

129. Awasthi R, Rathore RK, Soni P, et al. Discriminant analysis to classify glioma grading using dynamic contrast-enhanced MRI and immunohistochemical markers. Neuroradiology. 2012; 54:205–13.

130. Awasthi R, Pandey CM, Sahoo P, et al. Dynamic contrast-enhanced magnetic resonance imaging-derived kep as a potential biomarker of matrix metalloproteinase 9 expression in patients with glioblastoma multiforme: A pilot study. J Comput Assist Tomogr. 2012; 36:125–30.

131. Zikou AK, Alexiou GA, Kosta P, et al. Diffusion tensor and dynamic susceptibility contrast MRI in glioblastoma. Clin Neurol Neurosurg. 2012; 114:607–12.

132. Price SJ, Green HA, Dean AF, Joseph J, Hutchinson PJ, Gillard JH. Correlation of MR relative cerebral blood volume measurements with cellular density and proliferation in high-grade gliomas: an image-guided biopsy study. AJNR Am J Neuroradiol. 2011; 32:501–6.

133. Leon SP, Folkerth RD, Black PM. Microvessel density is a prognostic indicator for patients with astroglial brain tumors. Cancer. 1996; 77:362–72.

134. Korkolopoulou P, Patsouris E, Kavantzas N, et al. Prognostic implications of microvessel morphometry in diffuse astrocytic neoplasms. Neuropathol Appl Neurobiol. 2002; 28:57–66.

135. Jain R, Poisson L, Narang J, et al. Correlation of perfusion parameters with genes related to angiogenesis regulation in glioblastoma: A feasibility study. AJNR Am J Neuroradiol. 2012; 33:1343–8.

136. Tynninen O, Aronen HJ, Ruhala M, et al. MRI enhancement and microvascular density in gliomas: Correlation with tumor cell proliferation. Invest Radiol. 1999; 34:427–34.

137. Jackson RJ, Fuller GN, Abi-Said D, et al. Limitations of stereotactic biopsy in the initial management of gliomas. Neuro Oncol. 2001; 3:193–200.

138. Shin JH, Lee HK, Kwun BD, et al. Using relative cerebral blood flow and volume to evaluate the histopathologic grade of cerebral gliomas: Preliminary results. Am J Roentgenol. 2002; 179:783–9.

139. Law M, Yang S, Wang H, et al. Glioma grading: sensitivity, specificity, and predictive values of perfusion MR imaging and proton MR spectroscopic imaging compared with conventional MR imaging. AJNR Am J Neuroradiol. 2003; 24:1989–98.

140. Lev MH, Ozsunar Y, Henson JW, et al. Glial tumor grading and outcome prediction using dynamic spin-echo MR susceptibility mapping compared with conventional contrast-enhanced MR: confounding effect of elevated rCBV of oligodendrogliomas [corrected]. AJNR Am J Neuroradiol. 2004; 25:214–21.

141. Bulakbasi N, Kocaoglu M, Farzaliyev A, et al. Assessment of diagnostic accuracy of perfusion MR imaging in primary and metastatic solitary malignant brain tumors. AJNR Am J Neuroradiol. 2005; 26:2187–99.

142. Hakyemez B, Erdogan C, Ercan I, Ergin N, Uysal S, Atahan S. High-grade and low-grade gliomas: Differentiation by using perfusion MR imaging. Clin Radiol. 2005; 60:493–502.

143. Xu M, See SJ, Ng WH, et al. Comparison of magnetic resonance spectroscopy and perfusion-weighted imaging in presurgical grading of oligodendroglial tumors. Neurosurgery. 2005; 56:919–26.

144. Spampinato MV, Smith JK, Kwock L, et al. Cerebral blood volume measurements and proton MR spectroscopy in grading of oligodendroglial tumors. AJR Am J Roentgenol. 2007; 188:204–12.

145. Young R, Babb J, Law M, Pollack E, Johnson G. Comparison of region-of-interest analysis with three different histogram analysis methods in the determination of perfusion metrics in patients with brain gliomas. J Magn Reson Imaging. 2007; 26:1053–63.

146. Zonari P, Baraldi P, Crisi G. Multimodal MRI in the characterization of glial neoplasms: the combined role of single-voxel MR spectroscopy, diffusion imaging and echo-planar perfusion imaging. Neuroradiology. 2007; 49:795–803.

147. Arvinda HR, Kesavadas C, Sarma PS, et al. Glioma grading: sensitivity, specificity, positive and negative predictive values of diffusion and perfusion imaging. J Neurooncol. 2009; 94:87–96.

148. Bisdas S, Kirkpatrick M, Giglio P, Welsh C, Spampinato MV, Rumboldt Z. Cerebral blood volume measurements by perfusion-weighted MR imaging in gliomas: Ready for prime time in predicting short-term outcome and recurrent disease? AJNR Am J Neuroradiol. 2009; 30:681–8.

149. Park MJ, Kim HS, Jahng GH, Ryu CW, Park SM, Kim SY. Semiquantitative assessment of intratumoral susceptibility signals using non-contrast-enhanced high-field high-resolution susceptibility-weighted imaging in patients with gliomas: Comparison with MR perfusion imaging. AJNR Am J Neuroradiol. 2009; 30:1402–8.

150. Morita N, Wang S, Chawla S, Poptani H, Melhem ER. Dynamic susceptibility contrast perfusion weighted imaging in grading of nonenhancing astrocytomas. J Magn Reson Imaging. 2010; 32:803–8.

151. Hilario A, Ramos A, Perez-Nuñez A, et al. The added value of apparent diffusion coefficient to cerebral blood volume in the preoperative grading of diffuse gliomas. AJNR Am J Neuroradiol. 2012; 33:701–7.

152. Jia Z, Geng D, Xie T, Zhang J, Liu Y. Quantitative analysis of neovascular permeability in glioma by dynamic contrast-enhanced MR imaging. J Clin Neurosci.; 2012; 19:820–3.

153. Nguyen TB, Cron GO, Mercier JF, et al. Diagnostic accuracy of dynamic contrast-enhanced MR imaging using a phase-derived vascular input function in the preoperative grading of gliomas. AJNR Am J Neuroradiol. 2012; 33:1539–45.

154. Ding B, Ling HW, Chen KM, Jiang H, Zhu YB. Comparison of cerebral blood volume and permeability in preoperative grading of intracranial glioma using CT perfusion imaging. Neuroradiology. 2006;48 (10):773–81.

155. Ellika SK, Jain R, Patel SC, et al. Role of perfusion CT in glioma grading and comparison with conventional MR imaging features. AJNR Am J Neuroradiol. 2007; 28:1981–7.

156. Xyda A, Haberland U, Klotz E, et al. Brain volume perfusion CT performed with 128-detector row CT system in patients with cerebral gliomas: a feasibility study. Eur Radiol. 2011 ; 21:1811–9.

157. Beppu T, Sasaki M, Kudo K, et al. Prediction of malignancy grading using computed tomography perfusion imaging in nonenhancing supratentorial gliomas. J Neurooncol. 2011; 103:619–27.

158. Scott JN, Brasher PM, Sevick RJ, Rewcastle NB, Forsyth PA. How often are nonenhancing supratentorial gliomas malignant? A population study. Neurology. 2002; 59:947–9.

159. Maia AC Jr, Malheiros SM, da Rocha AJ, et al. Stereotactic biopsy guidance in adults with supratentorial nonenhancing gliomas: Role of perfusion-weighted magnetic resonance imaging. J Neurosurg. 2004; 101:970–6.

160. Danchaivijitr N, Waldman A, Tozer DJ, et al. Low-Grade Gliomas: Do changes in rCBV measurements at longitudinal perfusion-weighted MR imaging predict malignant transformation? Radiology. 2008; 247:170–8.

161. Saito T, Yamasaki F, Kajiwara Y, et al. Role of perfusion-weighted imaging at 3T in the histopathological differentiation between astrocytic and oligodendroglial tumors. Eur J Radiol. 2012; 81:1863–9.

162. Whitmore RG, Krejza J, Kapoor GS, et al. Prediction of oligodendroglial tumor subtype and grade using perfusion weighted magnetic resonance imaging. J Neurosurg. 2007; 107:600–9.

163. Schiff D. Single Brain Metastasis. Curr Treat Options Neurol. 2001; 3:89–99.

164. Kremer S, Grand S, Berger F, et al. Dynamic contrast-enhanced MRI: differentiating melanoma and renal carcinoma metastases from high-grade astrocytomas and other metastases. Neuroradiology. 2003; 45:44–9.

165. Hakyemez B, Erdogan C, Bolca N, Yildirim N, Gokalp G, Parlak M. Evaluation of different cerebral mass lesions by perfusion-weighted MR imaging. J Magn Reson Imaging. 2006; 24:817–24.

166. Law M, Cha S, Knopp EA, Johnson G, Arnett J, Litt AW. High-grade gliomas and solitary metastases: Differentiation by using perfusion and proton spectroscopic MR imaging. Radiology. 2002; 222:715–21.

167. Lüdemann L, Grieger W, Wurm R, Wust P, Zimmer C. Quantitative measurement of leakage volume and permeability in gliomas, meningiomas and brain metastases with dynamic contrast-enhanced MRI. Magn Reson Imaging. 2005; 23:833–41.

168. Bendini M, Marton E, Feletti A, et al. Primary and metastatic intraaxial brain tumors: Prospective comparison of multivoxel 2D chemical-shift imaging (CSI) proton MR spectroscopy, perfusion MRI, and histopathological findings in a group of 159 patients. Acta Neurochir (Wien). 2011; 153:403–12.

169. Young GS, Setayesh K. Spin-echo echo-planar perfusion MR imaging in the differential diagnosis of solitary enhancing brain lesions: distinguishing solitary metastases from primary glioma. AJNR Am J Neuroradiol. 2009; 30:575–7.

170. Mouthuy N, Cosnard G, Abarca-Quinones J, Michoux N. Multiparametric magnetic resonance imaging to differentiate high-grade gliomas and brain metastases. J Neuroradiol. 2012; 39:301–7.

171. Hakyemez B, Erdogan C, Gokalp G, Dusak A, Parlak M. Solitary metastases and high-grade gliomas: Radiological differentiation by morphometric analysis and perfusion-weighted MRI. Clin Radiol. 2010; 65:15–20.

172. Chiang IC, Kuo YT, Lu CY, et al. Distinction between high-grade gliomas and solitary metastases using peritumoral 3-T magnetic resonance spectroscopy, diffusion, and perfusion imagings. Neuroradiology. 2004; 46:619–27.

173. Lehmann P, Saliou G, de Marco G, et al. Cerebral peritumoral oedema study: does a single dynamic MR sequence assessing perfusion and permeability can help to differentiate glioblastoma from metastasis? Eur J Radiol. 2012; 81:522–7.

174. Server A, Orheim TE, Graff BA, Josefsen R, Kumar T, Nakstad PH. Diagnostic examination performance by using microvascular leakage, cerebral blood volume, and blood flow derived from 3-T dynamic susceptibility-weighted contrast-enhanced perfusion MR imaging in the differentiation of glioblastoma multiforme and brain me. Neuroradiology. 2011; 53:319–30.

175. Blasel S, Jurcoane A, Franz K, Morawe G, Pellikan S, Hattingen E. Elevated peritumoural rCBV values as a mean to differentiate metastases from high-grade gliomas. Acta Neurochir (Wien) . 2010; 152:1893–9.

176. Ma JH, Kim HS, Rim NJ, Kim SH, Cho KG. Differentiation among glioblastoma multiforme, solitary metastatic tumor, and lymphoma using whole-tumor histogram analysis of the normalized cerebral blood volume in enhancing and perienhancing lesions. AJNR Am J Neuroradiol. 2010; 31:1699–706.

177. Wang S, Kim S, Chawla S, et al. Differentiation between glioblastomas, solitary brain metastases, and primary cerebral lymphomas using diffusion tensor and dynamic susceptibility contrast-enhanced MR imaging. AJNR Am J Neuroradiol. 2011; 32:507–14.

178. Raore B, Schniederjan M, Prabhu R, Brat DJ, Shu HK, Olson JJ. Metastasis infiltration: an investigation of the postoperative brain-tumor interface. Int J Radiat Oncol Biol Phys. 2011; 81:1075–80.

179. Weber MA, Zoubaa S, Schlieter M, et al. Diagnostic performance of spectroscopic and perfusion MRI for distinction of brain tumors. Neurology. 2006; 66:1899–906.

180. Calli C, Kitis O, Yunten N, Yurtseven T, Islekel S, Akalin T. Perfusion and diffusion MR imaging in enhancing malignant cerebral tumors. Eur J Radiol. 2006; 58:394–403.

181. Hartmann M, Heiland S, Harting I, et al. Distinguishing of primary cerebral lymphoma from high-grade glioma with perfusion-weighted magnetic resonance imaging. Neurosci Lett. 2003; 338:119–22.

182. Liao W, Liu Y, Wang X, et al. Differentiation of primary central nervous system lymphoma and high-grade glioma with dynamic susceptibility contrast-enhanced perfusion magnetic resonance imaging. Acta Radiol. 2009; 50:217–25.

183. Schramm P, Xyda A, Klotz E, Tronnier V, Knauth M, Hartmann M. Dynamic CT perfusion imaging of intra-axial brain tumours: Differentiation of high-grade gliomas from primary CNS lymphomas. Eur Radiol. 2010; 20:2482–90.

184. Hakyemez B, Yildirim N, Erdoğan C, Kocaeli H, Korfali E, Parlak M. Meningiomas with conventional MRI findings resembling intraaxial tumors: Can

perfusion-weighted MRI be helpful in differentiation? Neuroradiology. 2006; 48:695–702.

185. Narang J, Jain R, Scarpace L, et al. Tumor vascular leakiness and blood volume estimates in oligodendrogliomas using perfusion CT: An analysis of perfusion parameters helping further characterize genetic subtypes as well as differentiate from astroglial tumors. J Neurooncol. 2011; 102:287–93.

186. Law M, Young R, Babb J, et al. Comparing perfusion metrics obtained from a single compartment versus pharmacokinetic modeling methods using dynamic susceptibility contrast-enhanced perfusion MR imaging with glioma grade. AJNR Am J Neuroradiol. 2006; 27:1975–82.

187. Chang SM, Nelson S, Vandenberg S, et al. Integration of preoperative anatomic and metabolic physiologic imaging of newly diagnosed glioma. J Neurooncol. 2009; 92:401–15.

188. Eliat PA, Olivié D, Saïkali S, Carsin B, Saint-Jalmes H, de Certaines JD. Can dynamic contrast-enhanced magnetic resonance imaging combined with texture analysis differentiate malignant glioneuronal tumors from other glioblastoma? Neurol Res Int. 2012; 2012:195176.

189. Law M, Meltzer DE, Wetzel SG, et al. Conventional MR imaging with simultaneous measurements of cerebral blood volume and vascular permeability in ganglioglioma. Magn Reson Imaging. 2004; 22:599–606.

190. Tsien C, Galbán CJ, Chenevert TL, et al. Parametric response map as an imaging biomarker to distinguish progression from pseudoprogression in high-grade glioma. J Clin Oncol. 2010; 28:2293–9.

191. Kong DS, Kim ST, Kim EH, et al. Diagnostic dilemma of pseudoprogression in the treatment of newly diagnosed glioblastomas: The role of assessing relative cerebral blood flow volume and oxygen-6-methylguanine-DNA methyltransferase promoter methylation status. AJNR Am J Neuroradiol. 2011; 32:382–7.

192. Brandsma D, Stalpers L, Taal W, Sminia P, van den Bent MJ. Clinical features, mechanisms, and management of pseudoprogression in malignant gliomas. Lancet Oncol. 2008; 9:453–61.

193. Gahramanov S, Raslan AM, Muldoon LL, et al. Potential for differentiation of pseudoprogression from true tumor progression with dynamic susceptibility-weighted contrast-enhanced magnetic resonance imaging using Ferumoxytol vs. Gadoteridol: A pilot study. Int J Radiat Oncol Biol Phys. 2011; 79:514–23.

194. Young RJ, Gupta A, Shah AD, et al. MRI perfusion in determining pseudoprogression in patients with glioblastoma. Clin Imaging. 2013; 37:41–9.

195. Baek HJ, Kim HS, Kim N, Choi YJ, Kim YJ. Percent change of perfusion skewness and kurtosis: a potential imaging biomarker for early treatment response in patients with newly diagnosed glioblastomas. Radiology. 2012; 264:834–43.

196. Kim HS, Kim JH, Kim SH, Cho KG, Kim SY. Posttreatment high-grade glioma: Usefulness of peak height position with semiquantitative MR perfusion histogram analysis in an entire contrast-enhanced lesion for predicting volume fraction of recurrence. Radiology. 2010; 256:906-15.

197. Prat R, Galeano I, Lucas A, et al. Relative value of magnetic resonance spectroscopy, magnetic resonance perfusion, and 2-(18F) fluoro-2-deoxy-D-glucose positron emission tomography for detection of recurrence or grade increase in gliomas. J Clin Neurosci. 2010; 17:50–3.

198. Barajas RF Jr, Chang JS, Segal MR, et al. Differentiation of recurrent glioblastoma multiforme from radiation necrosis after external beam radiation therapy with dynamic susceptibility-weighted contrast-enhanced perfusion MR imaging. Radiology. 2009; 253(2):486–96.

199. Dandois V, Rommel D, Renard L, Jamart J, Cosnard G. Substitution of 11C-methionine PET by perfusion MRI during the follow-up of treated high-grade gliomas: Preliminary results in clinical practice. J Neuroradiol. 2010; 37:89–97.

200. Xu JL, Shi DP, Dou S, Li YL, Yan FS. Distinction between postoperative recurrent glioma and delayed radiation injury using MR perfusion weighted imaging. J Med Imaging Radiat Oncol. 2011; 55:587–94.

201. Narang J, Jain R, Arbab AS, et al. Differentiating treatment-induced necrosis from recurrent/progressive brain tumor using nonmodel-based semiquantitative indices derived from dynamic contrast-enhanced T1-weighted MR perfusion. Neuro Oncol. 2011; 13:1037–46.

202. Bisdas S, Naegele T, Ritz R, et al. Distinguishing recurrent high-grade gliomas from radiation injury: A pilot study using dynamic contrast-enhanced MR imaging. Acad Radiol. 2011; 18:575–83.

203. Chung WJ, Kim HS, Kim N, Choi CG, Kim SJ. Recurrent glioblastoma: Optimum area under the curve method derived from dynamic contrast-enhanced T1-weighted perfusion MR imaging. Radiology. 2013; 269:561–8.

204. Larsen VA, Simonsen HJ, Law I, Larsson HB, Hansen AE. Evaluation of dynamic contrast-enhanced T1-weighted perfusion MRI in the differentiation of tumor recurrence from radiation necrosis. Neuroradiology. 2013; 55:361–9.

205. Jain R, Narang J, Schultz L, et al. Permeability estimates in histopathology-proved treatment-induced necrosis using perfusion CT : Can these add to other perfusion parameters in differentiating from recurrent/progressive tumors? AJNR Am J Neuroradiol. 2011; 32:658–63.

206. Jain R, Scarpace L, Ellika S, et al. First-pass perfusion computed tomography: Initial experience in differentiating recurrent brain tumors from radiation effects and radiation necrosis. Neurosurgery. 2007; 61:778–87.

207. Fink JR, Carr RB, Matsusue E, et al. Comparison of 3 Tesla proton MR spectroscopy, MR perfusion and MR diffusion for distinguishing glioma recurrence from posttreatment effects. J Magn Reson Imaging. 2012; 35:56–63.

208. Bobek-Billewicz B, Stasik-Pres G, Majchrzak H, Zarudzki L. Differentiation between brain tumor recurrence and radiation injury using perfusion, diffusion-weighted imaging and MR spectroscopy. Folia Neuropathol. 2010; 48:81–92.

209. Matsusue E, Fink JR, Rockhill JK, Ogawa T, Maravilla KR. Distinction between glioma progression and post-radiation change by combined physiologic MR imaging. Neuroradiology. 2010; 52:297–306.

210. Hu LS, Baxter LC, Pinnaduwage DS, et al. Optimized preload leakage-correction methods to improve the diagnostic accuracy of dynamic susceptibility-weighted contrast-enhanced perfusion MR imaging in posttreatment gliomas. AJNR Am J Neuroradiol. 2010; 31:40–8.

211. Hu LS, Baxter LC, Smith KA, et al. Relative cerebral blood volume values to differentiate high-grade glioma recurrence from posttreatment radiation effect:

Direct correlation between image-guided tissue histopathology and localized dynamic susceptibility-weighted contrast-enhanced perfusion MR imaging measurements. AJNR Am J Neuroradiol. 2009; 30:552–8.

212. Hu X, Wong KK, Young GS, Guo L, Wong ST. Support vector machine multi-parametric MRI identification of pseudoprogression from tumor recurrence in patients with resected glioblastoma. J Magn Reson imaging. 2012; 33:296–305.

213. Hu LS, Eschbacher JM, Heiserman JE, et al. Reevaluating the imaging definition of tumor progression: Perfusion MRI quantifies recurrent glioblastoma tumor fraction, pseudoprogression, and radiation necrosis to predict survival. Neuro Oncol. 2012; 14:919–30.

214. Akella NS, Twieg DB, Mikkelsen T, et al. Assessment of brain tumor angiogenesis inhibitors using perfusion magnetic resonance imaging: Quality and analysis results of a phase I trial. J Magn Reson Imaging. 2004; 20:913–22.

215. Cao Y, Tsien CI, Nagesh V, et al. Clinical investigation survival prediction in high-grade gliomas by MRI perfusion before and during early stage of RT [corrected]. Int J Radiat Oncol Biol Phys. 2006; 64:876–85.

216. Chaskis C, Stadnik T, Michotte A, Van Rompaey K, D'Haens J. Prognostic value of perfusion-weighted imaging in brain glioma: A prospective study. Acta Neurochir (Wien). 2006; 148:277–85.

217. Emblem KE, Bjornerud A, Mouridsen K, et al. T(1)- and T(2)(*)dominant extravasation correction in DSC-MRI: Part II-predicting patient outcome after a single dose of Cediranib in recurrent glioblastoma patients. J Cereb Blood Flow Metab. 2011; 31:2054–64.

218. Essock-Burns E, Lupo JM, Cha S, et al. Assessment of perfusion MRI-derived parameters in evaluating and predicting response to antiangiogenic therapy in patients with newly diagnosed glioblastoma. Neuro Oncol. 2011; 13:119–31.

219. Galbán CJ, Chenevert TL, Meyer CR, et al. Prospective analysis of parametric response map-derived MRI biomarkers: Identification of early and distinct glioma response patterns not predicted by standard radiographic assessment. Clin Cancer Res. 2011; 17:4751–60.

220. Galbán CJ, Chenevert TL, Meyer CR, et al. The parametric response map is an imaging biomarker for early cancer treatment outcome. Nat Med. 2009; 15:572–6.

221. Hirai T, Murakami R, Nakamura H, et al. Prognostic value of perfusion MR imaging of high-grade astrocytomas: long-term follow-up study. AJNR Am J Neuroradiol. 2008; 29:1505–10.

222. Jenkinson MD, Smith TS, Joyce KA, et al. Cerebral blood volume, genotype and chemosensitivity in oligodendroglial tumours. Neuroradiology. 2006; 48:703–13.

223. Jiang Z, Le Bas JF, Grand S, et al. Prognostic value of perfusion MR imaging in patients with oligodendroglioma: A survival study. J Neuroradiol. 2011; 38:53-61.

224. Law M, Young RJ, Babb JS, et al. Gliomas: Predicting time to progression or survival with cerebral blood volume measurements at dynamic susceptibility-weighted contrast-enhanced perfusion MR imaging. Radiology. 2008; 247:490-8.

225. Leimgruber A, Ostermann S, Yeon EJ, et al. Perfusion and diffusion MRI of glioblastoma progression in a four-year prospective temozolomide clinical trial. Int J Radiat Oncol Biol Phys. 2006; 64:869–75.

226. Li Y, Lupo JM, Polley MY, et al. Serial analysis of imaging parameters in patients with newly diagnosed glioblastoma multiforme. Neuro Oncol. 2011; 13:546–57.

227. Mangla R, Singh G, Ziegelitz D, et al. Changes in relative cerebral blood volume 1 month after radiation-temozolomide therapy can help predict overall survival in patients with glioblastoma. Radiology. 2010; 256:575–84.

228. Saraswathy S, Crawford FW, Lamborn KR, et al. Evaluation of MR markers that predict survival in patients with newly diagnosed GBM prior to adjuvant therapy. J Neurooncol. 2009; 91:69–81.

229. Sawlani RN, Raizer J, Horowitz SW, et al. Glioblastoma: A method for predicting response to antiangiogenic chemotherapy by using MR perfusion Imaging—Pilot study. Radiology. 2010; 255:622–8.

230. Sorensen AG, Emblem KE, Polaskova P, et al. Increased survival of glioblastoma patients who respond to antiangiogenic therapy with elevated blood perfusion. Cancer Res. 2012; 72:402–7.

231. Vöglein J, Tüttenberg J, Weimer M, et al. Treatment monitoring in gliomas: Comparison of dynamic susceptibility-weighted contrast-enhanced and

spectroscopic MRI techniques for identifying treatment failure. Invest Radiol. 2011; 46:390-400.

232. Shankar JJ, Woulfe J, Silva VD, Nguyen TB. Evaluation of perfusion CT in grading and prognostication of high-grade gliomas at diagnosis: A pilot study. AJR Am J Roentgenol. 2013; 200:W504–9.

233. Jain R, Narang J, Griffith B, et al. Prognostic vascular imaging biomarkers in high-grade gliomas: Tumor permeability as an adjunct to blood volume estimates. Acad Radiol. 2013; 20:478–85.

234. Cabrera AR, Cuneo KC, Desjardins A, et al. Concurrent stereotactic radiosurgery and bevacizumab in recurrent malignant gliomas: A prospective trial. Int J Radiat Oncol Biol Phys; 2013; 86:873–9.

235. Spampinato MV, Schiarelli C, Cianfoni A, et al. Correlation between cerebral blood volume measurements by perfusion-weighted magnetic resonance imaging and two-year progression-free survival in gliomas. Neuroradiol J. 2013; 26:385–95.

236. Jain R, Poisson L, Narang J, et al. Genomic mapping and survival prediction in glioblastoma: Molecular subclassification strengthened by hemodynamic imaging biomarkers. Radiology. 2013; 267:212–20.

237. Gahramanov S, Muldoon LL, Varallyay CG, et al. Pseudoprogression of glioblastoma after chemo- and radiation therapy: Diagnosis by using dynamic susceptibility-weighted contrast-enhanced perfusion MR imaging with Ferumoxytol versus Gadoteridol and correlation with survival. Radiology. 2013; 266:842–52.

238. Batchelor TT, Sorensen AG, di Tomaso E, et al. AZD2171, a pan-VEGF receptor tyrosine kinase inhibitor, normalizes tumor vasculature and alleviates edema in glioblastoma patients. Cancer Cell. 2007; 11:83–95.

239. Verhoeff JJC. Angiogenesis inhibition in high grade glioma [PhD thesis]. Amsterdam: University of Amsterdam; 2009 [cited on June 24, 2014]. Available from: http://dare.uva.nl/record/323536

240. Zhang W, Kreisl T, Solomon J, et al. Acute effects of bevacizumab on glioblastoma vascularity assessed with DCE-MRI and relation to patient survival. Proc Intl Soc Mag Reson Med. 2009; 17(30):5125.

241. Vidiri A, Pace A, Fabi A, et al. Early perfusion changes in patients with recurrent high-grade brain tumor treated with Bevacizumab: Preliminary results by a quantitative evaluation. J Exp Clin Cancer Res. 2012; 31:33

242. Port RE, Bernstein LJ, Barboriak DP, Xu L, Roberts TP, van Bruggen N. Noncompartmental kinetic analysis of DCE-MRI data from malignant tumors: Application to glioblastoma treated with bevacizumab. Magn Reson Med. 2010; 64:408–17.

243. Ferl GZ, Xu L, Friesenhahn M, Bernstein LJ, Barboriak DP, Port RE. An automated method for nonparametric kinetic analysis of clinical DCE-MRI data: Application to glioblastoma treated with bevacizumab. Magn Reson Med. 2010; 63:1366–75.

244. Sorensen AG, Batchelor TT, Zhang WT, et al. A "vascular normalization index" as potential mechanistic biomarker to predict survival after a single dose of Cediranib in recurrent glioblastoma patients. Cancer Res. 2009; 69:5296–300.

245. Verhoeff JJC, Lavini C, van Linde ME, et al. Bevacizumab and dose-intense temozolomide in recurrent high-grade glioma. Ann Oncol. 2010; 21:1723–7.

246. Kreisl TN, Zhang W, Odia Y, et al. A phase II trial of single-agent bevacizumab in patients with recurrent anaplastic glioma. Neuro Oncol. 2011;13(10):1143–50.

247. Lavini C, Verhoeff JJ, Majoie CB, Stalpers LJ, Richel DJ, Maas M. Model-based, semiquantitative and time intensity curve shape analysis of dynamic contrast-enhanced MRI: A comparison in patients undergoing antiangiogenic treatment for recurrent glioma. J Magn Reson Imaging. 2011; 34:1303–12.

248. Takano S, Kimu H, Tsuda K, et al. Decrease in the apparent diffusion coefficient in peritumoral edema for the assessment of recurrent glioblastoma treated by Bevacizumab. Acta Neurochir Suppl. 2013;118:185–9.

249. Batchelor TT, Gerstner ER, Emblem KE, et al. Improved tumor oxygenation and survival in glioblastoma patients who show increased blood perfusion after Cediranib and chemoradiation. Proc Natl Acad Sci U S A. 2013; 110:19059–64.

250. LaViolette PS, Cohen AD, Prah MA, et al. Vascular change measured with independent component analysis of dynamic susceptibility contrast MRI predicts bevacizumab response in high-grade glioma. Neuro Oncol. 2013; 15:442–50.

251. Wintermark M, Smith WS, Ko NU, Quist M, Schnyder P, Dillon WP. Dynamic perfusion CT: Optimizing the temporal resolution and contrast volume for calculation of perfusion CT parameters in stroke patients. AJNR Am J Neuroradiol. 2004; 25:720–9.

252. Miles KA, Lee TY, Goh V, et al. Current status and guidelines for the assessment of tumour vascular support with dynamic contrast-enhanced computed tomography. Eur Radiol. 2012; 22:1430–41.

253. Kudo K, Christensen S, Sasaki M, et al. Accuracy and reliability assessment of CT and MR perfusion analysis software using a digital phantom. Radiology. 2013; 267:201–11.

254. Huszthy PC, Daphu I, Niclou SP, et al. In vivo models of primary brain tumors: Pitfalls and perspectives. Neuro Oncol. 2012; 14:979–93.

255. Barth RF, Kaur B. Rat brain tumor models in experimental neuro-oncology: The C6, 9L, T9, RG2, F98, BT4C, RT-2 and CNS-1 gliomas. J Neurooncol. 2009; 94:299–312.

256. Zhao Y, Xiao A, diPierro CG, et al. An extensive invasive intracranial human glioblastoma xenograft model: Role of high level matrix metalloproteinase 9. Am J Pathol. 2010; 176:3032–49.

257. Mahesparan R, Read TA, Lund-Johansen M, Skaftnesmo KO, Bjerkvig R, Engebraaten O. Expression of extracellular matrix components in a highly infiltrative in vivo glioma model. Acta Neuropathol. 2003; 105:49–57.

258. Benda P, Lightbody J, Sato G, Levine L, Sweet W. Differentiated rat glial cell strain in tissue culture. Science. 1968; 161:370–1.

259. Pfeiffer SE, Herschman HR, Lightbody J, Sato G. Synthesis by a clonal line of rat glial cells of a protein unique to the nervous system. J Cell Physiol. 1970; 75(3):329-39.

260. Kondziolka D, Lunsford LD, Claassen D, Pandalai S, Maitz AH, Flickinger JC. Radiobiology of radiosurgery: Part II. The rat C6 glioma model. Neurosurgery . 1992; 31:280–7.

261. Kondziolka D, Somaza S, Comey C, et al. Radiosurgery and fractionated radiation therapy: Comparison of different techniques in an in vivo rat glioma model. J Neurosurg. 1996; 84:1033–8.

262. Wang TC, Hsiao IT, Cheng YK, Wey SP, Yen TC, Lin KJ. Noninvasive monitoring of tumor growth in a rat glioma model: Comparison between neurological assessment and animal imaging. J Neurooncol. 2011; 104:669–78.

263. Devineni D, Klein-Szanto A, Gallo JM, Devineni D. Uptake of temozolomide in a rat glioma model in the presence and absence of the angiogenesis inhibitor TNP-470. Cancer Res. 1996; 56:1983–7.

264. Branle F, Lefranc F, Camby I, et al. Evaluation of the efficiency of chemotherapy in in vivo orthotopic models of human glioma cells with and without 1p19q deletions and in C6 rat orthotopic allografts serving for the evaluation of surgery combined with chemotherapy. Cancer. 2002; 95:641–55.

265. Peroulis I, Jonas N, Saleh M. Antiangiogenic activity of endostatin inhibits C6 glioma growth. Int J cancer. 2002; 97:839–45.

266. Grobben B, De Deyn PP, Slegers H. Rat C6 glioma as experimental model system for the study of glioblastoma growth and invasion. Cell Tissue Res. 2002; 310:257–70.

267. Parsa AT, Chakrabarti I, Hurley PT, et al. Limitations of the C6/Wistar rat intracerebral glioma model: Implications for evaluating immunotherapy. Neurosurgery. 2000; 47:993–9.

Chapter 2

2 The Effect of Scan Duration on the Measurement of Perfusion Parameters in CT Perfusion Studies of Brain Tumours

This chapter is adapted from the research article, "The effect of scan duration on the measurement of perfusion parameters in CT perfusion studies of brain tumours" published in *Academic Radiology*, 2013;20(1):59-65 by Yeung TPC, Yartsev S, Bauman G, He W, Fainardi E, Lee TY.

2.1 Introduction

Malignant gliomas are highly aggressive brain tumours that are characterized by increased vascularity with immature and highly permeable blood vessels (1). Given that blood-brain barrier disruption and neovascularity play an essential role in the progression of malignant gliomas, recent studies have investigated the use of perfusion imaging for evaluating brain tumours. Blood flow (BF), blood volume (BV), and permeability–surface area product (PS) obtained from computed tomography (CT) perfusion studies have been demonstrated to be useful in differentiating glioma grade (2–4) and distinguishing treatment-induced necrosis from recurrent or progressive tumours (5). CT perfusion parameters have also demonstrated correlations with microvascular cellular proliferation (6) and proangiogenic gene expressions (7).

Although CT perfusion may be helpful in providing important physiologic information for evaluating brain tumours, there is no consensus regarding the optimal scan protocol. A scan duration of ≥2 minutes has been suggested for accurate calculation of tumour permeability (8,9), but scan durations in the range of 45 to 199 seconds have been used to evaluate tumour perfusion parameters for brain and other tumour sites (7,10). For example, a 65-second scan was recommended when the Johnson-Wilson model was used for the calculation of permeability (ie, PS) in colorectal cancer (11),

while a scan duration of $\geq$40 seconds was recommended when the Patlak method was used to calculate permeability (ie, K_{trans}, transfer constant) in lung cancer (12).

Given that scan duration is a key factor influencing perfusion measurements, it would be beneficial to investigate the effect of scan duration on CT perfusion studies of brain tumours. Standardizing a CT perfusion protocol for diagnostic and research settings could facilitate comparison among different studies. We evaluated the effect of scan duration ($\leq$150 seconds) on perfusion parameter measurements in human gliomas and evaluated the systematic and random errors associated with different reduced scan durations (<150 seconds) relative to the values obtained from the 150-second scans.

2.2   Materials and Methods

2.2.1   CT Perfusion Imaging

The local research ethics boards approved this study, and all patients provided written informed consent prior to imaging. Patients (n = 14) with histopathologically confirmed malignant glioma (World Health Organization grade III and IV) underwent CT perfusion imaging. Eight patients were scanned on a hybrid positron emission tomography/CT scanner (Discovery VCT; GE Healthcare, Waukesha, WI) with a nonionic contrast bolus (Omnipaque, 300 mg iodine/mL, 60–70 mL; GE Healthcare, Princeton, NJ), and six patients were scanned on a CT scanner (GE LightSpeed VCT; GE Healthcare, Waukesha, WI) with a nonionic contrast bolus (Iomeron, 350 mg iodine/mL, 40 mL; Bracco Imaging Scandinavia, Göteborg, Sweden). A two-phase CT perfusion scan, guided by a prior noncontrast CT scan that identified eight 5-mm sections to maximally cover the tumour, was performed for each patient. The bolus of contrast was injected into the antecubital vein at a rate of 2 to 4 mL/s at 3 to 5 seconds after the first phase started. The preselected brain sections were scanned for 45 seconds at 1-second intervals during the first phase and for a period of 105 seconds at 15-second interval during the second phase. A tube current of 190 mA was used for the hybrid positron

emission tomography/CT scanner, and 100 mA was used for the CT scanner. All patients were scanned at 80 kVp with a 25-cm field of view.

2.2.2   Image Analysis

The 150-second human CT perfusion studies were truncated to scan times of 120, 90, and 60 seconds to simulate the effect of shorter scans. Fifty-six CT perfusion studies were analyzed using the prototype version of CT Perfusion 4D (GE Healthcare, Waukesha, WI), which is based on the Johnson-Wilson model and is insensitive to the delay between arterial and tissue time-attenuation curve (TAC) to generate maps of BF, BV, and PS.

For each patient, the arterial and venous regions of interest (ROIs) were automatically chosen by the software from the 150-second study, and the same ROIs were used for the truncated studies to minimize estimated parameter variability due to differences in arterial and venous TACs. The arterial and venous ROIs were usually found in one of the anterior cerebral arteries and the posterior superior sagittal sinus, respectively. Partial volume averaging of the arterial TAC was corrected using the venous TAC as a reference (8). Tissue TACs were measured from 2×2 pixel blocks of CT images. Parametric maps of BF, BV, and PS were calculated by deconvolving the arterial TAC with each tissue TAC using the Johnson-Wilson model (8). The generation of parametric maps was repeated for different scan durations by using the same arterial and venous ROIs for each patient. ROIs of 15 mm^2 were randomly placed in the normal white and gray matter and contrast-enhanced tumour rim and nonenhancing tumour core to measure BF, BV, and PS (20 ROIs per tissue).

2.2.3   Measurement Errors of Perfusion Parameters Due to Truncation

We used the systematic and random errors to evaluate the mean and standard deviation of measurement errors associated with a reduced scan time relative to the 150-

second scan time, respectively. The differences between parameter values obtained from the original study and the truncated study in the same ROI of the same tissue type were accepted as the measurement error. The mean and standard deviation of measurement errors were, respectively, the systematic and random errors for each tissue type for each patient.

We also used the percentage error to examine whether the differences in parameter values associated with a reduced scan time were clinically meaningful. The percentage error for each parameter in each ROI was calculated using the equation

$$\text{Percent Error}(\%) = \frac{|\text{value from a shorter scan - value from the original scan}|}{(\text{value from a shorter scan + value from the original scan})/2} \times 100$$

(2.1)

2.2.4   Statistical Analysis

Values of BF, BV, and PS were first transformed using the Box-Cox transformation to obtain a normal distribution (13). The normality of the Box-Cox–transformed data for each parameter and each tissue type was checked using the Shapiro-Wilk test ($P > .05$). Student's t test confirmed that there was no difference between the hybrid positron emission tomography/CT and CT scanners when measuring BF, BV, and PS in the different tissue types at 150 seconds ($P > .05$). Differences in each parameter obtained from different scan durations were tested using repeated-measures analysis of variance with post hoc paired t test and Bonferroni correction applied. Systematic and random errors were correlated with scan durations using Spearman's rank correlation. All statistical tests were done using SPSS version 19.0 (SPSS, Inc, Chicago, IL), and P values $< .05$ were considered significant.

2.3 Results

Box plots of BF, BV, and PS values of different tissue types measured from different scan durations are shown in Figure 2-1. BF and BV values were not affected by

shorter scan durations ($P > .05$). PS values in the tumour rim at 60 seconds were significantly higher than in the 150-second scans ($P < .01$). Median percentage errors and interquartile ranges associated with different scan durations are presented in Table 2-1. Median percentage error was highest at 60 seconds for tumour core PS (median, 32.1%; interquartile range, 16.5%–43.0%). Systematic and random errors associated with different scan durations are displayed in Figure 2-2 and Figure 2-3, respectively. Tumour rim BV and PS and tumour core BF systematic errors were correlated with scan durations ($r = 0.42$, -0.50, and -0.50, respectively; $P < .01$). Random errors were negatively correlated with scan durations for all tissue types ($P \leq .01$) except for white matter BV (Table 2-2). Figure 2-4 demonstrates the visual differences in the maps of BF, BV, and PS due to scan-time truncation in a sample patient.
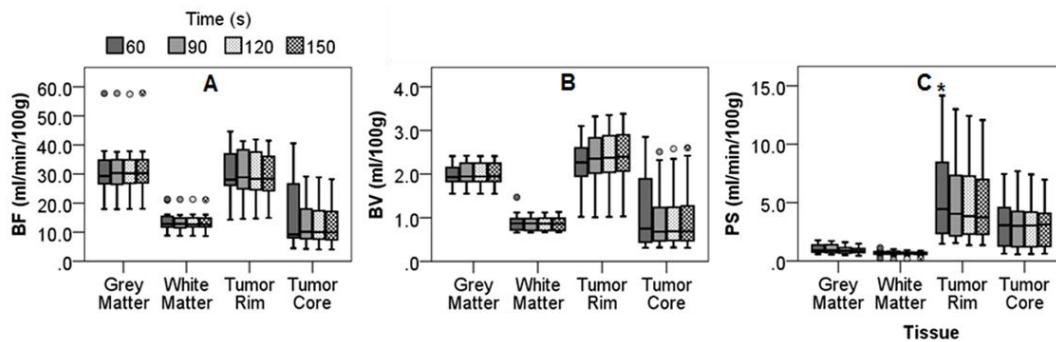
Figure 2-1: Box plots of (a) blood flow (BF), (b) blood volume (BV), and (c) permeability–surface area product (PS) values measured from different scan durations. Outliers (circles) are defined as data that are 1.5 box lengths away from the 25th or 75th quartile. *Significantly different from the 150-second scan ($P < .01$).

Table 2-1: Median (interquartile range) percentage errors associated with scan durations of < 150 seconds.

Parameter	Scan Duration (seconds)	Gray Matter	White Matter	Tumor Rim	Tumor Core
Blood flow	60	2.7 (1.9–4.5)	4.3 (3.3–5.9)	7.9 (6.0–10.3)	10.6 (8.7–16.8)
	90	2.4 (1.5–3.3)	2.9 (2.6–4.4)	4.7 (3.1–6.3)	6.1 (5.2–7.1)
	120	1.6 (1.2–2.2)	2.3 (2.0–2.9)	3.2 (2.5–3.8)	4.0 (2.6–6.6)
Blood volume	60	1.0 (0.7–2.0)	2.1 (1.5–3.1)	5.8 (4.8–7.5)	13.9 (8.1–21.4)
	90	0.9 (0.6–1.1)	1.6 (1.1–3.0)	3.3 (2.4–4.3)	7.6 (4.7–9.6)
	120	0.5 (0.4–0.9)	0.9 (0.7–1.6)	2.0 (1.4–2.4)	4.2 (2.4–6.9)
Permeability–surface area product	60	29.2 (21.3–32.8)	28.7 (24.2–34.3)	21.9 (17.1–28.6)	32.1 (16.5–43.0)
	90	22.0 (15.4–30.5)	21.7 (12.5–27.6)	11.3 (7.9–16.0)	19.3 (11.3–24.3)
	120	15.5 (13.3–17.6)	16.6 (11.0–20.3)	6.4 (4.0–8.1)	9.6 (4.9–12.7)
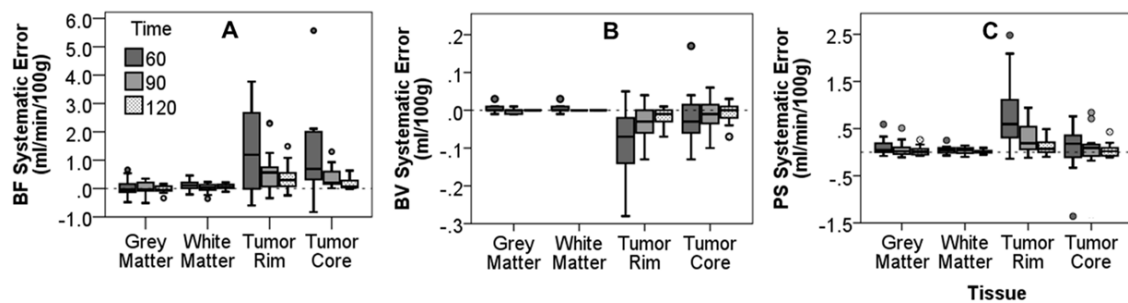
Figure 2-2: Box plots of (a) blood flow (BF), (b) blood volume (BV), and (c) permeability–surface area product (PS) systematic errors associated with different scan durations. Outliers (*circles*) are defined as data that are 1.5 box lengths away from the 25th or 75th quartile. Extreme outliers that are three box lengths away from the quartiles are not displayed.
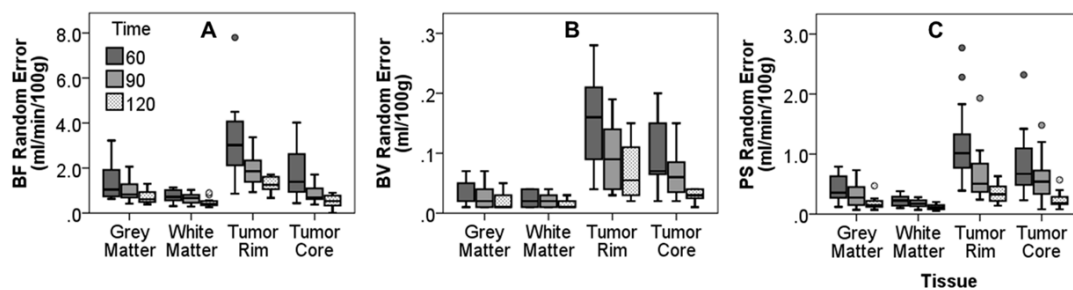
Figure 2-3: Box plots of (a) blood flow (BF), (b) blood volume (BV), and (c) permeability–surface area product (PS) random errors associated with different scan durations. Outliers (*circles*) are defined as data that are 1.5 box lengths away from the 25th or 75th quartile. Extreme outliers that are three box lengths away from the quartiles are not displayed.

Table 2-2: Spearman's rank correlation of systematic and random errors with scan duration.

Error Type	Tissue Type	Blood Flow	Blood Volume	Permeability–Surface Area Product
Systematic error	Gray matter	−0.01	−0.09	−0.19
	White matter	−0.12	−0.06	−0.19
	Tumor rim	−0.30	0.42[†]	−0.50[†]
	Tumor core	−0.50[†]	0.15	−0.13
Random error	Gray matter	−0.43[†]	−0.34*	−0.54[†]
	White matter	−0.47[†]	−0.25	−0.56[†]
	Tumor rim	−0.50[†]	−0.53[†]	−0.62[†]
	Tumor core	−0.60[†]	−0.46[†]	−0.64[†]

*.01 < P < .05.

[†]P < .01.
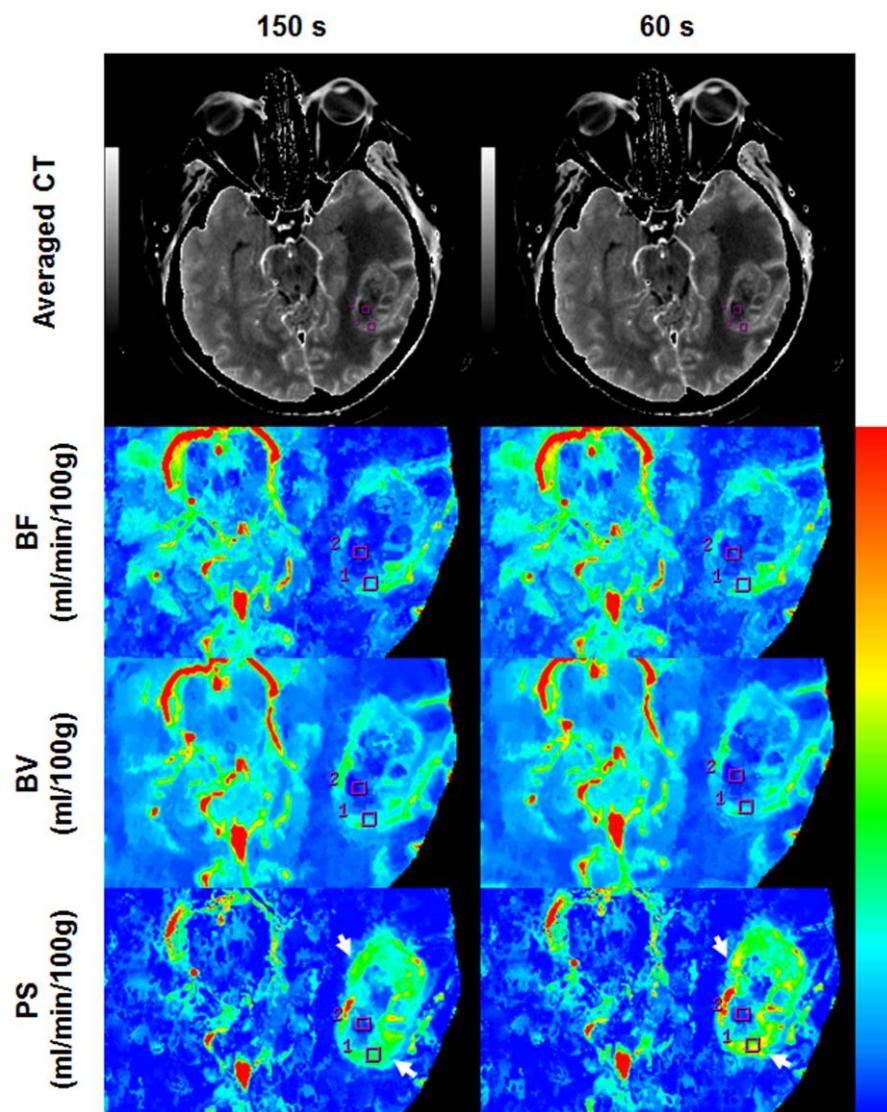
Figure 2-4: Differences between perfusion maps obtained from a 150-second scan versus a 60-second scan. The 15-mm^2 regions of interest in the contrast-enhancing rim (1) and nonenhancing core (2) are displayed. Maps of blood flow (BF), blood volume (BV), and permeability–surface area (PS) are enlarged and centered at the tumour. White arrows point to regions with PS values that appeared to be higher at 60 seconds relative to 150 seconds. The window and level used for computed tomography, BF, BV, and PS were 20 to 100 Hounsfield units, 0 to 180 mL/min/100 g, 0 to 12 mL/100 g, and 0 to 25 mL/min/100 g, respectively.

2.4 Discussion

There is no consensus regarding the optimal CT perfusion scan duration, and durations of 45 to 199 seconds have been reported in the literature for calculating tumour perfusion parameters (7,10). This study sought to investigate the effect of scan duration on the measurements of BF, BV, and PS.

Perfusion parameters were calculated using the Johnson-Wilson model (8,14). It models the diffusion of a bolus of contrast across the capillary endothelium into the interstitial space as it traverses from the arterial to the venous end of a tissue region. A theoretical function, called the impulse residue function, represents the fraction of contrast that remains in the tissue as a function of time after a bolus injection of a unit amount of contrast into the arterial inlet. The impulse residue function has two distinct phases. The first phase is a rectangular function at a height of unity that represents the retention of the contrast in the tissue region, regardless of its distribution either in the vascular or extravascular space, before any venous outflow occurs. The duration (or width) of the first phase is the minimum transit time of this bolus. The second phase starts at a height of the extraction fraction at the minimum transit time and decays exponentially toward baseline with time. This describes the clearance of the extravasated

contrast from the interstitial space via back flux into the bloodstream. The BF-scaled impulse residue function is derived by deconvolving the arterial TAC with the tissue TAC (8). The peak value and area under the first phase of the BF-scaled impulse residue function are the BF and BV, respectively. PS is obtained using the equation PS = −BF × ln(1 − extraction fraction).

We did not find a statistical difference in BF and BV when comparing the 150-second to the 120-second, 90-second, and 60-second studies. Hirata et al (15) found that the first circulation time is approximately 40 seconds in brain tissue, and scanning up to the first circulation time is sufficient for measurements of BF and BV. Our results are consistent with their results and are expected given that a scan time of 60 seconds is well beyond the first circulation time of contrast through the brain and would permit an accurate determination of the first phase of the impulse residue function.

A scan time of 60 seconds is not adequate for the estimation of PS in brain tumour rim. The significantly higher permeability that we observed with a shorter scan is consistent with other studies (11,12). Goh et al (11) found that 45 seconds was too short for PS measurements in colorectal cancer. The longer scan time required could be explained by the fact that the accumulation of contrast in a brain tumour is much slower than that of colorectal cancer because PS is lower in a brain tumour. A longer scan duration is required to have sufficient signal-to-noise ratio to estimate PS values accurately and reproducibly. PS values in the normal brain, which should be close to zero, were unaffected by scan duration because the estimation algorithm was constrained only to give nonzero PS values.

The effect of scan duration on the systematic and random errors of CT perfusion parameters was also investigated. With the exception of white matter BV, the random error of perfusion parameter measurements increased with shorter scan duration. Systematic error in tumour rim BV and PS and tumour core BF also increased with shorter scan durations because fewer data were available for estimating BF, BV, and PS. The optimization algorithm for estimating these parameters was a constrained optimization algorithm, in which all parameters were constrained to give only values that

are zero or higher. The random error increased with a shorter scan time because the signal-to-noise ratio deteriorated with a shorter scan time. This is analogous to the decrease in the standard error when more samples are used to estimate the mean. With the use of a constrained optimization algorithm, the random error would not go up as much as a nonconstrained optimization process, because all parameter values had to be zero or higher. This constraint led to the increase in systematic bias that we observed when the signal-to-noise ratio deteriorated with reduced scan time.

Other technical settings of a CT perfusion protocol can also affect perfusion parameter values. For instance, the frequency of image acquisition, particularly in the first circulation phase, could result in significantly different values of BF and BV (16-18). The molecular weight of contrast agent can influence the estimation of tissue permeability as well. Most iodinated CT contrast agents are low–molecular weight agents (about 0.75 kDa) and leak more easily from the blood into the interstitial space compared to higher molecular weight contrast agents (19,20). Because endothelial permeability is dependent on the molecular weight of a contrast agent, PS values measured with a lower molecular weight agent will be higher than the values measured with a higher molecular weight agent. As such, perfusion protocols to measure PS need standardization with respect to contrast agent used as well as scan time.

Radiation dose is of concern when performing a CT perfusion scan. At 80 kVp and 190 mA, the estimated effective doses for scan durations of 150, 120, 90, and 60 seconds are 5.4, 5.2, 5.0, and 4.8 mSv, respectively. Similarly, the imaging doses at 80 kVp and 100 mA are 2.9, 2.7, 2.6, and 2.5 mSv, respectively. Because the second phase of a CT perfusion scan involves x-ray exposures that are taken every 15 seconds, the reduction in radiation dose by truncating the scan time is minimal. Reducing the scan time is not an effective way to reduce radiation dose. Adaptive statistical iterative reconstruction and reducing the imaging frequency during the first phase are more effective at reducing the radiation dose (17,21).

Some limitations of this study must be considered. The number of patients was relatively small, and there was little variation in terms of brain tumour types, because all

patients were diagnosed with malignant glioma, which accounts for approximately 70% of all adult primary brain tumours (22). In addition, patients were not scanned with the same CT scanner or the same contrast agent. As the molecular weights for the two contrast agents used in this study were both approximately 0.8 kDa, the small difference in molecular weights should have minimal effect on the measurement of CT perfusion parameters. Although there was no statistical difference in terms of perfusion parameter values measured from the two scanners using two different tube currents, a simulation study showed that x-ray tube current could potentially affect the accuracy of perfusion parameters in the brain (23). A subgroup analysis using the patients acquired with 100-mA tube current showed that BF and BV at 60 seconds were significantly different from the values obtained at 150 seconds (data not shown). A lower signal-to-noise ratio due to a lower tube current could have affected the measurement of BF and BV when the scan time was reduced. Our recommendation of 90 seconds is a conservative estimate of the shortest scan time required to be consistent with the above results. In both cases (100 and 190 mA), the 120-second and 90-second data were not significantly different from the 150-second data. Additional study scanning patients with various types of brain tumours using the same scanner and contrast agent is needed to confirm the current results.

2.5 Conclusions

Relative to a 150-second scan duration, BF and BV values in the normal brain and brain tumours were not affected by reducing scan duration to 60 seconds, whereas PS values in the tumour rim were significantly higher at 60 seconds. The random errors associated with BF, BV, and PS could suffer with shorter scan durations. A scan duration of ≥90 seconds is recommended, and investigation of the effects of other scanning parameters on the measurement of perfusion parameters is warranted.

2.6 References

1. Jain R. CT imaging of brain tumors: an overview. AJNR Am J Neuroradiol 2011; 32:1570–77.

2. Ding B, Ling HW, Chen KM, et al. Comparison of cerebral blood volume and permeability in preoperative grading of intracranial glioma using CT perfusion imaging. Neuroradiology 2006; 48:773–81.

3. Ellika SK, Jain R, Patel SC, et al. Role of perfusion CT in glioma grading and comparison with conventional MR imaging features. AJNR Am J Neuroradiol 2007; 28:1981–7.

4. Jain R, Ellika SK, Scarpace L, et al. Quantitative estimation of permeability-surface area product in astroglial brain tumors using perfusion CT and correlation with histopathologic grade. AJNR Am J Neuroradiol 2008; 29:694–700.

5. Jain R, Narang J, Schultz L, et al. Permeability estimates in histopathology-proved treatment induced necrosis using perfusion CT: can these add to other perfusion parameters in differentiating from recurrent/progressive tumors? AJNR Am J Neuroradiol 2011; 32:658–63.

6. Jain R, Gutierrez J, Narang J, et al. In vivo correlation of tumor blood volume and permeability with histologic and molecular angiogenic markers in gliomas. AJNR Am J Neuroradiol 2011; 32:388–94.

7. Jain R, Poisson L, Narang J, et al. Correlation of perfusion parameters with genes related to angiogenesis regulation in glioblastoma: a feasibility study. AJNR Am J Neuroradiol 2012; 33:1343–8.

8. Lee TY, Purdie TG, Stewart E. CT imaging of angiogenesis. Q J Nucl Med 2003; 47:171–87.

9. Miles KA. Perfusion CT for the assessment of tumor vascularity: which protocol? Br J Radiol 2003; 76:S36–42.

10. Sahani DV, Kalva SP, Hamber LM, et al. Assessing tumor perfusion and treatment response in rectal cancer with multisection CT: initial observations. Radiology 2005; 234:785–92.

11. Goh V, Halligan S, Hugill JA, et al. Quantitative colorectal cancer perfusion measurement using dynamic contrast-enhanced multidetector-row computed tomography: effect of acquisition time and implications for protocols. J Comput Assist Tomogr 2005; 29:59–63.

12. Spira D, Gerlach JD, Spira SM, et al. Effect of scan time on perfusion and flow extraction product (K-trans) measurements in lung cancer using low-dose volume perfusion CT (VPCT). Acad Radiol 2012; 19: 78–83.

13. Peltier MR, Wilcox CJ, Sharp DC. Technical note: application of the Box- Cox data transformation to animal science experiments. J Anim Sci 1998; 76:847–9.

14. Johnson JA, Wilson TA. A model for capillary exchange. Am J Physiol 1966; 210:1299–1303.

15. Hirata M, Sugawara Y, Murase K, et al. Evaluation of optimal scan duration and end time in cerebral CT perfusion study. Radiat Med 2005; 23: 351–63.

16. Wintermark M, Smith WS, Ko NU, et al. Dynamic perfusion CT: optimizing the temporal resolution and contrast volume for calculation of perfusion CT parameters in stroke patients. AJNR Am J Neuroradiol 2004; 25: 720–9.

17. Wiesmann M, Berg S, Bohner G, et al. Dose reduction in dynamic perfusion CT of the brain: effects of the scan frequency on measurements of cerebral blood flow, cerebral blood volume, and mean transit time. Eur Radiol 2008; 18:2967–74.

18. Goh V, Liaw J, Bartram CI, et al. Effect of temporal interval between scan acquisitions on quantitative vascular parameters in colorectal cancer: Implications for helical volumetric perfusion CT techniques. AJR Am JRoentgenol 2008; 191:W288–92.

19. de Lussanet QG, Langereis S, Beets-Tan RG, et al. Dynamic contrast enhanced MR imaging kinetic parameters and molecular weight of dendritic contrast agents in tumor angiogenesis in mice. Radiology 2005; 235:65–72.

20. Choyke PL. Contrast agents for imaging tumor angiogenesis: is bigger better? Radiology 2005; 235:1–2.

21. Prakash P, Kalra MK, Kambadakone AK, et al. Reducing abdominal CT radiation dose with adaptive statistical iterative reconstruction technique. Invest Radiol 2010; 45:202–10.

22. Central Brain Tumor Registry of the United States. CBTRUS 2008 statistical report: primary brain tumors in the United States 1998-2002. Available at: http://www.cbtrus.org/reports/2007-2008/2007report.pdf. Accessed June 29, 2012.

23. Murase K, Najo T, Ii S, et al. Effect of x-ray tube current on the accuracy of cerebral perfusion parameters obtained by CT perfusion studies. Phys Med Bio 2005; 50:5019–29.

Chapter 3

3 Improving Quantitative CT Perfusion Parameter Measurements Using Principal Component Analysis

This chapter is adapted from the research article, "Improving quantitative CT perfusion parameter measurements using principal component analysis" published in *Academic Radiology*, 2014;21(5):624-632 by Yeung TPC, Dekaban M, De Haan N, Morrison L, Hoffman L, Bureau Y, Chen X, Yartsev S, Bauman G, Lee TY.

3.1 Introduction

Computed tomography (CT) perfusion is a diagnostic tool for the evaluation of acute ischemic stroke, and it is becoming increasingly used for measuring blood flow (BF), blood volume (BV), and permeability–surface area product (PS) in malignant brain tumours (1). The measurements of BF, BV, and PS in tumours are affected by CT perfusion image contrast-to-noise ratio (CNR). Recently, Balvay et al. (2) showed that filtering CT perfusion images with principal component analysis (PCA) improved CNR in CT perfusion images of patients with ovarian and metastatic renal tumours. It is not known whether PCA can improve CNR of CT perfusion images of patients with malignant brain tumours, which have a lower CNR because of lower tumour blood flow in the brain compared to other malignancies such as metastatic renal tumours (3-6). In preclinical imaging of cancer models with a clinical CT scanner, a high spatial resolution is desirable to detect small tumours. However, CNR from scanning small animals is low because: (1) image noise increases with higher spatial resolution (ie, smaller pixel size); and (2) the effect of partial volume averaging is more prominent in small animals than in humans. Therefore, we hypothesized that CT perfusion images of a preclinical model of malignant glioma are useful to evaluate the ability of PCA in improving image quality under low-CNR condition. It has not been demonstrated that an increase in CNR after PCA filtering improves the measurements of BF, BV, and PS. Accurate and precise measurements of these parameters are important because they have been shown to be

valuable for grading gliomas (1,6) and for distinguishing recurrent tumour from treatment-induced necrosis (7).

In this study, we first designed a digital phantom to validate PCA image filtering by comparing the accuracies and precisions of BF, BV, and PS without and with PCA filtering of simulated CT perfusion images. We then evaluated the improvement in CNR and changes in BF, BV, and PS measurements after PCA filtering CT perfusion images of a malignant rat glioma model.

3.2   Materials and Methods

3.2.1   Validation of PCA by Simulation

A digital phantom of CT perfusion images with time-attenuation curves (TAC) reflecting known values of BF, BV, and PS was developed. The phantom consisted of 16 CT slices and 44 sequential images for each slice simulating a two-phase CT perfusion protocol. Images were simulated at 1.4-second intervals during the first phase of 30-seconds and then at 15-second intervals during the second phase of 300-seconds. Each image contained 3×4 tiles of 10×10 pixels, which resembled the number of pixels in an axial rat brain CT image. Pixels in each tile had the same TAC simulating known values of BF, BV, and PS. Each tile was assigned with increasing mean transit times (MTTs; 4, 4.5, 5.0, …, 9.5 s) and extraction fraction (E; 0.05, 0.06, …, 0.14, 0.3, 0.4). Each slice was assigned to two different BV values, the range of values were 0.5, 1.0, 1.5, …, 8 mL/100 g. BF values (3.2–120 mL/min/100 g) were calculated as BV/MTT, and PS values (0.4–25.8 mL/min/100 g) were obtained using −BF × ln(1−E) (8). Based on the Johnson–Wilson model, these values were used to simulate different impulse residue functions for each tile (9). A population-averaged arterial TAC was generated by averaging TACs from carotid arteries of nine Wistar rats.

Each impulse residue function was convolved with the population-averaged arterial TAC to generate a tissue TAC. A time-attenuation curve (TAC), *Q(t)*, can be described by the following equation:

$$Q(t) = BF \cdot C_a(t) \otimes H(t) = C_a(t) \otimes [BF \cdot H(t)] \qquad\qquad \text{Equation 3-1}$$

where BF is blood flow, $C_a(t)$ is the arterial TAC (also known as the arterial input function), $\otimes$ is the convolution operator, $H(t)$ is the impulse residue function. This mathematical operation is graphically illustrated in Figure 3-1.
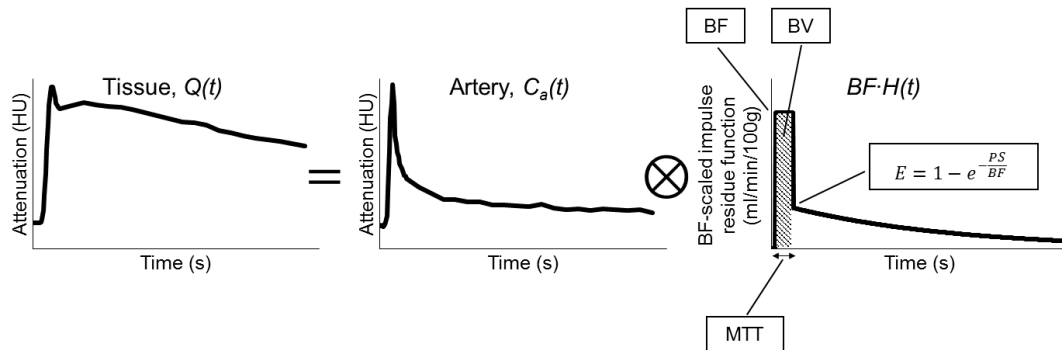
Figure 3-1: Graphical illustration showing how a tissue time-attenuation curve (TAC), *Q(t)*, is simulated from a population-averaged arterial TAC, *C_a(t)*, and a blood flow–scaled impulse residue function, *H(t)*, with known values of blood flow (BF), blood volume (BV), permeability–surface area product (PS), extraction fraction (E), and mean transit time (MTT).

The arterial TAC used in this simulation was a population-averaged arterial TAC. The impulse residue function describes the fraction of contrast that remains in the tissue as a function of time after a bolus injection into the arterial inlet. The blood flow–scaled impulse residue function, *BF·H(t)*, has two phases. The first phase is a rectangular function with a height of BF that is maintained for the duration of the mean transit time and has an area equal to blood volume (BV). It represents the retention of contrast in the tissue region before venous outflow. The second phase starts at a height of the extraction fraction and decays exponentially; it describes the back flux of extravasated contrast from the interstitial space into the intravascular space. The values of the TACs at different time points were embedded into the corresponding pixels to generate CT perfusion images of the digital phantom. In total, the set of noise-free CT perfusion images in the digital phantom gave rise to 192 different TACs with different combinations of BF, BV, and PS

values. This phantom reflected values of BF, BV, and PS in the physiological range of a rat. The design of this phantom is illustrated in Figure 3-2.
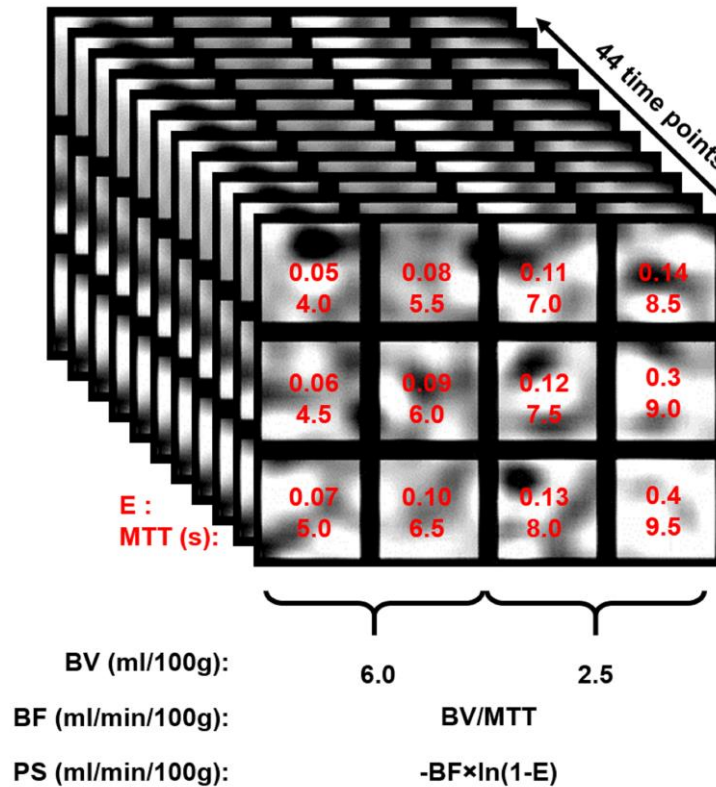
Figure 3-2: An example of one slice (out of 16 slices) of the digital computed tomography (CT) perfusion phantom with image noise. Each tile contains tissue-enhancement curves reflecting a combination of extraction fraction (E), mean transit time (MTT), blood volume (BV), blood flow (BF), and permeability–surface area product (PS).

To add image noise to the set of noise-free CT perfusion images, a rat was scanned without contrast injection in high-resolution mode with a clinical CT scanner (Discovery 750 HD; GE Healthcare, Waukesha, WI) using the same two-phase CT perfusion protocol as the simulation. The scanning parameters were 80 kVp, 120 mAs,

0.4 s/rotation, 10 cm field of view, 16 slices, and 1.25 mm slice thickness (voxel size is $0.2 \times 0.2 \times 1.25$ mm). A high-definition bone filter with a limiting in-plane resolution of 0.33 mm was used to reconstruct the images. Adaptive statistical iterative reconstruction (ASIR) was used to reconstruct the images. The skull was used to rigidly register the images using the prototype version of CT Perfusion 4D (GE Healthcare) to minimize misregistration due to motion in the axial plane. A "noiseless" CT image for each slice was generated by averaging the series of noncontrast CT images of the same slice. The set of noise only images of each slice was obtained by subtracting the average CT image from each CT image of the same slice. This set of noise images was added one by one to the set of noise-free CT perfusion images. The final set of noisy images was designated as the unfiltered CT perfusion images of the digital phantom, and they were then filtered using PCA.

3.2.2   Principal Component Analysis

Principal component analysis (PCA) is a statistical technique that linearly transforms a set of multidimensional observations into different principal components that describe the variance of the original set of observations (2). In the context of a series of m dynamic images from a computed tomographic perfusion study, attenuation in each pixel p as a function of time was measured as a time-attenuation curve (TAC). If one interprets a TAC as a set of observations of x-ray attenuation changes (due to contrast) versus time, then each TAC consists of m number of variables and can be written as an $m \times 1$ vector Q_p with p as the index for the image pixel. PCA linearly transforms the possibly correlated m variables into a set of transformed variables called principal components, which are linear combinations of the original variables and are uncorrelated with each other. These linear transformations are defined so that the first principal component has the largest variance. Each subsequent principal component would describe the next largest variance with the condition that it is uncorrelated to all the previous principal components.

It can be shown that the coefficients defining these linear transformations are the eigenvectors of the covariance matrix of the TACs whereas the corresponding eigenvalues are the variances of the principal components. In addition, each TAC can be noise filtered by expressing it as the weighted sum of the eigenvectors with the weights given by the scores of the TAC on the principal components (or loadings of the eigenvector in the TAC):

$$\tilde{Q}_p = \sum_{i=1}^{N} w_{ip} \cdot a_i \qquad\qquad \text{Equation 3-2}$$

where N is the number of principal components with the largest variances used to noise filter Q_p, a_i is the ith eigenvector and w_{ip} is the corresponding weight which can be calculated as:

$$w_{ip} = a_i^T \cdot \left(Q_p - \overline{Q} \right) \qquad\qquad \text{Equation 3-3}$$

where $\overline{Q}$ is the mean of all TACs and a_i^T is the transpose of a_i.

CT perfusion images can be noise filtered using the first few principal components. In general, more temporal TAC smoothing is achieved with lesser number of principal components used. CT perfusion images of each slice of the phantom were analyzed with an in-house PCA program developed using the C++ programming language. Two, four, six, eight, and ten principal components were used to reconstruct five different sets of noise-filtered CT perfusion images.

3.2.3   *In Vivo* Experiments

All experiments were approved by the Animal Use Subcommittee of the Canadian Council on Animal Care at our institution. C6 glioma cells (10^6 cells in 10 μL) were stereotactically implanted into the right caudate putamen of eight Wistar rats (10). At an average of 13 days (range, 11–17 days) after tumour implantation, the brain of each animal was scanned in high-resolution mode with a clinical CT scanner using the same

two-phase protocol as the simulation. A bolus of contrast (Isovue; Bracco Diagnostics Inc, Vaughan, Canada; 300 mg iodine/mL, 2.5 mL/kg body weight) was injected into the lateral tail vein at a rate of 8 mL/min, at 3–4 seconds after the start of the first phase. Two, four, and six principal components were used to reconstruct three different sets of noise-filtered CT perfusion images for each animal.

3.2.4 Assessment of Image Quality and Information Loss after PCA Filtering

For both simulation and in vivo experiments, pixel noise and CNR were used to evaluate the image quality of CT perfusion images after PCA noise filtering (2). To evaluate the enhancement of contrast, the mean baseline attenuation is subtracted from the TAC to give the corresponding time-enhancement curve. The standard deviations (SD) of the baseline (first four to five time points) and the late steady state phase (last 10 time points) were calculated and averaged for each of the original and filtered image sets to give $\overline{SD_o}$ and $\overline{SD_f}$, respectively. These values ($\overline{SD_o}$ and $\overline{SD_f}$) were used as measurements of pixel noise.

For each CT perfusion image set, the average norm of the time-enhancement curves $\overline{\|Q\|}$ is composed of the average norm of signal $\overline{\|S\|}$ and average norm of noise $\sqrt{m \cdot \overline{SD^2}}$, where m is the number of time points. The average norm of signal $\overline{\|S\|}$ was estimated using $\sqrt{\overline{\|Q\|} - m \cdot \overline{SD^2}}$. The CNR of the original and filtered image sets were defined as $\frac{\overline{\|S\|}_o}{m \cdot \overline{SD_o}^2}$ and $\frac{\overline{\|S\|}_f}{m \cdot \overline{SD_f}^2}$, respectively.

The fractional residual information (FRI) was described by Balvay *et al* (2) and was used to evaluate the amount of information loss due to filtering. The residual signal of pixel p, R_p, was the difference between the original TAC, Q_p, and the filtered TAC ($\tilde{Q}_p$). The residual signal (R_p) of pixel p has two components: informative signal (S_p) and noise (N_p). The FRI for a pixel (FRI_p) after filtering with PCA was defined as:

$$FRI_p = \frac{\|S_p\|^2}{\|R_p\|^2} = \frac{\|S_p\|^2}{\|S_p + N_p\|^2}$$

Equation 3-4

FRI_p ranges from 0 to 1, and the optimal number of principal components that should be used for filtering TACs minimizes the FRI in order to keep as much valuable information as possible in the filtered data in both the tumour and normal brain tissue. To estimate $\|S_p\|^2$ we used the autocorrelation function of the residual, R_p, between the original and filtered TAC of pixel p, which is defined as:

$$C_p(k) = \frac{1}{m - |k|} \sum_{i=1}^{m-k} R_p(i) \cdot R_p(i+k)$$

Equation 3-5

where m is the number of time points, k is the time lag and $R_p(i)$ is the ith element of the $m \times 1$ residual vector R_p. $C_p(k)$ can identify signal (S_p) hidden in the noise (N_p) of R_p in the following way. In general, the autocorrelations of N_p and S_p are approximately zero for time lag $k > k_n$ and k_s, respectively. If $k_s > k_n$, then the autocorrelation of the residual $C_p(k)$ can be used to approximate S_p for time lag $k_n < k < k_s$. In particular, extrapolation of $C_p(k)$ in the range $k_n < k < k_s$ to $k = 0$ will give the autocorrelation of S_p at k = 0, which by analogy to Equation 3-5 gives $\|S_p\|^2$ when multiplied by (m-$/k/$). We used a second order polynomial to extrapolate $C_p(k)$ in the range $k_n < k < k_s$ to $k = 0$. The k_n and k_s used were fixed to 1 and 30 time lags, respectively.

3.2.5 Calculation of BF, BV, and PS

For both simulation and in vivo experiments, maps of BF, BV, and PS of the unfiltered and filtered image sets were generated using CT Perfusion 4D. Tissue TACs were measured from 2×2 pixel blocks of CT images. Parametric maps of BF, BV, and PS were calculated by deconvolving the arterial TAC with each tissue TAC using the Johnson–Wilson model (8,9). The population-averaged TAC was used for the simulation

while a region of interest (ROI) was placed in the carotid artery to measure the arterial TAC for each animal.

3.2.6   Statistical Analysis

For digital phantom maps, a square-shaped ROI of 8×8 pixels was placed at the center of each tile to measure the mean BF, BV, and PS. Intraclass correlation coefficient was used to assess the reliability of measurements between the simulated true values and the values obtained without or with PCA filtering (11). Measurement error was the difference between the mean with the simulated true value of each tile. Map noise was the SD of each tile. The agreement in measurement errors and map noises in BF, BV, and PS without and with PCA filtering was assessed using Bland–Altman analysis (12). Repeated measures analysis of variance (ANOVA) followed by Bonferroni multiple comparisons was used to compare the differences in absolute measurement errors and map noise before and after PCA filtering (SPSS, version 20.0; SPSS, Chicago, IL) (13).

For animal experiments, the tumour and contralateral normal brain were delineated. Noise level, CNR, BF, BV, and PS in each ROI were expressed as mean ± SD. These metrics before and after filtering were compared using repeated measures ANOVA followed by Bonferroni multiple comparisons to evaluate the differences between the normal brain and tumour without or with PCA filtering. The mean percentages of pixels that had an FRI $\geq$ 5% in the normal brain and tumour were calculated. All statistical tests were done using SPSS (SPSS, version 20.0; SPSS, Chicago, IL), and a $P \leq .05$ was considered significant.

3.3   Results

For simulation, filtering with four or lesser principal components resulted in intraclass correlation coefficients that were significantly greater than the intraclass correlation coefficients without PCA filtering for BF, BV, and PS (Table 3-1). Figure 3-3 illustrates

visual improvements in maps of BF, BV, and PS after PCA filtering. The mean error and the 95% limits of agreement (mean ± 2 SD) decreased after PCA filtering and with lesser number of principal components (Figure 3-4). Similarly, the mean map noise and 95% limits of agreement decreased after PCA filtering (Figure 3-5). Reductions in absolute measurement errors and map noises for BF, BV, and PS were significant ($P < .05$). The mean FRI ± SD was ≤0.5% ± 0.7% after filtering with any number of principal components. The maximum mean FRI for ten, eight, six, four, and two principal components were 3.0%, 2.9%, 3.7%, 4.9%, and 6.5%, respectively.

Table 3-1: Intraclass correlation coefficient of different CT perfusion parameters with the true values.

	BF		BV		PS	
Number of PCs	Intraclass correlation coefficient (95% CI)	P value[*]	Intraclass correlation coefficient (95% CI)	P value[†]	Intraclass correlation coefficient (95% CI)	P value[‡]
No PCA	0.73 (0.34 − 0.86)	0.57	0.96 (0.95 − 0.97)	0.42	0.77 (0.16 − 0.91)	0.59
10 PCs	0.79 (0.64 − 0.87)	0.19	0.98 (0.96 − 0.98)	0.05	0.87 (0.73 − 0.93)	0.06
8 PCs	0.79 (0.68 − 0.86)	0.12	0.98 (0.97 − 0.99)	**0.00[#]**	0.91 (0.83 − 0.95)	**0.00[#]**
6 PCs	0.79 (0.66 − 0.86)	0.15	0.98 (0.97 − 0.99)	**0.00[#]**	0.91 (0.84 − 0.94)	**0.00[#]**
4 PCs	0.82 (0.75 − 0.87)	**0.01[#]**	0.98 (0.97 − 0.98)	**0.00[#]**	0.90 (0.87 − 0.93)	**0.00[#]**
2 PCs	0.82 (0.77 − 0.86)	**0.00[#]**	0.98 (0.97 − 0.98)	**0.00[#]**	0.92 (0.89 − 0.94)	**0.00[#]**

[*]Statistical comparison with intraclass correlation coefficient = 0.73

[†]Statistical comparison with intraclass correlation coefficient = 0.96

[‡]Statistical comparison with intraclass correlation coefficient = 0.77

[#]Statistically significant at a $P < 0.01$

Abbreviations: PCs = principal components; BF = blood flow; BV = blood volume; PS = permeability-surface area product; PCA = principal component analysis; CI = confidence interval
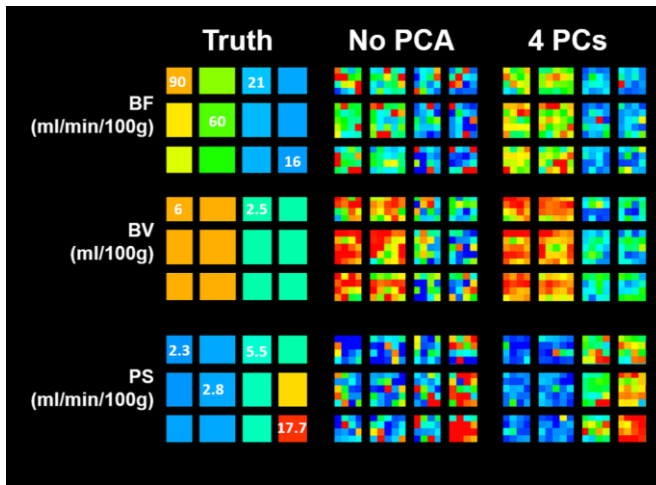
Figure 3-3: Maps of blood flow (BF), blood volume (BV), and permeability–surface area product (PS) of the digital phantom without noise (ie, truth), with noise, and after principal component analysis (PCA) filtering with four principal components. Some values of BF, BV, and PS are labeled.
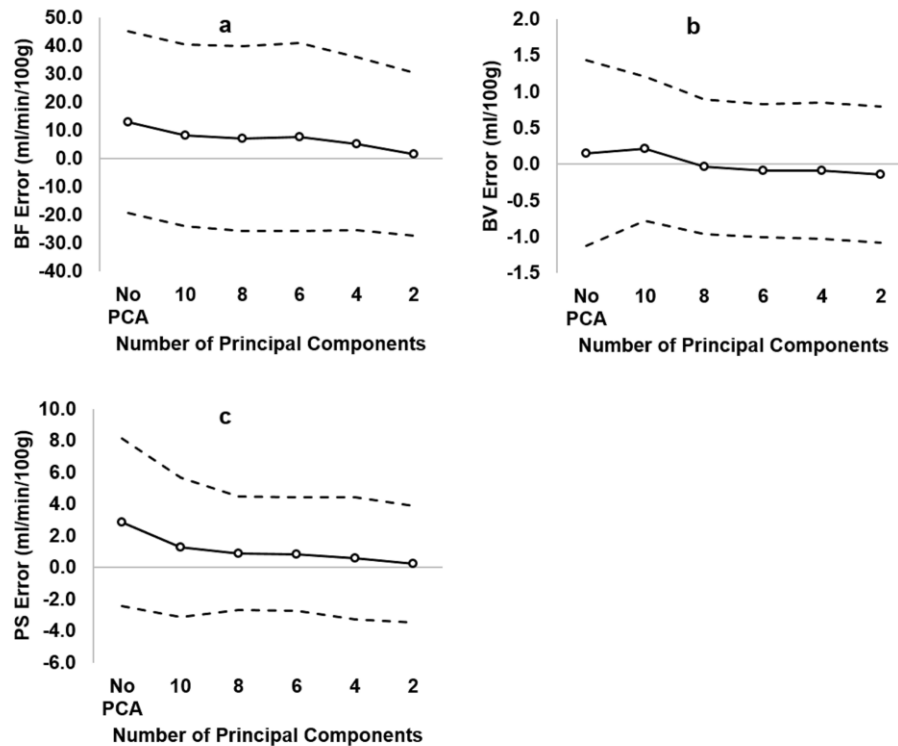
Figure 3-4: Mean error and 95% limits of agreement (ie, mean ± 2 standard deviation from Bland–Altman analysis) without and with principal component analysis (PCA) filtering for (a) blood flow (BF), (b) blood volume (BV), and (c)

permeability–surface area product (PS). Solid line is the mean and dashed lines are the upper and lower limits of agreement.
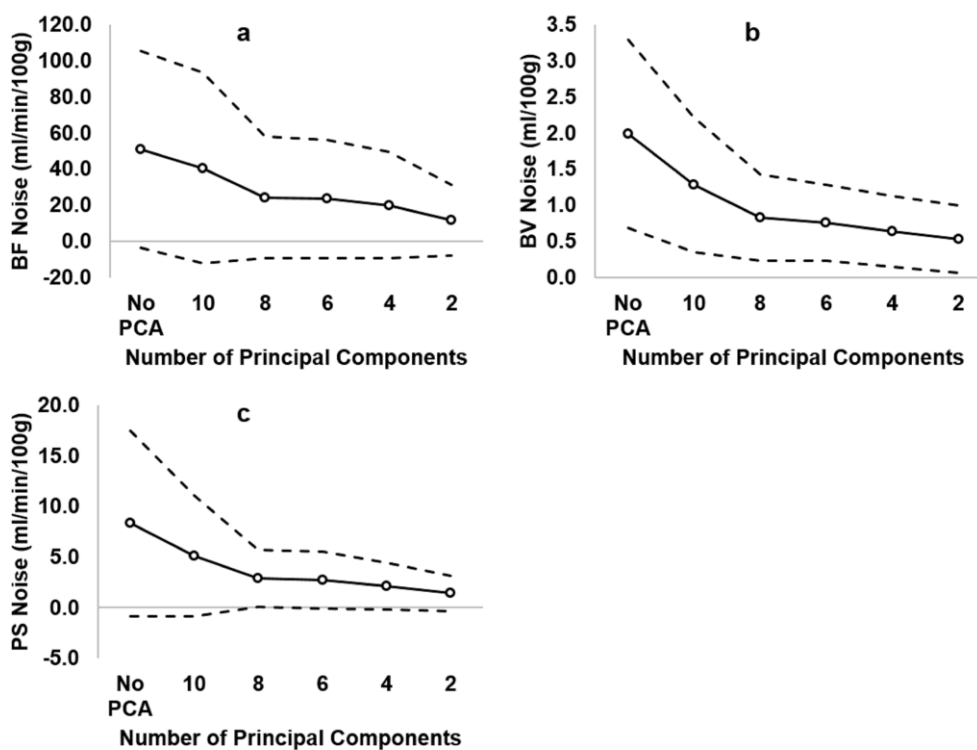
Figure 3-5: Mean map noise and 95% limits of agreement (ie, mean ± 2 standard deviation from a Bland–Altman analysis) without and with principal component analysis (PCA) filtering for (a) blood flow (BF), (b) blood volume (BV), and (c) permeability–surface area product (PS). Solid line is the mean and dashed lines are the upper and lower limits of agreement.

For experiments, Figure 3-6 shows the removal of noise from a sample time-enhancement curve in the tumour. Figure 3-7 shows examples of source CT perfusion images and maps of BF, BV, and PS without and with PCA filtering; the first four principal components used for filtering are also shown. Table 3-2 reports the significant improvements in noise reduction and CNR in animal CT perfusion images. The loss of signal was minimal after filtering the images with four or more principal components, in which no >1% of pixels had an FRI of ≤5% in both the normal brain and the tumour. An

average of 26% (range, 11%–49%) of pixels in the tumour had an FRI of $\geq 5\%$ when filtering with only two principal components (Table 3-2). PCA showed significant effect on BV and PS irrespective of ROI (ie, normal brain vs. tumour), and ROI had a significant effect on BF, BV, and PS irrespective of PCA (Table 3-3). Although PCA had no overall effect on BF, the interaction between PCA and ROI had a significant effect, suggesting that ROI had an effect on PCA filtering. Figure 3-8 shows that there was no regional difference in BF without PCA ($P = .72$), but tumour BF was significantly different than brain BF after filtering with four or lesser principal components ($P < .03$). This supports the effect of region on the PCA as indicated in Table 3-3, which led to a higher contrast between tumour and normal brain tissue in BF maps. Figure 3-8 also illustrates measurements of BV and PS in the normal brain and tumour before and after PCA filtering.
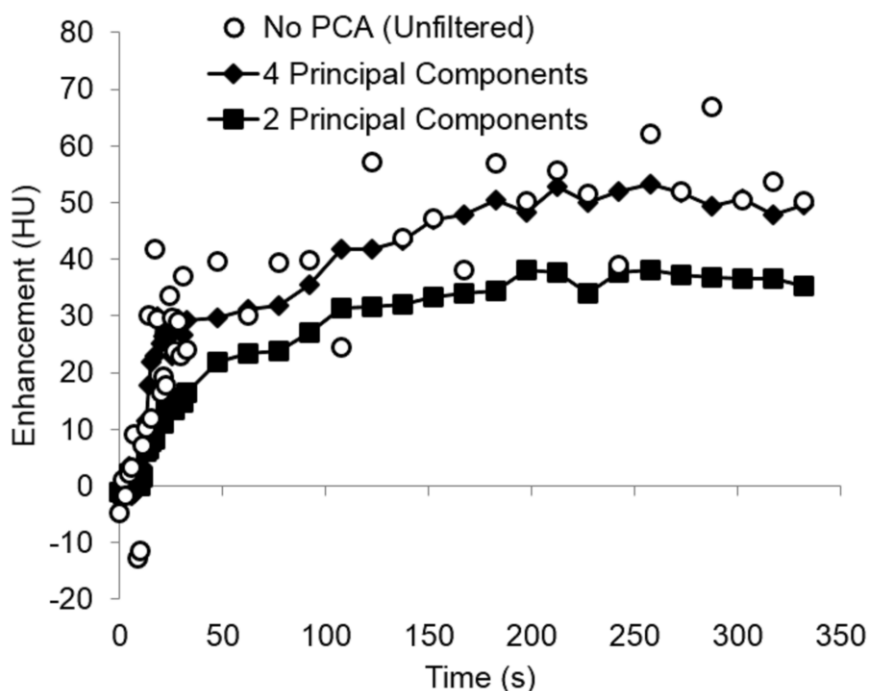
Figure 3-6: Examples of tumour time-enhancement curves obtained without and with principal component analysis (PCA) filtering. Filtering with two principal components can lead to loss of information as represented by the reduced height in the time-enhancement curve.
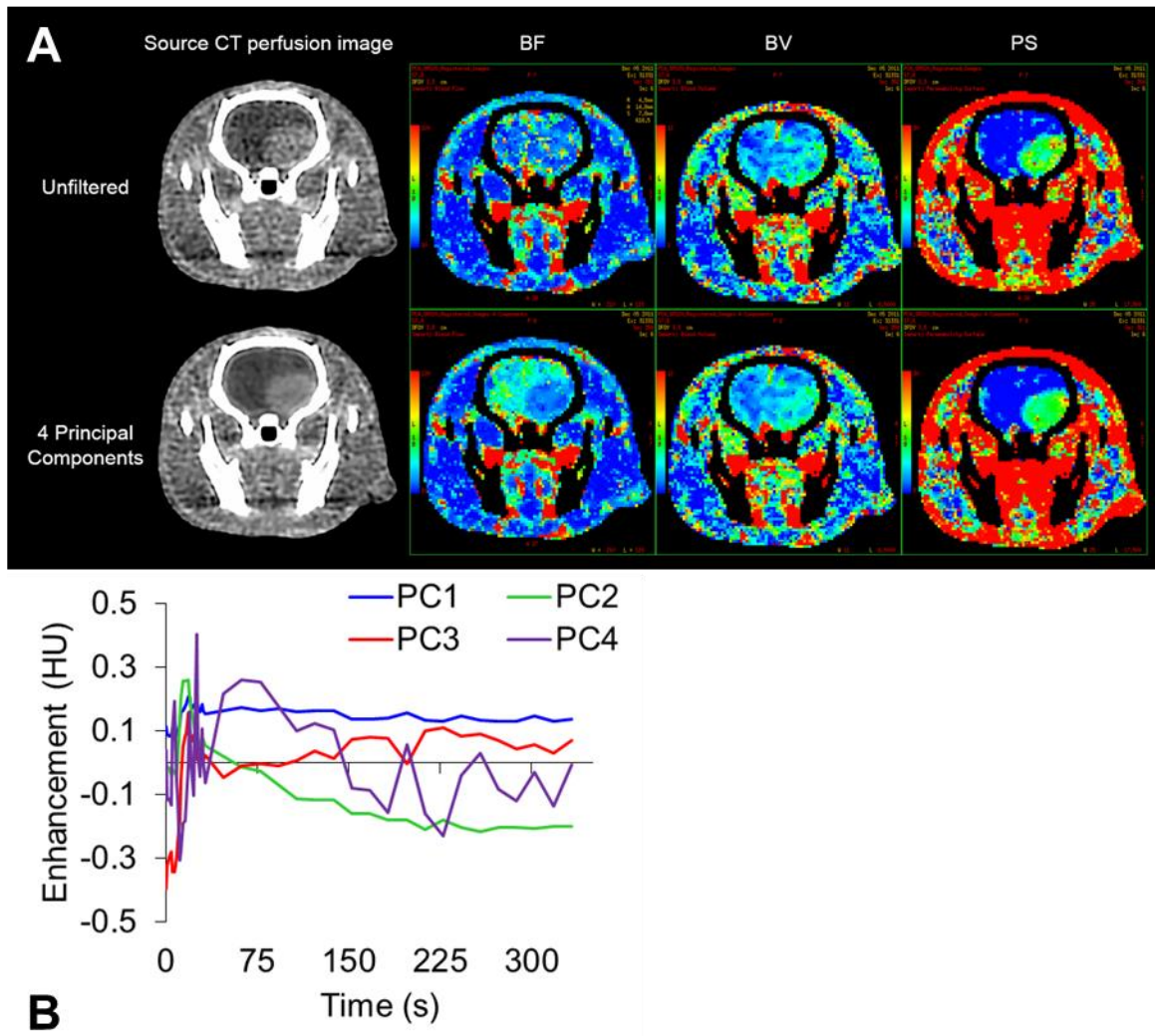
Figure 3-7: (A) Examples of source computed tomography (CT) images and maps of blood flow (BF), blood volume (BV), and permeability–surface area product (PS) without and with filtering using four principal components (PCs) . (B) The first four PCs as a function of time.

Table 3-2: Evaluation of quality of computed tomography perfusion image filtering.

Number of PCs	Noise level ± SD (HU)		CNR ± SD		% of voxels with FRI ≥ 5%	
	Brain	Tumour	Brain	Tumour	Brain	Tumour
No PCA	16.9 ± 0.5	16.6 ± 0.6	0.6 ± 0.1	1.4 ± 0.4	N/A	N/A
6 PCs	5.2 ± 0.6*	5.6 ± 0.6*	1.9 ± 0.3*	3.8 ± 1.2*	0.2 ± 0.2	0.3 ± 0.5
4 PCs	3.3 ± 0.4*	3.9 ± 0.7*	2.9 ± 0.4*	5.5 ± 2.4*	0.5 ± 0.3	1.1 ± 1.0
2 PCs	1.6 ± 0.3*	2.2 ± 0.6*	6.2 ± 1.3*	6.5 ± 1.8*	4.2 ± 2.2	26.4 ± 14.2

*Significantly different than No PCA of the same region ($P < 0.05$)

Abbreviations: PCA = principal component analysis; PCs = principal components; SD = standard deviation; HU = Hounsfield unit; CNR = contrast-to-noise ratio; FRI = fractional residual information; N/A = not applicable

Table 3-3: *P* values of repeated-measures ANOVA for measurements of BF, BV, and PS.

Factor	BF	BV	PS
PCA	0.21	<0.02	<0.01
Region	<0.05	<0.03	<0.01
Interaction between PCA and region	<0.01	<0.01	<0.01

Abbreviations: BF, blood flow; BV, blood volume; PCA, principal component analysis;

PS, permeability–surface area product.
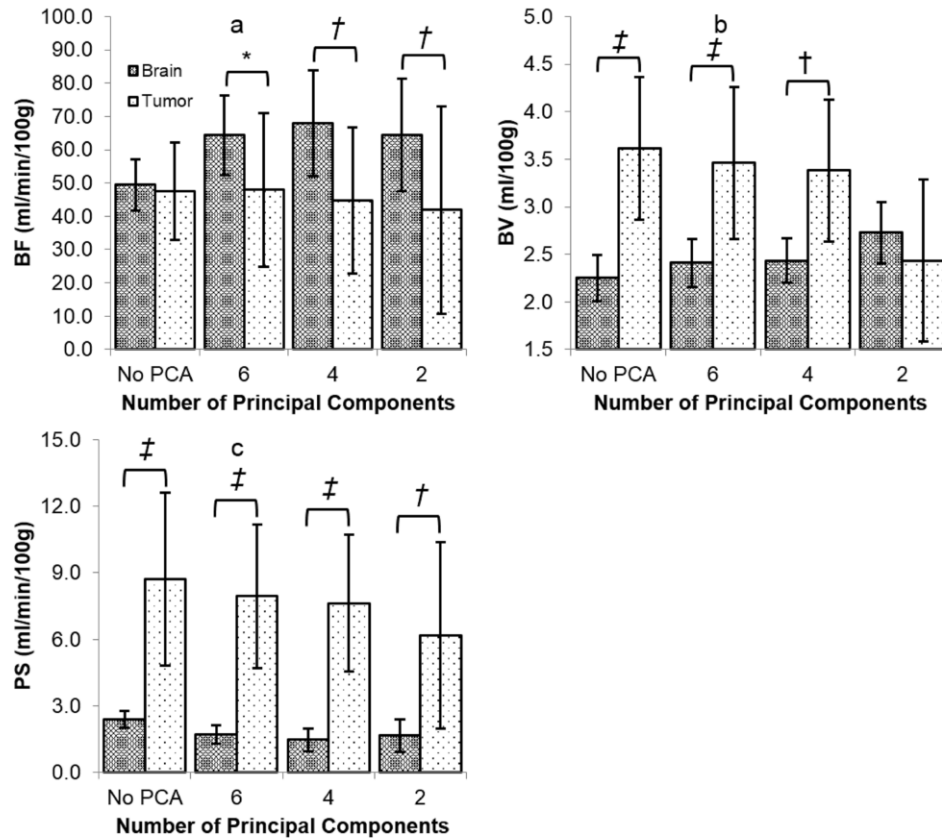
Figure 3-8: Brain and tumour blood flow (BF), blood volume (BV), and permeability–surface area product (PS) before and after filtering with different number of principal components. Asterisk (*) indicates a marginal significance of P = .06. Dagger (†) indicates $0.01 \leq P < .03$. Double dagger (‡) indicates $P < .01$.

3.4 Discussion

CT perfusion provides crucial information regarding brain tumour hemodynamics for the evaluation of tumour angiogenesis (1). The visualization of small objects of interest, such as tumours and ischemia, and accurate and precise measurements of BF, BV, and PS require good CNR. Balvay et al. (2) demonstrated an automated method to perform PCA. Our simulation provides the first evidence that PCA is effective in improving the reliability, accuracy, and precision of BF, BV, and PS measurements.

We applied PCA in this study to improve CNR of CT perfusion images of malignant rat gliomas that have an even lower CNR than previously reported (2). PCA is a statistical technique that separates image noise from signal by determining principal components with successively decreasing variance. Filtering with too many principal components results in ineffective denoising of the data whereas filtering with too few principal components runs the risk of removing genuine signal from the original data. We used the noise level, CNR, and FRI as metrics to evaluate the tradeoff between the improvement in image contrast and the loss of information. In this study, both image noise and CNR of CT perfusion images were improved after PCA. Filtering with only two principal components resulted in substantial information loss in the tumour that was not observed with greater than four principal components. Rat brain CT perfusion images required few principal components for filtering because there are few tissue types with different patterns of contrast enhancement in rat brain tissues. Unlike human brain, which has substantial amount of white matter, the rat brain consists mostly of gray matter (14). Furthermore, the rat brain, like human brain, is not permeable to most exogenous molecules including iodinated contrast. The shape of the time-enhancement curve in the normal rat brain is mainly governed by that of the arterial input and venous output. However, in the implanted glioma, contrast agent is able to extravasate into the brain parenchyma. The extravasation of contrast agent contributes to the higher contrast enhancement during the latter phase of the time-enhancement curves. Because there are only two major tissue types (normal and tumour) with two different patterns of contrast uptake (minimal vs. high extravasation) in the rat gliomas of this study, four principal components were able to filter the CT perfusion images without substantial loss of information. After filtering the CT perfusion images, differences in BF, BV, and PS measured in the tumour and contralateral normal brain were consistent with reported data measured using synchrotron radiation CT perfusion of the same tumour model (15).

There have been advances in the development of new CT reconstruction methods that can improve CT image quality. ASIR is one example of these advances and has been shown to provide equal image quality in brain imaging with ≥30% reduction in radiation dose when compared to filtered back projection (16). Images from this study were reconstructed with 80% ASIR. Thus, the improvement in image quality from PCA was

additional gain in CNR of the time-enhancement curves after ASIR was applied, suggesting that PCA further contributes to the improvement in CT perfusion image quality.

PCA has important potential application for lowering radiation dose when performing repeated CT perfusion studies to evaluate treatment response. A typical human brain CT perfusion protocol produces an effective dose of 2.9–5.4 mSv (17). Radiation dose is inversely proportional to the square of image noise. For instance, a nine-fold reduction in radiation dose can be achieved by filtering CT perfusion images with six principal components to achieve a three-fold improvement in image noise (Table 3-2). PCA filtering of CT perfusion images can improve the accuracy and precision of BF, BV, and PS measurements obtained with low CNR CT perfusion images; thus, making repeated low dose CT perfusion studies feasible. Lowering radiation exposure for better radiation safety or increasing spatial resolution of CT images will increase image noise, which in turn lowers CNR. Effective filtering of CT perfusion source images without the loss of information to obtain more accurate and precise measurements of BF, BV, and PS is imperative for both improving visibility of small objects of interest and for lowering radiation dose.

There are several limitations in this study. A simulation was performed to evaluate the improvement in accuracy and precision of BF, BV, and PS measurements. Although we did not perform an in vivo validation, CT perfusion imaging of brain tumour tissue has been validated in vivo (18). PCA analysis of the experimental data was applied to each slice of the brain separately (ie, two-dimensional analysis). A three-dimensional PCA of the entire brain could improve the quality of filtering by increasing the number of pixel TACs used to determine the principal components. It is important to note that the simulation results obtained in this study may not be applicable to other pharmacokinetic models (ie, the analysis software). Using a similar digital phantom, Kudo et al. (19) showed that different commercial software packages showed discrepancies in BF and BV measurements from simulated values. This is because available commercial software may or may not correct the arrival delays of the TACs, and the impulse residue functions are constrained differently in these software packages

because of the different assumptions used in their tracer kinetic models. A separate simulation using our digital phantom is needed to validate the measurement of different tracer kinetic parameters after PCA filtering of CT perfusion images for each commercial software.

3.5 Conclusions

PCA filtering of CT perfusion images improved CNR in vivo and reduced measurement errors of BF, BV, and PS by simulation. PCA is an effective tool for filtering CT perfusion images of malignant rat gliomas with low CNR. Filtering with four principal components could achieve the gain in CNR without substantial loss of information.

3.6 References

1. Jain R. Perfusion CT imaging of brain tumors: an overview. AJNR Am J Neuroradiol 2011; 32:1570–7.

2. Balvay D, Kachenoura N, Espinoza S, et al. Signal-to-noise ratio improvement in dynamic contrast-enhanced CT and MR imaging with automated principal component analysis filtering. Radiology 2011; 258:435–45.

3. Fournier LS, Oudard S, Thiam R, et al. Metastatic renal carcinoma: evaluation of antiangiogenic therapy with dynamic contrast-enhanced CT. Radiology 2010; 256:511–8.

4. Kremer S, Grand S, Berger F, et al. Dynamic contrast-enhanced MRI: differentiating melanoma and renal carcinoma metastases from high grade astrocytomas and other metastases. Neuroradiology 2003; 45:44–9.

5. Bulakbasi N, Kocaoglu M, Farzaliyev A, et al. Assessment of diagnostic accuracy of perfusion MR imaging in primary and metastatic solitary malignant brain tumors. AJNR Am J Neuroradiol 2005; 26:2187–99.

6.   Jain R, Ellika SK, Scarpace L, et al. Quantitative estimation of permeability surface-area product in astroglial brain tumors using perfusion CT and correlation with histopathologic grade. AJNR Am J Neuroradiol 2008; 29: 694–700.

7.   Jain R, Narang J, Schultz L, et al. Permeability estimates in histopathology-proved treatment-induced necrosis using perfusion CT: can these add to other perfusion parameters in differentiating from recurrent/progressive tumors? AJNR Am J Neuroradiol 2011; 32:658–63.

8.   Lee TY, Purdie TG, Stewart E. CT imaging of angiogenesis. Q J Nucl Med 2003; 47:171–87.

9.   Johnson JA, Wilson TA. A model for capillary exchange. Am J Physiol 1966; 210:1299–303.

10.   Paxinos G, Watson C. The rat brain. In: Stereotaxic coordinates. 6th ed. Burlington: Academic Press, 2007.

11.   Shrout PE, Fleiss JL. Intraclass correlations: uses in assessing rater reliability. Psychol Bull 1979; 86:420–8.

12.   Bland JM, Altman DG. Statistical methods for assessing agreement between two methods of clinical measurement. Lancet 1986; 1:307–10.

13.   Norušis MJ. SPSS® Statistics 17.0: statistical procedure companion. Upper Saddle River, NJ: Prentice Hall Inc, 2008; 599–609.

14.   Zhang K, Sejnowski TJ. A universal scaling law between gray matter and white matter of cerebral cortex. Proc Natl Acad Sci U S A 2000; 97:5621–6.

15.   Balvay D, Troprès I, Billet R, et al. Mapping the zonal organization of tumor perfusion and permeability in a rat glioma model by using dynamic contrast-enhanced synchrotron radiation CT. Radiology 2009; 250:692–702.

16.   Ren Q, Dewan SK, Li M, et al. Comparison of adaptive statistical iterative and filtered back projection reconstruction techniques in brain CT. Eur J Radiol 2012; 81:2597–601.

17.   Yeung TP, Yartsev S, Bauman G, et al. The effect of scan duration on the measurement of perfusion parameters in CT perfusion studies of brain tumors. Acad Radiol 2013; 20:59–65.

18. Cenic A, Nabavi DG, Craen RA, et al. A CT method to measure hemodynamics in brain tumors: validation and application of cerebral blood flow maps. AJNR Am J Neuroradiol 2000; 21:462–70.

19. Kudo K, Christensen S, Sasaki M, et al. Accuracy and reliability assessment of CT and MR perfusion analysis software using a digital phantom. Radiology 2013; 267:201–11.

Chapter 4

4 CT Perfusion Imaging as an Early Biomarker of Differential Response to Stereotactic Radiosurgery

This chapter is adapted from the manuscript entitled "CT perfusion imaging as an early biomarker of differential response to stereotactic radiosurgery". This manuscript will be submitted to the journal *PLOS ONE* in July 2014 to be considered for publication. The authors of this manuscript are Yeung TPC, Kurdi M, Wang Y, Al-Khazraji B, Morrison L, Hoffman L, Jackson D, Crukley C, Lee TY, Bauman G, Yartsev S.

4.1 Introduction

Patients with glioblastoma multiforme, the most common form of adult brain tumours, have a median survival of approximately $12 - 15$ months (1). Radiotherapy has played an important role in prolonging the survival of these patients since the 1970s (2). Magnetic resonance (MR) and computed tomography (CT) are currently the standard imaging modalities for assessing treatment response. Tumour progression is usually detected by increased contrast-enhancement on gadolinium-enhanced T1-weighted MR images, and T2-weighted or fluid-attenuated inversion recovery MR images (3). However, early changes in contrast enhancement after radiotherapy is not a specific tool to predict treatment failure as changes in contrast enhancement can occur in pathophysiological processes that disrupt the blood brain barrier. For instance, radiation-induced injury (e.g. radiation-induced necrosis and pseudoprogression) can mimic the appearance of tumour progression on T1-weighted MR (3).

Due to the poor survival rates, timely and accurate assessment of response to radiation is important as treatment can be altered if a non-responder to radiation can be identified early enough. In preclinical studies, radiotherapy is usually delivered using a technique called stereotactic radiosurgery (SRS). It is delivered in one or few large dose fractions of $8 - 30$ Gy and would result in tumour growth delay and survival benefit (4-7). Radiotherapy, particularly SRS, can result in vascular damage in the irradiated area

(4, 8-10), and radiosensitivity of tumour vasculature can augment response to SRS (11). Hypofractionation schemes that also use a large dose per fraction to treat patients with malignant gliomas is also an attractive treatment strategy. Recently, clinical studies have investigated the use of hypofractionated intensity modulated radiotherapy to treat these patients (12-14). Hypofractionation have some advantages over conventional fractionation. Hypofractionation is expected to increase the biological effect of radiation due to increased cell damage resulting from a higher dose per fraction (15). It also reduces the effect of tumour repopulation by reducing treatment time (16). Thus, imaging of tumour perfusion is a promising biomarker of response to high dose per fraction radiotherapy (e.g. SRS and hypofractionation) that warrants investigation.

The C6 rat glioma is a widely used experimental model for the study of malignant glioma (17), including the effects of SRS (6,7,9,10). Tumour microcirculation can be noninvasively measured by CT or MR perfusion imaging techniques. In particular, CT perfusion imaging is a validated method that allows simultaneous mapping of blood flow (BF), blood volume (BV), and permeability-surface area product (PS) (18,19). CT scanners and iodinated contrast agents are also widely available, and they are ubiquitous in radiation oncology departments. The purpose of this study was to evaluate vascular changes following SRS using CT perfusion, and determine whether acute vascular changes within one week of SRS is predictive of survival. In addition, early (four days post-SRS) and late (eight weeks post-SRS) histopathologic findings were examined.

4.2   Materials and Methods

4.2.1   C6 Glioma Model

All experiments were compliant with our institutional Animal Use Subcommittee guidelines. Wistar rats weighing $300 - 400$ g ($N = 33$) were used in this study. The animals were anaesthetized with 2% isoflurane during all procedures. C6 glioma cells (American Type Culture Collection, Manassas, VA) were cultured in F12k 15% horse serum, 2.5% bovine serum, and 1% penicillin-streptomycin. For the implantation of C6

glioma cells, each animal was secured into a stereotactic surgical frame. After scalp incision at midline and exposing the bregma, a 1 mm diameter burr hole was drilled at 1 mm anterior and 3 mm right of the bregma. A total of 10^6 C6 glioma cells were slowly injected for 5 minutes at $3 - 4$ mm below the burr hole, which corresponded to the location of the caudate putamen (20). The burr hole was sealed with bone wax, and the scalp was closed with sutures.

4.2.2 Baseline CT Perfusion Imaging

All rats underwent the first CT perfusion scan on an average of 11 days (range, 7 $-$ 16 days) after implantation of C6 glioma cells to monitor tumour growth and prepare for SRS. The rats were scanned using a clinical CT scanner (Discovery 750 HD, GE Healthcare, Waukesha, WI). A two-phase CT perfusion scan, guided by a prior non-contrast CT scan that identified 16×1.25 mm thick sections to cover the entire brain, was performed for each animal. The brain was scanned with high resolution mode for 32 s at 1.4 s intervals during the first phase and for a period of 165 s at 15 s intervals during the second phase. A bolus of contrast (Isovue, Bracco Diagnostics Inc, Vaughan, Canada, 300 mg iodine/ml, 2.5 mL/kg body weight) was injected into the lateral tail vein at a rate of 8 mL/min at $3 - 4$ s after the start of the first phase. The scanning parameters were 80 kVp, 120 mAs, 10 cm field of view, and high-definition bone filter. The visibly distinguishable spatial resolution was 1 line pair per 500 μm measured on a rat-size phantom (21).

CT perfusion images of the same slice were averaged over the whole scan duration using the prototype version of CT perfusion 4D (GE Healthcare) to produce a set of contrast-enhanced images called averaged CT images. The tumour diameter on the averaged CT images was measured immediately after the scan. The rats were assigned randomly to either the control group ($N = 8$) or the SRS group ($N = 25$) once a tumour diameter of 4 mm was reached.

4.2.3   Stereotactic Radiosurgery

A custom-made plastic stereotactic frame was used to secure the animals for treatment planning. A non-contrast helical CT scan was performed (25 cm field-of-view, 80 kV, 110 mAs, 1.25 mm slice thickness) for treatment planning. CT images were transferred to the Helical Tomotherapy Treatment Planning System (Accuray Inc, Madison, WI, USA). Using the averaged CT images for anatomical guidance, a dose of 12 Gy was prescribed to at least 80% of the contrast-enhanced tumour volume with the brainstem receiving no more than 4 Gy and less than 10% of the normal brain receiving more than 8 Gy.

For SRS, the rats were fixed in the same plastic stereotactic frame. A 3.5 MV CT study was acquired prior to treatment. This MV CT study was co-registered with the planning kV CT study and couch position was shifted in the lateral, anterior-posterior, and superior-inferior directions. The rats were repositioned in the stereotactic frame if there were rotational positioning errors. The average SRS delivery time was 6 minutes. Rats in the control group were put under anesthesia and secured in the stereotactic frame for 6 minutes to mimic the procedure without radiation.

4.2.4   Follow-up CT Perfusion Imaging

Rats in the SRS group were further assigned to either 1) acute imaging group (N = 12) or 2) the longitudinal imaging group (N = 13). Rats in the acute imaging group were imaged with CT perfusion at 4 days post-SRS, and were euthanized on the same day. Rats in the longitudinal group and control group were imaged for a maximum of 8 weeks post-SRS to monitor tumour changes and survival. Rats were euthanized if they showed any of the following signs and symptoms: weight loss of $\geq$ 15% from the heaviest recorded weight, lethargy, refusal to eat, neurologic signs such as one-sided limb weakness.

4.2.5   Image Analysis

Maps of BF, BV, and PS were generated using the prototype version of CT perfusion 4D (GE Healthcare). The time-attenuation curve (TAC) from the carotid artery was selected as the arterial input. The arterial TAC was deconvolved with tissue TACs measured from 2×2 pixel blocks of CT images using the Johnson-Wilson model to produce maps of BF, BV, and PS (18,22). Using the averaged CT images for anatomical guidance, tumour volume, BF, BV, and PS in the tumour, peritumoural region, and contralateral normal brain were measured. Peritumoural region was defined as normal brain that is $2 - 3$ mm adjacent to the tumour. Mean BF and BV values were normalized to the contralateral normal brain to obtain the relative BF (rBF) and relative BV (rBV) values.

4.2.6   Histopathologic Examination

On the same day as the last CT perfusion scan, the animals were euthanized with an overdose of potassium chloride. The animals were perfusion-fixed with phosphate buffered saline followed by 4% paraformaldehyde. The brains were removed and fixed in 4% paraformaldehyde for 24 hours. The brain specimens were sectioned into 3 mm thick blocks, paraffin-embedded, then sectioned at 5 μm. Hematoxylin and eosin stain (H&E) was applied on each section.

A blinded neuropathology resident (M.K.) examined all H&E slides at different magnifications (20x and 40x) to evaluate histologic signs of radiation damage. The presence of tumour was evaluated as "no", "yes", or "diminished due to radiation effect". "Diminished due to radiation effect" means the presence of a circumscribed hypocellular lesion showing features of irradiation. The diameter of each lesion (control and SRS-treated animals) was measured. Tumour cellularity was defined as 1) hypercellular when less than 30% of the tumour area appeared pale or major tumour was found, and 2) hypocellular when more than 50% of the tumour area appeared pale excluding necrosis. Tumour was graded based on the World Health Organization criteria (23). Tumour edema was defined as the presence of extensive intracellular cytoplasmic swelling or

intercellular spaces between tumour cells. Peritumoural edema was defined as intracellular cytoplasmic swelling or presence of intercellular spaces and reactive gliosis in the peritumoural region. Necrosis was described as 1) pseudopalisading necrosis that indicates high-grade glioma, 2) fibrinoid necrosis, or 3) background necrosis (neither pseudopalisading nor fibrinoid necrosis) that indicate post-radiation effect. 8) Presence of endothelial hyperplasia was recorded as a feature of angiogenesis in high-grade glioma. Increased vascularity and hyalinzed blood vessels were recorded as features of post-radiation effect. Percentage of animals exhibiting these signs was calculated. Mean percent necrosis by area was also calculated.

The brain sections were also stained with monoclonal anti-actin, α-smooth muscle antibody (α-SMA) (1:500, clone 1A4, Sigma-Aldrich) to identify mature vessels (24-26). The α-SMA positive vessels were qualitatively classified as intact or fragmented vessels. α-SMA positive vessel density was defined as the number of vessels that stained positive for α-SMA in 6 separate fields (20×) in the most vascular region of the tumour and peritumoural region. Intact and fragmented α-SMA positive vessel densities were measured separately. The percentage of fragmented α-SMA positive vessels was also recorded.

4.2.7   Statistical Analysis

The Shapiro-Wilk test was used to test the normality of the data. Temporal changes in the acute imaging group were tested by the Wilcoxon signed-rank test. The end point of the longitudinal imaging group was survival at 8 weeks post-SRS. The longitudinal group was also subdivided into those that survived more than 2 weeks (responder group), and those that survived less than 2 weeks post-SRS (nonresponder group). The omnibus Kruskal-Wallis test was used for comparisons between groups followed by the Mann-Whitney U test. The omnibus Friedman test was used for longitudinal comparisons within-group followed by the Wilcoxon signed-rank test. All data were reported as mean ± standard error of the mean (SE). Survival of the groups was compared using the log-rank test. Spearman's rank correlation was used to assess the

associations between different imaging parameters (tumour volume, rBF, rBV, PS) and the percentage of fragmented α-SMA positive vessels. PS is the product between microvessel surface area and permeability, and BV has been shown to correlate with microvessel area (27). We used the PS:BV ratio as a surrogate of permeability and correlated this parameter with the percentage of fragmented α-SMA positive vessels as well.

We investigated whether the imaging parameters correlated with overall survival, and whether these parameters on day 7 post-SRS could predict survival. Each imaging parameter was assessed by applying a threshold that is below the lower 50% confidence interval (CI) boundary of the variations across all treated animals derived from the between-subject variation on day 7 post-SRS. This threshold was used to categorize each animal into two groups (i.e. higher or lower than the threshold). Survivals of the different groups were compared. The sensitivity, specificity, and accuracy of each parameter in predicting survival were assessed. A $P \leq 0.05$ was considered statistically significant.

4.3   Results

4.3.1   Acute Vascular Changes and Histopathologic Features

Irradiated rats received 12 Gy in the tumour and peritumoural region, and different CT perfusion changes were observed in these two regions. Tumour volume, rBF, and rBV decreased significantly while peritumoural rBF, rBV, and PS increased significantly in the SRS group (Table 4-1). These opposite CT perfusion changes in the tumour and peritumoural regions are illustrated in Figure 4-1.

Table 4-1: Acute changes (± standard error) in CT perfusion parameters.

Regions-of-interest	Treatment	Percent Change (%)			
		Tumour volume	rBF	rBV	PS
Tumour	SRS	-37.3 ± 13.2*	-18.2 ± 7.9*	-23.1 ± 7.6*	-9.2 ± 9.7
	Control	95.1 ± 34.7*	-13.1 ± 9.3	-6.4 ± 9.4	7.4 ± 15.1
Peritumoural	SRS	N/A	20.9 ± 7.9*	28.7 ± 7.7**	54.3 ± 11.6**
	Control	N/A	-5.0 ± 5.3	2.0 ± 5.0	13.9 ± 20.2

Abbreviations: SRS, stereotactic radiosurgery; rBF, relative blood flow; rBV, relative blood volume; PS, permeability-surface area product.
* Significantly different compared to baseline at $P \leq 0.05$ level
** Significantly different compared to baseline at $P \leq 0.01$ level
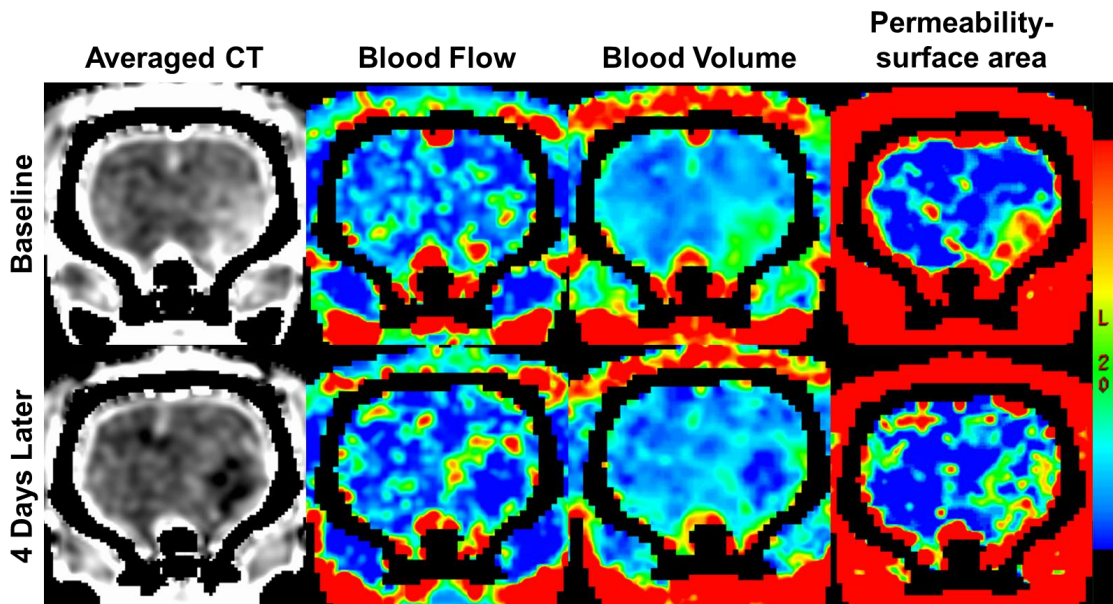
Figure 4-1: Acute CT perfusion changes on the fourth day after stereotactic radiosurgery (SRS). Tumour relative blood flow (rBF) decreased from 1.48 to 0.68, relative blood volume (rBV) decreased from 1.70 to 0.78, while permeability surface-area (PS) decreased from 4.67 to 3.87 ml/min/100g. On the contrary, peritumoural rBF increased from 0.96 to 1.49, rBV increased from 1.06 to 1.52, and PS increased from 2.13 to 3.81 ml/min/100g.

H&E histological examination revealed that all tumours were grade IV gliomas. Hypercellularity, mitosis, pseudopalisading necrosis, and endothelial hyperplasia were observed as signs of grade IV glioma in the control animals. For the acute imaging group that received SRS, fibrinoid or background necrosis, increased vascularity, and

hyalinized blood vessels were identified. Atypical nuclei, calcification, and gliosis were also observed in some lesions. Examples of H&E images of unirradiated tumour, acute effects of SRS, and late effects of SRS are demonstrated in Figure 4-2, and a summary of histological findings is provided in Table 4-2.
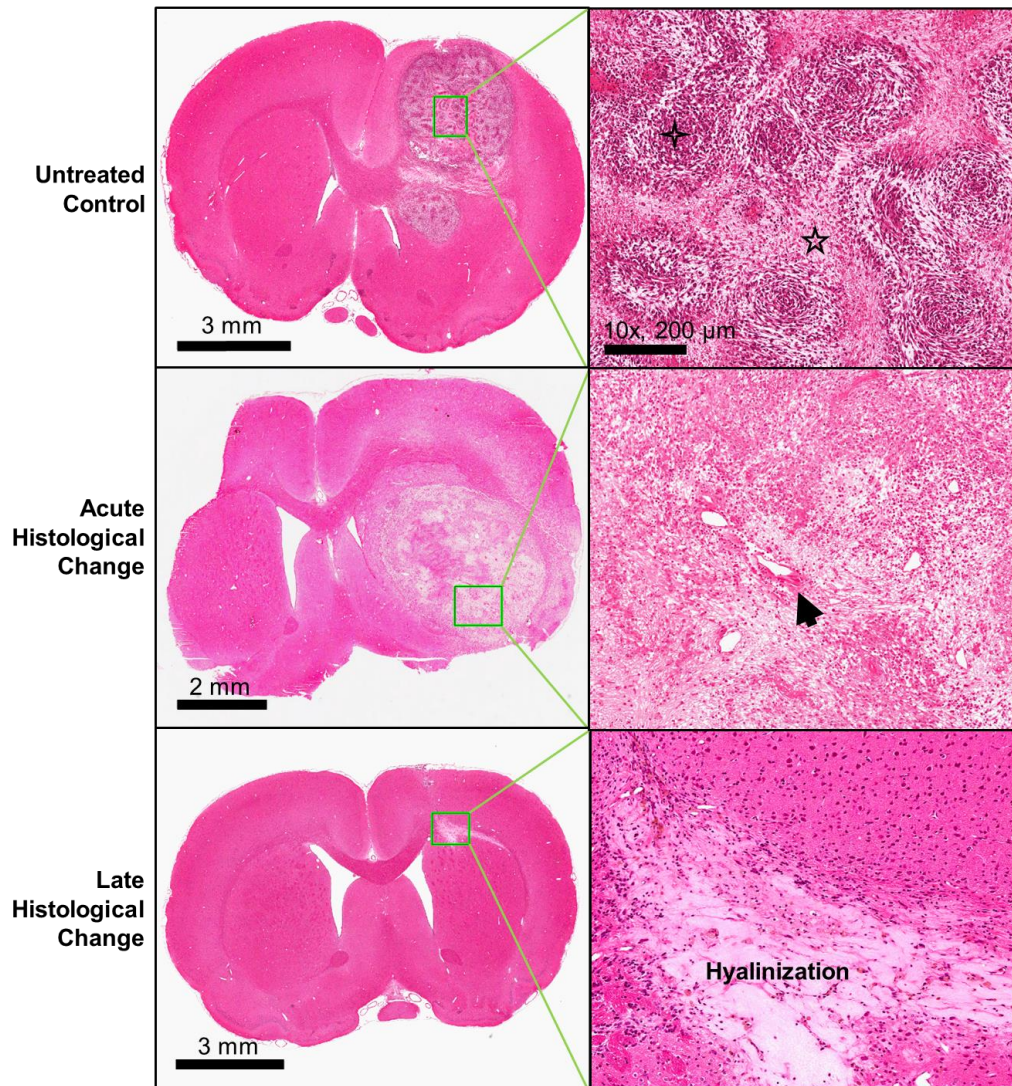
Figure 4-2: Histological examples of stereotactic radiosurgery (SRS) effects. Representative Hematoxylin & Eosin images of an untreated control, acute histological change at 4 days post-SRS, and late histological change at 59 days post-SRS. Hypercellularity (four point star) and pseudopalisading necrosis (five point star) are classic signs of grade IV glioma, and these were observed in the control animals. Hyalinized blood vessels (arrow) and hypocellularity can be observed shortly after SRS. Regression of tumour and hyalinization of tissue were observed at a later stage after SRS.

Table 4-2: Summary of histological finding on Hematoxylin and Eosin (H&E) specimens.

	Presence of Tumour	Tumour Diameter (mm)	Hypo-cellularity	Types of Necrosis	% Area Necrosis	Vascularity	Tumour Edema	Peritumoural Edema
Controls	88% Yes 0% Diminished	7.3 ± 4.0	0%	88% PPN 13% FN	46 ± 27	75% EH 25% Increased 25% HBV	0%	0%
Acute Histology	75% Yes 25% Diminished	5.8 ± 3.0	25%	50% PPN 25% FN 33% BN	37 ± 19	58% EH 58% Increased 100% HBV	25%	42%
Responder	0% Yes 0% Diminished	N/A	N/A	None	N/A	0% EH 43% Increased 14 % HBV	0%	0%
Non-responder	50% Yes 33% Diminished	4.6 ± 1.5	33%	67% PPN 0% FN 17% BN	55 ± 13	67% EH 50% Increased 67% HBV	17%	33%

Abbreviations: PPN, pseudopalisading necrosis; FN, fibrinoid necrosis; BN, background necrosis; EH, endothelial hyperplasia; HBV, hyalinized blood vessels

Immunohistochemical staining revealed fragmented α-SMA positive vessels were identified mostly in the SRS-treated tumours (Figure 4-3). Fragmented α-SMA positive vessel densities in the tumour ($P = 0.006$) and peritumoural regions ($P < 0.001$) were significantly higher in the irradiated animals than the control animals (Figure 4-4). In the tumour, a positive borderline significant correlation between the percentage of fragmented α-SMA positive vessels and PS:BV ratio was identified for the treated animals ($\rho = 0.58$, $P = 0.06$) while a significant negative correlation was found for the control animals ($\rho = -0.84$, $P = 0.02$). However, the amount of fragmented α-SMA positive vessels in the controls was very small (Figure 4-4). In the peritumoural region of the treated animals, negative correlations were found between the percentage of fragmented α-SMA positive vessels with rBF ($\rho = -0.62$, $P = 0.03$) and rBV ($\rho = -0.58$, $P = 0.05$).
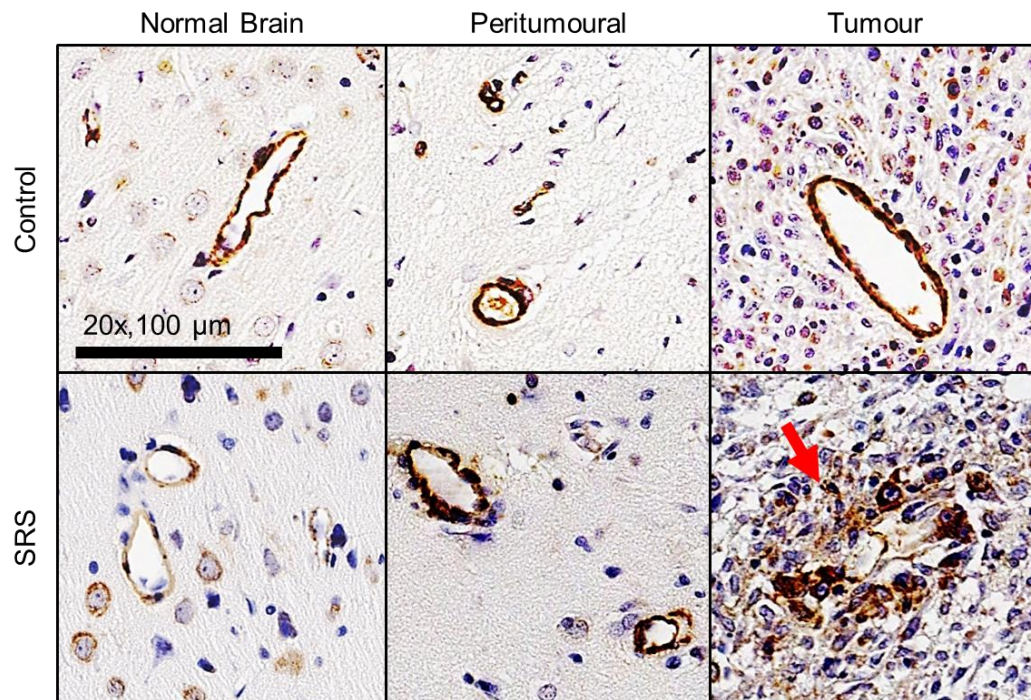
Figure 4-3: α-smooth muscle actin (α-SMA) positive vessels in the normal brain, peritumoural region, and tumour of a control and a treated animal after stereotactic radiosurgery (SRS). Intact α-SMA positive vessels were observed in control animals, but fragmented coverage of vessels by α-SMA is mostly seen in treated animals (red arrow).
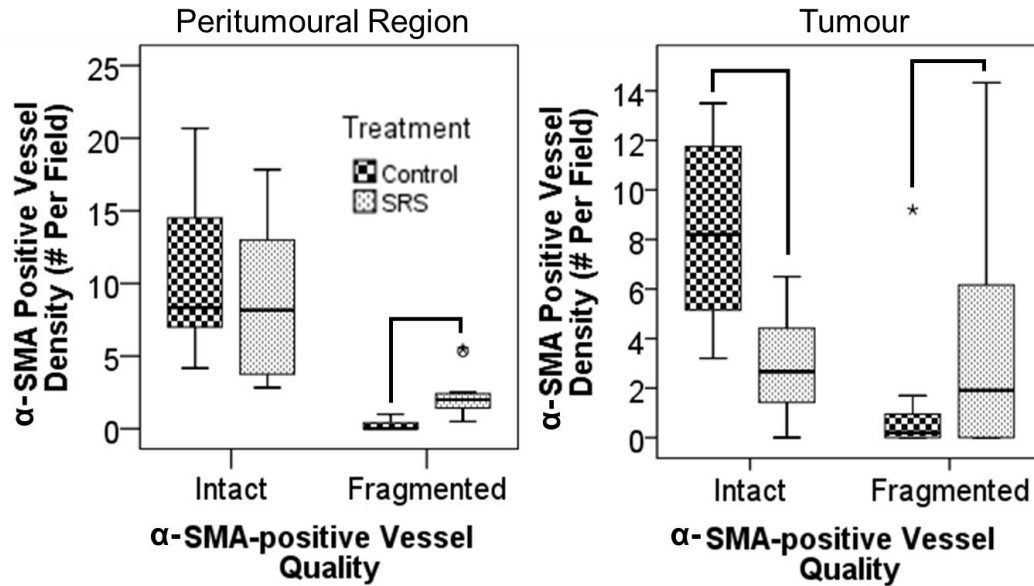
Figure 4-4: Boxplots of intact and fragmented α-smooth muscle actin (α-SMA) positive vessels in the control and SRS groups. Pairs with *P* < 0.01 are connected by black lines.

4.3.2 Treatment Response, Longitudinal Changes, and Late Histopathologic Features

Median survival of the control group was 10 days post-baseline scan (95% CI = 6 − 14 days), and median survival of the SRS group was not reached (log-rank *P* < 0.04). However, survival in the SRS group was heterogeneous with 46% of the animals not surviving for more than 15 days. We designated these relative low survival animals as non-responders and animals with survival > 15 days as responders. Statistical comparisons were performed for the first 4 time points because all controls died before the 5th time point. Changes in tumour volume, rBF, rBV, and PS of these three groups are shown in Figure 4-5. Significant tumour growth was observed in the controls (Friedman *P* = 0.001, Wilcoxon signed-rank *P* < 0.03). Significant tumour shrinkage was observed in the responders (Friedman *P* = 0.04, Wilcoxon signed-rank *P* < 0.05). There was no significant tumour volume change in the non-responders. Tumour rBF in the responders was significantly lower than the non-responders and controls on day 14 post-SRS

(Kruskal Wallis $P = 0.01$, Mann-Whitney U $P < 0.04$). Tumour rBV in responders were significantly lower than the non-responders and controls on day 4 (Kruskal Wallis $P = 0.04$, Mann-Whitney U $P < 0.04$) and day 7 post-SRS (Kruskal Wallis $P = 0.01$, Mann-Whitney U $P = 0.01$). Responders' tumour PS was significantly lower than the other groups on day 7 post-SRS (Kruskal Wallis $P = 0.007$, Mann Whitney U $P \leq 0.008$). Between-group differences and longitudinal changes in PS:BV ratio in the tumour were not significant.
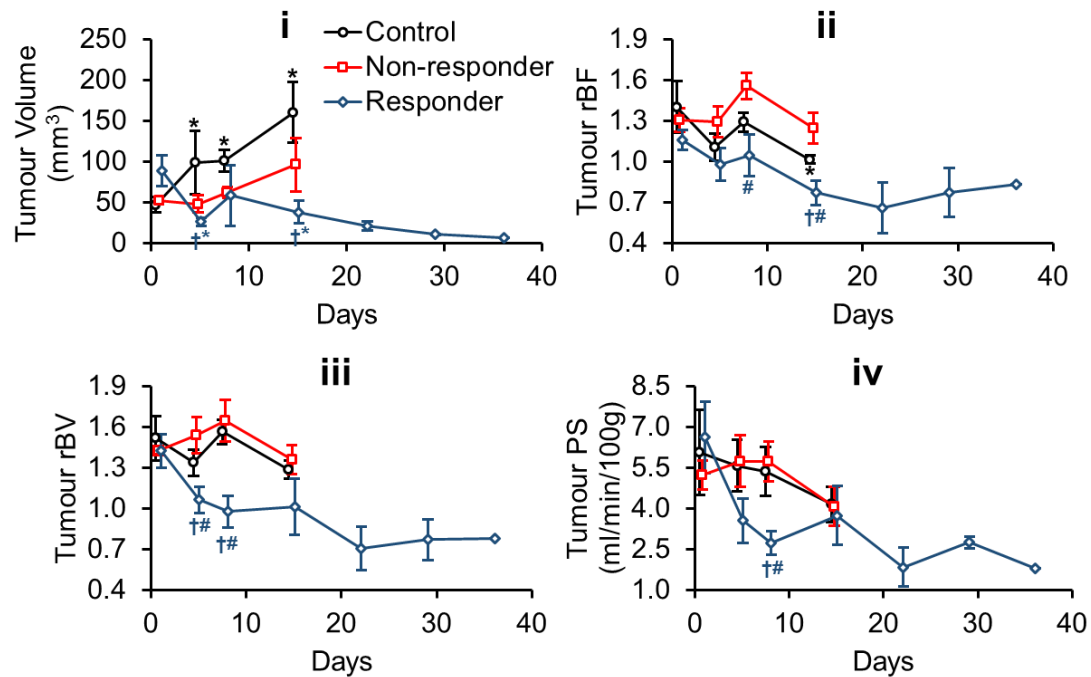
Figure 4-5: Changes in (i) tumour volume, (ii) relative blood flow (rBF), (iii) relative blood volume (rBV), and (iv) permeability-surface area (PS) in the tumour for controls, responders, and non-responders. *Significantly different from baseline (Friedman test and Wilcoxon-signed rank test). †Significantly different from controls and #significantly different from non-responders (Kruskal-Wallis followed by Mann-Whitney *U* test).

Figure 4-6 shows an elevation in peritumoural rBF in both responders and non-responders on days 4 and 7 post-SRS compared to the controls (Kruskal Wallis $P \leq$

0.006, Mann-Whitney U $P \leq 0.008$). Significant elevation was observed in peritumoural rBV of responders when compared to controls (Kruskal Wallis $P < 0.01$, Mann-Whitney U $P = 0.001$), and a similar trend was observed for peritumoural PS albeit not significant. This elevation in CT perfusion parameters eventually dissipated with time. Between-group differences and longitudinal changes in PS:BV ratio in the peritumoural region were not significant.
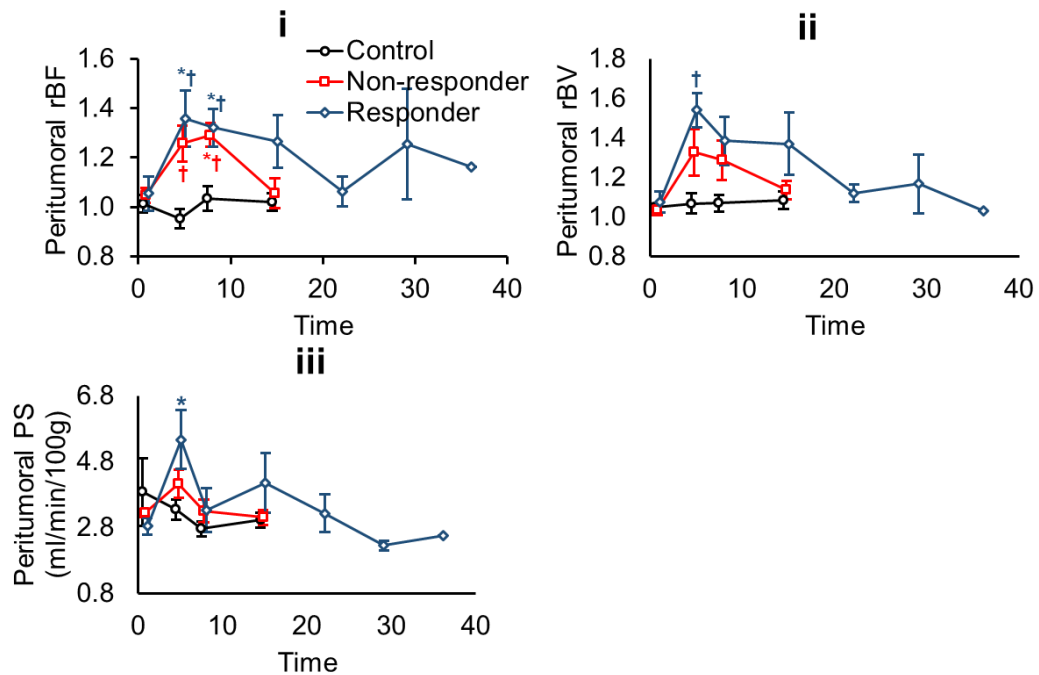
Figure 4-6: Changes in (i) rBF, (ii) rBV, and (iii) PS in the peritumoural region for controls, responders, and non-responders. *Significantly different from baseline (Friedman test and Wilcoxon-signed rank test). †Significantly different from controls (Kruskal-Wallis followed by Mann-Whitney *U* test).

Histological examination revealed no presence of tumour in any of the responders. Increased vascularity was the major sign of late radiation-induced histologic change (Table 4-2). Figure 4-2 shows an example of late radiation-induced damage after the regression of tumour. For the non-responders, tumours were detected on H&E histology;

pseudopalisading necrosis was the major type of necrosis observed. Increased vascularity, endothelial hyperplasia, and hyalinized blood vessels were also observed.

4.3.3   Early Prediction of Survival after Stereotactic Radiosurgery

Tumour volume, rBF, rBV, PS, and PS:BV ratio at baseline and on day 4 post-SRS did not correlate with overall survival. However, tumour rBV (ρ = -0.61, P < 0.05) and PS (ρ = -0.85, P = 0.001) on day 7 post-SRS correlated with overall survival. We evaluated whether each of the imaging parameter was predictive of overall survival by grouping the treated animals based on the measurement on day 7 post-SRS. Kaplan-Meier survival plots are shown on Figure 4-7. SRS-treated animals with lower tumour rBF, rBV, and PS had significantly longer survival than SRS-treated animals with higher rBF, rBV, and PS (log-rank $P \leq 0.02$). Treated animals with lower tumour volumes were associated with longer survival than those with higher tumour volumes, but this was not significant. Similarly, animals with a low PS:BV ratio did not have significantly different survival than those with high PS:BV ratio. In terms of predictive performance, both rBV and PS had the highest sensitivity (86%), specificity (100%), and accuracy (92%). rBF had a sensitivity, specificity, and accuracy of 71%, 100%, and 83%, respectively. Tumour volume had a sensitivity, specificity, and accuracy of 57%, 80%, and 67%, respectively. The PS:BV ratio had sensitivity, specificity, and accuracy of 67%, 60%, and 64%, respectively.
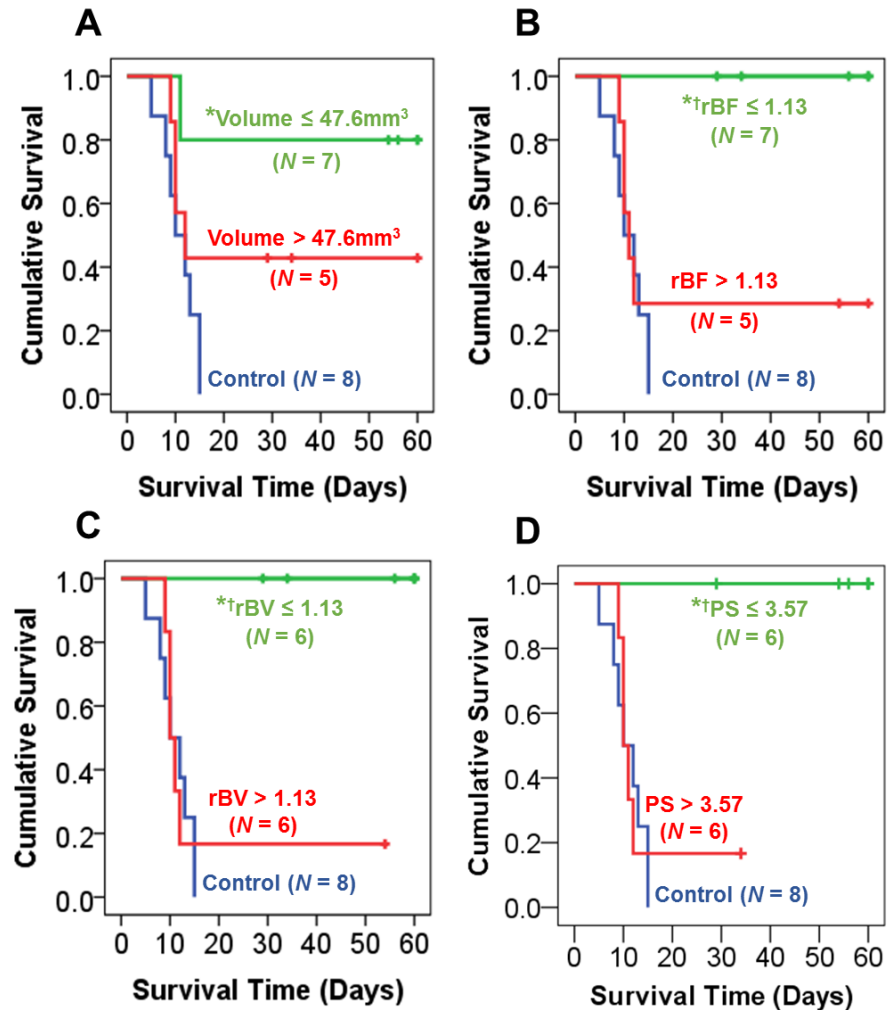
Figure 4-7: Kaplan-Meier plots of response to treatment categorized by (A) tumour volume, (B) relative blood flow (rBF), (C) relative blood volume (rBV), and (D) permeability-surface area product (PS). For each imaging parameter, two response groups were identified based on whether the measured value was less than the lower 50% confidence interval of variations across all treated animals derived from the between-subject variation on day 7 post-SRS. Those that met this criteria were ranked as "low" by applying this threshold, and the others were ranked as "high". Animals with low rBF, rBV, and PS on day 7 post-SRS showed significantly longer survival than the rest of the treated animals (i.e. high rBF, rBV, and PS) and control animals. *Significantly different from control group. †Significantly different from the other treated animals with a "high" value. Significant at $P \le 0.02$ level (log-rank test).

4.4 Discussion

Although radiotherapy offers an overall survival benefit at the population level, accurate assessment of tumour response for each patient is crucial for treatment modification if no response to radiation is detected. Therefore, we need to develop non-invasive imaging biomarkers as early indicators of response to radiation. Such biomarkers may help design combination therapies (drugs + radiation) in future clinical trials. Combining SRS with an anti-angiogenic agent is an attractive treatment option (28) because Bevacizumab appeared to ameliorate radiation-induced necrosis (29). Preclinical studies also suggested that anti-angiogenic agent like DC101 is a radiosensitizer to SRS (30).

From preclinical studies, overall survival benefits post-SRS are commonly reported, with some treated animals surviving substantially longer than others (4-6). In our study, SRS demonstrated an overall survival benefit and histological confirmation of radiation-induced damage. Similar to previous studies, we observed substantial heterogeneity in treatment response. We found that CT perfusion can be a potential noninvasive imaging method to predict response to SRS, and that rBF, rBV, and PS showed better predictive performance of survival than tumour volume.

In clinical studies, the survival benefit of SRS in combination with fractionated radiotherapy is unclear with some studies suggesting a 2-year overall survival benefit (31,32), while randomized trials showed that SRS did not confer a survival benefit over fractionated radiotherapy alone (33,34). Current clinical evidence from fractionated radiotherapy support our preclinical results in that a higher rBV after the completion of radiotherapy is associated with poor survival (35,36). However, the correlation between survival post-SRS and perfusion imaging parameters is lacking in the clinical literature, and there is no imaging biomarker to assess patients who might respond to SRS. Our results provide corroborating evidence to support the hypothesis that CT perfusion is an early biomarker of response to SRS. Use of CT perfusion parameters to characterize tumour vascular profiles and correlate with treatment response might identify patients who would benefit from SRS or hypofractionation treatment schemes. The use of an early

imaging biomarker to assess response to SRS or hypofractionated treatment schemes in randomized clinical trials might better define the role of altered fractionation schemes in this group of patients.

From the acute imaging study, PS did not correlate with the percentage of fragmented α-SMA positive vessels, this could because PS is the product between permeability and surface area of the endothelium (18). Since BV has been shown to correlate with microvessel area (27), we investigated the PS:BV ratio as a surrogate marker of permeability. After SRS, a positive correlation between PS:BV and the percentage of fragmented α-SMA positive vessels points to the effect of radiation on the permeability of the blood-tumour barrier. From our survival study, it is PS that correlated with survival and not the PS:BV ratio. This suggests a low permeability (i.e. poor delivery) but a high surface area of SMA coverage after SRS is associated with poor survival. Vessels that are covered by SMA are mature vessels (24-26), and tumour vessel maturity is associated radiation resistance (8,37-38). Together, this points to a possible link between the vessel SMA coverage and survival. We were unable to show a correlation between survival and SMA coverage of mature vessels directly since any assessment of tumour vessels would require the sacrifice of animals. Further investigation into the direct associations between tumour PS and SMA coverage of mature vessels with tumour response is warranted.

It is important to study the effect of radiation on the adjacent normal brain tissue (i.e. peritumoural region) because it is usually included in the irradiated volume that receives a significant dose of radiation in clinical practice, particularly for linear accelerator-based SRS. Complications and radiation-induced changes of brain tissue, such as edema and blood-brain barrier breakage, after SRS of arteriovenous malformations correlated with the volume of irradiated tissue that received 12 Gy (39-40). The effect of SRS on peritumoural normal brain region in malignant glioma is not well understood and seldom reported (10). Zawaski et al. showed that radiation caused significant changes in permeability and leukocyte-endothelial interactions in the peritumoural normal brain that were indicative of acute inflammatory reaction and

radiation-induced astrogliosis. Our study provides supporting evidence by showing an increase in blood-brain barrier PS.

A few limitations of this study must be considered. First, a relationship exists between radiation effect and dose (2,4). We chose 12 Gy because this dose can be delivered safely using Helical Tomotherapy, and it is used in the SRS boost of newly diagnosed glioblastoma (31-32) and salvage therapy of recurrent glioblastoma for linear accelerator-based SRS (41). Second, different tumour cell lines display different radiosensitivities (42). Therefore, dose-response of vascular changes measured by CT perfusion in other glioma models could be different. Thirdly, the sample size was relatively small and all untreated rats and most of the non-responders have died after the fourth CT perfusion scan. Thus, we could not compare the imaging data between these groups at later time points. Finally, while we used stereotactic techniques for radiation of the tumours, treatment volumes were still large relative to the size of the rat brain with the irradiated volume encompassing the ipsilateral cerebral hemisphere. Thus, the volume of normal brain irradiated was larger than would be the case in clinical radiosurgery treatments. It is possible that these volume differences have contributed to the perfusion changes seen in the peritumoural region.

4.5   Conclusions

This study showed that CT perfusion is a candidate to be an early biomarker of response to SRS. A CT perfusion imaging study in the clinical setting would potentially allow for timely and accurate assessment of early response to radiosurgery. It could help understand the role of SRS in these patients and also in combination with anti-angiogenic therapies. Evaluation of CT perfusion in prospective clinical studies are necessary to validate this technique as a predictive assay. Validation of the relevant CT perfusion indices used in this study for response assessment is warranted.

4.6   References

1. Wen PY, Kesari S. Malignant gliomas in adults. N Engl J Med. 2008; 359:492-507.

2. Walker MD, Strike TA, Sheline GE. An analysis of dose-effect relationship in the radiotherapy of malignant gliomas. Int J Radiat Oncol Biol Phys. 1979; 5:1725-31.

3. Wen PY, Macdonald DR, Reardon TF, et al. Updated response assessment criteria for high-grade gliomas: Response assessment in neuro-oncology working group. J Clin Oncol. 2010; 28:1963-72.

4. Hong X, Liu L, Wang M, et al. Quantitative multiparametric MRI assessment of glioma response to radiotherapy in a rat model. Neuro Oncol. 2013; In press. doi: 10.1093/neuonc/not245

5. Schuuring J, Bussink J, Bernsen HJ, Peeters W, van Der Kogel AJ. Irradiation combined with SU5416: microvascular changes and growth delay in a human xenograft glioblastoma tumor line. Int J Radiat Oncol Biol Phys. 2005; 61:529-34.

6. Kondziolka D, Somaza S, Comey C, et al. Radiosurgery and fractionated radiation therapy: comparison of different techniques in an in vivo rat glioma model. J Neurosurg. 1996; 84:1033-8.

7. Kondziolka D, Lunsford LD, Claassen D, Pandalai S, Maitz AH, Flickinger JC. Radiobiology of radiosurgery: Part II. The rat C6 glioma model. Neurosurgery. 1992; 31:280-7

8. Park HJ, Griffin RJ, Hui S, Levitt SH, Song CW. Radiation-induced vascular damage in tumors: implications of vascular damage in ablative hypofractionated radiotherapy (SBRT and SRS). Radiat Res. 2012; 177:311-27.

9. Guan LM, Qi XX, Xia B, Li ZH, Zhao Y, Xu K. Early changes measured by CT perfusion imaging in tumor microcirculation following radiosurgery in rat C6 brain gliomas. J Neurosurg. 2011; 114:1672-80.

10. Zawaski JA, Gaber MW, Sabek OM, Wilson CM, Duntsch CD, Merchant TE. Effects of irradiation on brain vasculature using an in situ tumor model. Int J Radiat Oncol Biol Phys. 2012; 82:1075-82.

11. Garcia-Barros M, Paris F, Cordon-Cardo C, et al. Tumor response to radiotherapy regulated by endothelial cell apoptosis. Science. 2003; 300:1155-9.

12. Iuchi T, Hatano K, Kodama T, et al. Phase 2 trial of hypofractionated high-dose intensity modulated radiation therapy with concurrent and adjuvant temozolomide for newly diagnosed glioblastoma. Int J Radiat Oncol Biol Phys. 2014; 88:793-800.

13. Yoon SM, Kim JH, Kim SJ, et al. Hypofractionated intensity-modulated radiotherapy using simultaneous integrated boost technique with concurrent and adjuvant temozolomide for glioblastoma. Tumori. 2013; 99:480-7.

14. Reddy K, Gaspar LE, Kavanagh BD, et al. Prospective evaluation of health-related quality of life in patients with glioblastoma multiforme treated on a phase II trial of hypofractionated IMRT with temozolomide. J Neurooncol. 2013; 114:111-6.

15. Hingorani M, Colley WP, Dixit S, Beavis AM. Hypofractionated radiotherapy for glioblastoma: strategy for poor-risk patients or hope for the future? Br J Radiol. 2012; 85:e770-81.

16. Wang JZ, Li XA. Impact of tumor repopulation on radiotherapy planning. Int J Radiat Oncol Biol Phys. 2005; 61:220-7.

17. Grobben B, De Deyn PP, Slegers H. Rat C6 glioma as experimental model system for the study of glioblastoma growth and invasion. Cell Tissue Res. 2002; 310:257-70.

18. Lee TY, Purdie TG, Stewart E. CT imaging of angiogenesis. Q J Nucl Med. 2003; 47:171-87.

19. Cenic A, Nabavi DG, Craen RA, Gelb AW, Lee TY. A CT method to measure hemodynamics in brain tumors: validation and application of cerebral blood flow maps. AJNR Am J Neuroradiol. 2000; 21:462-70.

20. Paxinos G and Watson C. The rat brain: In stereotaxic coordinates 6th ed. Burlington: Academic Press; 2007.

21. Du LY, Umoh J, Nikolov HN, Pollmann SI, Lee TY, Holdsworth DW. A quality assurance phantom for the performance evaluation of volumetric micro-CT systems. Phys Med Biol. 2007; 52:7087-108.

22. Johnson JA, Wilson TA. A model for capillary exchange. Am J Physiol. 1966; 210:1299-1303.

23. Louis DN, International Agency for Research on Cancer. WHO classification of tumours of the central nervous system. Lyon: International Agency for Research on Cancer. 2007.

24. Burrell JS, Walker-Samuel S, Baker LC, et al. Evaluation of novel combined carbogen USPIO (CUSPIO) imaging biomarkers in assessing the antiangiogenic effects of cediranib (AZD2171) in rat C6 gliomas. Int J Cancer. 2012; 131:1854-62.

25. Gilead A, Meir G, Neeman M. The role of angiogenesis, vascular maturation, regression and stroma infiltration in dormancy and growth of implanted MSL ovarian carcinoma spheroids. Int J Cancer. 2004; 108:524-31.

26. Abramovitch R, Dafni H, Smouha E, Benjamin LE, Neeman M. In vivo prediction of vascular susceptibility to vascular endothelial growth factor withdrawal: Magnetic resonance imaging of C6 rat glioma in nude mice. Cancer Res. 1999; 59:5012-16.

27. Hu LS, Eschbacher JM, Dueck AC, et al. Correlations between perfusion MR imaging cerebral blood volume, microvessel quantification, and clinical outcome using stereotactic analysis in recurrent high-grade glioma. AJNR Am J Neuroradiol. 2012; 33:69-76.

28. Cabrera AR, Cuneo KC, Desjardins A, et al. Concurrent stereotactic radiosurgery and bevacizumab in recurrent malignant gliomas: a prospective trial. Int J Radiat Oncol Biol Phys. 2013; 86:873-9.

29. Levin VA, Bidaut L, Hou P, et al. Randomized double-blind placebo-controlled trial of bevacizumab therapy for radiation necrosis of the central nervous system. Int J Radiat Oncol Biol Phys. 2011; 79:1487-95.

30. Truman JP, García-Barros M, Kaag M, et al. Endothelial membrane remodeling is obligate for anti-angiogenic radiosensitization during tumor radiosurgery. PLoS One. 2010; 5. doi: 10.1371/annotation/6e222ad5-b175-4a00-9d04-4d120568a897.

31. Sarkaria JN, Mehta MP, Loeffler JS, et al. Radiosurgery in the initial management of malignant gliomas: survival comparison with the RTOG recursive partitioning analysis. Radiation Therapy Oncology Group. Int J Radiat Oncol Biol Phys. 1995; 32:931-41.

32. Mehta MP, Masciopinto J, Rozental J, et al. Stereotactic radiosurgery for glioblastoma multiforme: report of a prospective study evaluating prognostic factors and analyzing long-term survival advantage. Int J Radiat Oncol Biol Phys. 1994; 30:541-9.

33. Tsao MN, Mehta MP, Whelan TJ, et al. The American Society for Therapeutic Radiology and Oncology (ASTRO) evidence-based review of the role of radiosurgery for malignant glioma. Int J Radiat Oncol Bio Phys 2005; 63:47-55.

34. Souhami L, Seiferheld W, Brachman D, et al. Randomized comparison of stereotactic radiosurgery followed by conventional radiotherapy with carmustine to conventional radiotherapy with carmustine for patients with glioblastoma multiforme: report of Radiation Therapy Oncology Group 93-05 protocol. Int J Radiat Oncol Biol Phys. 2004; 60:853-60.

35. Mangla R, Singh G, Ziegelitz D, et al. Changes in relative cerebral blood volume 1 month after radiation-temozolomide therapy can help predict overall survival in patients with glioblastoma. Radiology 2010; 256: 575–84.

36. Gahramanov S, Muldoon LL, Varallyay CG, et al. Pseudoprogression of glioblastoma after chemo- and radiation therapy: Diagnosis by using dynamic susceptibility-weighted contrast-enhanced perfusion MR imaging with ferumoxytol versus gadoteridol and correlation with survival. Radiology 2013; 266: 842–52.

37. Grabham P, Hu B, Sharma P, Geard C. Effects of ionizing radiation on three-dimensional human vessel models: differential effects according to radiation quality and cellular development. Radiat Res. 2011; 175:21-8.

38. Sabatasso S, Laissue JA, Hlushchuk R, et al. Microbeam radiation-induced tissue damage depends on the stage of vascular maturation. Int J Radiat Oncol Biol Phys. 2011; 80:1522-32.

39. Levegrün S, Hof H, Essig M, Schlegel W, Debus J. Radiation-induced changes of brain tissue after radiosurgery in patients with arteriovenous malformations: correlation with dose distribution parameters. Int J Radiat Oncol Biol Phys. 2004; 59:796-808.

40. Flickinger JC, Kondziolka D, Lunsford LD, et al. Development of a model to predict permanent symptomatic postradiosurgery injury for arteriovenous malformation patients. Arteriovenous Malformation Radiosurgery Study Group. Int J Radiat Oncol Biol Phys. 2000; 46:1143-8.

41. Romanelli P, Conti A, Pontoriero A, et al. Role of stereotactic radiosurgery and fractionated stereotactic radiotherapy for the treatment of recurrent glioblastoma multiforme. Neurosurg Focus. 2009; 27:E8

42. Wang J, Hu L, Gupta N, et al. Induction and characterization of human glioma clones with different radiosensitivities. Neoplasia. 1999; 1:138-44.

Chapter 5

5 Relationship of Computed Tomography Perfusion and Positron Emission Tomography to Tumour Progression in Malignant Glioma

This chapter is adapted from the research article, "Relationship of computed tomography perfusion and positron emission tomography to tumour progression in malignant glioma" published in *Journal of Medical Radiation Sciences*, 2014;61(1):4-13 by Yeung TPC, Yartsev S, Lee T-Y, Wong E, He W, Fisher B, VanderSpek LL, Macdonald D, Bauman G.

5.1 Introduction

In malignant glioma, over 80% of tumour progression occurs within 2 cm of the original tumour site after radiotherapy and concurrent and adjuvant temozolomide chemotherapy (1). Radiological assessment of tumour progression is primarily based on gadolinium-enhanced magnetic resonance (MR) or iodinated contrast-enhanced computed tomography (CT) (2). An increase in the size of the contrast-enhancing lesion is one of the criteria for diagnosing progression (2). However, early changes in contrast enhancement after treatment lack utility in identifying active tumour sites that are likely to persist after treatment.

Functional imaging is gaining popularity as it has demonstrated utility in differentiating tumour grade, predicting treatment response and survival and in identifying active tumour after treatment prior to progression (3). Pre-treatment functional imaging measurements of tumour perfusion and metabolism have been shown to predict survival in newly diagnosed and recurrent malignant glioma (4-7). Similarly, changes in blood flow (BF) and blood volume (BV) during radiotherapy have been shown to be predictive of survival (8,9). The use of multiparametric imaging data may have an added value for predicting survival. For example, tumour metabolism and BF were combined into a metric called the metabolism-flow ratio, and this was found to be

predictive of poor survival in pancreatic cancer (10). Metabolism and BF are usually tightly coupled in normal tissue; however, an increase in metabolism in the presence of low BF may be indicative of a tumour's adaptation to hypoxia (11). This suggests that the metabolism-flow ratio may be a valuable biomarker of hypoxia, which is associated with treatment resistance.

CT perfusion can simultaneously measure BF, BV and permeability-surface area product (PS) in brain tumours (12), and 18-Fluorodeoxyglucose positron emission tomography (FDG-PET) is in routine clinical use for measuring tumour metabolism. The combination of FDG-PET and CT perfusion using a hybrid PET/CT scanner is a practical technique for assessing metabolism and perfusion in quick succession. This can also be used to calculate the metabolism-flow ratio, which circumvents the need for specialized synthesis capabilities to produce hypoxia tracers such as 18-Fluoro-azomycin arabinoside.

No functional imaging studies have been reported near the completion of radiotherapy as an attempt to detect residual malignant gliomas. This study investigated the associations between the pre-radiotherapy gross tumour as defined on contrast-enhanced MR, near-end-of-radiotherapy enhancing lesion as defined on contrast-enhanced CT, near-end-of-radiotherapy CT perfusion and FDG-PET parameters with post-treatment MR-defined tumour progression. We then assessed the value of using these imaging parameters for predicting post-treatment MR-defined tumour progression. Therefore, the goal of this study was to assess whether functional imaging has the potential in predicting sites of future progressive tumour on a voxel-by-voxel basis after radiotherapy and chemotherapy. This can help identify biologically significant volumes of disease present at the end of conventional radiotherapy that could serve as a target for treatment intensification.

5.2   Methods

5.2.1   Patients

All study procedures were approved by Institutional Research Ethics Board. Patients with newly diagnosed malignant glioma were prospectively recruited to the study with informed consent prior to the last week of radiotherapy. The inclusion criteria were: (1) at least 18 years of age, (2) histologically confirmed malignant glioma, (3) Karnofsky Performance Status ≥60, (4) no previous cranial radiotherapy and (5) pre-radiotherapy MR were performed within 12 weeks of radiotherapy treatment planning. Recurrent gliomas, multiple intracranial lesions, or patients that were not suitable for radical radiotherapy (40–60 Gy in 15–30 fractions) were excluded.

5.2.2   Multi-modality Imaging Schedule

After surgery but before radiotherapy, each patient underwent a standard MR imaging comprised of at least one series of T1- and T2-weighted images using a 1.5 T MR scanner (Signa Excite, General Electric Medical Systems, Milwaukee, WI). This MR scan was performed within 12 weeks of the treatment planning CT. Contrast-enhanced T1-weighted images were acquired using a fast spoiled gradient echo sequence (repetition time = 10 msec, echo time = 4 msec and flip angle = 15°) after an intravenous injection of gadopentetate dimeglumine (0.2 mL/kg; Magnevist; Berlex Laboratories, Wayne, NJ).

A FDG-PET and CT perfusion scan was performed during the final week of radiotherapy using a hybrid PET/CT scanner (Discovery VCT, General Electric Healthcare, Waukesha, WI). After an intravenous injection of FDG (385 MBq), positron emission data were collected in list mode for 60 min and binned into 5 min frames in the last 40 min. Each PET data set consisted of 47 axial PET images with a 3.26 mm slice thickness and a 26 cm axial field of view (FOV).

The FDG-PET CT attenuation correction maps in the FDG-PET study were used to select eight 5 mm sections to maximally cover the tumour for a 150 sec two-phase CT perfusion scan. A non-ionic contrast bolus (Omnipaque, General Electric Healthcare,

Princeton, NJ, 300 mg iodine per mL, 0.8 mL/kg of body weight) was injected at a rate of 2–4 mL/sec at 3–5 sec before the start of the scan. While the selected brain sections were scanned continuously for 45 sec and the images reconstructed at 1-sec intervals during the first phase, the same sections were scanned once every 15 sec for seven times during the second phase. The scanning parameters for both phases were 80 kVp, 190 mA, 1 sec per rotation and a 25-cm FOV.

Post-radiotherapy follow-ups were both clinical and radiological. Routine MR images were obtained at 4–6 weeks post-radiotherapy and every 3 months thereafter, and were reviewed by a neuro-oncologist or radiation oncologist. Tumour progression was defined as a continual enlargement of new enhancing lesion (without subsequent resolution) on serial MR imaging along with deterioration of clinical signs and symptoms (2).

5.2.3   Image Processing

CT perfusion images were analyzed using the prototype version of CT Perfusion 4D (Advantage Windows, GE Healthcare, Waukesha, WI). Arterial and venous time-attenuation curves were measured from an anterior cerebral artery and the posterior superior sagittal sinus respectively. BF, BV and PS maps were calculated by deconvolving the arterial time-attenuation curve with the tissue time-attenuation curve from 2×2 voxel blocks of CT images (12). The CT images were averaged together to produce average CT images, which have better grey and white matter contrast than conventional contrast-enhanced CT images.

Software provided with the PET/CT scanner was used to correct the PET emission data for random and scatter coincidences, dead time and attenuation. PET images from the last 5 min bin were rigidly co-registered with the average CT using the 3D Slicer software (13). The registered PET voxel values were converted to standard uptake values (SUV) corrected for body surface area (14). SUV maps were divided by the BF maps to generate SUV:BF ratio maps.

Gadolinium-enhanced T1-weighted MR images from pre-radiotherapy and at progression were rigidly co-registered with the near-end-of-radiotherapy average CT. All images (MR and average CT) and functional maps (CT perfusion and PET SUV) were then resampled to 170×170 voxels to minimize registration error. From here on, the contrast-enhancing lesion in the pre-radiotherapy T1-weighted MR lesion is the gross tumour, the contrast-enhancing lesion on the average CT acquired at the last week of radiotherapy is the near-end-of-radiotherapy enhancing lesion, and the contrast-enhancing lesion on follow-up T1-weighted MR at the time of progression is the progressive tumour. Contours around the pre-radiotherapy gross tumour, near-end-of-radiotherapy enhancing lesion and progressive tumour were delineated by a radiation oncologist (G.B.). Table 5-1 summarizes the labelling and time of acquisition of the images.

Table 5-1: Summary of images acquired in this study.

Name	Type of Image(s)	Image signal	Time of acquisition
Gross tumour volume	T1-weighted MR	Gadolinium enhancement	Post-surgery/biopsy and pre-radiotherapy (must be within 12 weeks of treatment planning CT)
Near-end-of-radiotherapy enhancing lesion	Averaged CT	Iodine enhancement (HU)	Last week of radiotherapy
BF	BF map	mL/min/100g	Last week of radiotherapy
BV	BV map	mL/100g	Last week of radiotherapy
PS	PS map	mL/min/100g	Last week of radiotherapy
PET	SUV map	FDG uptake	Last week of radiotherapy
Progressive tumour	T1-weighted MR	Gadolinium enhancement	Time of progression based on routine clinical and radiological follow-up assessments (4 – 6 weeks post-radiotherapy and every 3 months after)

Abbreviations: MR, magnetic resonance; CT, computed tomography; BF, blood flow; BV, blood volume; PS, permeability-surface area product; PET, positron emission tomography; SUV, standard uptake value; FDG, 18-Fluorodeoxyglucose.

5.2.4   Logistic Regression

A custom MATLAB (MathWorks Incorporated, Natick, MA) program was developed for this analysis. A 2-cm bounding box around the union of the pre-radiotherapy gross tumour and the progressive tumour was created to reduce the amount of information for analysis for each patient. Major blood vessels, surgical cavities, ventricles and voxels outside the bounding box were excluded. Each voxel inside the bounding box was assigned three binary statuses: pre-radiotherapy gross tumour (yes/no), near-end-of-radiotherapy enhancing lesion (yes/no) and progressive tumour (yes/no). Logistic regression was used to assess the association between tumour progression and the following sets of independent imaging variables: (1) pre-radiotherapy gross tumour, (2) near-end-of-radiotherapy enhancing lesion, (3) BF, BV, PS and SUV and (4) BV, PS, SUV:BF (15). The last regression was used to investigate the association between tumour progression and SUV:BF as a marker of hypoxia. The strength of association between each parameter and progressive tumour status was evaluated by the odds ratio. Odds ratios were converted to probabilities of recurrence for easier interpretations.

5.2.5   Cross-validation

Leave-one-out cross-validation was used to assess the value of using different imaging parameters to predict tumour progression (16). Each round of cross-validation used one patient data set as the validation set and the data sets from the other patients as the training set. Probability maps of progression for an individual patient (i.e. the validation set) were calculated using the logistic regression equation from the training set. We first considered seven single variable models: (1) Pre-radiotherapy gross tumour, (2) Near-end-of-radiotherapy enhancing lesion, (3) BF, (4) BV, (5) PS, (6) SUV and (7) SUV:BF. We then considered two multivariate models: (1) BV, PS, SUV:BF and (2) BF, BV, PS and SUV. Using receiver operating characteristic (ROC) analysis, the area under the ROC (AUC) curve was calculated. The optimal sensitivity and specificity was calculated using the Youden Index, which is the probability threshold that maximizes the sum of sensitivity and specificity for all possible probabilities from 0% to 100% (16).

5.2.6   Statistical Analysis

Pre-radiotherapy gross tumour, near-end-of-radiotherapy enhancing lesion and progressive tumour volumes within the 4 cm CT perfusion scan length were compared using the Wilcoxon signed-rank test. AUCs of the different logistic models were compared using the Friedman test followed by the Wilcoxon signed-rank test. Models with AUCs that are significantly higher than the AUCs of the pre-radiotherapy gross tumour and end-of radiotherapy enhancing lesion were reported. All statistical tests were done using SPSS version 19.0 (SPSS Incorporated, Chicago, IL), and P-values <0.05 were considered significant.

5.3   Results

Ten patients with newly diagnosed malignant glioma were prospectively recruited to the study between the years 2008 and 2011. After surgery, all patients underwent radiotherapy (60 Gy in 30 fractions) with concurrent and adjuvant temozolomide chemotherapy. Patient characteristics are listed in Table 5-2. Tumour progression with no evidence of necrosis was histopathologically confirmed in two patients (Patient 9 and 10 in Table 5-2); the remaining patients had tumour progression defined on clinical and imaging grounds only.

Table 5-2: Patient Characteristics.

Patient No.	Age	WHO Grade	Tumour Location	Type of Resection	Months Between RT and Appearance of Progressive Tumours	Site of Tumour Progression	Treatment	Steroid Use	Survival Status
1	36	3	Left Frontal Temporal	Partial	8.6	[a]In-field	RT, TMZ	Yes	Deceased
2	47	4	Left Parietal	Partial	12.0	In-field	RT, TMZ	Yes	Deceased
3	55	4	Left temporal	Partial	2.3	In-field	RT, TMZ	Yes	Deceased
4	37	3	Left frontal temporal	Partial	8.4	In-field and [b]out-of-field	RT, TMZ	No	Deceased
5	50	4	Left Frontal lobe	Partial	5.0	In-field	RT, TMZ	Yes	Deceased
6	71	4	Right temporal parietal	Biopsy	2.1	In-field	RT, TMZ	Yes	Deceased
7	71	4	Left frontal	Biopsy	4.3	In-field	RT, TMZ	Yes	Deceased
8	61	4	Left posterior frontal parietal inter-axial tumour	Partial	14.8	In-field	RT, TMZ	Yes	Deceased
9	60	4	Left Frontal Parietal	Partial	11.0	In-field	RT, TMZ	Yes	Alive
10	54	4	Left Temporal	Partial	15.6	In-field	RT, TMZ	Yes	Alive

Abbreviations: WHO, World Health organization; RT, radiation therapy; TMZ, concurrent + adjuvant temozolomide
[a]In-field = within 2 cm of the primary contrast-enhancing tumour; [b]Out-of-field = beyond 2 cm of the primary contrast-enhancing tumour

The mean volumes ± standard deviation (SD) of pre-radiotherapy gross tumour, near-end-of-radiotherapy enhancing lesion and the progressive tumour within the CT perfusion scan volume were 10.8 ± 11.1, 14.1 ± 20.8 and 16.1 ± 18.0 cm^3 respectively. The differences in volumes were not significant ($P > 0.05$). Figure 5-1 displays the images of patient 3.
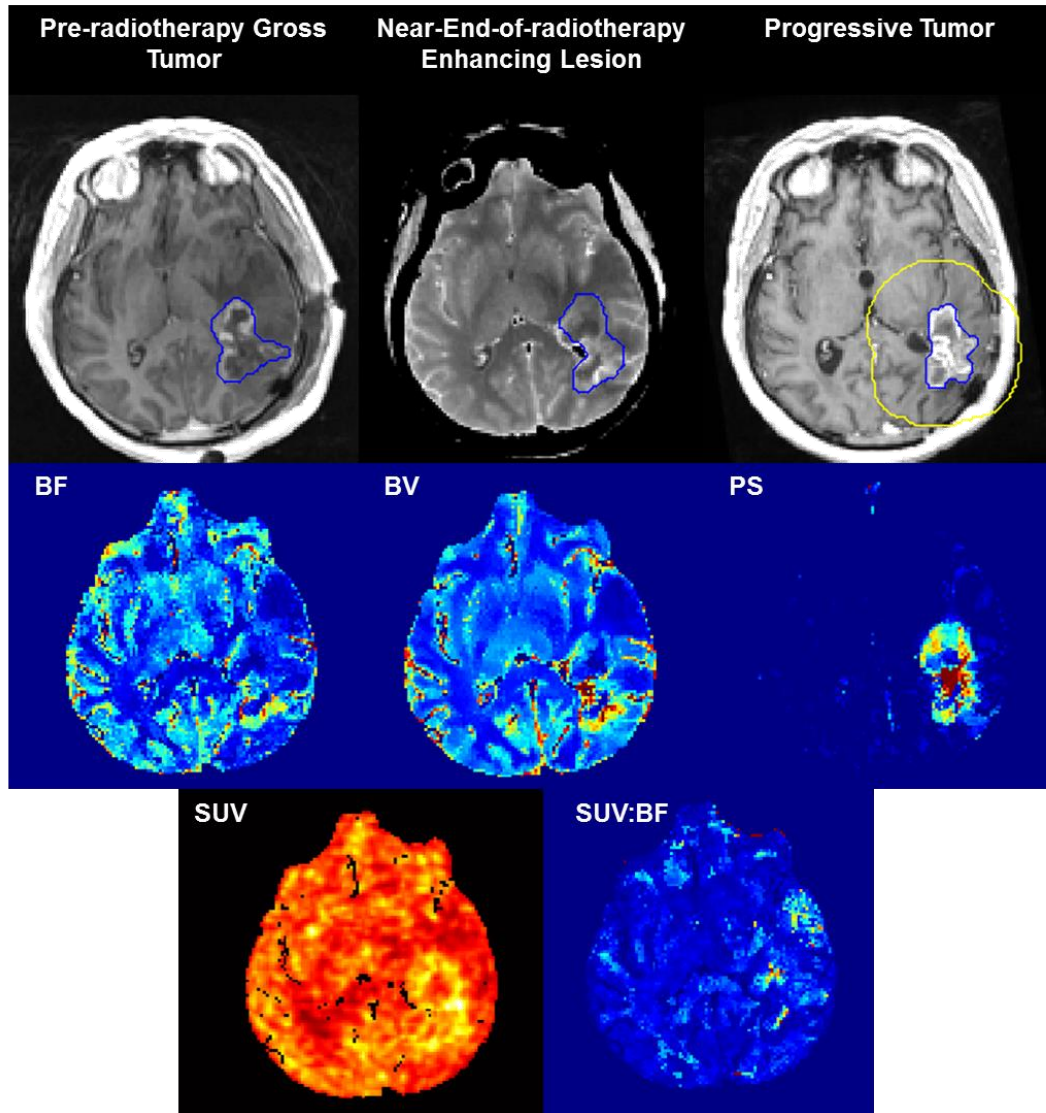
Figure 5-1: Pre-radiotherapy gross tumour (T1-weighted MR), near-end-of-radiotherapy enhancing lesion (averaged CT) and progressive tumour (T1-weighted MR); and the corresponding parametric maps of blood flow (BF), blood volume (BV), permeability-surface area (PS) product, standard uptake value (SUV) and

SUV:BF acquired using CT perfusion and FDG-PET. Blue outlines show the contrast-enhancing lesions delineated by a radiation oncologist. Yellow outline is the 2-cm bounding box that was set for performing logistic regression. MR, magnetic resonance; CT, computed tomography; FDG-PET, 18-Fluorodeoxyglucose positron emission tomography.

5.3.1 Multivariate Logistic Regression

When compared with normal brain tissue, the pre-radiotherapy gross tumour and the near-end-of-radiotherapy enhancing lesion had odds ratios of 12.7 (95% confidence interval [CI], 12.1–13.4) and 43.3 (95% CI, 41.4–45.3), respectively, for tumour recurrence. These odds can be expressed as recurrence probabilities of 54.4% and 69.8% respectively. Multivariate logistic regression showed that the odds of tumour progression increased with lower BF, BV and SUV; and with higher PS and SUV:BF ($P < 0.0001$) (Table 5-3).

Table 5-3: Multivariate logistic regression.

Model	Parameter	P	[a]Regression Coefficients (β)	Odds Ratio (e^β)	95% Confidence Interval +95%	-95%	Probability (%)
1	BV	<0.0001	-0.15	0.86	0.84	0.87	7.1
	PS	<0.0001	0.41	1.51	1.49	1.52	11.9
	SUV:BF	<0.0001	2.63[b]	13.88	11.38	16.94	55.4
	Constant	<0.0001	-2.41	0.09	0.09	0.09	8.2
2	BF	<0.0001	-0.01	0.99	0.99	0.99	23.1
	BV	<0.0001	-0.07	0.93	0.91	0.95	22.1
	PS	<0.0001	0.39	1.48	1.47	1.50	31.0
	SUV	<0.0001	-0.93	0.39	0.37	0.41	10.7
	Constant	<0.0001	-1.19	0.30	0.29	0.32	23.3

Abbreviations: BV, blood volume; PS, permeability-surface area product; SUV, standard uptake value; BF, blood flow.

[a]Degrees of freedom = 128,330
[b]An increase in SUV:BF value by 0.01 was associated with an odds ratio = 1.03; this corresponded to a probability of 8.4%.

5.3.2 Cross-validation

The AUCs for the three models (1) PS alone, (2) BV, PS, SUV:BF and (3) BF, BV, PS and SUV were 0.72 ± 0.12, 0.74 ± 0.13 and 0.77 ± 0.11 respectively. These AUCs were significantly higher than the AUCs of the pre-radiotherapy gross tumour and near-end-of-radiotherapy enhancing lesion (Friedman $P < 0.001$; Wilcoxon signed-rank $P \leq 0.03$), which were 0.64 ± 0.14 and 0.65 ± 0.14 respectively. Although the AUCs of the two multivariate models were higher than that of PS, the differences were not statistically significant ($P > 0.05$). Table 5-4 shows model pairs that are significantly higher than the pre-radiotherapy gross tumour and the end-of-radiotherapy enhancing lesion. The model using PS alone had a sensitivity and specificity of 0.6 ± 0.1 and 0.7 ± 0.1, respectively (Figure 5-2). The model using BF, BV, PS and SUV had the highest combination of sensitivity and specificity (0.7 ± 0.1 and 0.7 ± 0.1). Probability maps of progression were generated using these logistic models, examples of probability maps for patient 3 are shown in Figure 5-3.

Table 5-4: Statistical differences in area under the receiver operating characteristics curve.

Model 1	Model 2	% Difference = (Model 2 − Model 1)/(Model 1)×100	± SD	p
Pre-radiotherapy gross tumour	PS	14.2	18.1	0.03
	BV, PS, SUV:BF	16.4	18.6	0.03
	BF, BV, PS, SUV	21.4	18.6	< 0.01
End-of-radiotherapy enhancing lesion	PS	12.7	10.7	0.02
	BV, PS, SUV:BF	15.4	16.7	0.03
	BF, BV, PS, SUV	21.1	20.4	0.02
PS	BV, PS, SUV:BF	2.1	7.2	0.29
	BF, BV, PS, SUV	7.5	15.9	0.29
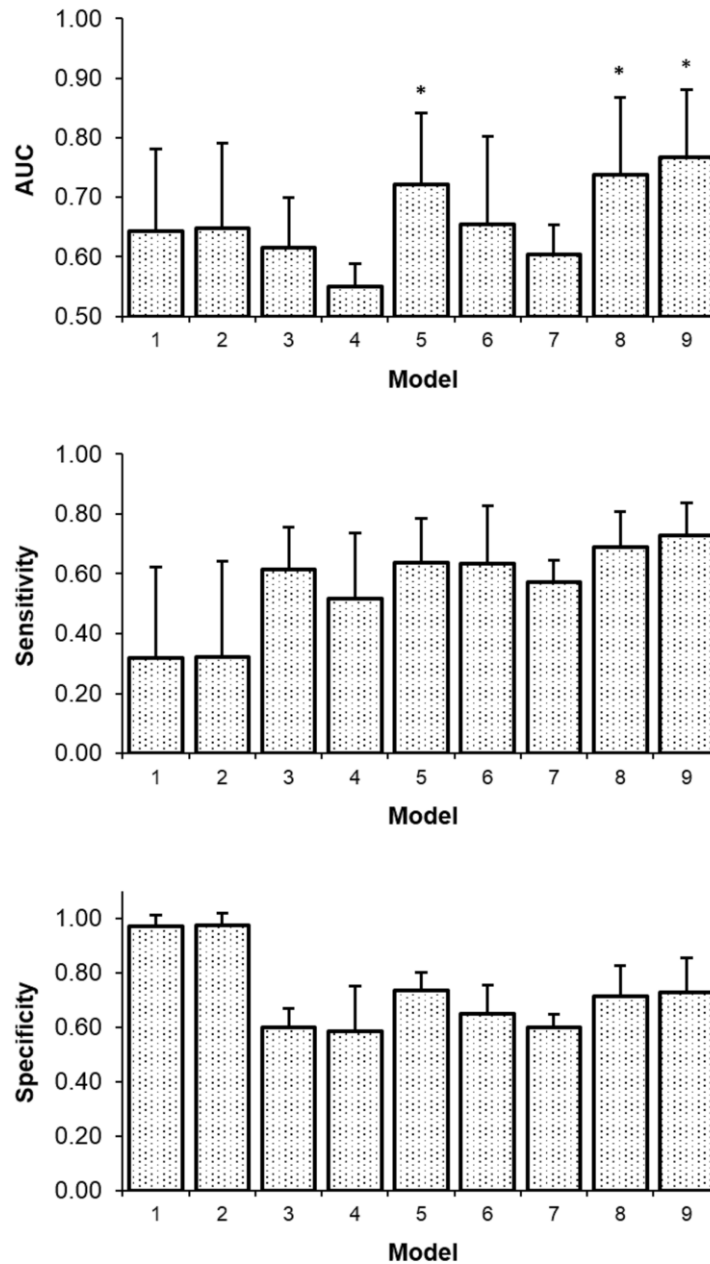
Figure 5-2: Area under the operating characteristic curve (AUC) (top), sensitivities (middle) and specificities (bottom) for the selected logistic regression models. Models with an AUC that is significantly higher than the pre-radiotherapy gross tumour and the end-of-radiotherapy enhancing lesion are indicated with an asterisk (*). 1, Pre-radiotherapy gross tumour; 2, End-of-radiotherapy enhancing lesion; 3, BF; 4, BV; 5, PS; 6, SUV; 7, SUV:BF; 8, BF, PS, SUV:BF; 9, BF, BV, PS, SUV.
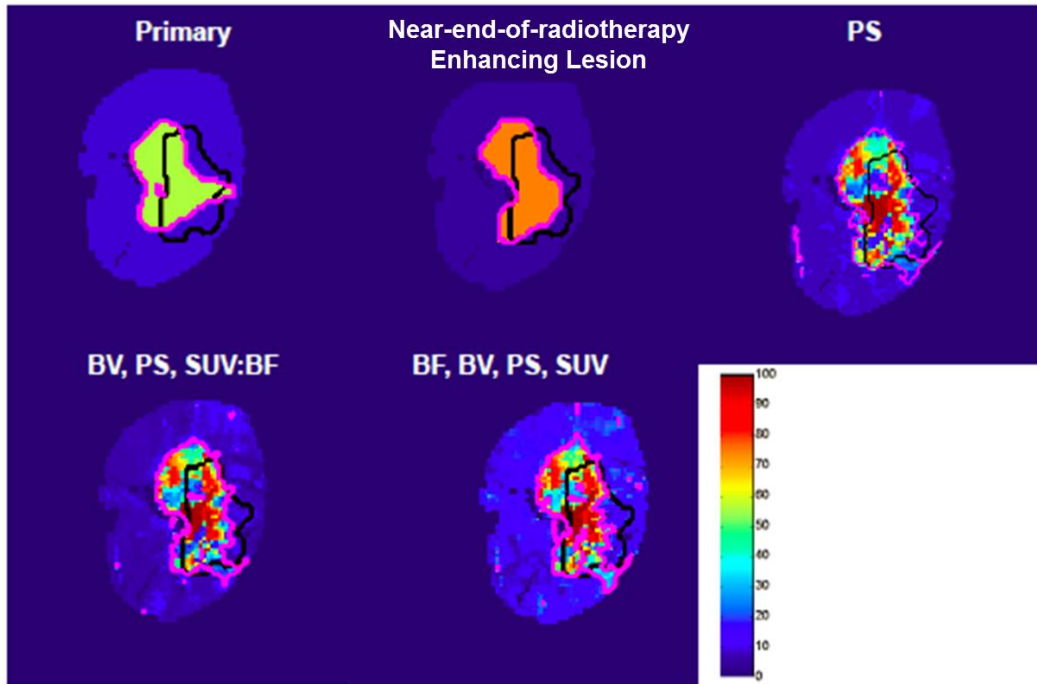
Figure 5-3: Probability of tumour progression (patient 3) within the 2-cm bounding box generated using the different logistic regression models. Black line outlines the boundary of the progressive tumour. Based on cross-validation, the magenta line delineates the region with the probability threshold that maximizes the sum of sensitivity and specificity in predicting progression.

5.4 Discussion

We investigated whether near-end-of-radiotherapy CT perfusion and FDG-PET can add value to the assessment of malignant glioma in terms of predicting voxels that are likely to progress after treatment. PS alone was found to be the best predictor of tumour progression when compared to other CT perfusion and FDG-PET parameters; however, voxel-based prediction of progression had only modest sensitivity and specificity.

PS describes the unidirectional flow of contrast as it leaks from the intravascular space into the interstitial space (i.e. brain parenchyma) (12). It is not the same as contrast

enhancement because it quantitatively measures the rate of contrast extravasation. In this study, not only did PS show a significant association with progressive tumour but it had a higher AUC than the pre-radiotherapy gross tumour and near-end-of-radiotherapy enhancing lesion for identifying tumour voxels that are more likely to progress. This suggests that PS adds value to contrast enhancement in determining active tumour regions after treatment, and also provides corroborating evidence to support that PS is associated with tumour aggressiveness. PS can be a potential biomarker of tumour aggressiveness because of the underlying pathological aspect that it represents. PS has larger value in high-grade gliomas compared to low-grade gliomas (17), which is important for prognosis. It also showed correlations with aggressive phenotypes including microvascular cellular proliferation (18) and the expression of pro-angiogenic genes (19). Finally, PS has been used to distinguish true tumour progression from treatment effect like treatment-induced necrosis (20).

The observation that both lower BF and BV showed significant associations with tumour progression is noteworthy. A lower BF and BV may suggest resistance to therapy due to the presence of hypoxia. In support of this, dynamic susceptibility contrast MR studies at pre- and mid-radiotherapy showed that a drop in relative BF and BV were predictors of poor survival (8,9). However, the associations observed in this study were obtained from one time point only, and they do not suggest a causal relationship with progression.

We found that a lower SUV, when considering the entire tumour, is associated with an increased risk of progression. This is contrary to studies that showed an increased FDG uptake is associated with poor survival in patients at various stages of treatment (21) or in patients with recurrent tumours (7,22). In these prior studies, FDG uptake in the hypermetabolic region was used to assess correlation with survival. This usually coincides with the contrast-enhancing region of the tumour where the perfusion is high; hence, an FDG delivery was unimpeded. Our results suggest that when considering the tumour as a whole, a lower FDG uptake is associated with higher odds of progression. A low FDG uptake does not necessarily infer a lack of metabolic demand. We instead showed a higher SUV:BF ratio was associated with an increased risk of recurrence,

which suggests that a low SUV was due to poor delivery resulting in uncoupling between metabolism and perfusion. This is consistent with PET-based measure of SUV:BF in pancreatic cancer in which a higher SUV:BF was associated with poor survival (10). These observations provide evidence to support the Warburg Effect hypothesis (10,11). Cancer cells can maintain anaerobic respiration to keep up with its metabolic demand under hypoxic stress and can be therapeutically resistant. This could lead to tumour regions that remain active despite treatment.

Some limitations of this study must be considered. Although the AUCs of the multivariate models were higher than those of the univariate PS model, we were unable to demonstrate the statistical significance of multivariate models superiority. A larger sample size is required to determine whether (1) BF, BV, PS and SUV and (2) BV, PS and SUV:BF can provide more information than PS alone for identifying tumour regions that are likely to progress. Other radiotracers with a higher tumour-to-background ratio in the brain can improve the detection of residual tumour at the end of radiotherapy. For example, both 3′-Deoxy-3′-18F-fluorothymidine (FLT) (23) and 11C-methionine PET (24) were reported to be more sensitive than FDG in evaluating progressive tumours. Deformable registration could potentially improve the quality of registration. Most deformation of the tumour would occur from before and after surgery. This study used only post-surgery images; thus, physical deformation of the tumour is minimal. In addition, the majority of patients received dexamethasone during radiotherapy, which could decrease tumour permeability resulting in less edema and hence less deformation (25). The use of dexamethasone can also decrease cerebral glucose metabolism (26,27). The effect of dexamethasone on glucose metabolism is global rather than localized; it is unlikely to affect the current results because the logistic regression is based on imaging data obtained from both the normal brain and tumour tissues. Finally, we focused our investigation on the tumour site and its immediate surroundings, the potential effects of radiation on normal brain tissue perfusion and metabolism were not investigated in detail. A small radiation dose-dependent relationship (<10%) was observed for both brain tissue metabolism and perfusion (28). We evaluated the relationship between normal brain tissue BF, BV and PS with radiation dose in seven patients and did not find a significant

relationship (data not shown). Thus, the effect of radiation on normal tissue BF, BV and PS is unlikely to affect the current results.

5.5 Conclusions

We developed a technique for voxel-wise analysis of CT perfusion and FDG-PET images acquired at the end of radiotherapy for patients treated for malignant glioma. On the basis of our analysis, near-end-of-radiotherapy PS was the best predictor of tumour progression on a voxel-by-voxel basis when compared to other CT perfusion and FDG-PET parameters. However, voxel-based analysis had only modest sensitivity and specificity. Exploration of these findings among a larger patient cohort would help confirm the value of PS imaging in predicting recurrence and in confirming the trend towards improved prediction with multivariate imaging data.

5.6 References

1. Milano MT, Okunieff P, Donatello RS, et al. Patterns and timing of recurrence after temozolomide-based chemoradiation for glioblastoma. Int J Radiat Oncol Biol Phys. 2010; 78:1147–55.
2. Wen PY, Macdonald DR, Reardon DA, et al. Updated response assessment criteria for high-grade gliomas: Response assessment in neuro-oncology working group. J Clin Oncol. 2010; 28:1963–72.
3. Peet AC, Arvanitis TN, Leach MO, Waldman AD. Functional imaging in adult and paediatric brain tumours. Nat Rev Clin Oncol. 2012; 9:700–11.
4. Hirai T, Murakami R, Nakamura H, et al. Prognostic value of perfusion MR imaging of high-grade astrocytomas: Long-term follow-up study. AJNR Am J Neuroradiol. 2008; 29:1505–10.
5. Bisdas S, Kirkpatrick M, Giglio P, Welsh C, Spampinato MV, Rumboldt Z. Cerebral blood volume measurements by perfusion-weighted MR imaging in gliomas: Ready for prime time in predicting short-term outcome and recurrent disease? AJNR Am J Neuroradiol. 2009; 30:681–8.

6. Colavolpe C, Metellus P, Mancini J, et al. Independent prognostic value of pre-treatment 18-FDG-PET in high grade gliomas. J Neurooncol. 2012; 107:527–35.

7. Colavolpe C, Chinot O, Metellus P, et al. FDG-PET predicts survival in recurrent high-grade gliomas treated with bevacizumab and irinotecan. Neuro Oncol. 2012; 14:649–57.

8. Galbán CJ, Chenevert TL, Meyer CR, et al. Prospective analysis of parametric response map-derived MRI biomarkers: Identification of early and distinct glioma response patterns not predicted by standard radiographic assessment. Clin Cancer Res. 2011; 17:4751–60.

9. Galbán CJ, Chenevert TL, Meyer CR, et al. The parametric response map is an imaging biomarker for early cancer treatment outcome. Nat Med 2009; 15:572–6.

10. Komar G, Kauhanen S, Liukko K, et al. Decreased blood flow with increased metabolic activity: A novel sign of pancreatic tumour aggressiveness. Clin Cancer Res. 2009; 15:5511–7.

11. Miles KA, Williams RE. Warburg revisited: Imaging tumour blood flow and metabolism. Cancer Imaging. 2008; 8:81–6.

12. Lee TY, Purdie TG, Stewart E. CT imaging of angiogenesis. Q J Nucl Med. 2003; 47:171–87.

13. Pieper S, Lorensen B, Schroeder W, Kikinis R. The NA-MIC Kit: ITK, VTK, pipelines, grids and 3D slicer as an open platform for the medical image computing community. Proc 3rd IEEE Int Symp Biomed Imaging: From Nano Macro. 2006; 1:698–701.

14. Graham MM, Peterson LM, Hayward RM. Comparison of simplified quantitative analyses of FDG uptake. Nucl Med Biol. 2000;27:647–55.

15. Bewick V, Cheek L, Ball J. Statistics review 14: Logistic regression. Crit Care. 2005; 9:112–8.

16. Bewick V, Cheek L, Ball J. Statistics review 13: Receiver operating characteristic curves. Crit Care 2004; 8:508–12.

17. Jain R, Ellika SK, Scarpace L, et al. Quantitative estimation of permeability surface-area product in astroglial brain tumours using perfusion CT and correlation with histopathologic grade.AJNR Am J Neuroradiol. 2008; 29: 694–700.

18. Jain R, Gutierrez J, Narang J, et al. In vivo correlation of tumour blood volume and permeability with histologic and molecular angiogenic markers in gliomas. AJNR Am J Neuroradiol. 2011; 32:388–94.

19. Jain R, Poisson L, Narang J, et al. Correlation of perfusion parameters with genes related to angiogenesis regulation in glioblastoma: A feasibility study. AJNR Am J Neuroradiol. 2012; 33: 1343–8.

20. Jain R, Narang J, Schultz L, et al. Permeability estimates in histopathology-proved treatment-induced necrosis using perfusion CT: Can these add to other perfusion parameters in differentiating from recurrent/progressive tumours? AJNR Am J Neuroradiol. 2011; 32: 658–63.

21. Padma MV, Said S, Jacobs M, et al. Prediction of pathology and survival by FDG PET in gliomas. J Neurooncol. 2003; 64: 227–37.

22. Santra A, Kumar R, Sharma P, Bal C, Julka PK, Malhotra A. F-18 FDG PET-CT for predicting survival in patients with recurrent glioma: A prospective study. Neuroradiology. 2011; 53: 1017–24.

23. Chen W, Cloughesy T, Kamdar N, et al. Imaging proliferation in brain tumors with 18F-FLT PET: Comparison with 18F-FDG. J Nucl Med. 2005; 46: 945–52.

24. Tripathi M, Sharma R, Varshney R, et al. Comparison of F-18 FDG and C-11 methionine PET/CT for the evaluation of recurrent primary brain tumors. Clin Nucl Med. 2012; 37: 158–63.

25. Yeung WT, Lee TY, Del Maestro RF, Kozak R, Bennett J, Brown T. Effect of steroids on iopamidol blood-brain transfer constant and plasma volume in brain tumors measured with X-ray computed tomography. J Neurooncol. 1994; 18: 53–60.

26. Fulham MJ, Brunetti A, Aloj L, Raman R, Dwyer AJ, Di Chiro G. Decreased cerebral glucose metabolism in patients with brain tumors: An effect of corticosteroids. J Neurosurg. 1995; 83: 657–64.

27. Brock CS, Meikle SR, Price P. Does fluorine-18 fluorodeoxyglucose metabolic imaging of tumours benefit oncology? Eur J Nucl Med 1997; 24: 691–705.

28. Hahn CA, Zhou SM, Raynor R, et al. Dose-dependent effects of radiation therapy on cerebral blood flow, metabolism, and neurocognitive dysfunction. Int J Radiat Oncol Biol Phys 2009; 73: 1082–7.

Chapter 6

6 Treatment monitoring in high-grade gliomas: A serial CT perfusion and MR study

This chapter is adapted from the manuscript entitled "Treatment monitoring in high-grade gliomas: A serial CT perfusion and MR study". This manuscript will be submitted to the *Journal of Neuro-Oncology* in July 2014 to be considered for publication. The authors of this manuscript are Yeung TPC, Wang Y, Urbini B, Yartsev S, Bauman G, Lee TY, Fainardi E, and the Project of Emilia-Romagna region on Neuro-Oncology (PERNO) Study Group. Member of the PERNO Study Group is provided in Appendix E.

6.1 Introduction

High-grade gliomas account for over 70% of all malignant brain tumours, and survival rates remain dismal even after maximal safe resection, radiotherapy, and temozolomide chemotherapy. The typical median survival for patients with World Health Organization (WHO) grade IV gliomas is typically $12 - 15$ months, and it is $2 - 5$ years for those with WHO grade III gliomas (1). However, there is considerable heterogeneity in patients' treatment response. At present, widely accepted prognostic factors of survival in high-grade gliomas are WHO grade, extent of surgical resection, age, and performance status (2). Molecular biomarkers, such as isocitrate dehydrogenase 1 (IDH1) methylation status, O6-methylguanine-DNA-methyltransferase (MGMT) methylation status and 1p19q loss of heterozygosity, are also recognized as predictive and prognostic biomarkers in these patients (3).

High-grade gliomas, particularly WHO grade IV gliomas, are highly infiltrative tumours with recurrence typically arising within 2 cm of the irradiated volume (4,5). Magnetic resonance (MR) imaging is the standard imaging method for brain tumour diagnosis, treatment planning, and response assessment. The typical MR protocol involves a T2-weighted or fluid-attenuated inversion recovery (FLAIR) MR and a

gadolinium-enhanced T1-weighted MR (6). Following this protocol is preferable because it detects two types of anatomical abnormalities. The gadolinium-enhanced T1-weighted MR images depict the contrast-enhancing lesion (CEL) with disrupted blood-brain barrier. The T2-weighted or FLAIR MR images detect regions of T2 hyperintensity that are suspicious of tumour infiltration and vasogenic edema. Such T2 hyperintense region is the non-enhancing lesion (NEL) that cannot be seen on T1-weighted MR.

Functional imaging techniques are non-invasive methods to provide quantifiable information regarding tumour biology that may be related to tumour aggressiveness and patient prognosis (7). One important functional imaging technique is perfusion imaging. Measurements of perfusion imaging parameters such as tumour blood flow (BF), blood volume (BV), and permeability have been shown to correlate with WHO grade (8,9), histopathologic marker of tumour angiogenesis (e.g. microvessel density) (10,11), and survival (12,13,14). Most perfusion imaging studies that evaluated the relationships between tumour perfusion parameters and overall survival (OS) have focused on MR perfusion at a single time point (15) or two time points (16). CT perfusion has not been studied extensively (17) despite the ubiquity of CT scanners in radiation oncology departments. However, CT perfusion can help distinguish between high and low grade gliomas (8,18-20) and between tumour recurrence and radiation necrosis (21,22). In addition, CT perfusion can simultaneously measure absolute BF, BV, and permeability-surface area (PS) in a single scan. Therefore, CT perfusion should be considered as a valuable perfusion imaging modality in oncology.

This study is the first study to evaluate serial changes in tumour BF, BV, and PS in the CEL and NEL of patients with high-grade gliomas for up to a year after radiotherapy. The objective of this study was to evaluate the prognostic value of CT perfusion for predicting overall survival (OS) of patients with high-grade gliomas.

6.2   Materials and Methods

6.2.1   Patient Population

This study was conducted in compliance with the local research ethics committee, and informed consent was obtained from patients. Patients with suspected WHO grade III and IV gliomas were prospectively recruited prior to surgery. Exclusion criteria were 1) a brain lesion that is not WHO grade III and IV gliomas after histopathologic confirmation, 2) prior diagnosis or therapy of brain lesion, 3) unwillingness to participate during follow-up examinations, 4) clinically unstable, 5) contraindications to intravenous administration of iodinated or gadolinium contrast materials, 6) poor quality images due to motion artifacts, and 7) inability to undergo MR due to contraindications such as metallic implants, claustrophobia, and obesity. Our study included 29 patients with high-grade gliomas. Patients with WHO grade III gliomas ($N = 5$) had anaplastic oligodendrogliomas and the rest had WHO grade IV glioblastoma multiforme. The median age of diagnosis was 61 years (range, $31 - 81$ years). Patients underwent serial MR and CT perfusion examinations prior to surgery and one, three, six, nine, and 12 months after radiotherapy. The median follow-up was 18.2 months (range, $4.7 - 60.4$ months).

After the pre-surgery MR and CT perfusion examinations, all patients underwent surgery followed by external beam radiotherapy (60 Gy in 30 fractions, $N = 28$; 45 Gy in 15 fractions with stereotactic boost of 24 Gy in 3 fractions, $N = 1$). Twenty-six patients received concurrent and adjuvant temozolomide chemotherapy. Six patients underwent additional surgery after radiotherapy, and corticosteroids were administered to patients before the second surgery. At the time of progression, glioblastoma patients were given Fotemustine while anaplastic oligodendrioglioma patients were given Procarbazine + CCNU (Lomustine).

6.2.2   Conventional MR and CT Perfusion Examinations

MR images were acquired with either a 1.5T Signa HDXT (GE Healthcare, Milwaukee, WI) or a 1.5 T Achieva scanner (Philips Medical Systems, Best, The Netherlands). The MR protocol consisted of the following sequences: axial T1-weighted spin-echo, axial T2-weighted spin-echo or axial FLAIR, coronal FLAIR, and post-gadolinium axial T1-weighted spin echo.

All CT perfusion studies were performed using a multidetector-row CT scanner (Lightspeed VCT, GE). A noncontrast CT scan (350 mA, 120 kV, 5 mm slice thickness) of the head was acquired to locate the brain volume for the CT perfusion scan that would cover eight 5-mm sections of tissue. Ten patients were imaged with a one-phase CT perfusion protocol while 19 patients were imaged with a two phase CT perfusion protocol. A bolus of non-ionic contrast (Iomeron, Bracco Imaging, Konstanz, Germany; 350 mg I/ml, 40 ml) was injected at a rate of 4 mL/s. For the one-phase CT perfusion protocol, a cine scan was initiated at 5 s after the injection. The imaging parameters were 100 mA, 80kV, 1 rotation/s for a duration of 50 s, and images were reconstructed at 0.5 s intervals. For the two-phase protocol, the initial 50 s cine scan was acquired with images reconstructed at 0.5 s intervals, then 8 additional axial images were acquired for each section at 15 s intervals for another 105 s. The total scan duration was 150 s. The CT gantry was tilted to avoid radiation dose to the lens, signs of radiation toxicities from CT perfusion scans were documented. Skin erythema, dizziness, loss of equilibrium, modified gait, stupor of thought, loss of memory, air loss, cataract formation during the CT and MR follow-ups were some of the radiation-induced side effects assessed by the attending radiologist.

6.2.3   Image Analysis

Maps of BF, BV, and PS were computed using the prototype version of CT Perfusion 4D (GE Healthcare) (23,24). Averaged CT images were produced by averaging the cine CT images of the same sections. Axial gadolinium-enhanced T1-weighted MR and axial T2-weighted or FLAIR MR images were rigidly registered to the averaged CT

images using 3D Slicer (25). A radiologist with 8 years of experience manually delineated the contrast-enhancing lesion (CEL) on gadolinium-enhanced T1-weighted images and the non-enhancing lesion (NEL). The NEL was the entire T2 hyperintense lesion outside the CEL, necrosis, and surgical cavity. Mean volume, BF, BV, and PS in both CEL and NEL at each time point were used for statistical analysis.

6.2.4   Statistical Analysis

Statistical analysis was performed using SPSS software package (IBM$^®$ SPSS$^®$, version 21.0, Chicago, IL). OS was the time between the first surgery and death. OS was censored for patients that were alive at their last follow-up. Patients were stratified by their OS using 12, 18, and 24 months OS as cut points. Longitudinal analyses examined the imaging parameter differences in patients with short versus long OS. The omnibus Friedman test followed by the Wilcoxon signed-rank test were used for longitudinal comparisons within-group, and the Mann-Whitney U test examined the differences between groups. The imaging time points that were analyzed were pre-surgery, one, three, and six months post-radiotherapy. Nine and 12 months post-radiotherapy data were not analyzed due to patient dropouts resulting from deaths or complete regression of tumours.

A series of statistical analyses were carried out to evaluate whether the imaging parameters were prognostic of OS. Receiver operating characteristic analyses were performed to consider all possible cut points to differentiate patients with long and short OS. The imaging parameter cut points with the highest combination of sensitivity and specificity were selected for use in Cox proportional hazards regression and Kaplan-Meier survival analyses.

Cox proportional hazards regression analyses were performed to determine the relationships between OS and each of the imaging parameters. Separate Cox proportional hazards regression models were computed for each of the imaging parameters (volume, BF, BV, and PS) at each time point while adjusting for age, performance status

(Karnofsky Performance Status), extent of surgical resection, and WHO grade. The hazard ratios (HR) and their 95% confidence intervals (CI) were computed. We did not consider the impact of change in imaging parameters over time on OS by treating the serial imaging measurements as time-dependent covariates. This is because this study sought to evaluate whether one of these imaging time points can be used as an early biomarker of OS in a prospective setting. We then used Kaplan-Meier survival analysis and log-rank test to compare the OS of patients with high versus low values of imaging parameters. A P value ≤ 0.05 was considered statistically significant.

6.3 Results

6.3.1   Patient Characteristics and Outcomes

A total of 150 CT perfusion and 150 MR examinations were obtained from 29 patients. No radiation toxicity from serial CT perfusion scans was noted. The median OS was 18 months (range, 5 – 60 months) with three patients censored. Table 6-1 summarizes the characteristics of this patient cohort and OS estimates based on patient characteristics. In univariate analyses, differences in gender, extent of surgical resection, Karnofsky Performance Status, and re-operation were not significant predictors of OS. Older patients ($\geq$ 50 years) had worse OS than younger patients, but this was marginally significant (P = 0.06). Patients with WHO grade IV tumours were associated with significantly shorter OS compared to those with WHO grade III tumours (P = 0.04). The six patients who received reoperation did not show significantly different OS than the rest.

Table 6-1: Patient characteristics, percentages of patients alive 12, 18, and 24 months, and median OS estimates.

Demographics	n	12 Months OS	18 Months OS	24 Months OS	Median OS in months (95% CI)	*P* Value[*]
Age						
< 50	5	100%	80%	75%	32.7 (20.7 - 44.7)	0.06

≥ 50	24	63%	38%	23%	16.6 (10.1 - 23.1)	
Gender						
Female	11	55%	45%	27%	16.7 (9.4 - 24.0)	0.58
Male	18	78%	44%	33%	18.2 (9.8 - 26.6)	
WHO Grade						
III	5	100%	80%	67%	29.7 (13.0 - 46.4)	0.04
IV	24	63%	38%	26%	16.6 (10.1 - 23.1)	
Extent of resection						
Total	18	89%	56%	38%	22.3 (12.5 - 32.1)	0.37
Subtotal	11	36%	27%	20%	11.4 (10.0 - 12.8)	
Karnofsky Performance Status						
≤ 80	18	61%	39%	28%	16.4 (7.9 - 24.9)	0.70
> 80	11	82%	55%	38%	24.4 (16.9 - 31.9)	
Re-operation						
Yes	6	83%	50%	0%	16.7 (12.2 - 21.2)	0.40
No	23	65%	52%	38%	22.3 (12.3 - 32.3)	

Abbreviations: OS, Overall survival; CI, Confidence interval; WHO, World Health Organization

*Log-rank *P* value comparing OS for the demographic factor

6.3.2 Longitudinal Analysis

Figure 6-1 shows the serial changes of each imaging parameter in the CEL in terms of 12, 18, and 24 months OS. Patients appeared to show a reduction in CEL volumes after surgery and radiotherapy compared to baseline, and this was significant for patients with OS over 18 months ($P < 0.04$). There were also decreasing trends in BF, BV, and PS in the CEL after surgery. These trends were significant for BF and BV in patients who lived over 12 ($P < 0.02$) and 18 months ($P < 0.05$ and $P < 0.03$, respectively), and for BV in patients who lived less 24 months ($P < 0.04$). With the exception of BV in the CEL of patients who survived beyond 18 months, CEL volumes, BF, BV, and PS were stable between one to six months post-radiotherapy. In general, CEL volumes, BF, BV, and PS appeared to be higher in patients that survived below 18 and 24 months compared to other patients. BV at three months ($P = 0.03$) and PS at one month ($P = 0.04$) post-radiotherapy were significantly higher in patients with OS < 24 months compared to other patients.
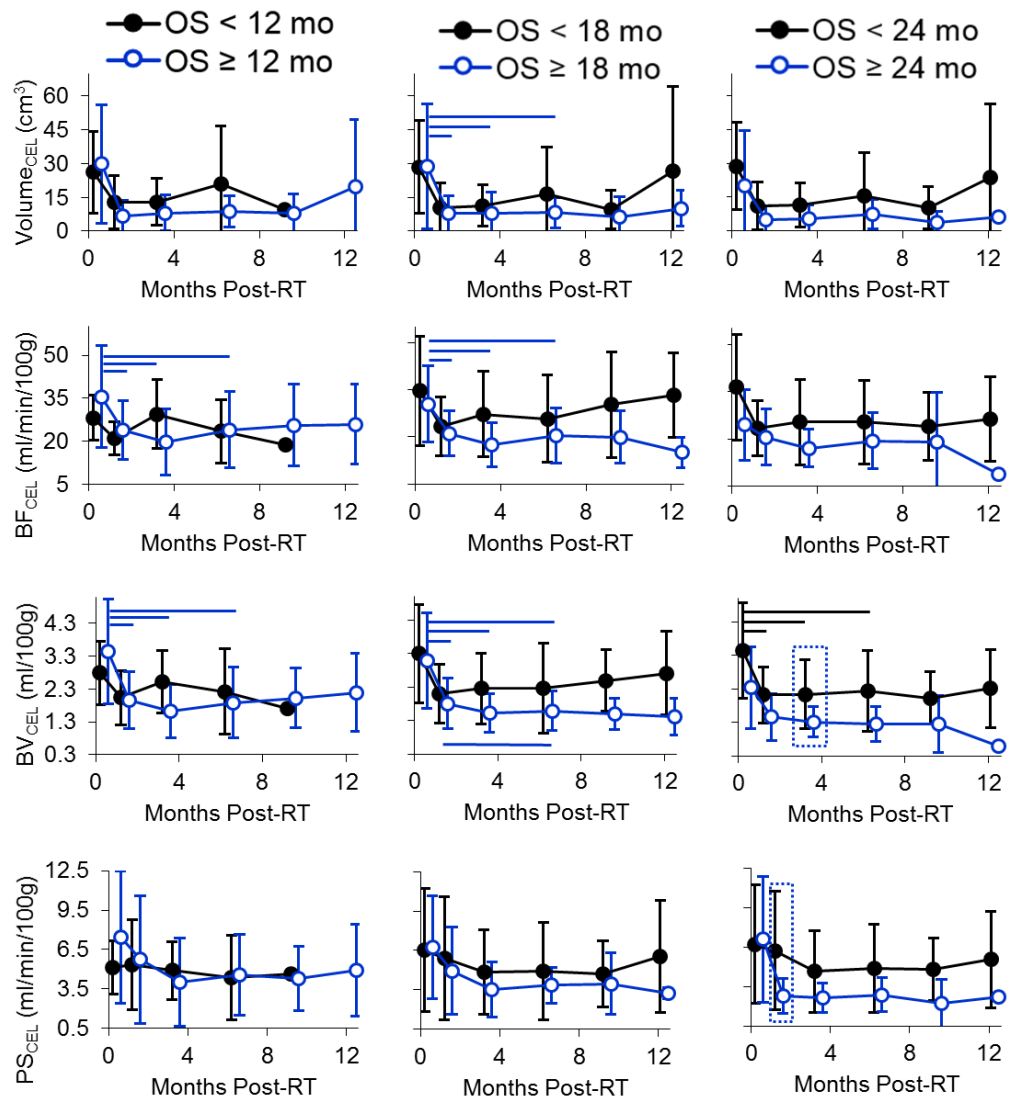
Figure 6-1: Serial changes in mean volumes (top row), blood flow (BF, second row), blood volume (BV, third row), and permeability-surface area product (PS, bottom row) in the contrast-enhancing lesions (CEL) of patients stratified by 12 (left column), 18 (middle column), and 24 months (mo) overall survival (OS, right column). Horizontal line represents significant changes between two highlighted time points of the same group. Dotted box represents a significant difference between the groups. Error bar represents one standard deviation.

Figure 6-2 illustrates the serial changes in the NEL by different OS. NEL volumes decreased after surgery and radiotherapy. This change (compared to baseline) was significant for patients who lived more than 12 months ($P < 0.05$), more than 18 months ($P < 0.03$), more than 24 months ($P < 0.05$), and also for patients who lived less than 24 months ($P < 0.03$). However, there was no between-group difference in NEL volumes in patients with long ($\geq$ 12, 18, and 24 months) versus short OS ($<$ 12, 18, and 24 months). BF values in the NEL were stable over time with the exception of a significant decrease between pre-surgery and 6 months post-radiotherapy in patients that lived less than 24 months ($P < 0.005$). BF values in the NEL before surgery were significantly higher in patients that deceased before 18 ($P = 0.003$) and 24 months ($P = 0.004$); and they were also significantly higher at three months post-radiotherapy ($P = 0.05$) in patients with OS below 18 months. In comparison with pre-surgery measurements, BV values in the NEL decreased significantly ($P < 0.04$) at three and six months post-radiotherapy in patients with OS below 24 months. However, BV values in the NEL were significantly higher at one and three months post-radiotherapy in patients with OS below 18 months ($P = 0.04$ and 0.02, respectively) when compared to those with OS beyond 18 months. BV values were also significantly higher at pre-surgery and one month post-radiotherapy for those with OS less than 24 months when compared to those that lived beyond 24 months ($P = 0.01$ and 0.03, respectively). PS values in the NEL significantly decreased after surgery and radiotherapy in patients who survived beyond 12 and 18 months ($P < 0.01$, and $\leq$ 0.03, respectively), and also in patients who survived less than 18 and 24 months ($P < 0.04$ and < 0.04, respectively). More importantly, PS values in the NEL at one month post-radiotherapy were significantly higher in patients who deceased before 18 and 24 months ($P < 0.01$), and these values measured at three months post-radiotherapy were also significantly higher in patients with OS below 18 months ($P = 0.02$).
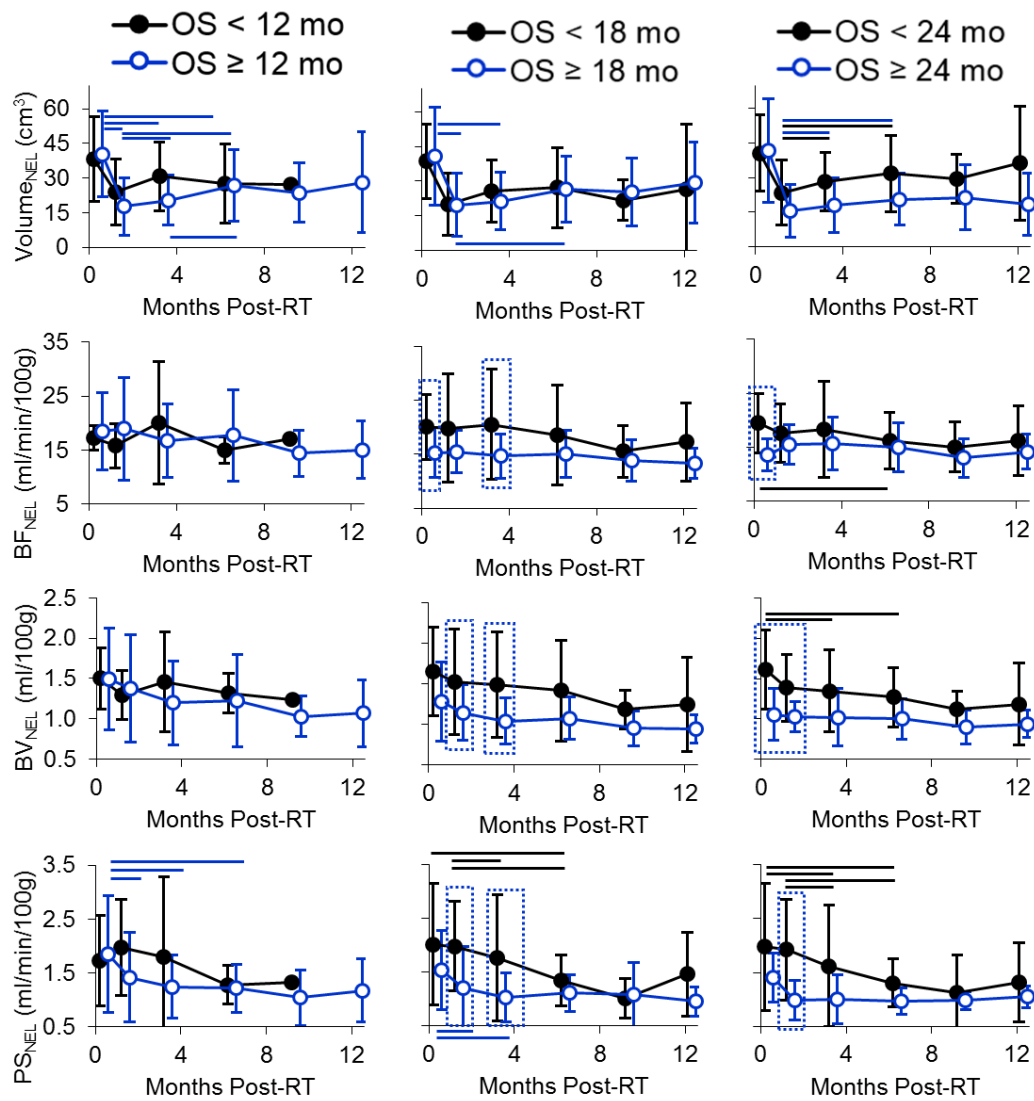
Figure 6-2: Serial changes in mean volumes (top row), blood flow (BF, second row), blood volume (BV, third row), and permeability-surface area product (PS, bottom row) in the non-enhancing lesions (NEL) of patients stratified by 12 (left column), 18 (middle column), and 24 months (mo) overall survival (OS, right column). Horizontal line represents significant changes between two highlighted time points of the same group. Dotted box represents a significant difference between the groups. Error bar represents one standard deviation.

6.3.3   Survival Analysis

The Cox proportional hazards regression model of the classical prognostic factors (i.e. age, performance status, extent of resection, and WHO grade) showed that higher WHO grade (HR = 49.6, 95% CI = $5.1 - 483.2$, $P < 0.001$) and lower extent of resection (HR = 19.0, 95% CI = $3.6 - 99.5$, P < 0.001) were associated with significant hazards of death. A total of 96 Cox proportional hazards regression models were considered while adjusting for age, performance status, extent of resection and WHO grade. Table 6-2 reports parameters with cut points that were associated with both significant hazard ratios and significant differences in OS, and Figure 6-3 illustrates the Kaplan-Meier plots of these parameters.

Table 6-2: Cox proportional hazards regression and Kaplan-Meier analysis results.

Imaging Time	Region	Cut point selected based on	Parameter Cut Point	Hazard ratios (95% CI)	Cox regression P Value	Median OS (95% CI)	Log-rank P Value
Pre-surgery	NEL	12 mo OS	BF ≥ 16.1 ml/min/100g	10.9 (2.9 – 41.5)	< 0.001	High: 16.4 (9.3 – 23.4) Low: 28.8 (19.3 – 38.3)	0.001
		18 mo OS	BF ≥ 16.8 ml/min/100g	9.9 (2.3 – 42.5)	0.002	High: 16.4 (9.8 – 23.0) Low: 24.4 (16.5 – 32.3)	0.003
		24 mo OS	BF ≥ 16.1 ml/min/100g	10.9 (2.9 – 41.5)	< 0.001	High: 16.4 (9.3 – 23.4) Low: 28.8 (19.3 – 38.3)	0.001
1 month post-radiotherapy	CEL	12 mo OS	Volume ≥ 12.3 cm^3	7.4 (1.9 – 28.5)	0.004	High: 9.1 (5.8 – 12.4) Low: 18.0 (15.0 – 20.9)	0.007
	NEL	18 mo OS	Volume ≥ 11.6 cm^3	4.1 (1.1 – 15.3)	0.04	High: 16.6 (7.2 – 26.0) Low: 32.7 (26.5 – 38.9)	0.03
	NEL	24 mo OS	Volume ≥ 11.6 cm^3	4.1 (1.1 – 15.3)	0.04	High: 16.6 (7.2 – 26.0) Low: 32.7 (26.5 – 38.9)	0.03
	NEL	24 mo OS	PS ≥ 1.4 ml/min/100g	4.9 (1.4 – 17.3)	0.01	High: 12.6 (6.3 – 18.9) Low: 28.8 (19.7 – 37.9)	0.002
3 months post-radiotherapy	CEL	12 mo OS 18 mo OS 24 mo OS	BV ≥ 1.7 ml/100g	5.2 (1.2 – 21.7)	0.03	High: 11.7 (9.2 – 14.2) Low: 23.6 (5.6 – 41.7)	0.007
6 months post-radiotherapy	CEL	18 mo OS 24 mo OS	VOL ≥ 13.9 cm^3	5.7 (1.1 – 28.7)	0.04	High: 12.6 (6.3 – 18.9) Low: 18.2 (12.2 – 24.1)	0.05
	NEL	18 mo OS 24 mo OS	BV ≥ 1.3 ml/100g	12.9 (2.8 – 58.9)	0.001	High: 12.6 (5.4 – 19.8) Low: 24.4 (20.7 – 28.1)	0.004

Abbreviations: NEL, non-enhancing lesion; CEL, contrast-enhancing lesion; mo, month, OS, overall survival; BF, blood flow; PS, permeability-surface area product; BV, blood volume
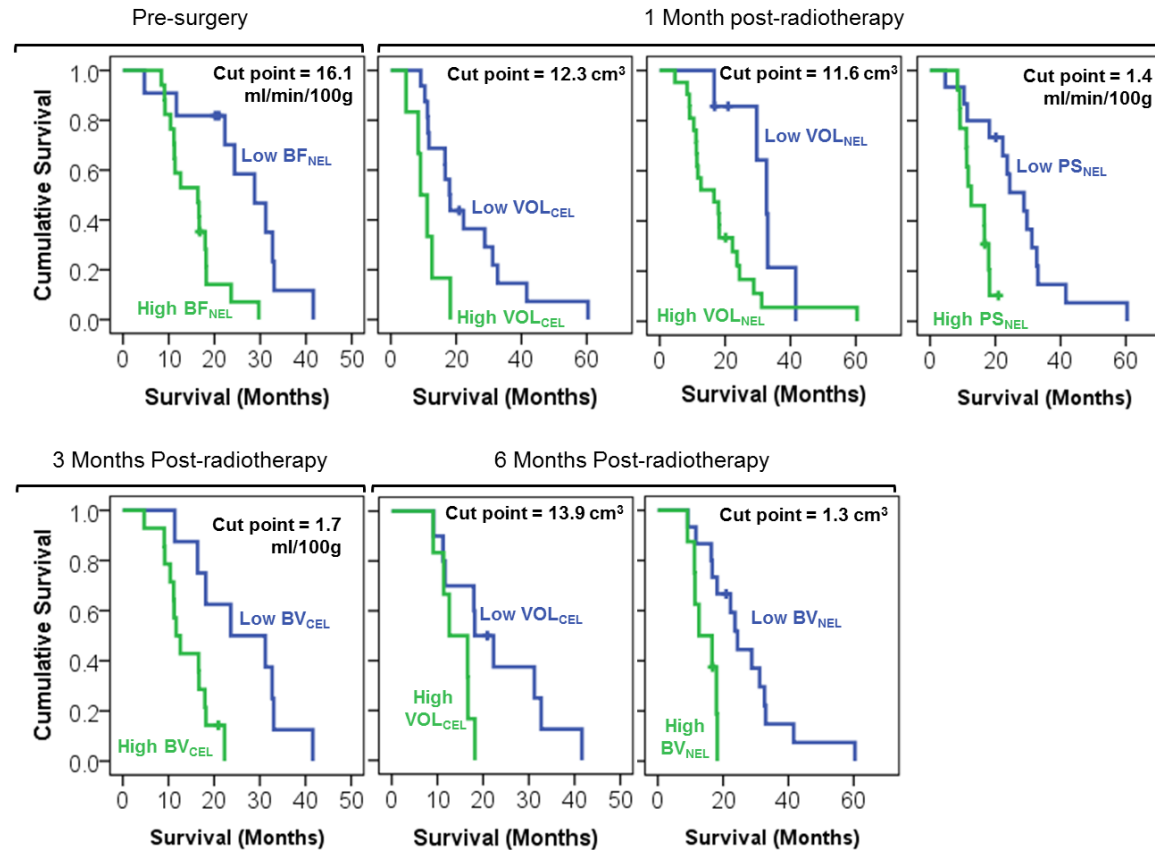
Figure 6-3: Kaplan-Meier survival plots of blood flow in the non-enhancing lesion (BF$_{NEL}$), volume of the contrast-enhancing lesion (VOL$_{CEL}$), volume in the NEL (VOL$_{NEL}$), permeability-surface area product in the NEL (PS$_{NEL}$), blood volume in the CEL (BV$_{CEL}$), and BV in the NEL (BV$_{NEL}$) measured at different time points. Higher values in these parameters were associated with worse overall survival (log-rank $P < 0.05$ for all comparisons).

Although some imaging parameters did not show a significant association with OS, they could still be useful in stratifying patients by OS. Table 6-3 shows the sensitivities and specificities of imaging parameters that are ≥ 70% in stratifying patients based on OS. While some CT perfusion parameters showed sensitivities and specificities ≥ 70%, volumes of NEL and CEL did not. In addition, BF in the NEL at pre-surgery and BV in the CEL at three months post-radiotherapy had the highest combination of sensitivities (83% and 82%, respectively) and specificities (86% and 100%, respectively) in stratifying patients based on 24 months OS. Figure 6-4 illustrates pre-surgery CT perfusion and MR images of two patients with different survival (16.7 vs. 41.6 months). Higher BF, BV, and PS in the NEL can be seen in the patient with shorter survival.

Table 6-3: Receiver operating characteristic analysis of imaging parameters with sensitivities and specificities ≥ 70%.

Imaging Time	Region	Cut-point selected based on	Parameter cut point	AUC	Sensitivity	Specificity
Pre-surgery	NEL	18 mo OS	BF ≥ 16.8 ml/min/100g	0.76	80%	77%
		24 mo OS	BF ≥ 16.1 ml/min/100g	0.88	83%	86%
	CEL	24 mo OS	BF ≥ 26.0 ml/min/100g	0.73	78%	71%
1 Month Post-radiotherapy	NEL	18 mo OS	PS ≥ 1.4 ml/min/100g	0.76	71%	79%
	CEL	24 mo OS	PS ≥ 3.4 ml/min/100g	0.81	75%	80%
3 Months Post-radiotherapy	CEL	24 mo OS	BV ≥ 1.7 ml/100g	0.85	82%	100%

Abbreviations: NEL, non-enhancing lesion; CEL, contrast-enhancing lesion; mo, months, OS; overall survival ; BF, blood flow; BV, blood volume; PS, permeability-surface area product; AUC, area under the receiver operating characteristic curve
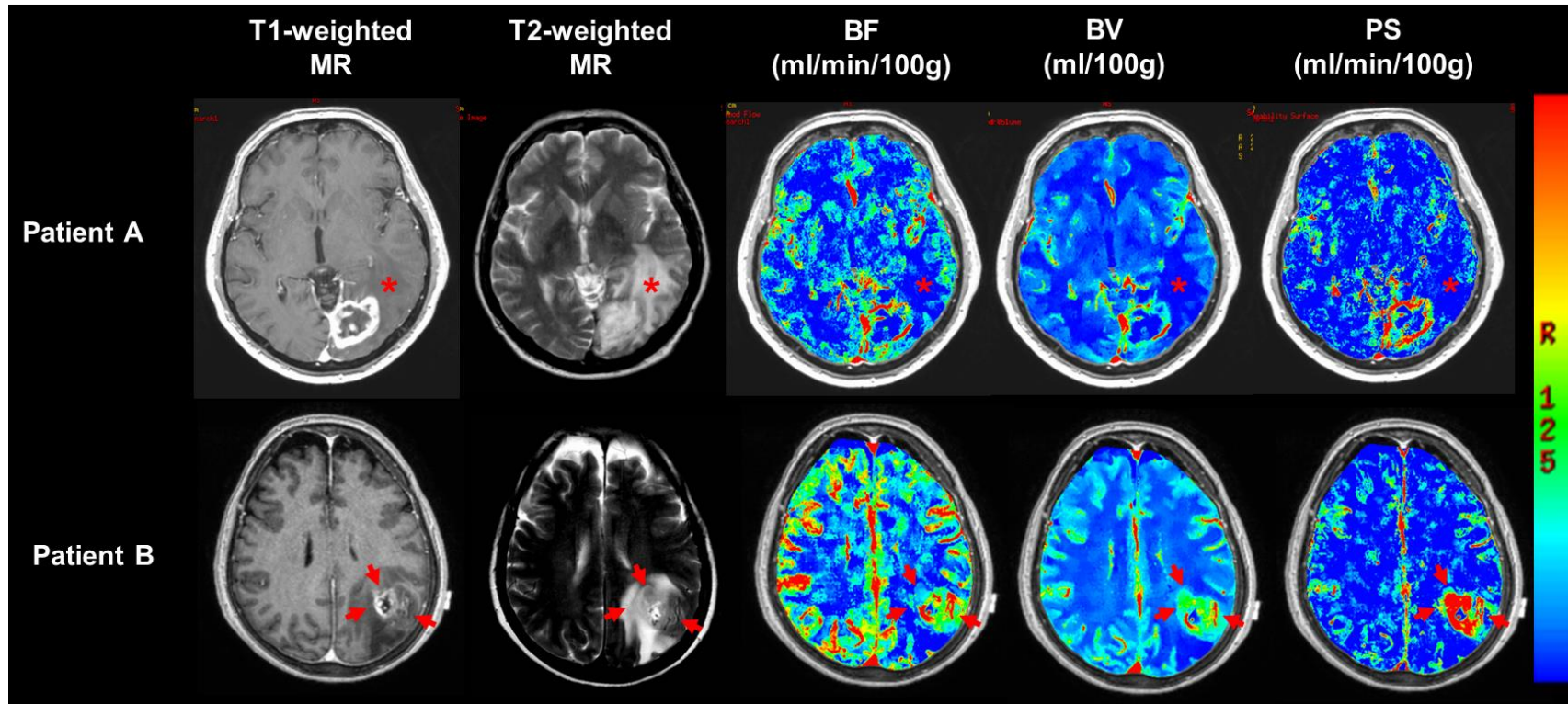
Figure 6-4: Illustrative pre-surgery CT perfusion and MR images of patients with WHO grade IV gliomas. Both patients presented with a contrast-enhancing lesion on post-gadolinium T1-weighted MR images, which also had elevated blood flow (BF), blood volume (BV), and permeability-surface area product (PS). Patient A presented with low BF, BV, and PS in the non-enhancing lesion (NEL, asterisk). However, Patient B presented with regions of elevated BF, BV, and PS in the NEL (red arrows). The survival for patient A was 41.6 months and Patient B was 16.7 months. Identical window and level were used for the color maps.

6.4 Discussion

OS in patients with high-grade gliomas remains poor despite aggressive treatments. Deployment of advanced functional imaging that can stratify patients by expected OS can potentially facilitate timely selection of appropriate treatments for these patients. This study examined the serial changes in CT perfusion parameters in conjunction with volumetric changes in the CEL and NEL of patients with high-grade gliomas. We also examined whether these imaging parameters could predict OS.

Perfusion changes after radiotherapy have previously been studied only in a few reports (26,27). An increase in BV was associated with progression (26) and poor survival (27). This is the first study to investigate serial changes in BF, BV, and PS in both the CEL and NEL for up to one year post-radiotherapy. The initial decline of all imaging parameters in the CEL after surgery and radiotherapy could be attributed to surgical debulking of the tumour and therapeutic effect of radiotherapy and chemotherapy. After stratifying patients based on 18 and 24 months OS, all three perfusion parameters in the CEL started to diverge three months after radiotherapy with elevated BF and BV seen in patients with shorter OS. On the other hand, BF, BV, and PS in the NEL were consistently higher in two groups of patients with shorter OS (< 18 and 24 months). Although statistical differences were identified only at some of the time points, in general our data provided corroborating evidence that part of the heterogeneity in OS is related to variation in tumour perfusion characteristics both in the CEL and NEL regions. This variation in perfusion characteristics presumably reflected the differences in angiogenesis and vascularity between patients. Angiogenesis as a mechanism for promoting tumour growth is now an active target in cancer therapies (28). Angiogenesis leads to an increase in tumour microvessel area, which has been shown to correlate with tumour BV and patient survival (11). More recently, vasculogenesis, a process by which bone marrow-derived cells are recruited to form new tumour blood vessels, has been shown to govern tumour recurrence after radiotherapy (29). It is not known what percentage of tumour vessels are derived from vasculogenesis, but given that recurrence occurs within 2 cm of the irradiated volume (4,5) it is critical to assess perfusion parameters in both the CEL and NEL after radiotherapy.

None of the imaging measurements made in the CEL before surgery showed a significant correlation with OS. This could be because total resection of the tumour (mostly CEL) is a stronger predictor of OS. Over 60% of patients in this study underwent total resection and the extent of resection showed a significant association with OS. Prediction of survival using pre-surgery CT perfusion parameters in the CEL may be more appropriate for patients who are not candidates for total resection. For example, pre-surgery tumour BV is a predictor of survival in a study with a mixture of patients that received biopsy, subtotal resection, and total resection (12). However, pre-surgery measurement of BF in the NEL proved to be useful in predicting OS in this study. This result points to the role of tumour burden in the T2 hyperintense lesion that is not typically removed by surgery.

Although a larger sample size is required to show consistent associations between OS and CT perfusion parameters across all time points, our results are consistent with previous reports that higher BV and PS are associated with poor outcomes (12,13,26,27). It is also noteworthy that while we showed significant hazards of death associated with both volumetric and CT perfusion parameters, only CT perfusion parameters resulted in sensitivities and specificities $\geq$ 70% in predicting OS. CT perfusion parameters can provide complementary information to volumetric MR measurements in predicting survival in high-grade glioma patients. Volume of the CEL may not be a reliable predictor of outcome because the volume of contrast-enhancement may be affected by many nontumoural processes including inflammation, postsurgical changes, pseudoprogression, and treatment-induced necrosis (30-33). Similarly, the volume of the NEL encompasses many causes of T2 hyperintensity such as vasogenic edema, gliosis, cystic changes, inflammation, and tumour infiltration (34-36). It is evident from Figure 6-4 that tumours can have regions of high BF, BV, and PS that are bigger than the CEL. These regions can potentially lead to future sites of recurrence. Although this is hypothesis-generating, there is preliminary evidence to suggest that there could be better spatial concordance between CT perfusion parameters with the site of future recurrence than the CEL with the site of future recurrence (23).

Some limitations must be considered. Our sample size was relatively small and five patients had anaplastic oligodendrogliomas, which are known to have a higher BV than astrocytic gliomas despite better survival (37,38). This can hamper the ability to stratify OS based on BV. In addition, we did not have information regarding other known biologic biomarkers like MGMT methylation status that are associated with OS and thus we could not correct for those effects in our regression models. Likewise, the variable use of salvage therapies like second surgery and chemotherapy may have influenced OS although in glioblastoma patients these effects could be expected to be modest (39). Another limitation was the use of a one-phase CT perfusion protocol in one third of the patients. The duration of the CT perfusion protocol can affect the measurements of CT perfusion parameters, in particularly PS (24). Although we did not find a statistical difference in these parameters in the CEL and NEL at baseline between the two protocols (data not shown), it is important to use a two-phase CT perfusion protocol in future studies. We did not consider the impact of change in each of the imaging parameters over time on OS by treating the serial measurements as time-dependent covariates in a joint model of survival and time-dependent covariates. This is because we first want to evaluate the predictive value of these imaging parameters as independent predictors of survival in order to limit the number of CT perfusion follow-ups in future studies. Finally, a perfusion imaging scan at the time point of pre-radiotherapy but post-surgery could be a better baseline scan than a pre-surgery perfusion imaging scan. This may have helped extract the relative contribution of perfusion imaging parameters versus the extent of surgical resection in predicting survival.

6.5 Conclusions

BF, BV, PS are potential biomarkers of OS in patients with high-grade gliomas treated with multi-modality therapy (surgery, radiation, chemotherapy) even after adjustments for age, WHO grade, Karnofsky Performance Status, and the extent of resection. The results of this study, if verified in a larger cohort of patients, could establish CT perfusion imaging as a reliable predictor of survival.

6.6 References

1. Wen PY, Kesari S. Malignant gliomas in adults. N Engl J Med. 2008; 359:492-307.

2. Curran WJ, Scott CB, Horton J, et al. Recursive Partitioning Analysis of Prognostic Factors in Three Radiation Therapy J Natl Cancer Inst. 1993; 85:704–10.

3. Weller M, Stupp R, Hegi ME, et al. Personalized care in neuro-oncology coming of age: why we need MGMT and 1p/19q testing for malignant glioma patients in clinical practice. Neuro Oncol. 2012; 14:iv100-8.

4. Weber DC, Casanova N, Zilli T, et al. Recurrence pattern after [(18)F]fluoroethyltyrosine-positron emission tomography-guided radiotherapy for high-grade glioma: a prospective study. Radiother Oncol. 2009;93:586–92.

5. Milano MT, Okunieff P, Donatello RS, et al. Patterns and timing of recurrence after temozolomide-based chemoradiation for glioblastoma. Int J Radiat Oncol Biol Phys. 2010; 78:1147–55.

6. Essig M, Anzalone N, Combs SE, et al. MR imaging of neoplastic central nervous system lesions: Review and recommendations for current practice. AJNR Am J Neuroradiol. 2012; 33:803-17.

7. Cha S. Update on brain tumor imaging: from anatomy to physiology. AJNR Am J Neuroradiol. 2006; 27:475-87.

8. Jain R, Ellika SK, Scarpace L, et al. Quantitative estimation of permeability surface-area product in astroglial brain tumors using perfusion CT and correlation with histopathologic grade. AJNR Am J Neuroradiol. 2008; 29:694-700.

9. Weber MA, Henze M, Tüttenberg J, et al. Biopsy targeting gliomas: do functional imaging techniques identify similar target areas? Invest Radiol. 2010; 45:755-68.

10. Jain R, Gutierrez J, Narang J, et al. In vivo correlation of tumor blood volume and permeability with histologic and molecular angiogenic markers in gliomas. AJNR Am J Neuroradiol. 2011; 32:388-94.

11. Hu LS, Eschbacher JM, Dueck AC, et al. Correlations between perfusion MR imaging cerebral blood volume, microvessel quantification, and clinical outcome using stereotactic analysis in recurrent high-grade glioma. AJNR Am J Neuroradiol. 2012; 33:69-76.

12. Jain R, Narang J, Griffith B, et al. Prognostic vascular imaging biomarkers in high-grade gliomas: tumor permeability as an adjunct to blood volume estimates. Acad Radiol. 2013; 20:478-85.

13. Shankar JJ, Woulfe J, Silva VD, Nguyen TB. Evaluation of perfusion CT in grading and prognostication of high-grade gliomas at diagnosis: A pilot study. AJR Am J Roentgenol. 2013; 200:W504-9.

14. Law M, Young RJ, Babb JS, et al. Gliomas: predicting time to progression or survival with cerebral blood volume measurements at dynamic susceptibility-weighted contrast-enhanced perfusion MR imaging. Radiology. 2008; 247:490-8.

15. Bisdas S, Kirkpatrick M, Giglio P, Welsh C, Spampinato MV, Rumboldt Z. Cerebral blood volume measurements by perfusion-weighted MR imaging in gliomas: Ready for prime time in predicting short-term outcome and recurrent disease? AJNR Am J Neuroradiol. 2009; 30:681-8.

16. Galbán CJ, Chenevert TL, Meyer CR, et al. Prospective analysis of parametric response map-derived MRI biomarkers: Identification of early and distinct glioma response patterns not predicted by standard radiographic assessment. Clin Cancer Res. 2011; 17:4751-60.

17. Jain R. Perfusion CT imaging of brain tumors: an overview. AJNR Am J Neuroradiol. 2011; 32:1570-1577.

18. Ding B, Ling HW, Chen KM, Jiang H, Zhu YB. Comparison of cerebral blood volume and permeability in preoperative grading of intracranial glioma using CT perfusion imaging. Neuroradiology. 2006; 48:773-781.

19. Fainardi E, Di Biase F, Borrelli M, et al. Potential role of CT perfusion parameters in the identification of solitary intra-axial brain tumor grading. Acta Neurochir Suppl. 2010; 10:283-87.

20. Ellika SK, Jain R, Patel SC, et al. Role of perfusion CT in glioma grading and comparison with conventional MR imaging features. AJNR Am J Neuroradiol. 2007; 28:1981-7.

21. Jain R, Narang J, Schultz L, et al. Permeability estimates in histopathology-proved treatment-induced necrosis using perfusion CT: can these add to other perfusion

parameters in differentiating from recurrent/progressive tumors? AJNR Am J Neuroradiol. 2011; 32:658-63.

22. Vidiri A, Guerrisi A, Pinzi V, et al. Perfusion Computed Tomography (PCT) adopting different perfusion metrics: recurrence of brain metastasis or radiation necrosis? Eur J Radiol. 2012; 81:1246-52.

23. Yeung TPC, Yartsev Y, Lee, TY, et al. Relationship of computed tomography perfusion and positron emission tomography to tumour progression in malignant glioma. J Med Radiat Sci. 2014; 61:4-13.

24. Yeung TPC, Yartsev S, Bauman G, He W, Fainardi E, Lee TY. The effect of scan duration on the measurement of perfusion parameters in CT perfusion studies of brain tumors. Acad Radiol. 2013; 20:59-65.

25. Pieper S, Lorensen B, Schroeder W, Kikinis R. The NA-MIC Kit: ITK, VTK, pipelines, grids and 3D slicer as an open platform for the medical image computing community. Proc 3rd IEEE Int Symp Biomed Imaging: From Nano Macro. 2006; 1: 698–701.

26. Vöglein J, Tüttenberg J, Weimer M, et al. Treatment monitoring in gliomas: comparison of dynamic susceptibility-weighted contrast-enhanced and spectroscopic MRI techniques for identifying treatment failure. Invest Radiol. 2011; 46:390-400.

27. Mangla R, Singh G, Ziegelitz D, et al. Changes in relative cerebral blood volume 1 month after radiation-temozolomide therapy can help predict overall survival in patients with glioblastoma. Radiology. 2010; 256:575-84.

28. Jain RK, di Tomaso E, Duda DG, Loeffler JS, Sorensen AG, Batchelor TT. Angiogenesis in brain tumours. Nat Rev Neurosci. 2007; 8:610-22.

29. Kioi M, Vogel H, Schultz G, Hoffman RM, Harsh GR, Brown JM. Inhibition of vasculogenesis, but not angiogenesis, prevents the recurrence of glioblastoma after irradiation in mice. J Clin Invest. 2010; 120:694-705.

30. van den Bent MJ, Vogelbaum MA, Wen PY, Macdonald DR, Chang SM. End point assessment in gliomas: novel treatments limit usefulness of classical Macdonald's Criteria. J Clin Oncol. 2009; 27:2905-8.

31. Finn MA, Blumenthal DT, Salzman KL, et al: Transient postictal MRI changes in patients with brain tumors may mimic disease progression. Surg Neurol. 2007; 67:246-250.

32. Ulmer S, Braga TA, Barker FG 2nd, et al: Clinical and radiographic features of peritumoral infarction following resection of glioblastoma. Neurology. 2006; 67:1668-1670.

33. Kumar AJ, Leeds NE, Fuller GN, et al: Malignant gliomas: MR imaging spectrum of radiation therapy- and chemotherapy-induced necrosis of the brain after treatment. Radiology.2000; 217:377-384.

34. Oh J, Cha S, Aiken, et al. Quantitative apparent diffusion coefficients and T2 relaxation times in characterizing contrast enhancing brain tumors and regions of peritumoral edema. J Magn Reson Imaging. 2005; 21:701–708.

35. Hattingen E, Jurcoane A, Daneshvar K, et al. Quantitative T2 mapping of recurrent glioblastoma under Bevacizumab improves monitoring for non-enhancing tumor progression and predicts overall survival. Neuro Oncol. 2013; 15:1395-404.

36. Li Y, Lupo JM, Polley MY, Crane JC, Bian W, Cha S, Chang S, Nelson SJ. Serial analysis of imaging parameters in patients with newly diagnosed glioblastoma multiforme. Neuro Oncol. 2011; 13:546-57.

37. Saito T, Yamasaki F, Kajiwara Y, et al. Role of perfusion-weighted imaging at 3T in the histopathological differentiation between astrocytic and oligodendroglial tumors. Eur J Radiol. 2012; 81:1863-9.

38. Narang J, Jain R, Scarpace L, et al. Tumor vascular leakiness and blood volume estimates in oligodendrogliomas using perfusion CT: An analysis of perfusion parameters helping further characterize genetic subtypes as well as differentiate from astroglial tumors. J Neurooncol. 2011; 102:287-93.

39. Weller M, Cloughesy T, Perry JR, Wick W. Standards of care for treatment of recurrent glioblastoma – are we there yet? Neuro Oncol. 2013; 15:4-27.

Chapter 7

7   Conclusion and Future Work

7.1   Summary of Findings

This thesis demonstrated 1) the importance of mitigating some of the uncertainties associated with CT perfusion imaging and 2) the possibilities of using CT perfusion imaging to stratify outcomes in brain tumour patients and in an experimental model of brain tumour. In this chapter, major findings of the five studies in this thesis are summarized, and future investigations are discussed.

7.1.1   Mitigating Uncertainties in CT Perfusion

Although much research has been done in the field of CT perfusion imaging, interpretation of these results can be confounded by variations in image acquisition protocols affecting the measurements of different CT perfusion parameters (e.g. blood flow, BF). The absence of a standardized protocol has led to the procedure variability observed amongst published studies. One imaging acquisition parameter that varied widely in the literature is the scan duration. Chapter 2 addressed the role of scan duration in the measurements of BF, blood volume (BV), and permeability-surface area product (PS). Systematic and random errors in BF, BV, and PS measurements increased with shorter scan duration. Tumour rim PS values computed from shorter (60 s) scans were significantly different from the corresponding values computed from the longer (150 s) scans ($P < 0.01$). As a result of these analyses, a minimum scan duration of 90 s is recommended.

CT image noise not only affects the visualization of anatomical structures; it affects the calculated BF, BV, and PS values. Chapter 3 evaluated the improvements in the measurements of these parameters after filtering CT perfusion images using principal component analysis (PCA). From the simulation, PCA filtering reduced the measurement errors of BF, BV, and PS. Similarly, the noise of BF, BV, and PS measurements also decreased after PCA filtering. From experiments, we showed that PCA improved the

contrast-to-noise ratio of CT perfusion images. At a noise level of 17 HU, a minimum of 4 principal components was recommended for filtering CT perfusion images.

While other aspects of CT perfusion imaging remain to be optimized, the development of recommended minimum scan duration and an optimized image noise filtering technique are important components of developing standardized approaches to perfusion imaging.

7.1.2   CT Perfusion as a Biomarker of Treatment Outcomes

Clinical outcomes of patients with malignant gliomas vary widely with some patients surviving longer than others despite standard treatments. Thus, a biomarker that can stratify patients by survival can potentially personalize treatments for these patients. To contribute to this goal, we examined the ability of CT perfusion in identifying "long-term survivors" and "short-term survivors" in both malignant glioma patients and a preclinical animal model.

Stereotactic radiosurgery (SRS) has garnered clinical interests over the years for the treatment of malignant gliomas, but clinical trials of SRS have not demonstrated clinically meaningful improvements in survival over conventional fractionated radiotherapy. Using the C6 glioma model for rats (Chapter 4), we investigated the efficacy of CT perfusion as a potential early imaging biomarker of response to SRS. Our results showed that response to SRS was heterogeneous. Stratification of treated animals based on 15 day survival showed that responders (surviving > 15 days) had lower relative BV and PS on day 7 post-SRS when compared to controls and non-responders ($P < 0.05$). In addition, relative BV and PS on day 7 post-SRS were predictive of survival with 92% accuracy while tumour volume was not predictive of survival. These findings point to the potential role of CT perfusion as an early biomarker of response to SRS.

Identifying active tumour regions that are likely to persist after treatment can help tailor radiotherapy to target these regions. Chapter 5 investigated whether multiparametric imaging with CT perfusion and 18F-Fluorodeoxyglucose positron

emission tomography (FDG-PET) can identify tumour sites that are likely to correlate with the eventual location of tumour progression. We developed a method to generate probability maps of tumour progression based on CT perfusion, FDG-PET, and anatomical MR imaging data. Our results showed that PS had the highest area under the receiver operating characteristic curve for identifying tumour regions that are likely to coincide with future sites of progression (AUC = 0.72 ± 0.12). Although the sensitivity and specificity were modest for identifying tumour regions that were likely to progress, this study demonstrated the use of voxel-based analysis of multi-parametric imaging data in relations to future sites of progression.

The final study of this thesis (Chapter 6) examined the serial changes in tumour volumetric and CT perfusion parameters and evaluated the predictive values of these data in stratifying malignant glioma patients by overall survival. Patients were imaged with conventional MR and CT perfusion before surgery and regularly after radiotherapy for up to a year. A trend towards higher BF, BV, and PS in the contrast-enhancing lesion (CEL) and the non-enhancing lesion (NEL) were found in patients with overall survival less than 18 and 24 months, and these values were significant at some time points ($P < 0.05$). Pre-surgery BF in the NEL and BV in the CEL three months after radiotherapy had the highest combination of sensitivities and specificities of $\geq 80\%$ in predicting 24 months overall survival. These results suggest using BF, BV, and PS as early predictors of survival.

7.2 Clinical Translational Potential

The findings of this thesis contributed important information for the clinical translation of CT perfusion in brain tumour imaging. Here, we describe how this research is clinically relevant.

Decision making based CT perfusion information relies on accurate and precise measurements of BF, BV, and PS. This thesis proposed two ways to improve the accuracy and precision of CT perfusion parameter measurements. Our investigation of

the effect of scan duration demonstrated that protocol standardization is a simple first step in reducing the uncertainties associated with CT perfusion parameters. This work is important and two more studies investigating the effect of CT perfusion scan duration have cited our work since our study was published in January, 2013 (1,2). Image filtering using PCA is another way to mitigate some of the uncertainties in the measurements of BF, BV, and PS. PCA filtering of CT perfusion images has important clinical relevance in terms of improving image quality and reducing radiation dose. Radiation dose is of concern when performing serial CT perfusion studies. Thus, dose reduction will facilitate the use of serial CT perfusion follow-ups in the clinic. Reducing the image acquisition frequency has been proposed as a method to reduce radiation dose (3-5). This method is simple to implement and reduces radiation dose effectively. However, the lesser number of acquired images translates into a reduction in the amount of data available for estimating BF, BV, and PS. As a result, it is recommended that the frequency of image acquisition be less than 4 s per image. Our method can be more effective in reducing image noise because PCA filtering is a post-image acquisition technique. Future investigation should examine the ability of PCA in maintaining image quality while reducing radiation dose.

One of the challenges in the treatment of malignant gliomas is the heterogeneity in clinical outcomes. Here we propose several roles that CT perfusion imaging can play to improve the care of these patients in terms of spatial targeting and temporal monitoring of these tumours.

Image-guidance has improved the precision of surgical resection of brain tumours and spatial targeting in radiotherapy. Image-guidance has largely been limited to post-gadolinium T1-weighted and T2-weighted or fluid attenuated inversion recovery (FLAIR) MR. These techniques predominately assess the structural abnormalities of tumours. The results described in chapters 5 and 6 point to a possible spatial mismatch between the CEL on MR and tumour regions with high CT perfusion parameter values. In radiotherapy, the CEL is called the gross tumour volume. Biologic imaging modalities, such as CT perfusion, have been proposed to help delineate a "biologic target volume" in radiotherapy (6). The spatial mismatch between the gross tumour volume (i.e. CEL) and

the biologically active tumour volume has been studied in a few PET imaging studies (7-10). The spatial mismatch suggested in this thesis could serve for improving the delineation of targets for radiotherapy dose escalation. CT perfusion is of particular importance in this respect because CT scanners/simulators are readily available in radiotherapy centers and an integral part of the radiation treatment planning workflow. The use of CT perfusion imaging facilitates the registration of treatment planning CT images with CT perfusion parameter maps. It is also inexpensive compared with other imaging techniques such as MR perfusion, and can acquire data for generating maps of BF, BV, and PS within a few minutes. Therefore, CT perfusion is currently the easiest modality to implement as a biologic imaging modality in radiation therapy.

Chapters 4 and 6 point to the potential role of CT perfusion in the follow-up of patients post-treatment. Results from the pre-clinical study (Chapter 4) are consistent with the results of the clinical study (Chapter 6). Both studies showed that higher BF, BV, and PS after radiation treatments are associated with worse survival. These findings are clinically important because they indicate that tumours with higher BF, BV, and PS are more aggressive and less likely to respond to radiotherapy. These patients might benefit from additional treatments. Currently, salvage treatments for recurrent glioblastomas are not standardized. Treatments options include second surgery, repeat irradiation, chemotherapy, and anti-angiogenic therapies (11). Therefore, early selection of patients with aggressive tumours based on CT perfusion parameters may facilitate earlier administration of salvage therapies.

7.3 Future Work

This thesis addressed many important questions regarding CT perfusion imaging of malignant gliomas. As with any research, this thesis generated a number of new and important questions. The following section outlines possible future projects.

7.3.1   A Framework for Quality Assurance (QA) in CT Perfusion Imaging

As alluded to earlier, quality assurance (QA) is important for widespread implementation of CT perfusion imaging in oncology trials and practice. Consensus guidelines for the use of CT perfusion were published in 2012 (12). However, a QA framework is needed to establish tolerance limits and best practices guidelines. Figure 7-1 proposes a QA framework for CT perfusion imaging so that tolerance limits and best practices guidelines can be established in the future. This framework proposes four areas of QA: (i) protocol QA, (ii) machine QA, (iii) user QA, and (iv) software QA. Protocol QA should include a checklist to ensure that a standardized CT perfusion protocol is followed. Machine QA involves the use of a physical phantom to check image quality and the variability in time concentration curves obtained from different scanning conditions (13). At present, flow phantoms are available to check the variability in time concentration curves (13,14). User education is needed to ensure proper analysis of CT perfusion datasets and minimize interobserver variability. Digital phantoms like the one developed in this thesis and other studies (15-17) can be used to assess the variability in CT perfusion parameter measurements computed from different software. It can also be used to assess the quality of image filtering. A physiological flow phantom that mimics tissue hemodynamics (flow, volume, and permeability) can potentially replace the physical phantom and digital phantom by evaluating measurements of CT perfusion parameters. However, research is needed to develop a physiological flow phantom that mimics tissue hemodynamics. Such a phantom can be used for accreditation of CT perfusion imaging across sites (13). By establishing this QA framework, we hypothesize that tolerance limits and best practices guidelines can be established.
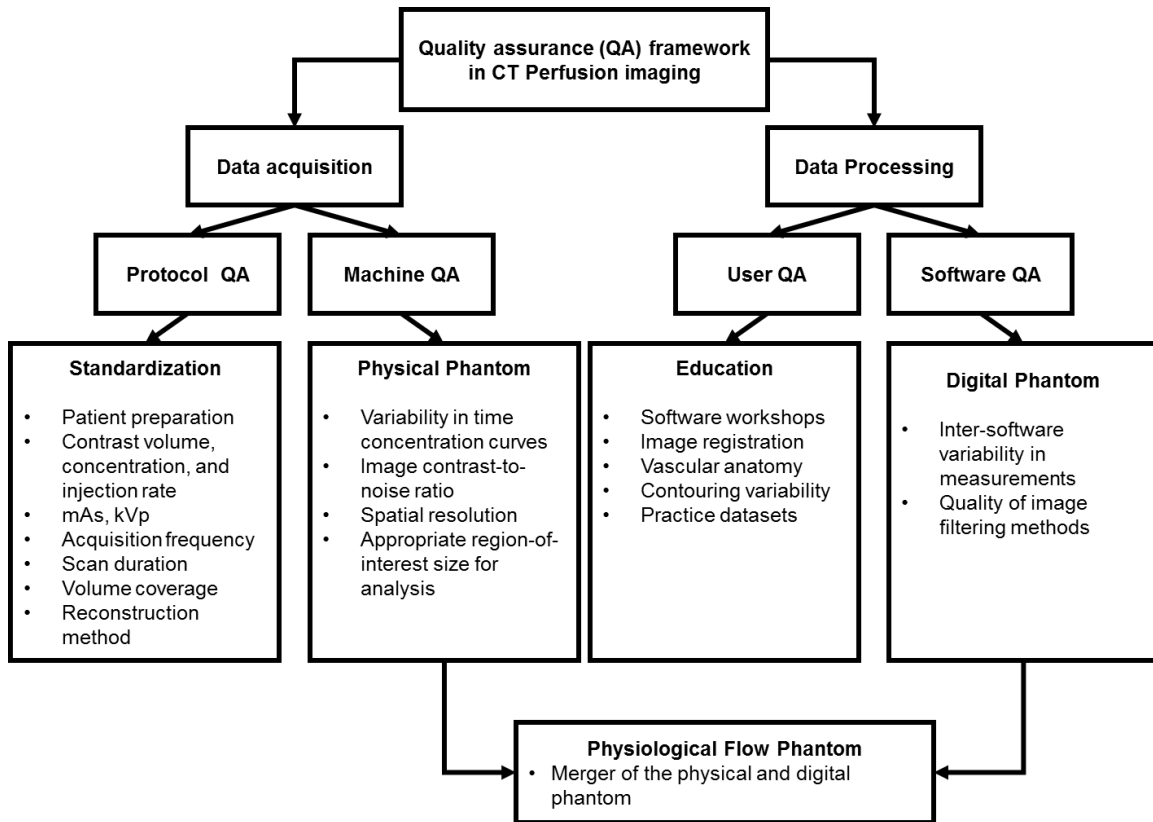
Figure 7-1: Quality assurance (QA) framework in CT perfusion imaging.

7.3.2   Delineating a Biologic Target Volume (BTV) in Radiotherapy

Our results point to a mismatch between regions of contrast enhancement and regions of high BF, BV, and PS in some patients with malignant gliomas. The potential application of using BF, BV, and PS maps for radiotherapy treatment planning warrants further investigations. Two important research questions need to be answered:

a. Will maps of BF, BV, and PS affect radiation oncologists' decision in defining a target volume for radiotherapy?

b. Will targeting a biological target volume based on these CT perfusion maps improve treatment outcomes when compared to conventional targeting of the gross tumour volume?

The above questions can potentially change clinical practice and the care of patients with malignant gliomas.

7.3.3 CT Perfusion Imaging to Monitor Response to Combined Anti-angiogenic Therapy, Radiotherapy, and Chemotherapy

Bevacizumab is an anti-angiogenic agent that is under active investigation for the treatment of newly diagnosed glioblastomas. Results from a randomized placebo-controlled trial showed that Bevacizumab did not prolong overall survival compared to conventional treatments (18). Bevacizumab treatments in this trial started during week four of radiotherapy. However, preclinical evidence showed that judicious timing of anti-angiogenic agent **before** radiotherapy could exert a synergistic effect on tumour control suggesting further optimization of radiotherapy and bevacizumab combinations may be possible (19). Further work could examine the combined effects of radiotherapy and Bevacizumab on tumour perfusion in pre-clinical models of glioma to further optimize the use of this agent. In doing so, the C6 glioma model may not be the optimal tumour model for this investigation because the efficacy of binding of Bevacizumab to rodent vascular endothelial growth factor (VEGF) is controversial (20-22). A xenograft model such as the human glioblastoma cell line U87MG model is a more appropriate tumour model to use in this investigation (23).

The ultimate goal remains to use functional imaging to tailor the appropriate treatments of cancer patients. It is hoped that the publications from this PhD dissertation will raise community awareness to the potential benefits of CT perfusion imaging – offering a readily accessible functional imaging modality that might personalize cancer treatments for patients affected by this disease.

7.3.4   References

1.   Ng CS, Hobbs BP, Chandler AG, et al. Metastases to the liver from neuroendocrine tumors: effect of duration of scan acquisition on CT perfusion values. Radiology. 2013; 269:758-67.

2.   Ng CS, Chandler AG, Wei W, et al. Effect of duration of scan acquisition on CT perfusion parameter values in primary and metastatic tumors in the lung. Eur J Radiol. 2013; 82:1811-8.

3.   Wintermark M, Smith WS, Ko NU, et al. Dynamic perfusion CT: optimizing the temporal resolution and contrast volume for calculation of perfusion CT parameters in stroke patients. AJNR Am J Neuroradiol 2004; 25:720–729.

4.   Wiesmann M, Berg S, Bohner G, et al. Dose reduction in dynamic perfusion CT of the brain: effects of the scan frequency on measurements of cerebral blood flow, cerebral blood volume, and mean transit time. Eur Radiol 2008; 18:2967–2974.

5.   Goh V, Liaw J, Bartram CI, et al. Effect of temporal interval between scan acquisitions on quantitative vascular parameters in colorectal cancer: Implications for helical volumetric perfusion CT techniques. AJR Am J Roentgenol 2008; 191:W288–W292

6.   Ling CC, Humm J, Larson S, et al. Towards multidimensional radiotherapy (MD-CRT): biological imaging and biological conformality. Int J Radiat Oncol Biol Phys. 2000; 47:551-60.

7.   Grosu AL, Weber WA, Franz M, et al. Reirradiation of recurrent high-grade gliomas using amino acid PET (SPECT)/CT/MRI image fusion to determine gross tumor volume for stereotactic fractionated radiotherapy. Int J Radiat Oncol Biol Phys. 2005; 63:511–9.

8.   Grosu AL, Weber WA, Riedel E, et al. L-(methyl-11C) methionine positron emission tomography for target delineation in resected high-grade gliomas before radiotherapy. Int J Radiat Oncol Biol Phys 2005; 63:64–74.

9.   Grosu AL, Feldmann H, Dick S, et al. Implications of IMT-SPECT for postoperative radiotherapy planning in patients with gliomas. Int J Radiat Oncol Biol Phys. 2002; 54:842–54.

10. Grosu AL, Weber W, Feldmann HJ, et al. First experience with I-123-alpha-methyl-tyrosine spect in the 3-D radiation treatment planning of brain gliomas. Int J Radiat Oncol Biol Phys. 2000; 47:517–26.

11. Franceschi E, Tosoni A, Bartolini S, Mazzocchi V, Fioravanti A, Brandes AA. Treatment options for recurrent glioblastoma: pitfalls and future trends. Expert Rev Anticancer Ther. 2009; 9:613-9.

12. Miles KA, Lee TY, Goh V, et al. Current status and guidelines for the assessment of tumour vascular support with dynamic contrast-enhanced computed tomography. Eur Radiol. 2012; 22:1430-41.

13. Driscoll B, Keller H, Jaffray D, Coolens C. Development of a dynamic quality assurance testing protocol for multisite clinical trial DCE-CT accreditation. Med Phys. 2013; 40:081906.

14. Driscoll B, Keller H, Coolens C. Development of a dynamic flow imaging phantom for dynamic contrast-enhanced CT. Med Phys. 2011; 38:4866-80.

15. Kudo K, Christensen S, Sasaki M, et al. Accuracy and reliability assessment of CT and MR perfusion analysis software using a digital phantom. Radiology. 2013;267(1):201-211.

16. van den Boom R, Manniesing R, Oei MTH, et al. A 4D digital phantom for patient-specific simulation of brain CT perfusion protocols. Med Phys. 2014; 41:071907.

17. Riordan AJ, Propkop M, Viergever MA, Dankbaar JW, Smit EJ, de Jon HWAM. Validation of CT brain perfusion methods using a realistic dynamic head phantom. Med Phys. 2011; 38:3212.

18. Gilbert MR, Dignam JJ, Armstrong TS, et al. A randomized trial of bevacizumab for newly diagnosed glioblastoma. N Engl J Med. 2014; 370:699-708.

19. Truman, J. P., Garcia-Barros, M., Kaag, M., et al. Endothelial membrane remodeling is obligate for anti-angiogenic radiosensitization during tumor radiosurgery. PloS One. 2010; 5:1-11.

20. Bock F, Onderka J, Dietrich T, et al. Bevacizumab as a potent inhibitor of inflammatory corneal angiogenesis and lymphangiogenesis. Invest Ophthalmol Vis Sci. 2007; 48:2545-52.

21. Yu L, Wu X, Cheng Z, et al. Interaction between bevacizumab and murine VEGF-A: a reassessment. Invest Ophthalmol Vis Sci. 2008; 49:522-7.

22. Gwak SJ, An SS, Yang MS, et al. Effect of combined bevacizumab and temozolomide treatment on intramedullary spinal cord tumor. Spine (Phila Pa 1976). 2014; 39:E65-73.

23. von Baumgarten L, Brucker D, Tirniceru A, et al. Bevacizumab has differential and dose-dependent effects on glioma blood vessels and tumor cells. Clin Cancer Res. 2011; 17:6192-205.

Appendix

Appendix A: Animal Ethics Approval for the Work Contained Within Chapter 4

January 20, 2010

This is the Original Approval for this protocol
A Full Protocol submission will be required in 2014

Dear Dr. Lee:

Your Animal Use Protocol form entitled:
Monitoring the radiation therapy treatment effect on the growth of C6 glioma brain tumors using clinical CT high resolution imaging
Funding Agency Internal

has been approved by the University Council on Animal Care. This approval is valid from **January 20, 2010 to January 31, 2011.** The protocol number for this project is **#2010-009 which replaces #2004-063.**

1. This number must be indicated when ordering animals for this project.
2. Animals for other projects may not be ordered under this number.
3. If no number appears please contact this office when grant approval is received.
    If the application for funding is not successful and you wish to proceed with the project, request that an internal scientific peer review be performed by the Animal Use Subcommittee office.
4. Purchases of animals other than through this system must be cleared through the ACVS office. Health certificates will be required.

ANIMALS APPROVED FOR 4 Years

Species	4 Year Total Numbers Estimated as Required	List All Strain(s)	Age / Weight
Rat	88	Wistar	200 - 250g

REQUIREMENTS/COMMENTS
Please ensure that individual(s) performing procedures on live animals, as described in this protocol, are familiar with the contents of this document.
The holder of this Animal Use Protocol is responsible to ensure that all associated safety components (biosafety, radiation safety, general laboratory safety) comply with institutional safety standards and have received all necessary approvals. Please consult directly with your institutional safety officers.

c.c. Approved Protocol   - T. Lee, J. Hadway, W. Lagerwerf
        Approval Letter   - T. Lee, J. Hadway, W. Lagerwerf

Appendix B: Human Ethics Approval for the Work Contained within Chapter 5

Western Research

Research Ethics

Use of Human Participants - Ethics Approval Notice

Principal Investigator: Dr. Glenn Bauman
File Number:4117
Review Level: Full Board
Protocol Title: Development of Radiation Treatment Planning Using Biologic and Anatomic Imaging for Malignant Glioma
Department & Institution: Schulich School of Medicine and Dentistry\Oncology,London Regional Cancer Program
Sponsor: Brain Tumour Foundation of Canada

Ethics Approval Date: December 03, 2013
Ethics Expiry Date: December 31, 2017

Documents Reviewed & Approved & Documents Received for Information:

Document Name	Comments	Version Date
Updated Approval		

This is to notify you that the University of Western Ontario Health Sciences Research Ethics Board (HSREB) which is organized and operates according to the Tri-Council Policy Statement: Ethical Conduct of Research Involving Humans and the Health Canada/ICH Good Clinical Practice Practices: Consolidated Guidelines; and the applicable laws and regulations of Ontario has reviewed and granted approval to the above referenced study on the approval date noted above. The membership of this HSREB also complies with the membership requirements for REB's as defined in Division 5 of the Food and Drug Regulations.

The ethics approval for this study shall remain valid until the expiry date noted above assuming timely and acceptable responses to the HSREB's periodic requests for surveillance and monitoring information. If you require an updated approval notice prior to that time you must request it using the University of Western Ontario Updated Approval Request form.

Member of the HSREB that are named as investigators in research studies, or declare a conflict of interest, do not participate in discussions related to, nor vote on, such studies when they are presented to the HSREB.

The Chair of the HSREB is Dr. Joseph Gilbert. The HSREB is registered with the U.S. Department of Health & Human Services under the IRB registration number IRB 00000940.

This is an official document. Please retain the original in your files.

Appendix C: Human Ethics Approval for the Work Contained Within Chapter 6

SERVIZIO SANITARIO REGIONALE
EMILIA-ROMAGNA
Azienda Ospedaliero - Universitaria di Ferrara

università di ferrara

SERVIZIO SANITARIO REGIONALE
EMILIA- ROMAGNA
Azienda Unità Sanitaria Locale di Ferrara

COMITATO ETICO DELLA PROVINCIA DI FERRARA

Ferrara, 29 gennaio 2009

"A primary brain tumours registry as a framework for promoting clinical research in Neuro-Oncology: Project of Emilia-Romagna region on Neuro-Oncology (PERNO). Valutazione delle capacità diagnostiche e prognostiche della tomografia computerizzata di perfusione."

Proponente responsabile: Prof. R. TAMAROZZI, Dipartimento di Neuroscienze/Riabilitazione, Unità Operativa di Neuroradiologia, Azienda Ospedaliero-Universitaria Arcispedale "S. Anna", Ferrara; Dott. E. FAINARDI, Dipartimento di Neuroscienze/Riabilitazione, Unità Operativa di Neuroradiologia, Azienda Ospedaliero-Universitaria Arcispedale "S. Anna", Ferrara.

Staff operativo: Dott. R. TAMAROZZI, Dott. E. FAINARDI, Dott. M. BORRELLI, Dott. F. CALZOLARI, Dott. S. CERUTI, Dott. A. SALETTI, U.O. di Neuroradiologia, Dipartimento di Neuroscienze/Riabilitazione, Azienda Ospedaliero-Universitaria Arcispedale "S.Anna", Ferrara

Ditta/sponsor: Programma di ricerca Regione-Università 2007-2009 (Area 1ª – Innovative Research)

Codice identificativo del piano clinico generale: PERNO

Specialità medicinale (nome o sigla): / /

Principio/i attivo/i: / /

Codice CAS (ove disponibile): / /

Classe farmacologica di appartenenza: / /

Codice ATC proposto (secondo codifica OMS): / /

Codice ICD: / /

Fase della sperimentazione clinica: / /

191

SERVIZIO SANITARIO REGIONALE
EMILIA-ROMAGNA
Azienda Ospedaliero - Universitaria di Ferrara

università di ferrara
DA SEICENTO ANNI GUARDIAMO AVANTI

SERVIZIO SANITARIO REGIONALE
EMILIA- ROMAGNA
Azienda Unità Sanitaria Locale di Ferrara

COMITATO ETICO DELLA PROVINCIA DI FERRARA

Indicazione proposta: si tratta di uno studio volto alla valutazione delle capacità diagnostiche della Tomografia Computerizzata (TC) e a verificare se la TC di Perfusione (TCP) può essere utile per distinguere i tumori primitivi cerebrali da altri tipi di lesione, per guidare la biopsia stereotassica e la resezione chirurgica, per distinguere fra la recidiva tumorale e il tessuto reso non più vitale dalla radioterapia, per predire la evoluzione del tumore, per monitorare la risposta alla terapia radiante e alla chemioterapia. La ricerca è anche orientata a chiarire se la TCP può essere di aiuto nella programmazione pre- e post operatoria, nel caso in cui correli con i dati clinici e, quando possibile, con i reperti Risonanza Magnetica Perfusionale (MR-PWI).

Forma farmaceutica: / /

Via di somministrazione: / /

Durata dello studio: 3 anni.

Schema dello studio e posologia: il disegno dello studio prevede due fasi:

1) la fase pre-operatoria riguarderà i pazienti con lesione espansiva sopratentoriale isolata, indicativa di tumore cerebrale intra-assiale: in questa prima fase saranno inclusi tutti pazienti con masse solitarie cerebrali sopratentoriali ammessi nel centro di Ferrara con indagini TC e/o MRI convenzionali che suggeriscono la diagnosi di sospetto tumore primitivo cerebrale. Tutti i pazienti inclusi in questa parte della ricerca verranno sottoposti ad uno studio TCP e ad un'indagine MR-PWI subito dopo l'ingresso. In tutti pazienti sottoposti a rimozione chirurgica del tumore verrà eseguito uno studio TC standard con un somministrazione endovenosa di mezzo di contrasto iodato entro 48 ore dall'operazione, per verificare la presenza di eventuali residui tumorali.

2) La fase post-operatoria interesserà i pazienti con glioma a basso ed alto grado a sede sovratentoriale, confermato istologicamente dopo resezione chirurgica o biopsia stereotassica. In tutti pazienti ammessi alla seconda parte dello studio, il deterioramento clinico o l'aumento della dimensione della lesione riscontrato con risonanza magnetica, saranno ritenuti indicatori di recidiva tumorale.

Tutti i pazienti saranno sottoposti a controlli TCP e/o MR-PWI sequenziali nel tempo, programmati:
a) ogni 3 mesi dall'intervento chirurgico per il primo anno;
b) ogni 6 mesi nei due anni successivi.

COMITATO ETICO DELLA PROVINCIA DI FERRARA

In tutti i pazienti con glioma ad alto grado sottoposti a radioterapia e/o chemioterapia post-operatoria verranno effettuati controlli con TCP e/o MR-PWI longitudinali nel tempo programmati: a) a 1 e a 3 mesi dal termine del trattamento; b) ogni 3-6 mesi successivamente.

In fase sia pre-operatoria che post-operatoria la performance verrà valutata in tutti i pazienti selezionati per lo studio utilizzando le scale di valutazione clinica correntemente accettate e, in particolare, il Karnofsky performance status.

Gli esami TC e MRI standard saranno valutati da due medici neuroradiologi che non saranno a conoscenza dei risultati della TCP e della MR-PWI, mentre le mappe di TCP e di MR-PWI saranno generate da medici che non saranno a conoscenza dei dati clinici e del quadro radiologico dei pazienti. Al termine dello studio tutti i risultati emersi dalle indagini TCP verranno confrontati e correlati con i dati provenienti dagli esami PWI e con quelli clinico-epidemiologici, molecolari e neurofisiologici acquisiti nelle altre unità. Le indagini TCP e MR-PWI saranno eseguite in accordo con protocolli precedentemente convalidati nella letteratura scientifica specifica.

In tutti i pazienti reclutati nei diversi stadi della ricerca gli studi di TCP saranno realizzati secondo il metodo di "first pass bolus-traking", che analizza l'effetto prodotto dal primo passaggio di un bolo di mezzo di contatto attraverso il letto vascolare cerebrale, utilizzando un apparecchio TC a scansione singola o multipla equipaggiato con un software dedicato per TCP. Per ogni paziente, in ciascuno degli intervalli temporali stabiliti in fase pre- e/o post-operatoria, verranno generate mappe perfusionali di flusso ematico cerebrale (CBF) di CBV, di tempo di transito medio (MTT) e di flusso di permeabilità di superficie (PSF) per misurare la permeabilità microvascolare.

Studi MR-PWI - in tutti i pazienti inclusi nelle varie fasi del progetto gli studi di MR-PWI verranno eseguiti secondo la metodologia del "Dynamic Susceptibility Contrast" (DSC), che misura ancora una volta l'effetto determinato dal primo passaggio di un bolo di mezzo di contrasto attraverso il letto vascolare cerebrale, impiegando una unità di risonanza magnetica da 1.5 Tesla equipaggiata con un software dedicato per la PWI. Per ogni paziente, in ciascuno degli intervalli temporali stabiliti in fase pre- e/o post-operatoria, verranno generate mappe perfusionali di CBV. Se possibile, negli stessi pazienti e nelle medesime fasi dello studio, verranno anche create mappe di "volume transfer constant" (K^{trans}), utili per la valutazione della permeabilità microvascolare, usando il metodo del "Dynamic Contrast-Enhanced (DCE)"

In ogni sezione in cui il tessuto tumorale senza o con accentuazione contrastografica sarà visibile, i parametri TCP e MR-PWI saranno misurati in due differenti regioni di interesse disegnate a mano libera sulla singola sezione della TC o MRI di base: 1) il tessuto tumorale con o senza accentuazione contrastografica; 2) un'area di tessuto nervoso apparentemente sano situata nell'emisfero controlaterale, disposta simmetricamente alla neoplasia e corrispondente alla zona lesionale.

Eventuale terapia concomitante: / /

AIC in Italia: / /
    all'estero: / /

Indicazioni all'AIC, posologia, vie di somministrazione e forme farmaceutiche autorizzate: / /

SERVIZIO SANITARIO REGIONALE
EMILIA-ROMAGNA
Azienda Ospedaliero - Universitaria di Ferrara

università di ferrara
DA SEICENTO ANNI GUARDIAMO AVANTI

SERVIZIO SANITARIO REGIONALE
EMILIA- ROMAGNA
Azienda Unità Sanitaria Locale di Ferrara

COMITATO ETICO DELLA PROVINCIA DI FERRARA

Precedenti approvazioni/autorizzazioni alla sperimentazione per la stessa indicazione proposta: /   / /

Obiettivo/i dello/degli studio/i:
Primari:
- verificare se l'approccio multiparametrico con TCP può servire per:
  1. distinguere i tumori primitivi cerebrali da altri tipi di lesione che simulano il tumore, quali le infezioni, le lesioni demielinizzanti tumescenti e le lesioni ischemiche;
  2. discriminare i gliomi da altre lesioni neoplastiche solitarie intra-assiali cerebrali come i linfomi e le metastasi;
  3. differenziare i gliomi ad alto grado da quelli a basso grado;
  4. guidare la biopsia stereotassica e la resezione chirurgica verso la porzione più aggressiva del tumore;
  5. diversificare fra la recidiva tumorale e la necrosi da radiazioni;
  6. predire l'evoluzione del tumore;
  7. monitorare la risposta alla terapia radiante e alla chemioterapia.

Secondari:
  1. chiarire se la tecnologia TCP può essere di aiuto nella programmazione pre-chirurgica e nella pianificazione post-operatoria;
  2. comprendere se esistano correlazioni fra i dati TCP e quelli clinici, molecolari e MR-PWI.

Tipologia dei soggetti da arruolare
(specificare se pazienti o volontari sani): saranno arruolati pazienti di entrambi i sessi, maggiorenni. Nella prima fase pre-operatoria dello studio saranno inclusi tutti i pazienti con masse solitarie cerebrali sopratentoriali ammessi nel nostro centro con indagini TC e/o la MRI convenzionali che suggeriscono la diagnosi di sospetto tumore primitivo cerebrale.
Nella seconda fase post-operatoria dello studio verranno inclusi tutti i pazienti con glioma a basso ed alto grado confermato istologicamente dopo resezione chirurgica o biopsia stereotassica.

Numero dei soggetti da arruolare: lo studio prevede l'inclusione di almeno 100 pazienti nella prima fase pre-operatoria e di almeno 50 pazienti con glomi ad alto e basso grado di malignità e di almeno 30 pazienti con glomi ad alto grado di aggressività sottoposto a radioterapia in quella post-operatoria.

194

COMITATO ETICO DELLA PROVINCIA DI FERRARA

Informazione al candidato: mediante scheda informativa, nella quale si riportano notizie sulla natura, durata e scopo dello studio, nonché il rapporto rischio/beneficio.

L'informazione del paziente, in virtù della propedeuticità di tale fase, dovrà essere fornita in un momento formalmente distinto dal recepimento del consenso.

Si raccomanda che l'avvenuta informazione venga formalizzata su cartella clinica o su scheda personale del paziente (in alternativa su modulo che ne faccia parte integrante), riportando contestualmente data e firma del medico sperimentatore e dell'arruolando stesso.

Recepimento del consenso: mediante apposito modulo

Si raccomanda che il recepimento del consenso/dissenso avvenga in un momento formalmente distinto dalla fase informativa e ad essa successivo e venga formalizzato su cartella clinica o su scheda personale del paziente (oppure su modulo che ne faccia parte integrante).

Criteri di inclusione/esclusione:

criteri di inclusione:

Fase pre-operatoria: in questa prima fase verranno arruolati nello studio tutti i pazienti che soddisferanno i seguenti criteri di inclusione:

- età maggiore o uguale a 18 anni;
- assenza di instabilità dei parametri clinici (agitazione, disorientamento, coma ed altri segni di grave ipertensione endocranica);
- assenza di segni riferibili a gravidanza in atto;
- assenza di controindicazioni alla TC ed alla MRI comprese quelle riguardanti la somministrazione intravenosa di contrasto iodato o di Gadolinio chelato;
- disponibilità dei dati clinici, compresa una valutazione della severità della malattia mediante il Karnofsky performance status.

Fase post-operatoria: in questa seconda fase verranno inclusi:

- tutti i pazienti con glioma a basso ed alto grado confermato istologicamente dopo resezione chirurgica o biopsia stereotassica.

Criteri di esclusione:

Fase pre-operatoria: in questa prima fase verranno esclusi dallo studio tutti i pazienti con le seguenti caratteristiche:

- età minore di 18 anni;
- presenza di instabilità dei parametri clinici (agitazione, disorientamento, coma ed altri segni di grave ipertensione endocranica);
- presenza di segni riferibili a gravidanza in atto;
- presenza di controindicazioni alla TC ed alla MRI comprese quelle riguardanti la somministrazione intravenosa di contrasto iodato o di Gadolinio chelato;
- mancata disponibilità dei dati clinici, compresa una valutazione della severità della malattia mediante il Karnofsky performance status.

SERVIZIO SANITARIO REGIONALE
EMILIA-ROMAGNA
Azienda Ospedaliero - Universitaria di Ferrara

università di ferrara

SERVIZIO SANITARIO REGIONALE
EMILIA- ROMAGNA
Azienda Unità Sanitaria Locale di Ferrara

COMITATO ETICO DELLA PROVINCIA DI FERRARA

Fase post-operatoria: in questa seconda fase verranno inclusi:
- tutti i pazienti con glioma a basso ed alto grado confermato istologicamente dopo resezione chirurgica o biopsia stereotassica.

Sorveglianza clinica: / /

Modalità di sospensione: è prevista l'interruzione dello studio qualora si verifichino eventi avversi, su decisione del medico sperimentatore e, comunque, per libera scelta e disposizione dell'arruolato.

Il Comitato Etico esprime parere favorevole allo studio proposto, ove siano soddisfatti i prerequisiti etici nei termini innanzi richiesti.
Si ricorda al proponente responsabile la necessità di comunicare alla Segreteria Tecnico-Scientifica del Comitato Etico la fine dello studio, nonché di trasmettere copia di eventuale/i pubblicazione/i ovvero del report finale.

Si dà atto che il Comitato Etico ha preso visione della seguente documentazione:
- n. 1 copia di lettera d'intenti;
- n. 1 copia di protocollo di studio;
- n. 1 copia di sinossi del protocollo di studio;
- n. 1 copia di foglio informativo per il paziente;
- n. 1 copia di modulo di consenso;
- n. 1 copia di lettera per il medico d base;
- n. 1 copia di approvazione definitiva del progetto di ricerca da parte dell'Agenzia Sanitaria Regionale;
- n. 1 copia di elenco dei centri partecipanti.

Il Presidente del Comitato Etico
(Prof. Adalberto Ciaccia)

Appendix D: Permission to Reproduce Previously Published Materials

ASPET
Transforming Discoveries into Therapies

June 23, 2014

Timothy Yeung

Dear Timothy Yeung:

This is to grant you permission to reproduce the following figure in your thesis entitled "Functional Imaging of Malignant Gliomas with CT Perfusion" for the University of Western Ontario:

> Figure 1 from Brian T. Hawkins and Thomas P. Davis, The Blood-Brain Barrier/Neurovascular Unit in Health and Disease, *Pharmacol Rev* June 2005 57:173-185

Permission to reproduce the figure is granted for worldwide use in all languages, translations, and editions, and in any format or medium including print and electronic. The authors and the source of the materials must be cited in full, including the article title, journal title, volume, year, and page numbers.

Sincerely yours,

Richard Dodenhoff
Journals Director

AMERICAN SOCIETY OF CLINICAL ONCOLOGY LICENSE
TERMS AND CONDITIONS

Jun 21, 2014

This is a License Agreement between Timothy Pok Chi Yeung ("You") and American Society of Clinical Oncology ("American Society of Clinical Oncology") provided by Copyright Clearance Center ("CCC"). The license consists of your order details, the terms and conditions provided by American Society of Clinical Oncology, and the payment terms and conditions.

All payments must be made in full to CCC. For payment instructions, please see information listed at the bottom of this form.

License Number	3413910641083
License date	Jun 21, 2014
Licensed content publisher	American Society of Clinical Oncology
Licensed content publication	The Journal of Clinical Oncology
Licensed content title	Updated Response Assessment Criteria for High-Grade Gliomas: Response Assessment in Neuro-Oncology Working Group
Licensed content author	Patrick Y. Wen, David R. Macdonald, David A. Reardon, Timothy F. Cloughesy, A. Gregory Sorensen, Evanthia Galanis, John DeGroot, Wolfgang Wick, Mark R. Gilbert, Andrew B. Lassman, Christina Tsien, Tom Mikkelsen, Eric T. Wong, Marc C. Chamberlain, Roger Stupp, Kathleen R. Lamborn, Michael A. Vogelbaum, Martin J. van den Bent, Susan M. Chang
Licensed content date	Apr 10, 2010
Type of Use	Dissertation/Thesis
Geographic Rights	North American
Will you be translating?	No
Title of your thesis / dissertation	Functional Imaging of Malignant Gliomas with CT Perfusion
Expected completion date	Aug 2014
Estimated size(pages)	300
Billing Type	Invoice
Billing address	
Total	0.00 USD

Terms and Conditions

General Terms& Conditions

Permission is granted upon the requester's compliance with the following terms and

conditions:

1. A creditline willbe prominently placed in your product(s) andinclude: for books-the author, book title, editor, copyright holder,year ofpublication; for journals-the author, title of article, title ofjournal,volume number, issue number, and the inclusive pages. The credit line must include the followingwording: "Reprinted with permission. © (Year of publication being used) AmericanSociety of Clinical Oncology. Allrights reserved." Thecitation format must be as follows:Author last name, first initial et al: J Clin Oncol (or substituteappropriatetitle) Vol. (Issue), Year: Page-Page.

2. The requesterwarrants that the material shall not be used inany manner that may be derogatory to the title, content, or authors ofthematerial or to ASCO, including but not limited to an association with(i)conduct that is fraudulent or otherwise illegal; or   (ii) the use or abuse ofalcohol, cigarettes, or illegal drugs.

3. Permission isgranted for the term (for Books/CDs-Shelf Life;for Internet/Intranet-In perpetuity; for all other forms of print-thelife ofthe title) and purpose specified in your request. Once term has expired, permission to renewmust be made in writing.

4. Permission grantedis nonexclusive, and is valid throughout theworld in English and the languages specified in your original request. A new permission must berequested forrevisions of the publication under current consideration.

5. ASCO cannot supplythe requester with the original artwork or a"clean copy."

6.If the ASCO material is to be translated, the following linesmust be included: Theauthors, editors,and ASCO are not responsible for errors or omissions in translations.

v1.3

If you would like to pay for this license now, please remit this license along with your payment made payable to "COPYRIGHT CLEARANCE CENTER" otherwise you will be invoiced within 48 hours of the license date. Payment should be in the form of a check or money order referencing your account number and this invoice number 501333662. Once you receive your invoice for this order, you may pay your invoice by credit card. Please follow instructions provided at that time.

Make Payment To:

Gratis licenses (referencing $0 in the Total field) are free. Please retain this printable license for your reference. No payment is required.

ELSEVIER LICENSE
TERMS AND CONDITIONS

Jun 21, 2014

This is a License Agreement between Timothy Pok Chi Yeung ("You") and Elsevier ("Elsevier") provided by Copyright Clearance Center ("CCC"). The license consists of your order details, the terms and conditions provided by Elsevier, and the payment terms and conditions.

All payments must be made in full to CCC. For payment instructions, please see information listed at the bottom of this form.

Supplier	Elsevier Limited
Registered Company Number	1982084
Customer name	Timothy Pok Chi Yeung
Customer address	
License number	3413910957754
License date	Jun 21, 2014
Licensed content publisher	Elsevier
Licensed content publication	Academic Radiology
Licensed content title	The Effect of Scan Duration on the Measurement of Perfusion Parameters in CT Perfusion Studies of Brain Tumors
Licensed content author	Timothy Pok Chi Yeung,Slav Yartsev,Glenn Bauman,Wenqing He,Enrico Fainardi,Ting-Yim Lee
Licensed content date	January 2013
Licensed content volume number	20
Licensed content issue number	1
Number of pages	7
Start Page	59
End Page	65
Type of Use	reuse in a thesis/dissertation
Intended publisher of new work	other
Portion	full article
Format	both print and electronic
Are you the author of this	Yes

Elsevier article?	
Will you be translating?	No
Title of your thesis/dissertation	Functional Imaging of Malignant Gliomas with CT Perfusion
Expected completion date	Aug 2014
Estimated size (number of pages)	300
Elsevier VAT number	GB 494 6272 12
Permissions price	0.00 USD
VAT/Local Sales Tax	0.00 USD / 0.00 GBP
Total	0.00 USD
Terms and Conditions	

INTRODUCTION

1. The publisher for this copyrighted material is Elsevier. By clicking "accept" in connection with completing this licensing transaction, you agree that the following terms and conditions apply to this transaction (along with the Billing and Payment terms and conditions established by Copyright Clearance Center, Inc. ("CCC"), at the time that you opened your Rightslink account and that are available at any time at http://myaccount.copyright.com).

GENERAL TERMS

2. Elsevier hereby grants you permission to reproduce the aforementioned material subject to the terms and conditions indicated.

3. Acknowledgement: If any part of the material to be used (for example, figures) has appeared in our publication with credit or acknowledgement to another source, permission must also be sought from that source. If such permission is not obtained then that material may not be included in your publication/copies. Suitable acknowledgement to the source must be made, either as a footnote or in a reference list at the end of your publication, as follows:

"Reprinted from Publication title, Vol /edition number, Author(s), Title of article / title of chapter, Pages No., Copyright (Year), with permission from Elsevier [OR APPLICABLE SOCIETY COPYRIGHT OWNER]." Also Lancet special credit - "Reprinted from The Lancet, Vol. number, Author(s), Title of article, Pages No., Copyright (Year), with permission from Elsevier."

4. Reproduction of this material is confined to the purpose and/or media for which permission is hereby given.

5. Altering/Modifying Material: Not Permitted. However figures and illustrations may be altered/adapted minimally to serve your work. Any other abbreviations, additions, deletions and/or any other alterations shall be made only with prior written authorization of Elsevier Ltd.

6. If the permission fee for the requested use of our material is waived in this instance, please be advised that your future requests for Elsevier materials may attract a fee.

7. Reservation of Rights: Publisher reserves all rights not specifically granted in the combination of (i) the license details provided by you and accepted in the course of this licensing transaction, (ii) these terms and conditions and (iii) CCC's Billing and Payment terms and conditions.

8. License Contingent Upon Payment: While you may exercise the rights licensed immediately upon issuance of the license at the end of the licensing process for the transaction, provided that you have disclosed complete and accurate details of your proposed use, no license is finally effective unless and until full payment is received from you (either by publisher or by CCC) as provided in CCC's Billing and Payment terms and conditions. If full payment is not received on a timely basis, then any license preliminarily granted shall be deemed automatically revoked and shall be void as if never granted. Further, in the event that you breach any of these terms and conditions or any of CCC's Billing and Payment terms and conditions, the license is automatically revoked and shall be void as if never granted. Use of materials as described in a revoked license, as well as any use of the materials beyond the scope of an unrevoked license, may constitute copyright infringement and publisher reserves the right to take any and all action to protect its copyright in the materials.

9. Warranties: Publisher makes no representations or warranties with respect to the licensed material.

10. Indemnity: You hereby indemnify and agree to hold harmless publisher and CCC, and their respective officers, directors, employees and agents, from and against any and all claims arising out of your use of the licensed material other than as specifically authorized pursuant to this license.

11. No Transfer of License: This license is personal to you and may not be sublicensed, assigned, or transferred by you to any other person without publisher's written permission.

12. No Amendment Except in Writing: This license may not be amended except in a writing signed by both parties (or, in the case of publisher, by CCC on publisher's behalf).

13. Objection to Contrary Terms: Publisher hereby objects to any terms contained in any purchase order, acknowledgment, check endorsement or other writing prepared by you, which terms are inconsistent with these terms and conditions or CCC's Billing and Payment terms and conditions. These terms and conditions, together with CCC's Billing and Payment terms and conditions (which are incorporated herein), comprise the entire agreement between you and publisher (and CCC) concerning this licensing transaction. In the event of any conflict between your obligations established by these terms and conditions and those established by CCC's Billing and Payment terms and conditions, these terms and conditions shall control.

14. Revocation: Elsevier or Copyright Clearance Center may deny the permissions described in this License at their sole discretion, for any reason or no reason, with a full refund payable to you. Notice of such denial will be made using the contact information provided by you. Failure to receive such notice will not alter or invalidate the denial. In no event will Elsevier or Copyright Clearance Center be responsible or liable for any costs, expenses or damage incurred by you as a result of a denial of your permission request, other than a refund of the amount(s) paid by you to Elsevier and/or Copyright Clearance Center for denied permissions.

LIMITED LICENSE

The following terms and conditions apply only to specific license types:

15. **Translation**: This permission is granted for non-exclusive world **English** rights only unless your license was granted for translation rights. If you licensed translation rights you may only translate this content into the languages you requested. A professional translator must perform all translations and reproduce the content word for word preserving the integrity of the article. If this license is to re-use 1 or 2 figures then permission is granted for non-exclusive world rights in all languages.

16. **Posting licensed content on any Website**: The following terms and conditions apply as follows: Licensing material from an Elsevier journal: All content posted to the web site must maintain the copyright information line on the bottom of each image; A hyper-text must be included to the Homepage of the journal from which you are licensing at http://www.sciencedirect.com/science/journal/xxxxx or the Elsevier homepage for books at http://www.elsevier.com; Central Storage: This license does not include permission for a scanned version of the material to be stored in a central repository such as that provided by Heron/XanEdu.

Licensing material from an Elsevier book: A hyper-text link must be included to the Elsevier homepage at http://www.elsevier.com . All content posted to the web site must maintain the copyright information line on the bottom of each image.

Posting licensed content on Electronic reserve: In addition to the above the following clauses are applicable: The web site must be password-protected and made available only to bona fide students registered on a relevant course. This permission is granted for 1 year only. You may obtain a new license for future website posting.

For journal authors: the following clauses are applicable in addition to the above: Permission granted is limited to the author accepted manuscript version* of your paper.

***Accepted Author Manuscript (AAM) Definition**: An accepted author manuscript (AAM) is the author's version of the manuscript of an article that has been accepted for publication and which may include any author-incorporated changes suggested through the processes of submission processing, peer review, and editor-author communications. AAMs do not include other publisher value-added contributions such as copy-editing, formatting, technical enhancements and (if relevant) pagination.

You are not allowed to download and post the published journal article (whether PDF or HTML, proof or final version), nor may you scan the printed edition to create an electronic version. A hyper-text must be included to the Homepage of the journal from which you are licensing at http://www.sciencedirect.com/science/journal/xxxxx. As part of our normal production process, you will receive an e-mail notice when your article appears on Elsevier's online service ScienceDirect (www.sciencedirect.com). That e-mail will include the article's Digital Object Identifier (DOI). This number provides the electronic link to the published article and should be included in the posting of your personal version. We ask that you wait until you receive this e-mail and have the DOI to do any posting.

Posting to a repository: Authors may post their AAM immediately to their employer's

institutional repository for internal use only and may make their manuscript publically available after the journal-specific embargo period has ended.

Please also refer to Elsevier's Article Posting Policy for further information.

18. **For book authors** the following clauses are applicable in addition to the above: Authors are permitted to place a brief summary of their work online only.. You are not allowed to download and post the published electronic version of your chapter, nor may you scan the printed edition to create an electronic version. **Posting to a repository:** Authors are permitted to post a summary of their chapter only in their institution's repository.

20. **Thesis/Dissertation:** If your license is for use in a thesis/dissertation your thesis may be submitted to your institution in either print or electronic form. Should your thesis be published commercially, please reapply for permission. These requirements include permission for the Library and Archives of Canada to supply single copies, on demand, of the complete thesis and include permission for UMI to supply single copies, on demand, of the complete thesis. Should your thesis be published commercially, please reapply for permission.

Elsevier Open Access Terms and Conditions

Elsevier publishes Open Access articles in both its Open Access journals and via its Open Access articles option in subscription journals.

Authors publishing in an Open Access journal or who choose to make their article Open Access in an Elsevier subscription journal select one of the following Creative Commons user licenses, which define how a reader may reuse their work: Creative Commons Attribution License (CC BY), Creative Commons Attribution – Non Commercial - ShareAlike (CC BY NC SA) and Creative Commons Attribution – Non Commercial – No Derivatives (CC BY NC ND)

Terms & Conditions applicable to all Elsevier Open Access articles:

Any reuse of the article must not represent the author as endorsing the adaptation of the article nor should the article be modified in such a way as to damage the author's honour or reputation.

The author(s) must be appropriately credited.

If any part of the material to be used (for example, figures) has appeared in our publication with credit or acknowledgement to another source it is the responsibility of the user to ensure their reuse complies with the terms and conditions determined by the rights holder.

Additional Terms & Conditions applicable to each Creative Commons user license:

CC BY: You may distribute and copy the article, create extracts, abstracts, and other revised versions, adaptations or derivative works of or from an article (such as a translation), to include in a collective work (such as an anthology), to text or data mine the article, including for commercial purposes without permission from Elsevier

CC BY NC SA: For non-commercial purposes you may distribute and copy the article, create extracts, abstracts and other revised versions, adaptations or derivative works of or from an article (such as a translation), to include in a collective work (such as an anthology), to text and data mine the article and license new adaptations or creations under identical terms without permission from Elsevier

CC BY NC ND: For non-commercial purposes you may distribute and copy the article and include it in a collective work (such as an anthology), provided you do not alter or modify the article, without permission from Elsevier

Any commercial reuse of Open Access articles published with a CC BY NC SA or CC BY NC ND license requires permission from Elsevier and will be subject to a fee.

Commercial reuse includes:

- Promotional purposes (advertising or marketing)

- Commercial exploitation (e.g. a product for sale or loan)

- Systematic distribution (for a fee or free of charge)

Please refer to Elsevier's Open Access Policy for further information.

21. Other Conditions:

v1.7

If you would like to pay for this license now, please remit this license along with your payment made payable to "COPYRIGHT CLEARANCE CENTER" otherwise you will be invoiced within 48 hours of the license date. Payment should be in the form of a check or money order referencing your account number and this invoice number 501333664. Once you receive your invoice for this order, you may pay your invoice by credit card. Please follow instructions provided at that time.

Make Payment To:

Gratis licenses (referencing $0 in the Total field) are free. Please retain this printable license for your reference. No payment is required.

ELSEVIER LICENSE
TERMS AND CONDITIONS

Jun 21, 2014

This is a License Agreement between Timothy Pok Chi Yeung ("You") and Elsevier ("Elsevier") provided by Copyright Clearance Center ("CCC"). The license consists of your order details, the terms and conditions provided by Elsevier, and the payment terms and conditions.

All payments must be made in full to CCC. For payment instructions, please see information listed at the bottom of this form.

Supplier	Elsevier Limited
Registered Company Number	1982084
Customer name	Timothy Pok Chi Yeung
Customer address	
License number	3413910870699
License date	Jun 21, 2014
Licensed content publisher	Elsevier
Licensed content publication	Academic Radiology
Licensed content title	Improving Quantitative CT Perfusion Parameter Measurements Using Principal Component Analysis
Licensed content author	Timothy Pok Chi Yeung,Mark Dekaban,Nathan De Haan,Laura Morrison,Lisa Hoffman,Yves Bureau,Xiaogang Chen,Slav Yartsev,Glenn Bauman,Ting-Yim Lee
Licensed content date	May 2014
Licensed content volume number	21
Licensed content issue number	5
Number of pages	9
Start Page	624
End Page	632
Type of Use	reuse in a thesis/dissertation
Intended publisher of new work	other
Portion	full article
Format	both print and electronic

Are you the author of this Elsevier article?	Yes
Will you be translating?	No
Title of your thesis/dissertation	Functional Imaging of Malignant Gliomas with CT Perfusion
Expected completion date	Aug 2014
Estimated size (number of pages)	300
Elsevier VAT number	GB 494 6272 12
Permissions price	0.00 USD
VAT/Local Sales Tax	0.00 USD / 0.00 GBP
Total	0.00 USD

Terms and Conditions

INTRODUCTION

1. The publisher for this copyrighted material is Elsevier. By clicking "accept" in connection with completing this licensing transaction, you agree that the following terms and conditions apply to this transaction (along with the Billing and Payment terms and conditions established by Copyright Clearance Center, Inc. ("CCC"), at the time that you opened your Rightslink account and that are available at any time at http://myaccount.copyright.com).

GENERAL TERMS

2. Elsevier hereby grants you permission to reproduce the aforementioned material subject to the terms and conditions indicated.

3. Acknowledgement: If any part of the material to be used (for example, figures) has appeared in our publication with credit or acknowledgement to another source, permission must also be sought from that source. If such permission is not obtained then that material may not be included in your publication/copies. Suitable acknowledgement to the source must be made, either as a footnote or in a reference list at the end of your publication, as follows:

"Reprinted from Publication title, Vol /edition number, Author(s), Title of article / title of chapter, Pages No., Copyright (Year), with permission from Elsevier [OR APPLICABLE SOCIETY COPYRIGHT OWNER]." Also Lancet special credit - "Reprinted from The Lancet, Vol. number, Author(s), Title of article, Pages No., Copyright (Year), with permission from Elsevier."

4. Reproduction of this material is confined to the purpose and/or media for which permission is hereby given.

5. Altering/Modifying Material: Not Permitted. However figures and illustrations may be altered/adapted minimally to serve your work. Any other abbreviations, additions, deletions and/or any other alterations shall be made only with prior written authorization of Elsevier Ltd.

6. If the permission fee for the requested use of our material is waived in this instance, please be

advised that your future requests for Elsevier materials may attract a fee.

7. Reservation of Rights: Publisher reserves all rights not specifically granted in the combination of (i) the license details provided by you and accepted in the course of this licensing transaction, (ii) these terms and conditions and (iii) CCC's Billing and Payment terms and conditions.

8. License Contingent Upon Payment: While you may exercise the rights licensed immediately upon issuance of the license at the end of the licensing process for the transaction, provided that you have disclosed complete and accurate details of your proposed use, no license is finally effective unless and until full payment is received from you (either by publisher or by CCC) as provided in CCC's Billing and Payment terms and conditions. If full payment is not received on a timely basis, then any license preliminarily granted shall be deemed automatically revoked and shall be void as if never granted. Further, in the event that you breach any of these terms and conditions or any of CCC's Billing and Payment terms and conditions, the license is automatically revoked and shall be void as if never granted. Use of materials as described in a revoked license, as well as any use of the materials beyond the scope of an unrevoked license, may constitute copyright infringement and publisher reserves the right to take any and all action to protect its copyright in the materials.

9. Warranties: Publisher makes no representations or warranties with respect to the licensed material.

10. Indemnity: You hereby indemnify and agree to hold harmless publisher and CCC, and their respective officers, directors, employees and agents, from and against any and all claims arising out of your use of the licensed material other than as specifically authorized pursuant to this license.

11. No Transfer of License: This license is personal to you and may not be sublicensed, assigned, or transferred by you to any other person without publisher's written permission.

12. No Amendment Except in Writing: This license may not be amended except in a writing signed by both parties (or, in the case of publisher, by CCC on publisher's behalf).

13. Objection to Contrary Terms: Publisher hereby objects to any terms contained in any purchase order, acknowledgment, check endorsement or other writing prepared by you, which terms are inconsistent with these terms and conditions or CCC's Billing and Payment terms and conditions. These terms and conditions, together with CCC's Billing and Payment terms and conditions (which are incorporated herein), comprise the entire agreement between you and publisher (and CCC) concerning this licensing transaction. In the event of any conflict between your obligations established by these terms and conditions and those established by CCC's Billing and Payment terms and conditions, these terms and conditions shall control.

14. Revocation: Elsevier or Copyright Clearance Center may deny the permissions described in this License at their sole discretion, for any reason or no reason, with a full refund payable to you. Notice of such denial will be made using the contact information provided by you. Failure to receive such notice will not alter or invalidate the denial. In no event will Elsevier or Copyright Clearance Center be responsible or liable for any costs, expenses or damage incurred by you as a result of a denial of your permission request, other than a refund of the amount(s) paid by you to Elsevier and/or Copyright Clearance Center for denied permissions.

LIMITED LICENSE

The following terms and conditions apply only to specific license types:

15. **Translation**: This permission is granted for non-exclusive world **English** rights only unless your license was granted for translation rights. If you licensed translation rights you may only translate this content into the languages you requested. A professional translator must perform all translations and reproduce the content word for word preserving the integrity of the article. If this license is to re-use 1 or 2 figures then permission is granted for non-exclusive world rights in all languages.

16. **Posting licensed content on any Website**: The following terms and conditions apply as follows: Licensing material from an Elsevier journal: All content posted to the web site must maintain the copyright information line on the bottom of each image; A hyper-text must be included to the Homepage of the journal from which you are licensing at http://www.sciencedirect.com/science/journal/xxxxx or the Elsevier homepage for books at http://www.elsevier.com; Central Storage: This license does not include permission for a scanned version of the material to be stored in a central repository such as that provided by Heron/XanEdu.

Licensing material from an Elsevier book: A hyper-text link must be included to the Elsevier homepage at http://www.elsevier.com . All content posted to the web site must maintain the copyright information line on the bottom of each image.

Posting licensed content on Electronic reserve: In addition to the above the following clauses are applicable: The web site must be password-protected and made available only to bona fide students registered on a relevant course. This permission is granted for 1 year only. You may obtain a new license for future website posting.

For journal authors: the following clauses are applicable in addition to the above: Permission granted is limited to the author accepted manuscript version* of your paper.

*****Accepted Author Manuscript (AAM) Definition**: An accepted author manuscript (AAM) is the author's version of the manuscript of an article that has been accepted for publication and which may include any author-incorporated changes suggested through the processes of submission processing, peer review, and editor-author communications. AAMs do not include other publisher value-added contributions such as copy-editing, formatting, technical enhancements and (if relevant) pagination.

You are not allowed to download and post the published journal article (whether PDF or HTML, proof or final version), nor may you scan the printed edition to create an electronic version. A hyper-text must be included to the Homepage of the journal from which you are licensing at http://www.sciencedirect.com/science/journal/xxxxx. As part of our normal production process, you will receive an e-mail notice when your article appears on Elsevier's online service ScienceDirect (www.sciencedirect.com). That e-mail will include the article's Digital Object Identifier (DOI). This number provides the electronic link to the published article and should be included in the posting of your personal version. We ask that you wait until you receive this e-mail and have the DOI to do any posting.

Posting to a repository: Authors may post their AAM immediately to their employer's institutional repository for internal use only and may make their manuscript publically available after the journal-specific embargo period has ended.

Please also refer to Elsevier's Article Posting Policy for further information.

18. **For book authors** the following clauses are applicable in addition to the above: Authors are permitted to place a brief summary of their work online only.. You are not allowed to download and post the published electronic version of your chapter, nor may you scan the printed edition to create an electronic version. **Posting to a repository:** Authors are permitted to post a summary of their chapter only in their institution's repository.

20. **Thesis/Dissertation:** If your license is for use in a thesis/dissertation your thesis may be submitted to your institution in either print or electronic form. Should your thesis be published commercially, please reapply for permission. These requirements include permission for the Library and Archives of Canada to supply single copies, on demand, of the complete thesis and include permission for UMI to supply single copies, on demand, of the complete thesis. Should your thesis be published commercially, please reapply for permission.

Elsevier Open Access Terms and Conditions

Elsevier publishes Open Access articles in both its Open Access journals and via its Open Access articles option in subscription journals.

Authors publishing in an Open Access journal or who choose to make their article Open Access in an Elsevier subscription journal select one of the following Creative Commons user licenses, which define how a reader may reuse their work: Creative Commons Attribution License (CC BY), Creative Commons Attribution – Non Commercial - ShareAlike (CC BY NC SA) and Creative Commons Attribution – Non Commercial – No Derivatives (CC BY NC ND)

Terms & Conditions applicable to all Elsevier Open Access articles:

Any reuse of the article must not represent the author as endorsing the adaptation of the article nor should the article be modified in such a way as to damage the author's honour or reputation.

The author(s) must be appropriately credited.

If any part of the material to be used (for example, figures) has appeared in our publication with credit or acknowledgement to another source it is the responsibility of the user to ensure their reuse complies with the terms and conditions determined by the rights holder.

Additional Terms & Conditions applicable to each Creative Commons user license:

CC BY: You may distribute and copy the article, create extracts, abstracts, and other revised versions, adaptations or derivative works of or from an article (such as a translation), to include in a collective work (such as an anthology), to text or data mine the article, including for commercial

purposes without permission from Elsevier

CC BY NC SA: For non-commercial purposes you may distribute and copy the article, create extracts, abstracts and other revised versions, adaptations or derivative works of or from an article (such as a translation), to include in a collective work (such as an anthology), to text and data mine the article and license new adaptations or creations under identical terms without permission from Elsevier

CC BY NC ND: For non-commercial purposes you may distribute and copy the article and include it in a collective work (such as an anthology), provided you do not alter or modify the article, without permission from Elsevier

Any commercial reuse of Open Access articles published with a CC BY NC SA or CC BY NC ND license requires permission from Elsevier and will be subject to a fee.

Commercial reuse includes:

- Promotional purposes (advertising or marketing)

- Commercial exploitation (e.g. a product for sale or loan)

- Systematic distribution (for a fee or free of charge)

Please refer to Elsevier's Open Access Policy for further information.

21. Other Conditions:

v1.7

If you would like to pay for this license now, please remit this license along with your payment made payable to "COPYRIGHT CLEARANCE CENTER" otherwise you will be invoiced within 48 hours of the license date. Payment should be in the form of a check or money order referencing your account number and this invoice number 501333663. Once you receive your invoice for this order, you may pay your invoice by credit card. Please follow instructions provided at that time.

Make Payment To:

Gratis licenses (referencing $0 in the Total field) are free. Please retain this printable license for your reference. No payment is required.

Copyright Clearance Center

RightsLink®

WILEY

Title: Relationship of computed tomography perfusion and positron emission tomography to tumour progression in malignant glioma

Author: Timothy P. C. Yeung,Slav Yartsev,Ting-Yim Lee,Eugene Wong,Wenqing He,Barbara Fisher,Lauren L. VanderSpek,David Macdonald,Glenn Bauman

Publication: Journal of Medical Radiation Sciences

Publisher: John Wiley and Sons

Date: Jan 16, 2014

© 2014 The Authors. Journal of Medical Radiation Sciences published by Wiley Publishing Asia Pty Ltd on behalf of Australian Institute of Radiography and New Zealand Institute of Medical Radiation Technology.

User ID

Password

☐ Enable Auto Login

LOGIN

Forgot Password/User ID?

If you're a copyright.com user, you can login to RightsLink using your copyright.com credentials. Already **a RightsLink user** or want to learn more?

Open Access Article

Permission is not required for **non-commercial** reuse. For **commercial** reuse, please hit the "back" button below and select the most appropriate **commercial** requestor type before completing your order.

BACK   CLOSE WINDOW

Appendix E: Membership of the PERNO Study Group

Steering Committee

Baruzzi A. (Chair), Albani F., Calbucci F., D'Alessandro R., Michelucci R. (IRCCS Institute of Neurological Sciences, Bologna, Italy), Brandes A. (Department of Medical Oncology, Bellaria-Maggiore Hospitals, Bologna, Italy), Eusebi V. (Department of Hematology and Oncological Sciences "L. & A. Seràgnoli", Section of Anatomic Pathology at Bellaria Hospital, Bologna, Italy), Ceruti S., Fainardi E., Tamarozzi R. (Neuroradiology Unit, Department of Neurosciences and Rehabilitation, S. Anna Hospital, Ferrara, Italy), Emiliani E. (Istituto Oncologico Romagnolo, Department of Medical Oncology, Santa Maria delle Croci Hospital, Ravenna, Italy), Cavallo M. (Division of Neurosurgery, Department of Neurosciences and Rehabilitation, S. Anna Hospital, Ferrara, Italy).

Executive Committee

Franceschi E., Tosoni A. (Department of Medical Oncology, Bellaria-Maggiore Hospitals, Bologna, Italy), Cavallo M. (Division of Neurosurgery, Department of Neurosciences and Rehabilitation, S. Anna Hospital, Ferrara, Italy), Fiorica F. (Department of Radiation Oncology, S. Anna Hospital, Ferrara, Italy), Valentini A. (Division of Neurosurgery, Nuovo Ospedale Civile S. Agostino-Estense, Baggiovara, Modena, Italy), Depenni R. (Department of Oncology, Policlinico di Modena, Italy), Mucciarini C. (Department of Oncology, Ramazzini Hospital, Carpi, Modena, Italy), Crisi G. (Department of Neuroradiology, Maggiore Hospital, Parma, Italy), Sasso E. (Department of Neurological Sciences, Maggiore Hospital, Parma, Italy), Biasini C., Cavanna L. (Department of Oncology and Hematology, Guglielmo da Saliceto Hospital, Piacenza, Italy), Guidetti D. (Department of Neurology, Guglielmo da Saliceto Hospital, Piacenza, Italy), Marcello N., Pisanello A. (Department of Neurology, Istituto in tecnologie avanzate e modelli assistenziali in oncologia, IRCCS, S. Maria Nuova

Hospital, Reggio Emilia, Italy), Cremonini A.M., Guiducci G. (Division of Neurosurgery, M. Bufalini Hospital, Cesena, Italy).

Registry Coordination Office: de Pasqua S., Testoni S. (IRCCS Institute of Neurological Sciences, Bologna, Italy).

Participants

Agati R., Ambrosetto G., Bacci A., Baldin E., Baldrati A., Barbieri E., Bartolini S., Bellavista E., Bisulli F., Bonora E., Bunkheila F., Carelli V., Crisci M., Dall'Occa P., Ferro S., Franceschi C., Frezza G., Grasso V., Leonardi M., Morandi L., Mostacci B., Palandri G., Pasini E., Pastore Trossello M., Poggi R., Riguzzi P., Rinaldi R., Rizzi S., Romeo G., Spagnolli F., Tinuper P., Trocino C. (Bologna), Dall'Agata M., Frattarelli M., Gentili G., Giovannini A., Iorio P., Pasquini U., Galletti G., Guidi C., Neri W., Patuelli A., Strumia S. (Forlì-Cesena), Faedi M., (IRCCS Istituto Scientifico Romagnolo per lo Studio e la Cura dei Tumori), Casmiro M., Gamboni A., Rasi F. (Faenza R.A.), Cruciani G. (Lugo, RA), Cenni P., Dazzi C., Guidi A.R., Zumaglini F. (Ravenna), Amadori A., Pasini G., Pasquinelli M., Pasquini E., Polselli A., Ravasio A., Viti B. (Rimini), Sintini M. (Cattolica, RN), Ariatti A., Bertolini F., Bigliardi G., Carpeggiani P., Cavalleri F., Meletti S., Nichelli P., Pettorelli E., Pinna G., Zunarelli E. (Modena), Artioli F., Bernardini I., Costa M., Greco G., Guerzoni R., Stucchi C. (Carpi M.O.), Iaccarino C., Ragazzi M., Rizzi R., Zuccoli G. (Istituto di Ricovero e Cura a Carattere Scientifico, Reggio Emilia), Api P., Cartei F., Colella M., Fallica E., Farneti M., Frassoldati A., Granieri E., Latini F., Monetti C., Saletti A., Schivalocchi R., Sarubbo S., Seraceni S., Tola M.R., Urbini B., Zini G. (Ferrara), Giorgi C., Montanari E. (Fidenza P.R.), Cerasti D., Crafa P., Dascola I., Florindo I., Giombelli E., Mazza S., Ramponi V., Servadei F., Silini EM., Torelli P. (Parma), Immovilli P., Morelli N., Vanzo C. (Piacenza), Nobile C. (Padova).

Curriculum Vitae of Timothy Pok Chi Yeung

Name:	Timothy Pok Chi Yeung
Post-secondary Education and Degrees:	The University of Western Ontario London, Ontario, Canada 2009 - 2014 PhD
	University of Toronto Toronto, Ontario, Canada 2003 - 2008 BSc (Med. Rad. Sci)
	The Michener Institute for Applied Health Sciences Toronto, Ontario, Canada 2003-2008 Diploma of Health Sciences
Honours and Awards:	Canadian Cancer Society "Celebrating Impact in Community Outreach" Award 2014
	The 11th Annual Oncology Research & Education Day Poster Award 2014
	CIHR Doctoral Research Award 2011-2014
	Third Prize, Poster Competition, 10th Imaging Network Ontario Symposium 2012
	Ontario Graduate Scholarship (Declined) 2011
	CIHR Institute of Cancer Research Travel Award Competition 2010
	CIHR Master's Award: Frederick Banting and Charles Best Canada Graduate Scholarship 2010-2011
	Western Graduate Scholarship 2010-2014

CIHR Strategic Training Program in Cancer Research and Technology Transfer Program (CIHR-STP)
2009-2014

Schulich Graduate Scholarship
2009-2010

Related Work Experience

Research Assistant
Princess Margaret Hospital & Spatio-Temporal Targeting and Amplification of Radiation Response (STTARR) Program
2008-2009

Undergraduate Thesis Project
London Regional Cancer Program, London Health Sciences Centre
2007-2008

Radiation Therapy Student
London Regional Cancer Program, London Health Sciences Centre
2007-2008

Summer Student Research Assistant
The Michener Institute for Applied Health Sciences
2006

Publications:

Published or Accepted Refereed Papers

1. **Yeung TPC**, Dekaban M, De Haan N, Morrison L, Hoffman L, Chen X, Yartsev S, Bauman G, Lee TY. Improving quantitative CT perfusion parameter measurements using principal component analysis. 2014;21:624-632.
2. **Yeung TPC**, Yartsev, Lee TY, Wong E, He W, Fisher B, VanderSpek L, Macdonald D, Bauman G. Relationship of computed tomography perfusion and positron emission tomography to tumour progression in malignant glioma. *Journal of Medical Radiation Sciences*. 2014:61:4-13.
3. **Yeung TPC,** Yartsev S, Bauman G, He W, Fainardi E, Lee TY. The Effect of scan duration on the measurement of perfusion parameters in CT perfusion studies of brain tumours. *Academic Radiology*. 2013;20(1):59-65.
4. **Yeung TPC**, Yartsev S, Rodrigues G, Bauman G. Image-guidance strategy for localized prostate cancer using setup corrections and anatomical characteristics. *Journal of Medical Imaging and Radiation Oncology*. 2011;55(2):220-228.
5. Bandali K, Niblett B, **Yeung TPC**, Gamble P. Beyond curriculum: embedding interprofessional collaboration into academic culture. *Journal of Interprofessional Care*,2011;25(1)75-76.

Completed Manuscripts

1. Yeung TPC, Kurdi M, Wang Y, Al-Khazraji B, Morrison L, Hoffman L, Jackson D, Crukley C, Lee TY, Bauman G, Yartsev S. CT perfusion imaging as an early biomarker of differential response to stereotactic radiosurgery". Submitted to *PLOS ONE* in July 2014
2. Yeung TPC, Wang Y, Urbini B, Yartsev S, Bauman G, Lee TY, Fainardi E, and the Project of Emilia-Romagna region on Neuro-Oncology (PERNO) study group. Treatment monitoring in high-grade gliomas: A serial CT perfusion and MR study". To be submitted to the *Journal of Neuro-Oncology* in September 2014

Book Chapter

1. So A, Stewart EE, d'Esterre CD, **Yeung TPC**, Bauman G, Jensen NKG, Wong E, Lee T-Y. (2013). Chapter 2: CT Perfusion: Principles, Implementations and Clinical Applications. In Saba L and Suri JS (Editors.) Multi-detector CT Imaging: Principles, Head, Neck and Vascular Systems. CRC Press. ISBN-13: 978-1439893807.

Refereed Abstracts

1. **Yeung TPC**, Al-Khazraji B, Morrison L, Hoffman L, Jackson D, Lee TY, Yartsev S, Bauman G. Distinguishing responders from non-responders to Bevacizumab using CT perfusion. *Neuro-oncology*, 2013;15, supplement 3:OM-076.
2. **Yeung TPC**, Al-Khazraji B, Morrison L, Hoffman L, Jackson D, Lee TY, Bauman G, and Yartsev S. Monitoring vascular response to stereotactic radiosurgery in a brain tumour model using CT perfusion. *Radiotherapy and Oncology*. 2013;108(supplement 1):S25.
3. **Yeung TPC**, Morrison L, Hoffman L, Lee TY, Bauman G, Yartsev S. CT perfusion study of vascular response to stereotactic radiosurgery in a preclinical model of glioma. *Neuro-oncology*. 2012;14(6,supplement):vi130.
4. Yeung I, Haider M, Gonzalez N, Kim S, Coolens C, **Yeung T**, Driscoll B, Jaffray D. The DCE Tool: A free analysis tool for DCE CT and MR Studies. *Medical Physics* 2011:38,3405.
5. **Yeung TPC**, Wong E, Lee TY, Yartsev S, Bauman G. Initial findings of perfusion and metabolic imaging of malignant glioma in radiation therapy. *International Journal of Radiation Oncology Biologic Physics*,2010;78(3,supplement),S279.
6. **Yeung TPC**, Yartsev S, Rodrigues G, and Bauman G. Characterization and prediction of patient positioning corrections evaluated with daily image-guidance for prostate cancer treatments using helical tomotherapy. *Journal of Medical Imaging and Radiation Sciences*,2009,40(2),79.

Newspaper and Media

1. Progress and Promise in Cancer Research, Hope for the future. Part 5: Clinical Research. http://www.youtube.com/watch?v=lCylaPSAgy0
2. Research Information Outreach Team. Canadian Cancer Society. Progress and promise in cancer research. *The Londoner*. Dec 27, 2012.
3. Coschi C, **Yeung TPC**. Debunking myths about cancer research. *The Londoner*. May 24, 2012.
4. **Yeung TPC**, Funding Unconventional BUT Innovative Ideas in Cancer Research. *The Londoner*.
5. Webcast, The DCE Tool; DCE-CT Analysis Tutorial, Webcast Part 1. http://www.youtube.com/watch?feature=player_embedded&v=T-N23D9CQfY
6. Webcast, The DCE Tool; DCE MR Analysis Tutorial, Webcast Part 2. http://www.youtube.com/watch?v=4yclqSfES7Y